# Structural Studies using Synchrotron X-Ray Powder Diffraction and Other Techniques.

**By**

Anthony Martin Thomas Bell

*Wolfson College, Cambridge*



**For the degree of Doctor of Philosophy in the University of Cambridge**

**December 1998**

**Structural Studies using Synchrotron X-Ray Powder Diffraction and Other Techniques.**

**A.M.T. Bell.**

**Summary of thesis.**

Chapter 1 gives an introduction to X-ray and neutron powder diffraction and the use of these techniques for crystal structure determination and refinement. The Rietveld structure refinement method is described and examples of different methods of structure determination from powder diffraction data are given. The techniques of EXAFS and Mössbauer spectroscopy, which were used to provide additional structural information, are also introduced. Chapter 2 describes the different radiation sources and experimental techniques used in this work.

Chapter 3 describes a structural study of magnetite, $Fe_3O_4$, below the Verwey phase transition (~120 K). The P2/c structure of $Fe_3O_4$ at 60 K has been refined with lattice parameters of a = 5.9412(3) Å, b = 5.9290(3) Å, c = 16.789(1) Å and $\beta = 90.196(4)^\circ$. A variable temperature study of the $Fe_3O_4$ lattice parameters between 2-280 K shows this transition is first-order. An EXAFS study between 80-270 K shows that there is no significant change in the average Fe-O distance in $Fe_3O_4$ around the transition.

Chapter 4 describes a structural study on a material related to magnetite, $Fe_2OBO_3$. Two phase transitions have been found for this material. The first of these is due to magnetic ordering and takes place at ~155 K. The second is due to charge ordering and takes place at 315 K, this is a structural ($P2_1/c \Leftrightarrow Pnma$) transition.

Chapter 5 describes a resonant scattering experiment done on CsI. Resonant scattering parameters have been refined from synchrotron X-ray powder diffraction data collected at room temperature and at 4 K close to the Cs and I K-edges. The refined $f'$ parameters are -6.2(2) e/atom (Cs, $\lambda$ = 0.3453 Å), -9.0(1) e/atom (I, $\lambda$ = 0.374105 Å) and -6.2(2) e/atom (I, 4 K, $\lambda$ = 0.37367 Å).

Chapter 6 describes the *ab initio* structure determination of 4-(2'3'4'-trifluorophenyl)-1235 dithiadiazolyl ($C_7S_2N_2F_3H_2$; $P2_1/n$, a = 11.543(4) Å, b = 20.666(8) Å, c = 7.045(2) Å and $\beta = 100.35(4)^\circ$) using synchrotron X-ray powder diffraction data. A global optimisation method was used to provide a starting model for Rietveld refinement.

## Declaration.

The work described in this thesis was carried out at the Department of Chemistry, University of Cambridge, during the period October 1995 to December 1998. This thesis represents the author's original work, except where otherwise stated, and no part of it has been submitted for a degree at any other university. Prior to the submission of this thesis, some work has been published, as listed in Appendix B at the end of the thesis. In accordance with the regulations of the Degree Committee of Physics and Chemistry, this thesis does not exceed 60,000 words in length.

A.M.T.Bell

*If I have seen further it is by standing on the shoulders of Giants.*

**Isaac Newton**

**This thesis is dedicated to my beautiful girlfriend Shelley.**

## Acknowledgements.

Thanks to my supervisor Dr. Paul Attfield for all of his help, advice and optimistic encouragement with my work. I would also like to thank my industrial supervisor, Prof. Bob Cernik for all his encouragement with my return to university at such an advanced age.
Thanks to the EPSRC for a studentship, Daresbury Laboratory for a CASE award and the University of Cambridge for an Isaac Newton award.
I would also like to thank the following people:-
**At CCLRC Daresbury Laboratory;** Dr Graham Bushnell-Wye, Dr Mark Roberts and Dr Chiu Tang for help with synchrotron X-ray powder diffraction, Bob Bilsborrow, Kan Cheung Cheung and Dr Fred Mosselmans for help with EXAFS.
**At CCLRC Rutherford Appleton Laboratory;** Prof. Bill David and Dr Ken Shankland for their global optimisation software.
**At the Université du Maine, Le Mans, France;** Prof. Marc Leblanc and Prof. Jean-Marc Greneche and everyone else in the Laboratoire des Fluorures and Laboratoire de Physique de L'Etat Condensé for all their interest in my Iron Borate work and their very kind hospitality on my visits to Le Mans, merci beaucoup mes amis.
**In Grenoble, France;** Dr Eric Dooryhee, Dr Andy Fitch and Dr Gavin Vaughan for their assistance with powder diffraction at the ESRF and Dr Alan Hewat and Dr Paulo Radaelli for assistance with powder diffraction at the ILL.
**In the Chemistry Department;** Dr Jeremy Rawson and Nick Smith for their help with the 4-(2'3'4'-trifluorophenyl)-1235 dithiadiazolyl structure determination. Steve Wilkinson and Zac Hassan and the rest of the department technical staff for help when I got my hands dirty with some chemistry.
And last but no means least everyone who has been there with me in the dungeon over three long and weary years.
Dr Adrian Wright for computer wizardry, collecting the data for me on D20 at the ILL and for help with EXAFS data collection.
Lide Rodriguez-Martinez for help with magnetisation and resistivity measurements and EXAFS data collection.
Judith McAllister for help with EXAFS data collection.
Joost van Duijn for being there as we waited for the cryostat to cool down at the ESRF.
Jon Wright for his contacts at the Rutherford Appleton Laboratory.
Dan Pederzolli for making Blackadder such an integral part of my working life in Cambridge
and all the other members of the Attfield group past and present. Dr Jon Chapman, Dr Helmut Ehrenberg, Dr Anna-Maria Ferrari, Dr Andrei Kharlanov, Abbie McLaughlin, Prof. Caridad Ruiz-Valero, Prof. Kazuya Suzuki and Dr Gernot Wltschek.

# Table of Contents.

# Chapter 1. Crystal structures from powder samples.

## 1.1. Diffraction.

Diffraction takes place by scattering and subsequent interference of radiation from a regular array of scattering centres. In a crystalline solid the atoms are arranged in a regular repeating pattern, if radiation with a wavelength of the same order of magnitude of the interatomic distances is used the regular array of atoms can act as a 3-dimensional diffraction grating. The Bragg treatment of the atoms in a crystalline solid considers that planes of these atoms can act as a mirror from which radiation can be reflected, when radiation of wavelength $\lambda$ strikes these planes at angle $\theta$ constructive interference can be observed between radiation reflected from planes of atoms with an interplanar spacing of $\mathbf{d_{hkl}}$ so that the **Bragg law** is satisfied so that

$$\lambda = 2\, d_{hkl} \sin\theta$$

The values of $d_{hkl}$ depend on the size and crystal symmetry of the unit cell. The intensity of the diffracted beam is dependent on the positions of the atoms in the unit cell and is proportional to the square of the amplitude of the structure factor $\mathbf{F_{hkl}}$

$$\mathbf{F_{hkl}} = \sum_n s_n . \left[ \exp\left( \frac{-B \sin^2\theta}{\lambda^2} \right) \right] . \exp\left[ 2\pi i \left( h x_n + k y_n + l z_n \right) \right]$$

$\mathbf{s_n}$ is the general scattering factor for atom n, this depends on the nature of the scattering and the

radiation used, $\mathbf{x_n}$, $\mathbf{y_n}$ and $\mathbf{z_n}$ are the fractional co-ordinates in the unit cell and $\mathbf{[exp(-Bsin^2\theta/\lambda^2)]}$ is the Debye-Waller factor which takes account of the thermal motion of the atomic scatterers. The temperature factor, **B**, is related to the mean square displacement of the atom **U** by $B = 8\pi^2U$. This thermal factor is usually described as isotropic ($\mathbf{U_{iso}}$) which describes a uniform sphere of thermal motion.

### 1.1.1. X-ray diffraction.

If X-rays are used as the radiation source for a scattering experiment the scattering centre is the electron cloud around each atom. Interference takes place from X-rays scattered by the electron cloud (diameter of about 1 Å, similar to the X-ray wavelength), interference is between X-rays scattered from different parts of the atom. The scattered amplitude decreases rapidly as the angle $\theta$ between the incident and scattered radiation decreases. The scattering is also proportional to the square of the density of the electron cloud around an atom and is therefore proportional to $Z^2$ where Z is the atomic number of an atom. In an X-ray scattering experiment the scattering due to light (low Z) atoms can be difficult to detect, especially in the presence of heavy (high Z) atoms.

### 1.1.2. Diffraction of X-rays by single crystals and powders.

Diffraction of a monochromatic X-ray beam by a single crystal (a single crystal has a continuous and unbroken regular array of atoms throughout the sample) will produce a pattern of spots showing the positions of the Bragg reflections. From the positions and intensities of these diffraction spots it is possible to determine the crystal structure of this material.

However, not all materials can be prepared with suitably large crystals for single crystal structure determination and sometimes only crystalline powdered materials are available for X-ray diffraction analysis. In a crystalline powder the sample consists of an aggregation of a large number of small crystals (crystallites) which lie in all orientations. The spotty Bragg reflections from these crystallites merge to produce diffraction cones (see Figure 1.1). By use of a suitable detector a 1-dimensional diffraction pattern can be produced by the diffraction of X-rays by a crystalline powder.

*Figure 1.1. Single crystal and powder X-ray diffraction.*

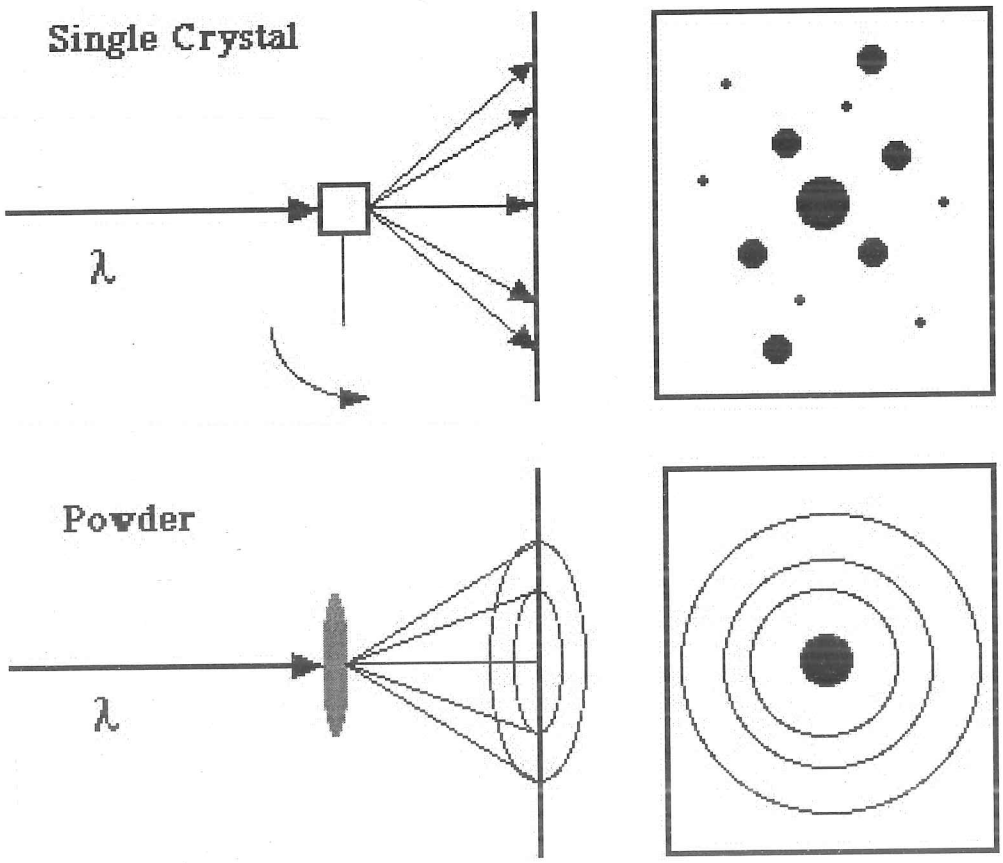


X-ray powder diffraction is a useful technique used to characterise material prepared by solid

state chemists. Materials with different crystal structures have different characteristic powder diffraction patterns and this technique can be used to check phase purity. X-ray powder diffraction is also a very useful technique for determining lattice parameters as the positions of the Bragg reflections can be more accurately determined from the positions of the diffraction cones than from single crystal diffraction spots.

The merging of the diffraction spots to form cones means that except for very simple structures there is usually not sufficient information in the powder diffraction pattern to determine a crystal structure by single crystal methods. However, if a suitable starting model is available crystal structures can be refined from X-ray powder diffraction data by the Rietveld method, see section 1.2.

With the advent of Synchrotron Radiation (SR) X-ray sources (see section 2.2) over the last 15-20 years X-ray powder diffraction has become a much more powerful technique for crystal structure determination. High flux from SR sources mean that weaker reflections in the powder diffraction pattern are observable. The parallel beam geometry results in less instrumental peak broadening. High energy resolution of modern SR monochromators results in an almost completely monochromatic X-radiation instead of $K\alpha_1\alpha_2$ doublets. Therefore there is less overlap between neighbouring Bragg reflections and intensities of Bragg reflections can be determined more accurately, this is good for structure determination using structure factors determined from these intensities.

### 1.1.3. Neutron diffraction.

An alternative radiation source for diffraction experiments is **neutrons** (see section 2.5). Neutrons are scattered by interaction with atomic nuclei (diameter $10^{-5}$ Å), the interference seen

for X-rays due to scattering from different parts of the atom is not seen and there is no drop in intensity as θ increases. The neutron nuclear scattering factor for an atom n is the coherent scattering length ($b_n$), the value of $b_n$ for a particular element is dependent on the isotopic composition of that element, different isotopes can have different scattering lengths.

Neutron diffraction experiments tend to be better for structure determination as there is no fall off in diffracted intensity with increasing θ and therefore more diffraction peaks can usually be obtained from neutrons compared to X-rays. Also the scattering lengths for different isotopes does not follow a regular trend with increase in Z and consequently scattering from light atoms can be greater than that from heavier atoms and it is also possible to easily differentiate between atoms with similar Z values.

However, neutrons are much more penetrating than X-rays and consequently scatter much less readily than X-rays. Therefore larger samples are usually needed for neutron diffraction (up to 10 g) experiments compared to the milligrams that can be used for X-ray diffraction. Also neutron sources are less intense than X-ray sources and are very expensive to operate so that much more time and effort is required to collect neutron diffraction data than X-ray diffraction data.

In addition to nuclear scattering neutrons can also undergo magnetic scattering by interaction with unpaired electrons. The form factor for magnetic neutron scattering is

$$s_n = -(e^2\gamma/mc^2)f_m.S_n$$

$s_n$ is the resolved component of the spin vector on the hkl reflection plane, m is the electron mass, e is the charge on an electron, γ is the nuclear magnetic moment and $f_m$ is the magnetic amplitude form factor. The magnetic scattering factor vector $s_n$ also gives rise to diffraction

peaks dependent on the ordering of magnetic domains in the solid and these magnetic peaks may or may not be coincident with the nuclear peaks. The magnetic form factor $f_m$ for neutron scattering for unpaired electrons is analogous to the form factor for scattering of electrons by X-rays and consequently the intensity of the magnetic interaction decreases with increase in θ.

### 1.2. Rietveld method.

With the advent of the **Rietveld method** (Rietveld, 1969), and the use of the whole powder diffraction profile rather than intensities extracted from individual Bragg reflections, it became possible to use powder diffraction to determine lower symmetry crystal structures with more atoms than before. This method is a least squares profile refinement method named after the Dutch scientist, H.M.Rietveld, who developed the method. It was originally developed for nuclear and magnetic structure refinements from neutron powder diffraction data but has since been extended to X-ray structures.

This method uses the profile intensities obtained from a step-scanned powder diffraction pattern for structure refinement. A function (e.g. pseudo-Voigt) is used to describe the peak shape for each Bragg reflection and the whole powder diffraction pattern is calculated using the following formula

$$y_i = (|F_{hkl}|^2 \times j_{hkl} \times L_{hkl} \times G_{hkl}) + B_i$$

$y_i$ is the profile intensity at each point i in the powder diffraction pattern,

$F_{hkl}$ is the structure factor of each Bragg reflection hkl, this is proportional to the square root of

the reflection intensity and is a function of the electron density in the crystal structure for each hkl plane.

$j_{hkl}$ is the multiplicity of each reflection, as determined from the crystallographic space group.

$L_{hkl}$ is the Lorentz factor, this is determines how the overall diffracted intensity varies with diffraction angle and the polarisation of the X-rays.

$G_{hkl}$ is the peak shape function. For Daresbury and ESRF synchrotron radiation powder diffraction data a pseudo-Voigt peak shape function is usually used. This function is a mixture of Gaussian and Lorentzian functions, the mixing parameter can be refined in the Rietveld refinement process. For D2B ILL neutron powder diffraction a pseudo-Voigt function with only a small Lorentzian component is used. For the lower resolution D20 ILL neutron powder diffraction a purely Gaussian profile function is used.

$B_i$ is the non-Bragg scattered background at point i.

This calculated pattern is fitted to the observed powder pattern and least squares refinement is used to vary the calculated pattern until the refinement converges to give a best fit between the observed and calculated patterns. The residual

$$\chi^2 = \Sigma_i (y_{i,obs} - y_{i,calc})^2 / y_{i,obs}$$

is minimised to get a close a match as possible between the observed and calculated patterns.

The quality of this match is given by the following R factors.

$$R_p = \frac{\sum_i |y_{i,obs} - y_{i,calc}|}{\sum_i y_{i,obs}}$$

$$R_{wp} = \sqrt{\frac{\sum_i w_i \left[ y_{i,obs} - y_{i,calc} \right]^2}{\sum_i w_i y_{i,obs}^2}}$$

Where $y_{i,obs}$ and $y_{i,calc}$ are the observed and calculated intensities at each datapoint i and $w_i$ is the weighting for each datapoint.

This method refines the structural parameters (atomic co-ordinates, site occupancies, temperature factors and lattice parameters) from an initial trial structure to produce the structure of the material giving the observed diffraction pattern. Other profile parameters must also be refined, these include the scale factor, 2θ zeropoint and parameters describing the peak shape and width. The starting model for Rietveld refinement must be a reasonably close match to the true crystal structure, if this is not so then it is probable that the least squares refinement process will either diverge or find a local rather than global minimum in the weighted sum and consequently result in a chemically unrealistic final structure. Care must always be taken at the end of a Rietveld refinement that the final structure is physically and chemically sensible. See Young (1995) for a more mathematical description of this method.

A related technique is the pattern decomposition method of Pawley (Pawley, 1981) and Le Bail (Le Bail et al, 1988). This is similar to the Rietveld method except that no structural parameters are refined. This method is useful in extracting structure factors for *ab-initio* structure determinations and also for more accurate determination of lattice parameters from powder diffraction data.

Most of the Rietveld refinements described in this thesis have been done using the **GSAS** (Larson and von Dreele) **g**eneral **s**tructural **a**nalysis **s**oftware. This software was originally developed for time of flight neutron refinements but has now been adapted for continuous

wavelength X-ray and neutron refinements. Refinements can be done with more than one dataset, e.g. the same structure can be refined from synchrotron X-ray and neutron data.

Some Rietveld refinements have also been done using the **MPROF** software from the Daresbury Powder Diffraction Program Library (PDPL; Murray et al, 1990). In this software only one dataset can be fitted at a time.

### 1.3. Rietveld structure refinements.

Crystal structures can be refined by the Rietveld method using a known isomorphous structure as the starting model. For example the structure of $KFeSi_2O_6$ was refined (Bell et al, 1994a) using the known isomorphous structure of $KAlSi_2O_6$ as a starting model with the co-ordinates of Al used for the Fe site. The starting model need not be in exactly the same space group provided the space group of the starting model and the structure to be determined are related. For example the room temperature crystal structure of $Fe_2BO_4$ (Attfield et al, 1992; see chapter 4) was refined from a starting model made by lowering the Pnma orthorhombic structure of warwickite ($Mg_{1.5}Ti_{0.5}BO_4$; Takeuchi et al, 1950) to $P2_1/c$ monoclinic.

The Rietveld method was originally determined for structure refinement using data collected using **neutrons** (see section 2.5). High resolution neutron powder diffraction was at the forefront of structure determination of the high temperature superconductor $YBa_2Cu_3O_{7-x}$ (Jorgensen et al, 1987). The large elemental contrast for oxygen in neutron diffraction experiments was crucial in determination of the O stoichiometry, this was critical in determining whether these materials were superconducting or not.

## 1.4. *ab-initio* structure determination.

The development of **synchrotron radiation** (see section 2.2) sources for X-ray powder diffraction over the last 20 years has also been a great advance in determination of structures from powder data. The high flux and angular resolution obtainable from synchrotron sources makes it much more practicable to determine crystal structures *ab-initio* from powder diffraction data, generating a Rietveld starting model using Patterson and direct methods techniques with software such as SIRPOW (Altomare et al, 1994). The high angular resolution from synchrotron powder data will result in fewer overlapped Bragg reflections and consequently more structure factors can be extracted.

Examples of structures determined *ab-initio* using synchrotron X-ray powder diffraction are the structures of $\alpha$-$CrPO_4$ (Attfield et al, 1988) and the drug cimetidine (Cernik et al, 1991).

It is also possible, if more difficult, to determine structures *ab-initio* from laboratory powder diffraction data, especially if care is taken to remove the $\alpha_2$ component from the X-ray source (Louer, 1993).

## 1.5. Resonant scattering.

The atomic scattering factor for X-rays is

$$s_n = f_o + f' + if''$$

$f_o$ is the normal (Thomson) contribution which depends on the electron distribution and is

wavelength independent.

$f' + if''$ is the resonant contribution, resonant scattering results from electronic transitions from core levels to unoccupied states and is wavelength dependent.

For normal laboratory X-ray diffraction experiments the resonant or anomalous scattering contribution is usually very small. However, the development of SR sources for X-ray powder diffraction has made the technique of resonant X-ray scattering practicable. The accessible energies from "white X-rays" obtainable from SR sources permit the use of many elemental K, L and M absorption edges for resonant scattering experiments. In resonant X-ray diffraction the X-ray wavelength selected is coincident with the absorption edge of the element under study. This technique has been extensively used for elemental or valence contrast studies so that neighbouring elements or ions (which have similar X-ray scattering) can be differentiated more easily. Resonant X-ray scattering at an absorption edge will significantly change the X-ray scattering of this element compared to that away from the edge and therefore the difference in X-ray scattering between these elements will be significantly greater so that they can be distinguished more easily. Figure 1.2 shows schematic energy variations for X-ray absorption and the two resonant scattering terms, $f'$ and $f''$. The broken lines show the same quantities for a higher oxidation state for the same element. If the X-ray energy is close to that of the absorption edge of a particular element the difference in scattering for neighbouring elements or ions the difference in scattering can be experimentally observable.

An example of a resonant scattering is structure refinement of $FeNi_2(BO_3)O_2$ (Attfield et al, 1991). In this structure the occupancies of 4 Fe/Ni octahedral sites have been refined using synchrotron radiation with an energy 16 eV below the Fe K-edge. Attfield (1991, 1996) gives a review of resonant powder X-ray diffraction.

*Figure 1.2. Variation of X-ray absorption (μ), $f'$ and $f''$ with energy, broken and solid lines show curves for different oxidation states of the same element.*

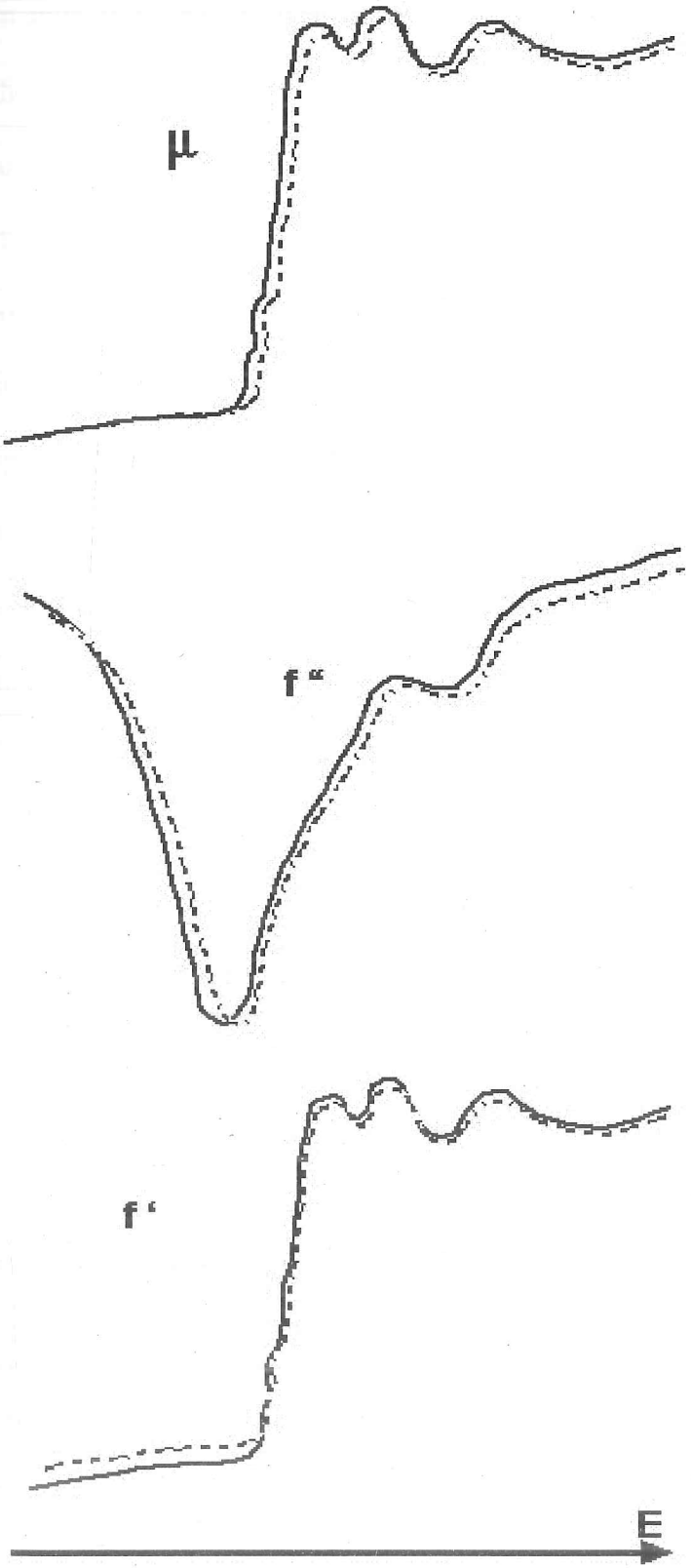

*Figure 1.2. Variation of X-ray absorption ($\mu$), $f'$ and $f''$ with energy, broken and solid lines show curves for different oxidation states of the same element.*

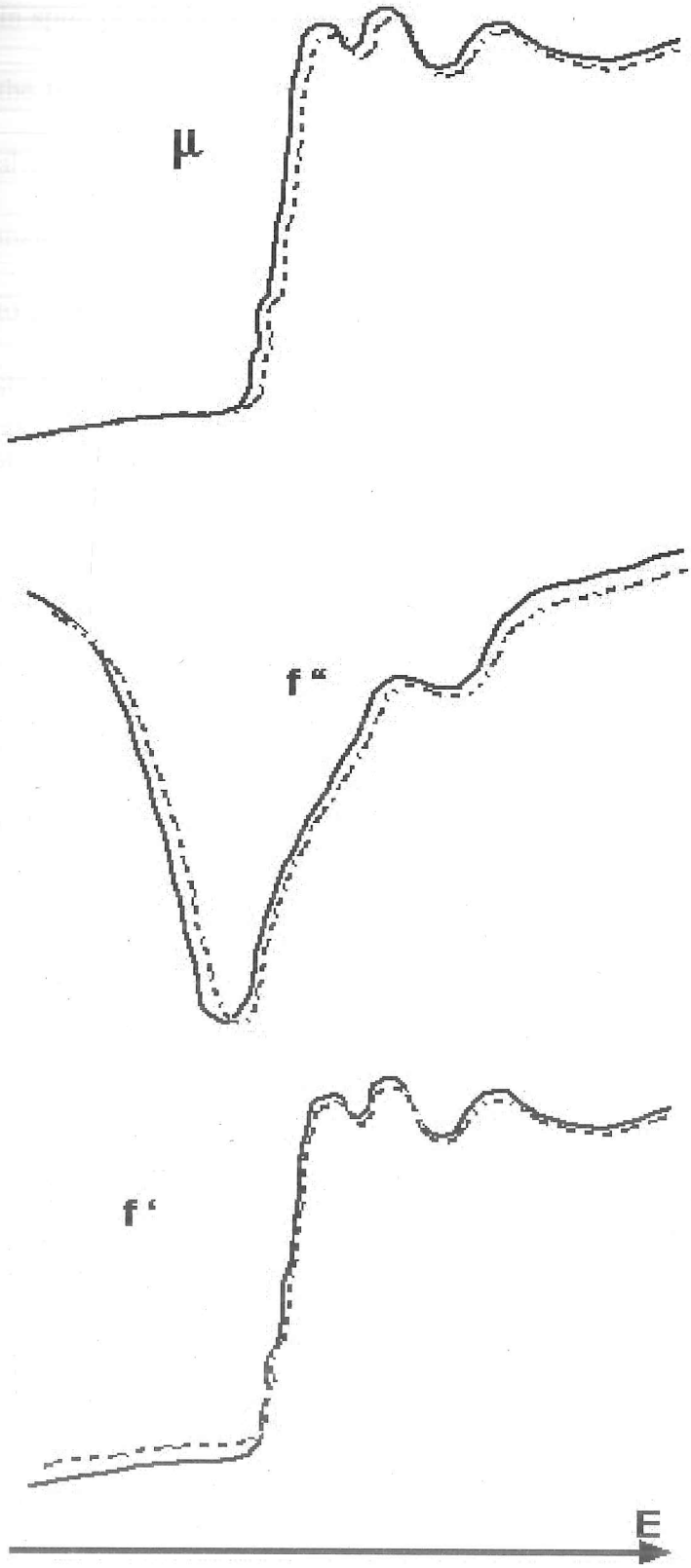

## 1.6. Model building techniques.

In spite of all the advances in solving structures by direct methods from powder diffraction data the technique is always going be limited by the problem of overlapping Bragg reflections. An alternative method of determining crystal structures can be to build a molecular model of the material under study. This model is then moved around many different positions in the unit cell to find a starting position which gives a sufficiently good fit to the observed data to give a starting model for Rietveld refinement. Such techniques take a lot of computing time but with the speed and power of modern computers these methods are now practicable.

These techniques tend to be applied to organic molecules. Organic structures usually consist of atoms with poor X-ray scattering and consequently the powder diffraction data can be limited, also the connectivities of atoms of organic molecules are usually well known and therefore building a molecular model is easy.

The Monte-Carlo method (Harris et al, 1998) involves starting with a structural fragment such as a ring from an organic compound, this fragment is then moved in a random manner around the unit cell until a good match is made to the observed data. Once the position of this fragment has been determined the rest of the molecule can be built on to the fragment and then the position of the whole molecule can be used as a starting model for Rietveld refinement.

### 1.6.1. Global optimisation method.

This method starts with the whole molecule instead of a fragment. The position, orientation and conformation of the molecule within the refined unit cell is postulated and the level of agreement

between the trial structure and the experimental diffraction data quantified by a global optimisation model building method (David et al, 1998).

$$\chi^2 = \sum_h \sum_k [(I_h - c|F_h|^2)(V^{-1})_{hk}(I_k - c|F_k|^2)]$$

where $I_h$ and $I_k$ are Lorentz-polarisation corrected, extracted integrated intensities from the Pawley refinement (Pawley, 1981) of the diffraction pattern, $V_{hk}$ is the covariance matrix from the Pawley refinement, $c$ is a scale factor, and $|F_h|$ and $|F_k|$ are the structure factor magnitudes calculated from the trial structure. The trial structure is then subjected to a global optimisation procedure that seeks to minimise the goodness of fit parameter $\chi^2$ and this trial structure can then be used as a starting model for Rietveld refinement.

The related genetic algorithm method (Csoka et al, 1998) can also generate random mutations in a trial structure to "breed" a structure with a closer match to the experimental data until a Rietveld starting model is generated. As these techniques compare structures with structure factors rather than the whole diffraction pattern this results in much shorter computation times.

### 1.7. Multiple techniques.

Other analytical techniques used in conjunction with powder diffraction can also be of great assistance in structure determination. The structures of two leucite analogues of $K_2MgSi_5O_{12}$ have been determined using synchrotron X-ray powder diffraction in conjunction with electron diffraction and MAS-NMR (Bell et al, 1994b). One analogue had a Ia3d cubic structure which was easily refined using the structure of another isomorphous leucite as a starting model. The

other analogue had a low-symmetry structure that it was not possible to determine purely from the powder data. Electron diffraction provided approximate lattice parameters and $^{29}Si$ MAS-NMR showed that there were 10 different Si sites, this information enabled a starting $P2_1/c$ model to be determined with Si and Mg ordered onto separate sites and this model was used to successfully refine the structure.

The use of both synchrotron radiation and neutron powder diffraction together has also been a great advance in structure determination with the differences in elemental contrast between the two radiation sources. Synchrotron X-rays can be used to accurately determine the positions of heavy (high Z) atoms and neutrons can be similarly used for light (low Z) atoms. A combined synchrotron/neutron study was used to determine *ab-initio* the low temperature structures of the $C_6F_6$:$C_6H_6$ adduct (Williams et al, 1992).

Resonant scattering synchrotron X-ray powder diffraction data collected in conjunction with neutron powder diffraction data has been used to determine the structures of several cuprate high temperature superconductor materials. The high angular resolution from synchrotron sources enables lattice parameters to be accurately determined and the elemental contrast from resonant scattering has enabled site occupancies for different cations to also be determined accurately. Neutron powder diffraction has enabled the co-ordinates of the light oxygen atoms to be determined more precisely, see Marcos et al, (1994) for an example.

## 1.8. EXAFS.

The **EXAFS** (**E**xtended **X**-ray **A**bsorption **F**ine **S**tructure) technique is a synchrotron based technique which can be used to determine the short-range order round an atom. It is complimentary to the diffraction based techniques mentioned above which give the long-range

order.

During X-ray absorption by an atom a photoelectron is ejected, the energy of this electron, E, is dependent on the energy of the incident X-radiation and the type of absorbing atom. The ejected photoelectrons are considered to be travelling as photoelectron waves of wavelength $\lambda_e$. These waves are backscattered from neighbouring atoms (see Figure 1.3) and they interfere either destructively or constructively with outgoing photoelectron waves from the central atom. The nature of the interference depends on the distance between the emitter and backscatterer and on the phase change occurring during the backscattering process. This interference produces a modulation of the absorption cross section of the emitter and is experimentally observed as oscillations in the X-ray absorption spectrum at energies just above the particular absorption edge. EXAFS is commonly measured in transmission mode so that the sample absorption can be directly measured. Section 2.3.3 describes the experimental set up used in this work. The absorption coefficient ($\mu_t$) is measured from the intensities of the incident ($I_o$) and transmitted ($I_t$) beams according to the expression (x = sample thickness).

$$\mu_t x = \ln (I_o/I_t)$$

These EXAFS oscillations are superimposed on the smoothly varying background above the absorption edge and can be extracted by modelling and subtraction of the background $\mu_o(E)$. The EXAFS spectrum, $\chi(E)$, is obtained and normalised using

$$\mu(E) = \mu_o(E)[\chi(E) + 1]$$

*Figure 1.3. Backscattering of photoelectron wave giving rise to EXAFS, A is the absorbing atom and B is the backscattering atom.*

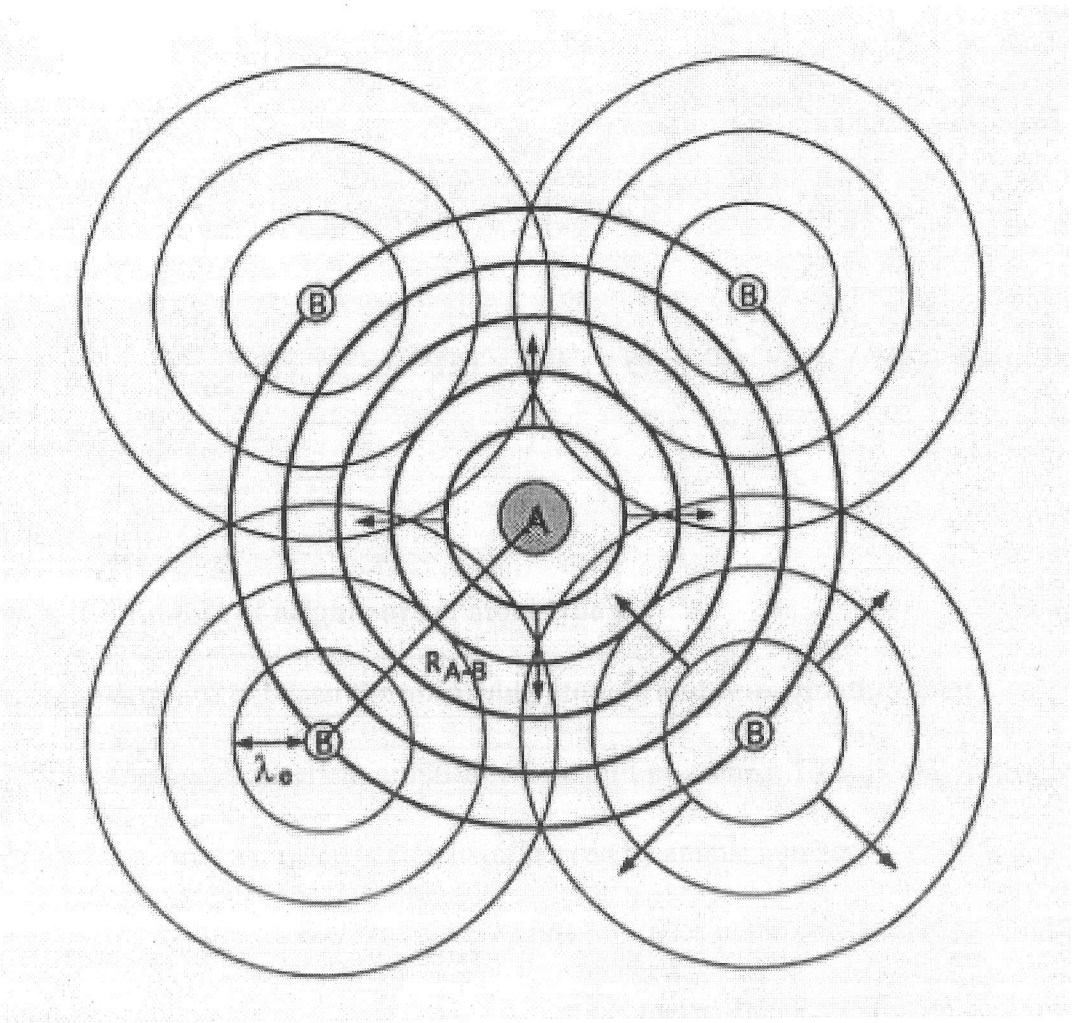


From this equation $\chi(E)$ is a modulation of the theoretical absorption edge without EXAFS structure. This spectrum is theoretical as it cannot be experimentally measured except for monatomic gases at low pressure. The theoretical background is thus obtained by line-fitting of the smooth-line trends of the post-edge region.

Typically EXAFS spectra are expressed in terms of $\chi(k)$, where k is the photoelectron wave vector so that $\chi$ can be related to structural parameters. E and k are related by

$$k = \sqrt{(8\pi mE^2/h^2)} = 2\pi/\lambda_e,$$

where m is the rest mass of the electron, h is Planck's constant, $\lambda_e$ is the photoelectron wavelength and $E = (E_{hv} - E_0)$.

The resulting $\chi(k)$, after various stages of background subtraction, may be modelled using the equation given below (Stern, 1974; Sayers et al, 1971), this was developed for a single-scattering, one-electron, short-range order model:

$$k^n\chi(k) = k^{n-1}\Sigma_j(N_j / r_j^2) \times F_j(k) \times S_i(k) \times \exp(-2\sigma_j^2 k^2 - 2r_j/\Lambda(k)) \times \sin[2kr_j + \phi_{ij}(k)]$$

where:

**$N_j$ is the number of neighbours of atom type j;**

**$r_j$ is the distance between the absorbing atom, i, and co-ordination shell j.**

**$F_j(k)$ is the backscattering amplitude function of atom j:** $F_j(k)$ is only dependent on the type of backscattering atom and is greatly influenced by atomic number.

**$S_i(k)$ is the reduction factor:** This accounts for losses in the backscattering amplitude caused by multiple excitations of the absorber. During photoelectron ejection from a central atom with Z electrons the (Z-1) passive electrons may not remain fully relaxed. The EXAFS amplitude is affected as the ejected photoelectron has less kinetic energy than $(E_{hv} - E_0)$ causing a shift in energy which can be accompanied by a phase shift.

**$\Lambda(k)$ is the inelastic mean free path of the photoelectron:** This is also due to inelastic scattering and approximates amplitude losses due to excitation of neighbouring atoms around the emitter. $\Lambda(k)$ increases as k increases and so damping from this term is greater at lower k.

**$\sigma_j$ is the Debye-Waller factor:** This is another important damping term encompassing thermal

vibrations ($\sigma_{vib}$) and static disorders ($\sigma_{stat}$). $\sigma_j$ is defined as the root mean square displacement of the average nearest-neighbour distance and can be separated into $\sigma_{vib}$ and $\sigma_{stat}$ by a variable temperature study.

**($2kr_j + \phi_{ij}(k)$) is the total phase change:** The first term is the phase shift experienced by travelling a distance $r_j$ to the backscatterer and back. The phase shift on travelling a distance $2r_j$ is given by $2\pi \times 2r_j/\lambda_e$ (i.e. $2kr_j$). $\phi_{ij}(k)$ is the sum of two phase shifts; $\delta_i'(k)$ due to the coulombic potential of the central atom and $\theta_j(k)$ due to the potential of backscattering atom j. Accurate phase shifts are required if the interatomic distances are to be accurately calculated because of their dependence on $r_j$.

This expression for $\chi(k)$ is strictly correct for the K-edge and represents the summation of backscattered waved for all backscattering atoms, j, around a central emitter, i. The Fourier transform of $k^3\chi(k)$ gives a real-space pseudo radial distribution function (PRDF), for atoms around the absorber. The individual peaks in this PRDF correspond to frequencies in $\chi(k)$ or radial co-ordination shells. The distances are slightly shifted to lower values of r because of the undetermined phase shift factor and are thus pseudo distances.

### 1.8.1. EXAFS data analysis.

The Daresbury EXBACK, EXCALIB and EXCURV92 software was used for data analysis. EXCALIB is used to join raw data sets together and to normalise the X-ray intensity against the change in X-ray flux due to the decay of the synchrotron beam with time. EXBACK subtracts the background from the normalised spectrum to leave the oscillations of the post-edge EXAFS region, this background subtracted data is then Fourier transformed to give a radial distribution

function. EXBACK is also used to define the $E_0$ energy where the EXAFS oscillations in the spectrum are judged to start.

EXCURV92 is used to least squares fit a model consisting of shells of atoms around the central scattering atom out to about 10 Å from the central atom, the EXAFS signal is too weak to be detected any further out from the central atom. The EXCURV92 fit is usually done starting with the inner shell of atoms with further shells being added until no more can be fitted, in the least squares fit the number of neighbouring atoms in the shell ($\mathbf{N_j}$), the Debye-Waller factor for the atoms in the shell ($\sigma_j$) and the radial distance from the central atom to the shell ($\mathbf{r_j}$) are refined. The $E_0$ energy term is also refined in EXCURV92.

Figure 3.10 gives an example of a fitted EXAFS spectrum. This technique is not limited to crystalline materials and it can be used to determine short-range structural information from non-crystalline materials.

## 1.9. Mössbauer Spectroscopy.

### 1.9.1. Mössbauer effect.

The Mössbauer effect, which is based on a nuclear resonance, is the emission and absorption of a γ-ray photon without loss of energy due to nuclear recoil and without thermal broadening. The effect is named after its discoverer, R.Mössbauer (Mössbauer, 1958).

This effect is only observable for materials in the solid state. In gases or liquids the emitted γ-ray photons will have energies distributed over a broad energy range due to nuclear recoil, this energy range will also be Doppler broadened due to the motion of the atoms. However, Mössbauer discovered that in the solid state for some fraction of emission events the effects of

recoil and Doppler broadening are effectively zero and the line width for the for the distribution of emitted photon energies is that determined by the uncertainty relation, $\delta E = h/\tau$.

The recoil energy of γ-ray photon can be smaller than the phonon energy, the energy of the quanta of lattice vibrational modes. Therefore there is some probability that the vibrational mode will not be excited and therefore the emitted photon will have the whole of the energy of the transition. Momentum is conserved but the recoil involves a very large number of atoms if the atoms are present in the solid state. This is a **zero phonon** event.

For the effect to be observed there should be a substantial number of **zero phonon** events. Assuming that the solid is an Einstein solid with only one vibrational frequency $\nu$, or angular frequency $\varpi = 2\pi\nu$. If a fraction (**f**) of emission events are **zero phonon** events all the rest involve excitation of a phonon. The average energy loss due to recoil is **R** therefore $(1-f)\hbar\varpi = R$ and $f = (1-R)/\hbar\varpi$. For a high proportion of **zero phonon** events **R** should be as small as possible and the Einstein $\nu$ of the solid as high as possible. This would imply that a hard, high melting point solid (such as a polar crystal) is most suited for observing this effect. The fraction (**f**) is usually called the **Mössbauer fraction.**

Mössbauer γ-ray energies are usually in the range $10^{4}$-$10^{5}$ eV. The Heisenberg natural line widths of Mössbauer photons are $10^{-9}$-$10^{-6}$ eV and this permits an intrinsic resolving power of γ-ray energies of $10^{-10}$-$10^{-14}$ eV. There is enormous potential for measuring minute proportionate energy differences with this effect. However, free-atom recoil and thermal broadening effects drops the resolution to $10^{-9}$-$10^{-6}$ eV. These γ-ray energies cannot be measured so accurately on an absolute scale. To use the precision of the Heisenberg natural line widths it is customary to use a radioactive γ-ray source in which all the emitting atoms are in the same chemical environment.

This γ-ray source is then compared to an absorber containing the same chemical element and the minute difference between the two transition energies is measured.

These differences are due to the nuclear energy levels being modified by the electric and magnetic fields around the nucleus. In different chemical environments the effect of the different arrangement of the orbital electrons will modify the nuclear energy levels. These effects are called **hyperfine interactions**.

### 1.9.2. Hyperfine interactions.

It is possible to obtain chemical information from these interactions. These are either electric or magnetic. The total interaction Hamiltonian ($\mathcal{H}$) for an atom can be written as

$$\mathcal{H} = \mathcal{H}_0 + E_0 + M_1 + E_2 + .....$$

$\mathcal{H}_0$ = all terms in $\mathcal{H}$ except hyperfine interactions, $E_0$ = coulombic interactions between nucleus and electrons, $M_1$ = magnetic dipole hyperfine interactions and $E_2$ = electric quadrupole interactions.

Hyperfine interactions arise from the interaction of the magnetic dipole of the nucleus with the magnetic field and the electric quadrupole moment with the electric field.

### 1.9.2.1. Chemical or Isomer shift.

This is due to the interaction of nucleus with orbital electrons. Because of the electrostatic interaction of the nucleus with the orbital electrons electric field, the nuclear energy levels are slightly different in atoms in different chemical environments. The change in nuclear energy levels means that γ-rays of different energies will be absorbed compared to that from a standard absorber. The difference in energy in the γ-rays between the measured energy and the energy measured for a standard sample is the **chemical** or **isomer** shift, see Figures 1.4 and 1.5.

*Figure 1.4. Differences in energy levels for a Mössbauer nucleus in different environments.*

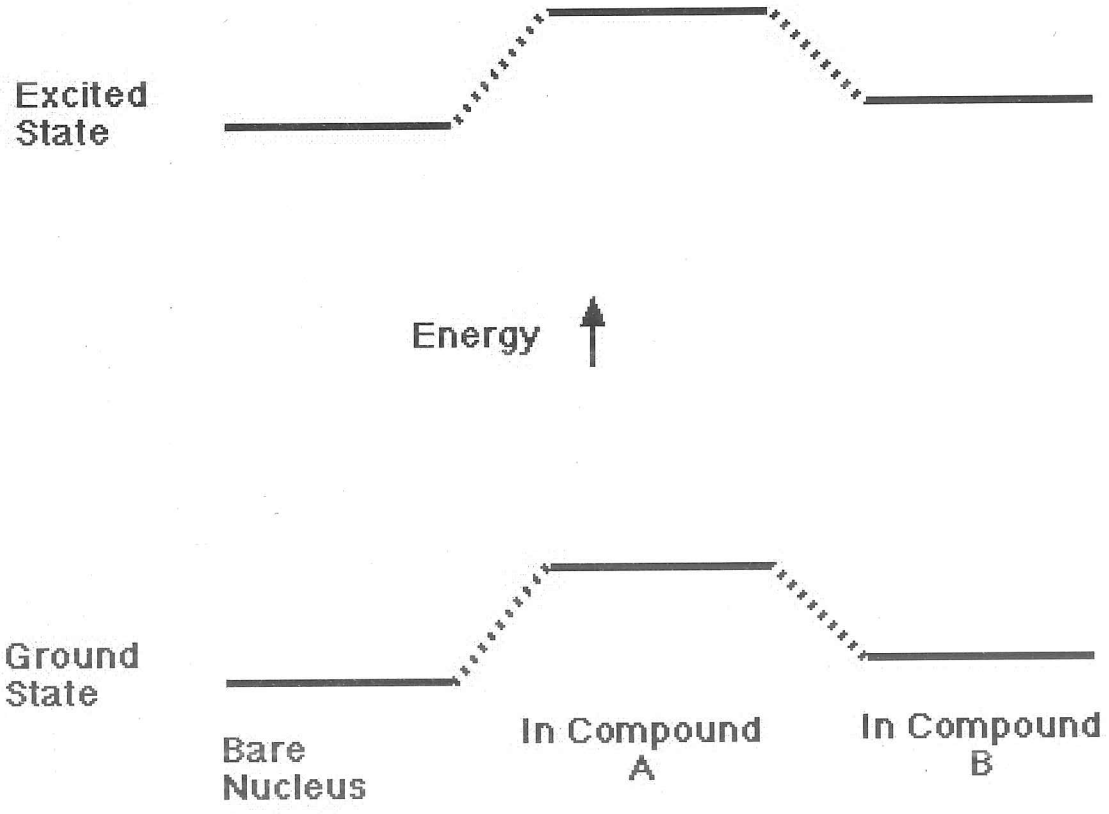

*Figure 1.5. Isomer shift of a Mössbauer peak compared to that of a reference material.*

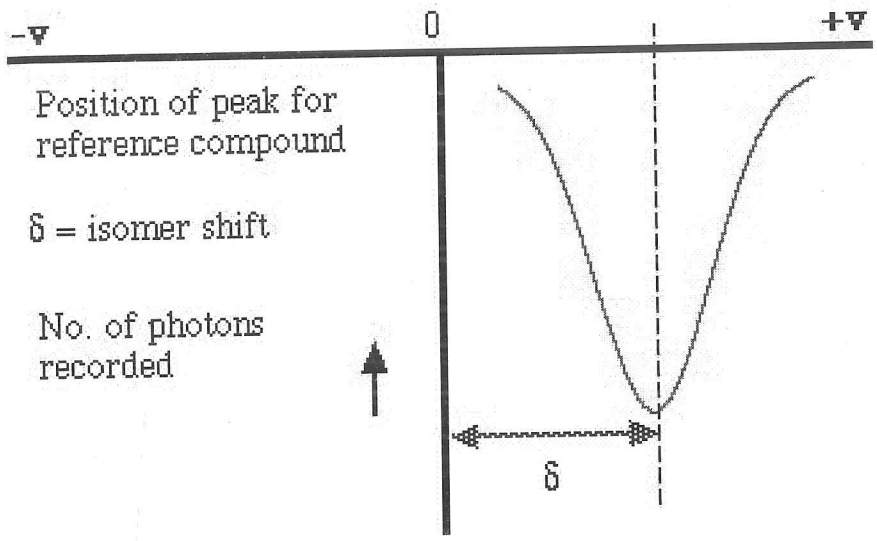


**1.9.2.2. Quadrupole splitting and shift.**

If a nucleus has a spin I > 1 it will possess a **quadrupole moment** arising from the non-uniform nuclear charge distribution. This will cause a splitting of the nuclear energy levels. When a nucleus is excited by γ-ray absorption the spin can go from I = 1/2 to I = 3/2, therefore these 2 energy levels will result in a Mössbauer absorption line being split into a doublet, see Figures 1.6.1-2. When the nucleus possesses a cubic symmetry, the two levels have the same energy, and consequently, the spectrum exhibits only one singlet.

This **quadrupole splitting** characterises the quadrupolar interaction when no magnetic interaction occurs, i.e. in the paramagnetic region.

In the presence of a dipolar magnetic interaction, this quadrupolar interaction is still present. However, if this quadrupolar interaction is very small compared to the magnetic interaction, it is

treated as a perturbation and it is called the **quadrupolar shift.**

*Figure 1.6.1. Energy levels due to electric field gradient in excited nucleus, m = spin quantum number.*

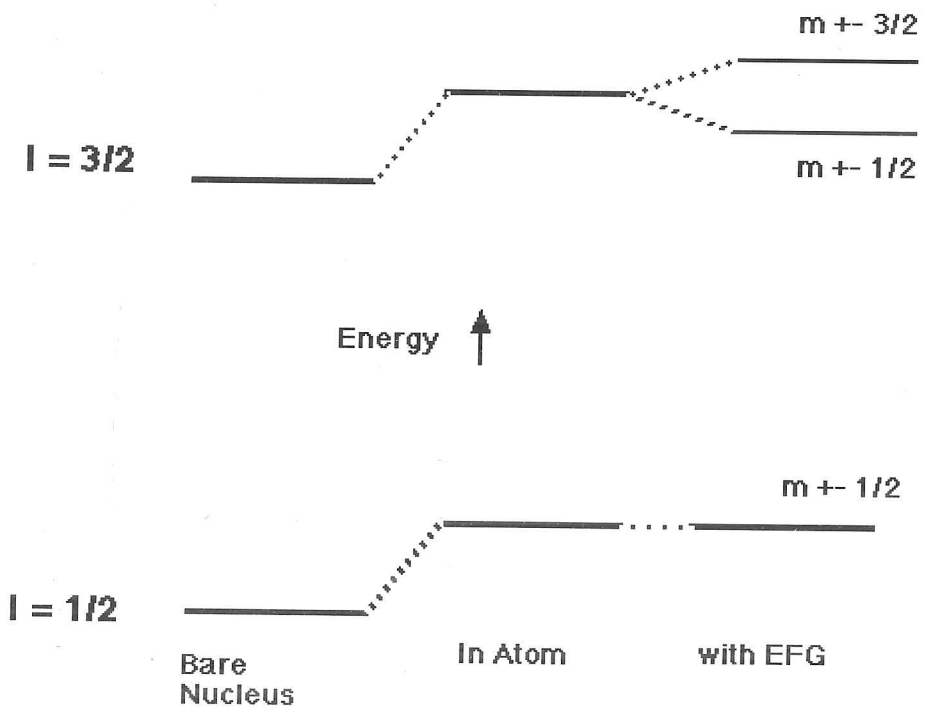


**1.9.2.3. Hyperfine field.**

This is due to the presence of a very strong external magnetic field or the presence of a magnetic sample. The magnetic dipolar moment of the nucleus interacts with the magnetic field experienced by the nucleus; this magnetic field results from an external field, or the actions of the neighbouring nuclei when magnetic order occurs. The magnetic field removes all the degeneracy of the nuclear levels, so a nuclear spin of **I** gives rise to **2I+1** energy levels. Therefore a Mössbauer doublet will become a sextet in the presence of a magnetic field, according to the

Zeeman Effect, due to the six permitted transitions in the case of a I = 3/2 ⇔ 1/2 transition.

*Figure 1.6.2. Schematic diagram of a quadrupole split spectrum for a I = 3/2 ⇔ 1/2 Mössbauer nucleus. δ is the isomer shift and Δ is the quadrupole splitting.*

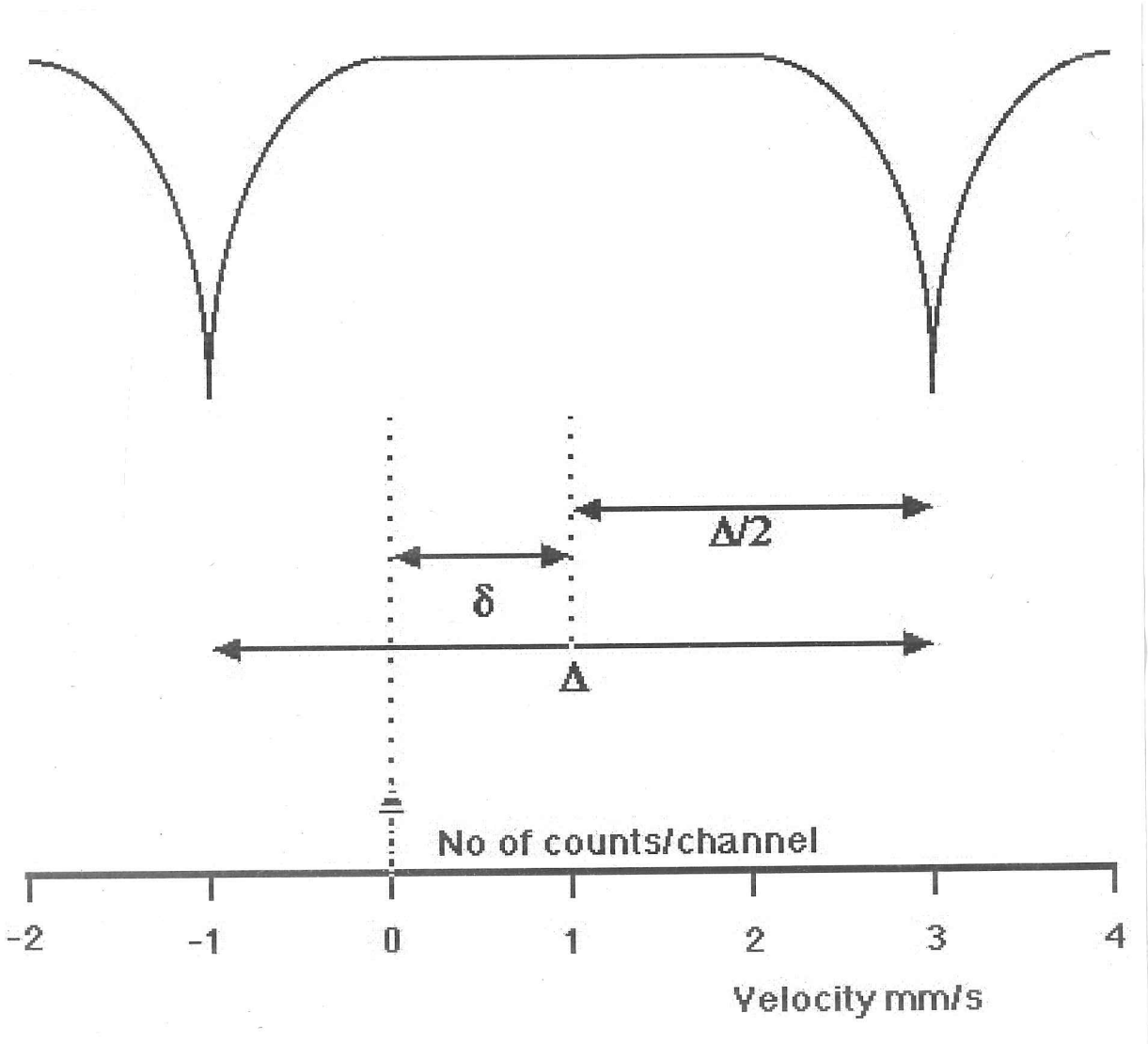


**1.9.3. Mössbauer spectra.**

Isomer Shift, Quadrupole splitting/shift and Hyperfine field are all refineable parameters for nuclei in different chemical environments. In most cases these different interactions are present simultaneously. Each different nucleus will contribute a doublet or sextet to the Mössbauer spectrum. The area of peaks in the spectrum for each different nucleus gives information about

the proportion of nuclei in each chemical environment. This chemical information available from this technique makes Mössbauer spectroscopy complementary to the other structure determination techniques discussed in this chapter. Figure 1.7 shows a schematic magnetically split Mössbauer spectrum for a soft iron foil.

*Figure 1.7. Schematic diagram of a magnetically split spectrum for a soft iron foil.*

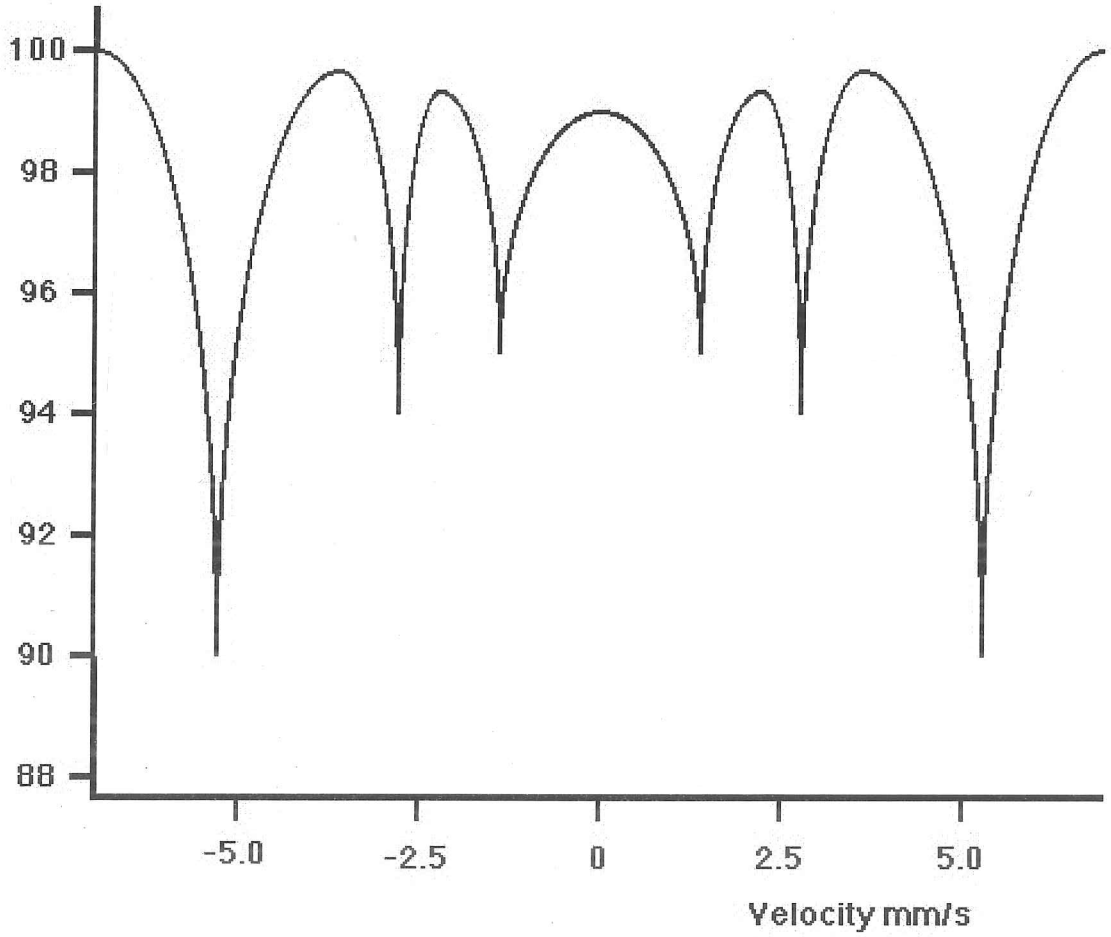


The effect of the hyperfine interactions is to slightly change the energy of the absorbed γ-ray photon on its remission. These changes in energy can be observed by velocity modulation of the γ-ray energy by the means of the Doppler effect. The recoil-free energy of a typical transition is so precisely defined that its line width corresponds to the energy change produced by an applied Doppler velocity of around 1-10 mm/s. Therefore at a particular relative velocity between source

and absorber the source energy will precisely match the nuclear energy level gap and resonant absorption will be at a maximum. If the source and absorber are chemically identical this Doppler velocity will be zero. As the velocity changes from matching the precise energy level the absorption will decrease and a sufficiently large change in velocity will destroy the resonant absorption.

### 1.9.4. Mössbauer nuclei.

The Mössbauer effect can only practicably be observed in solids containing certain Mössbauer nuclei. These nuclei must have an excited state in the Mössbauer transition with a half-life ($\tau/\ln 2$) between $10^{-6}$ and $10^{-9}$ s. If the half-life is too short the line width of the emitted photons becomes so large the hyperfine interactions cannot be seen. If the half-life is too long the line width becomes so narrow extraordinary care needs to be taken to avoid fortuitous line broadening due to vibration or other minute movements of the absorber with respect to the source. The Mössbauer nucleus must also be a stable or a long-lived radioactive species. The Mössbauer nucleus must also be present in the naturally occurring element to avoid the costly production of an absorber enriched in the Mössbauer nucleus. The $\gamma$-ray source must also be a reasonably long-lived species and must not have too much internal conversion in the decay of the Mössbauer excited state.

The most common absorber nucleus in Mössbauer spectroscopy is $^{57}$Fe and this nucleus was used in this study. $^{57}$Fe has a narrow theoretical line width (0.19 mm/s) and a large Mössbauer fraction ($f \sim 0.7$ at 300K and 0.9 at 4K). An unusually large absorption cross section means that the

magnitude of the absorption is good and therefore spectra can be measured at non-cryogenic temperatures for hard crystalline $^{57}Fe$ containing compounds. The narrow line width means that there is a larger "dip" in the peaks and therefore a higher resolution between lines in the spectra. $^{57}Fe$ compounds have large isomer shifts (high spin $Fe^{3+}$ has shifts in the range 0.3 to 0.6 mm/s and high spin $Fe^{2+}$ has shifts in the range 0.8 to 1.5 mm/s) which also increases the resolution between lines in the spectra.

Natural Fe contains 2% of $^{57}Fe$, so the Mössbauer effect can be observed with natural samples. The effect may be enhanced by enriching the absorber with $^{57}Fe$. Radioactive decay of $^{57}Co$ to $^{57}Fe$ in 3 steps produces $\gamma$-rays for $^{57}Fe$ Mössbauer spectroscopy. The last of these steps produces $\gamma$-rays with an energy of 14.41 keV which are used as $^{57}Fe$ Mössbauer photons.

## Chapter 1 - References.


A.Altomare, G.Cascarano, C.Giacovazzo, A.Guagliardi, M.C.Burla, G.Polidori and M.Camalli, J. Appl. Cryst, (1994), **27**, 435-6.

J.P.Attfield, J. Phys. Chem. Solids, (1991), **52(10)** 1243-1249.

J.P.Attfield, Materials Science Forum, (1996), **228(1-2)** 201-206.

J.P.Attfield, A.K.Cheetham, D.E.Cox and A.W.Sleight, J.Appl. Cryst., (1988), **21(5),** 452-457.

J.P.Attfield, J.F.Clarke and D.A.Perkins, Physica B., (1992), **180,** 581-584.

J.P.Attfield and D.A.Perkins, J. Chem. Soc. Chem. Comm., (1991), 229.

A.M.T.Bell and C.M.B.Henderson, Acta Cryst., (1994), **C50(10),** 1531-1536.

A.M.T.Bell, C.M.B.Henderson, S.A.T.Redfern, R.J.Cernik, P.E.Champness, A.N.Fitch and S.C.Kohn. Acta Cryst., (1994), **B50(1),** 31-41.

R.J.Cernik, A.K.Cheetham, C.K.Prout, D.J.Watkin, A.P.Wilkinson and B.T.M.Willis, J. Appl. Cryst., (1991), **24**, 222.

R.Csoka, W. I. F. David and K. Shankland, Materials Science Forum, (1998) **278-281**, 294-299.

W. I. F. David, K. Shankland and N. Shankland, Chem. Commun., (1998), 931-2.

K.D.M.Harris, B.M.Kariuki and M.Tremayne, Materials Science Forum, (1998), **278-281**, 32-37.

J.D.Jorgensen, M.A.Beno, D.G.Hinks, L. Soderholm, K.J.Volin, R.L.Hitterman, J.D.Grace, I.K.Schuller, C.U.Segre, K.Zhang and M.S.Kleefisch, Phys. Rev., (1987), **B36(7)**, 3608-16.

A.C.Larson and R.B. von Dreele, LANSCE, MS-H805, Los Alamos National Laboratory.

A.Le Bail, H.Duroy and J.L.Fourquet, Mater. Res. Bull., (1988), **23**, 447-452.

D.Louer, Materials Science Forum, (1993), **133-136**, 7-24.

M.D.Marcos, M.A.G.Aranda, D.C.Sinclair, J.P.Attfield, Physica C, (1994), **235(2)**, 967-968.

R.Mössbauer, Z.Physik., (1958), **151,** 121.

A.D.Murray, J.K.Cockcroft and A.N.Fitch, (1990) PDPL. Powder Diffraction Program Library, University College London.

G.S.Pawley, J. Appl. Cryst., (1981), **14**, 357.

H.M.Rietveld, J. Appl. Cryst., (1969), **2,** 65-71.

D.E.Sayers, E.A.Stern and F.W.Lytle, Phys. Rev. Lett., (1971), **27(18)**, 1204-1207.

E.A.Stern, Phys. Rev. B., (1974), **10**, 3027-3037.

Y.Takeuchi, T.Watanabe and T.Ito, Acta Cryst., (1950), **3**, 98-107.

J.H.Williams, J.K.Cockcroft and A.N.Fitch, Angew. Chemie Int. Ed. Engl., (1992), **31(12)**, 1655-1657.

R.A.Young (editor), The Rietveld Method, Oxford University Press (1995).

A.D.Murray, J.K.Cockcroft and A.N.Fitch, (1990) PDPL. Powder Diffraction Program Library, University College London.

G.S.Pawley, J. Appl. Cryst., (1981), **14**, 357.

H.M.Rietveld, J. Appl. Cryst., (1969), **2,** 65-71.

D.E.Sayers, E.A.Stern and F.W.Lytle, Phys. Rev. Lett., (1971), **27(18)**, 1204-1207.

E.A.Stern, Phys. Rev. B., (1974), **10**, 3027-3037.

Y.Takeuchi, T.Watanabe and T.Ito, Acta Cryst., (1950), **3**, 98-107.

J.H.Williams, J.K.Cockcroft and A.N.Fitch, Angew. Chemie Int. Ed. Engl., (1992), **31(12)**, 1655-1657.

R.A.Young (editor), The Rietveld Method, Oxford University Press (1995).

# Chapter 2. Experimental Techniques.

## 2.1. X-rays.

X-rays were discovered by Röntgen in 1895, they can be generated by bombardment of a target by electrons under vacuum. Electron bombardment causes excitation of inner shell electrons to higher energies, the return of these electrons to the inner shell causes an X-ray photon to be emitted with an energy corresponding to the energy difference between the ground and excited state of the electron. Figure 2.1 shows a typical X-ray spectrum for a target material used to generate X-rays. X-rays have been used for diffraction since the initial experiments of von Laue and the Braggs back in 1912.

*Figure 2.1. Typical X-ray spectrum.*

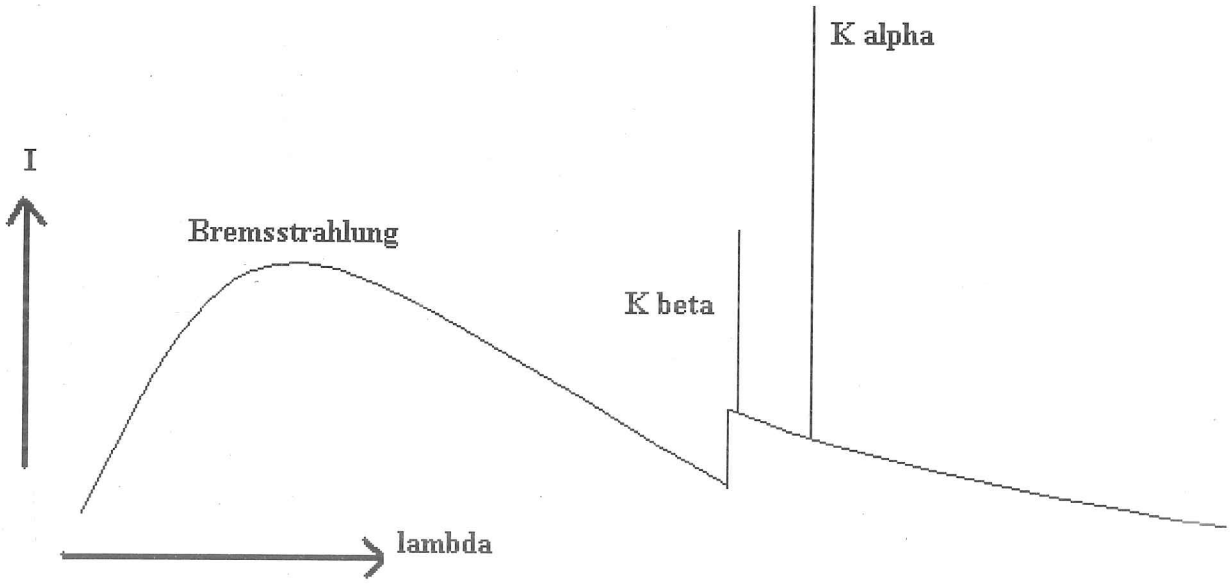


The characteristic $K_{\alpha}$ X-ray line is usually used for X-ray diffraction experiments. A filter made of a material with a Z number just below that of the target element (e.g. Ni filter used for Cu

target) is used to reduce the contribution from $K_\beta$ radiation and bremsstrahlung. These β filters are selected so that the energy of the filter element absorption edge is intermediate between that of the target $K_\beta$ and $K_\alpha$ lines. The mass absorption coefficient for the $K_\beta$ line will be much higher than that for the $K_\alpha$ line so that the transmission of $K_\beta$ X-radiation will be greatly reduced. A Pulse Height Selector in the detector electronics can also be used to select only a certain energy range in the X-ray detector, this can be used to remove some of the unwanted X-radiation from bremsstrahlung and sample fluorescence and improve the signal to noise ratio.

A much cleaner method of producing the $K_\alpha$ X-ray line involves using a monochromator crystal. This is set up so that only X-rays with a wavelength corresponding to the $K_\alpha$ line will be diffracted by the monochromator crystal to reach the sample (for a pre-sample monochromator) or the X-ray detector (for a post-sample monochromator). Monochromators significantly decrease the signal to noise ratio in the final powder diffractogram at the cost of decreased X-ray intensity from the characteristic $K_\alpha$ line. The characteristic $K_\alpha$ line is made up of a close doublet of $K_{\alpha1}$ and $K_{\alpha2}$ lines, it is also possible to use a monochromator to separate out these two lines so that only the $K_{\alpha2}$ line is used for diffraction but these results in an even greater decrease in X-ray intensity.

### 2.1.1. Philips X-ray powder diffractometer.

The Philips PW1060 diffractometer (see Figure 2.2) on the Philips PW1730 X-ray generator in the Department of Chemistry was used for the conventional X-ray powder diffraction work, $CuK_\alpha$ X-radiation was produced from an X-ray tube, with a Ni filter used to remove $CuK_\beta$

radiation, no monochromator is used in this diffractometer. The diffractometer has the Bragg-Brentano geometry and a scintillation counter detector is used. Flat plate samples were used on this diffractometer and powder diffraction patterns can be collected in the range 2-117° 2θ. This diffractometer was used to check the phase purity of synthesised samples.

*Figure 2.2. Philips powder diffractometer.*

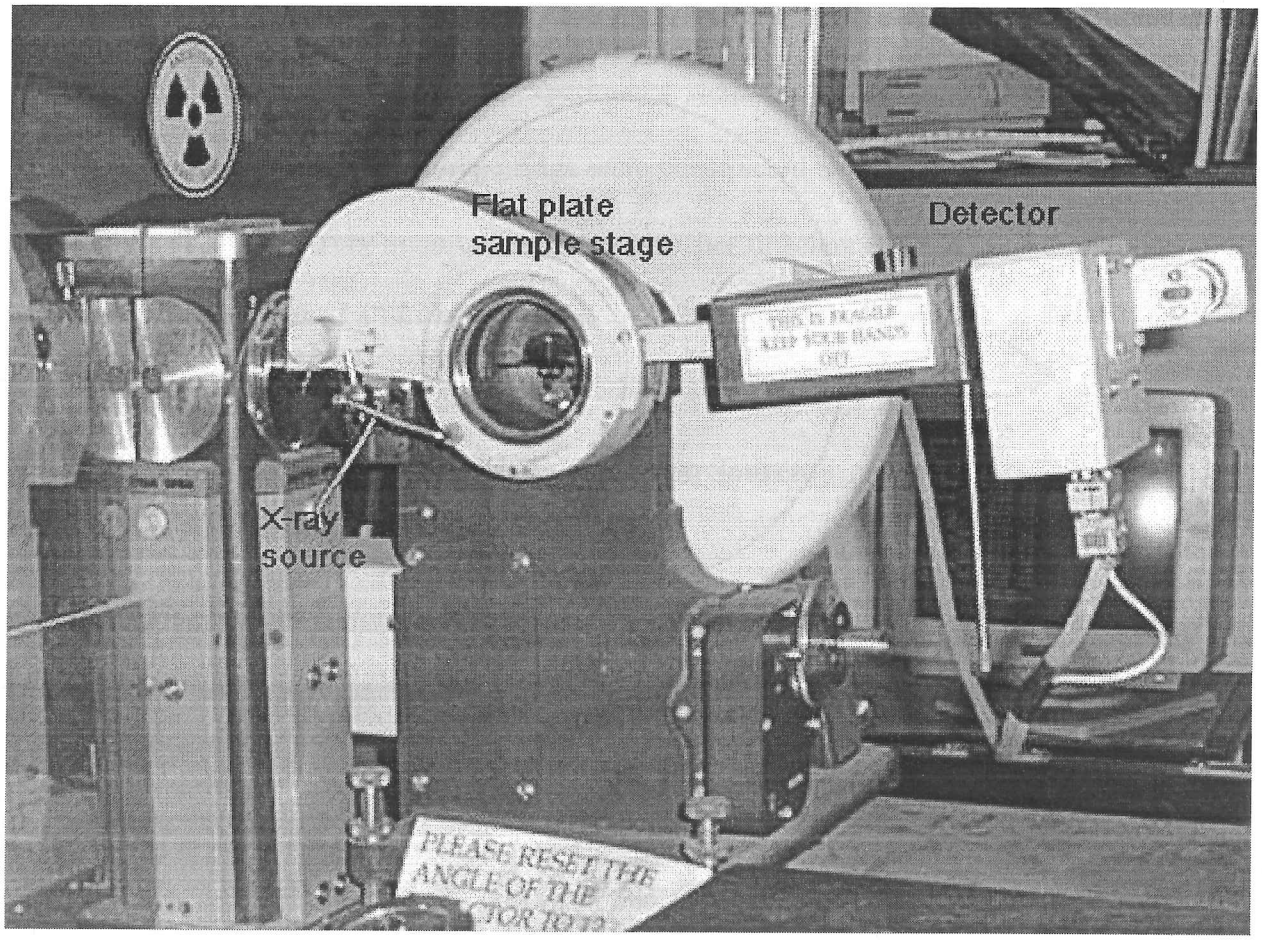


## 2.2. Synchrotron Radiation.

An alternative source of X-rays is **synchrotron radiation.** A synchrotron accelerates charged particles, such as electrons, to relativistic speeds. A series of magnets are used to bend the path of

the charged particles into a circular shape. As they pass these bending magnets, the path of the electrons is deflected and the electrons lose energy which is emitted as intense beams of electromagnetic radiation, known as **synchrotron radiation (SR).** The beam is in the form of a cone at a tangent to the electron orbit.

Synchrotrons were originally used for particle physics experiments, SR was thought to be a problem for particle physicists in that it caused energy loss in their experiments. However, it was eventually realised that this SR could be used as a source of electromagnetic radiation for scattering experiments. The first SR experiments were done parasitically on particle physics synchrotrons before dedicated storage rings were constructed as sources of SR for experiments. SR techniques are now very important in many branches of science, SR is used to investigate the structure and properties of all forms of matter.

## 2.3. Daresbury Laboratory Synchrotron Radiation Source.

The United Kingdom Synchrotron Radiation Source (SRS) at Daresbury Laboratory, Warrington, Cheshire is a 2nd generation 2 GeV electron storage ring and is the world's first dedicated SR source (see Figure 2.3). SR is produced in a continuous range of energies from the hard X-ray to the infra-red region of the electromagnetic spectrum. The SR flux from a 1.2 T bending magnet on the SRS is at its highest in the X-ray region around 4keV, $\lambda = 3$ Å. The SRS also has two superconducting Wiggler magnets, these magnets change the orbit of the electron beam so that the SR flux from these magnets is shifted to higher energies and shorter wavelengths ($\lambda < 1$ Å). With the highest fluxes in the X-ray region the SRS is a particularly suitable source for X-ray scattering experiments although experiments with lower energy SR are also done.

The SRS was used for X-ray powder diffraction experiments using stations 9.1 and 2.3 and

EXAFS experiments using station 7.1, see **2.3.1, 2.3.2** and **2.3.3** for more information on these experiments.

*Figure 2.3. Daresbury Laboratory Synchrotron Radiation Source.*

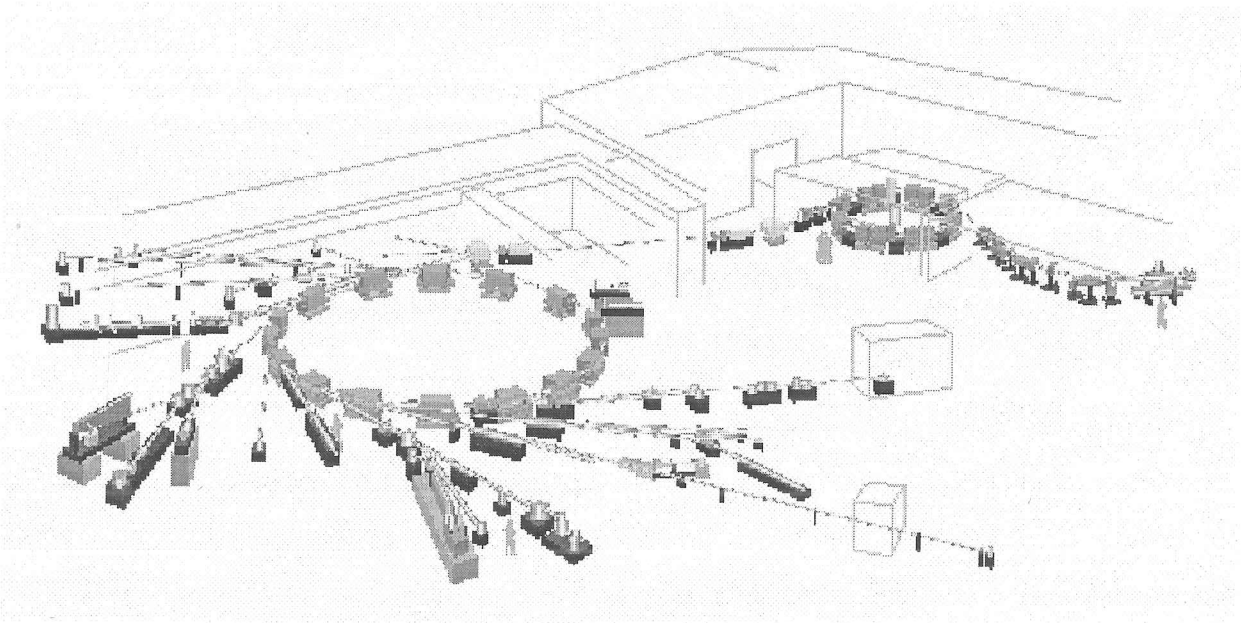

### 2.3.1. High resolution powder diffractometer, SRS Station 9.1.

The high resolution powder diffractometer on station 9.1 of the SRS is sited 15m from the 5T superconducting Wiggler magnet (see Figure 2.4). Monochromatic synchrotron radiation (SR) is produced using a water-cooled channel-cut silicon(111) monochromator crystal. The practical wavelength range is from $\lambda$ = 0.4-1.5 Å with the maximum flux occurring between 0.6 and 0.8 Å. The diffractometer can be used in both Debye-Scherrer and flat-plate geometry. High resolution powder diffraction data can be collected in the temperature range 15 - 300 K using a cryostat in the range and in the range from room temperature to 1023 K using a furnace. The angular resolution of the diffractometer in its normal mode of operation in Debye-Scherrer

geometry is ~0.03° to 0.05° 2θ, in flat-plate geometry the resolution is ~0.03° to 0.07° 2θ. See Bushnell-Wye et al (1992) for a more complete description of this instrument.

*Figure 2.4. High Resolution Powder Diffractometer on station 9.1 of the Daresbury Synchrotron Radiation Source.*

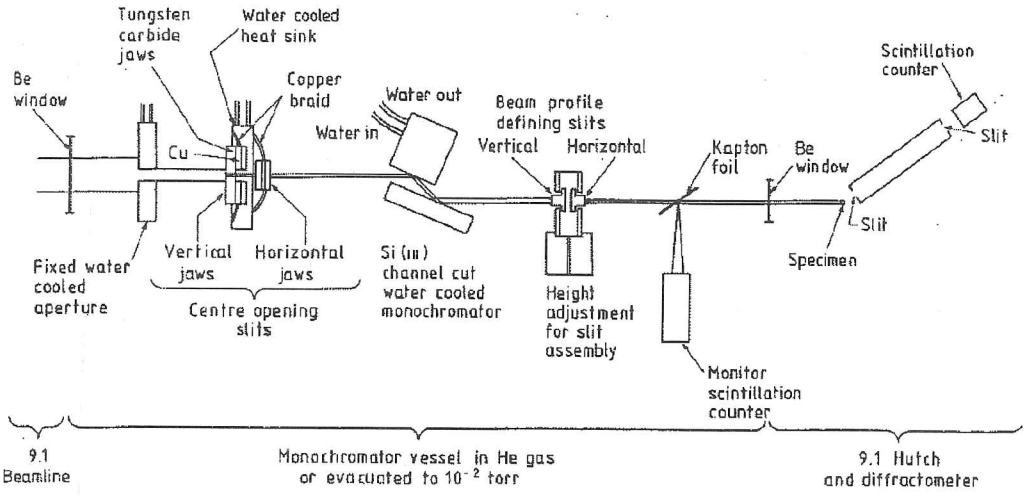


This diffractometer was used with two different types of detector. One was a "one-dimensional" scintillation counter used for a step scan over the 2θ range of interest.

### 2.3.1.1. Image plate detectors.

The other type of detector used was a "two-dimensional" image-plate area detector. In this case the detector is fixed and the whole diffraction pattern is collected simultaneously instead of step-wise.

The development of image plate detectors over the last 10 years has revolutionised the structure determination of materials under high pressure. Synchrotron X-ray powder diffraction data are collected with the samples in diamond anvil pressure cells with the full Debye-Scherrer cones of diffracted X-rays detected using image plates. This means that high quality powder diffraction

data can be routinely collected in a matter of hours on the very small samples present in pressure cells. Before the advent of these detectors it was always a severe problem collecting sufficiently good powder diffraction data with conventional "one-dimensional" detectors to get data of sufficient precision for structure determination. Since 1990 a group from Edinburgh University has determined several structures at high pressure using diamond anvil pressure cells and flat image plate detectors at the Daresbury Synchrotron Radiation Source (McMahon, 1998).

More recently curved image plates have been developed as detectors (Bushnell-Wye et al, 1995; Roberts et al, 1998). The advantage of using such a detector means that high quality synchrotron X-ray powder diffraction data can be collected in a timescale of a few minutes rather than hours. Figure 2.5 shows the curved image plate apparatus on station 9.1, Figure 2.6 shows the capillary sample stage and furnace attachment in close up.

The image-plate system is based on a Molecular Dynamics scanner and gives a FWHM of ~0.08° 2θ for a sample to plate distance of 400mm. Figure 2.7 shows an example of scanned image plate Debye-Scherrer pattern and the 1 dimensional powder diffraction pattern obtained from integrating around the Debye-Scherrer rings.

### 2.3.2. High resolution powder diffractometer, SRS Station 2.3.

The high resolution powder diffractometer on station 2.3 of the SRS is a similar instrument to that on station 9.1. It is sited 16m from a 1.2T bending magnet. Monochromatic synchrotron radiation (SR) is produced using a water-cooled channel-cut silicon(111) monochromator crystal. The practical wavelength range is from $\lambda$ = 0.7-2.5 Å with the maximum flux occurring around 1.4 Å. The angular resolution of the diffractometer in its normal mode of operation is 0.064° 2θ.

*Figure 2.5. (left) Curved Image Plate apparatus on station 9.1. Figure 2.6. (right) Capillary stage and furnace attachment of Curved Image Plate apparatus.*

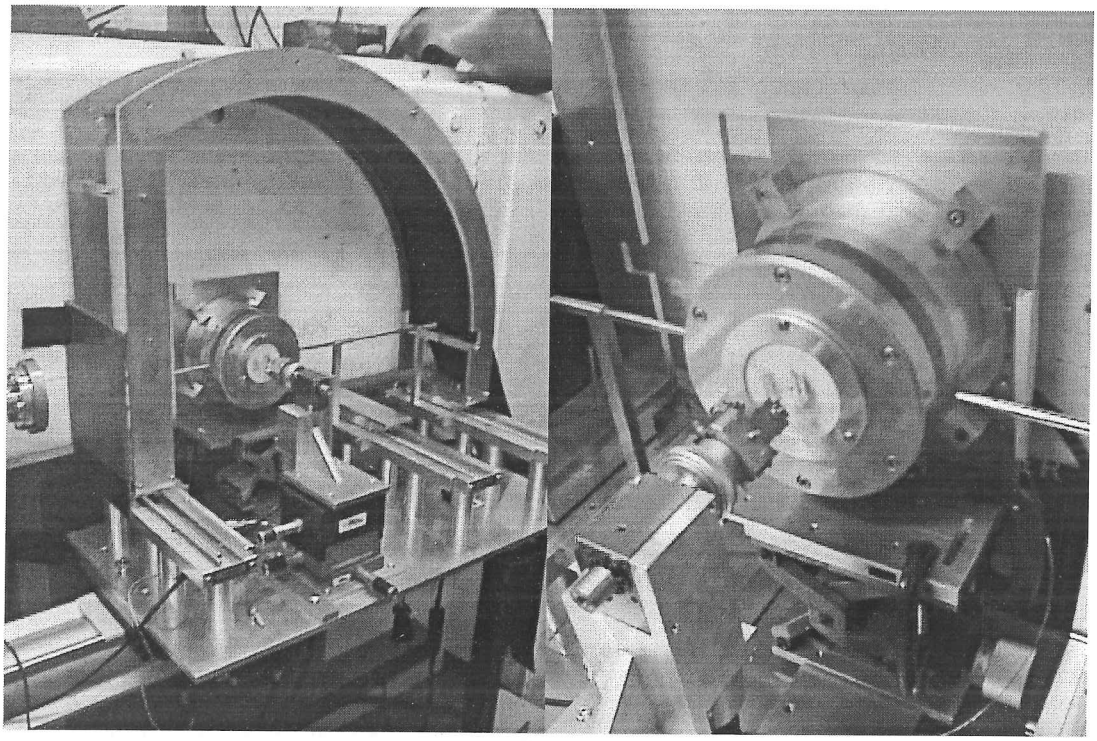

*Figure 2.7. An example of a scanned image plate 2-dimensional powder diffraction pattern and the 1-dimensional pattern obtained by integrating round the Debye-Scherrer rings.*

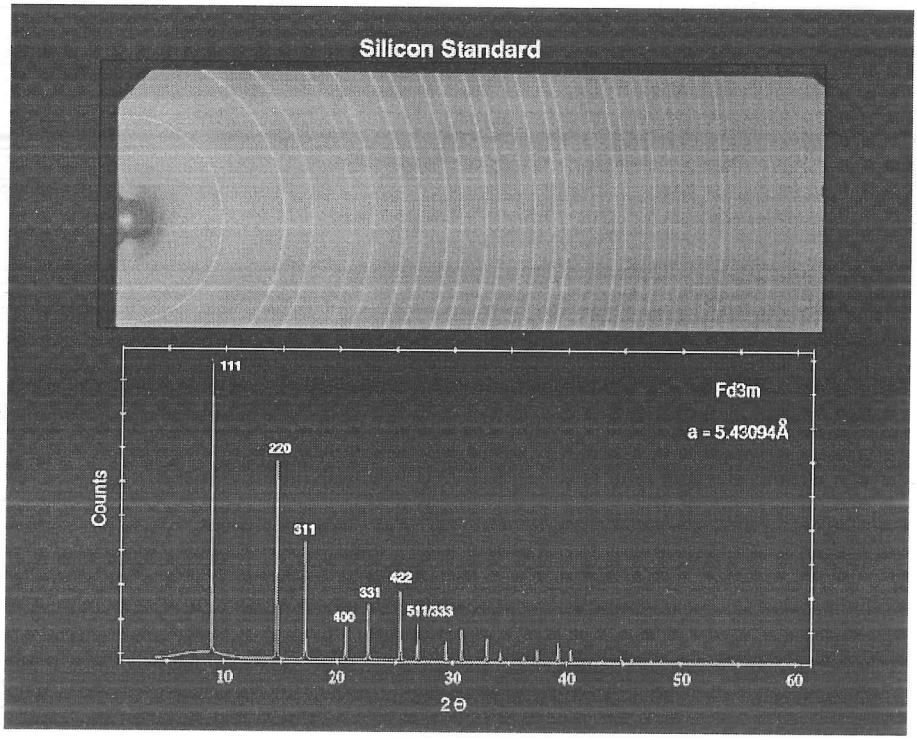

Ambient temperature powder diffraction data can be collected with both capillary and flat plate samples, data can be also collected on flat plate samples in the temperature range 10-1500 K (Tang et al, 1998). See Cernik et al (1990) and Collins et al (1992) for a more complete description of this instrument.

This diffractometer was used at ambient temperature in Debye-Scherrer mode with the sample on a capillary stage. A "one-dimensional" scintillation counter used for a step scan over the 2θ range of interest. This is indicated in Figure 2.8.

*Figure 2.8. High Resolution Powder Diffractometer on station 2.3 of the Daresbury Synchrotron Radiation Source.*

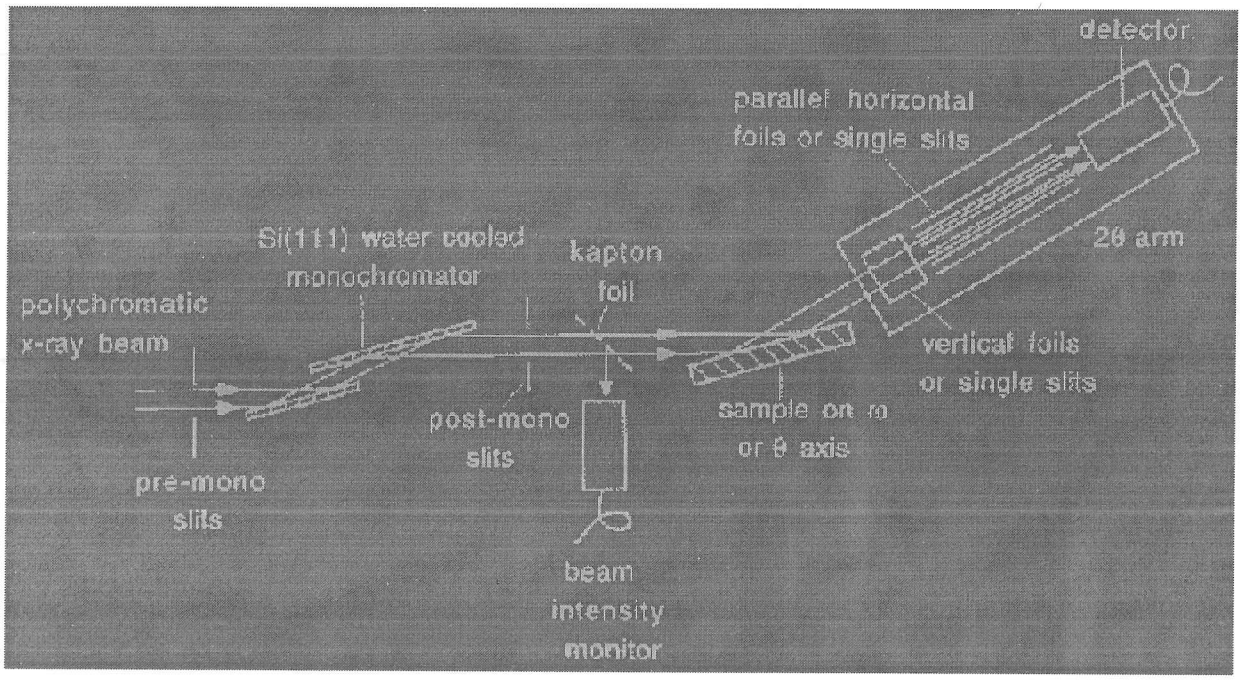

### 2.3.3. EXAFS spectrometer, SRS Station 7.1.

Station 7.1 is used for transmission and concentrated sample fluorescence EXAFS measurements in the range 4 keV to 11 keV. The SR source for this station is from bending magnet 7 with a 3.3 mrad horizontal acceptance. A 600 mm platinum coated plane mirror is used to focus the SR onto the water cooled double crystal Si(111) harmonic rejecting monochromator. X-rays are detected using standard ion chambers filled with Ar and He, for Fe K-edge EXAFS the $I_o$ (reference) detector chamber contains 20% Ar and the $I_t$ (transmission) detector contains 80% Ar, both detectors are backfilled to 1000 mbar with He. EXAFS measurements can be made on samples in an Oxford Instruments liquid nitrogen cooled cryostat between 80 K and room temperature. Figure 2.9 shows a schematic diagram of an EXAFS experiment.

*Figure 2.9. Schematic diagram of EXAFS experiment.*

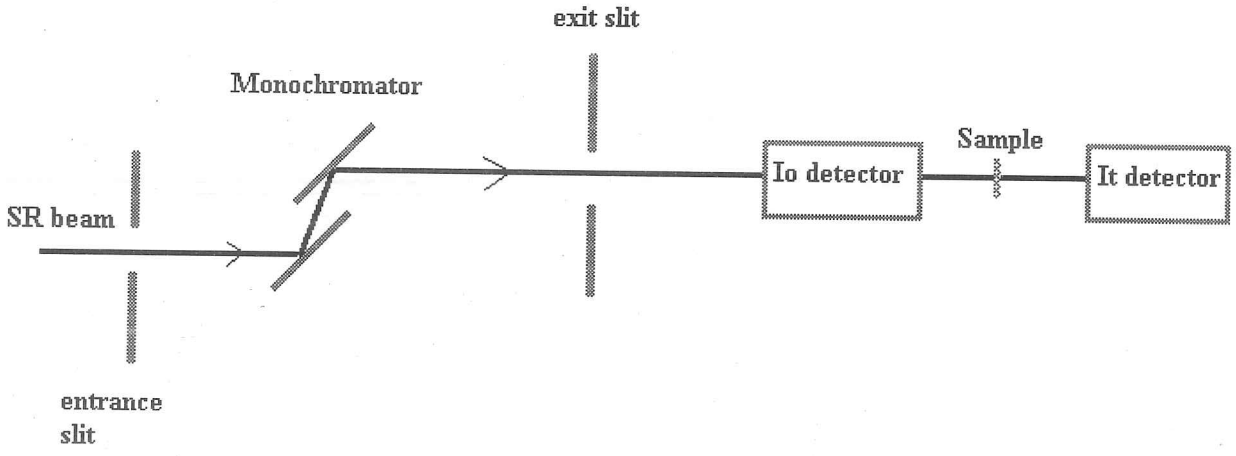


## 2.4. European Synchrotron Radiation Facility.

The European Synchrotron Radiation Facility (ESRF) in Grenoble, France, is a 3rd generation 6

GeV electron storage ring, SR is produced in a continuous range of energies in the hard X-ray region of the electromagnetic spectrum. Figures 2.10.1-2 show the layout of this synchrotron.

*Figure 2.10.1. Experimental beamlines at the European Synchrotron Radiation Facility.*

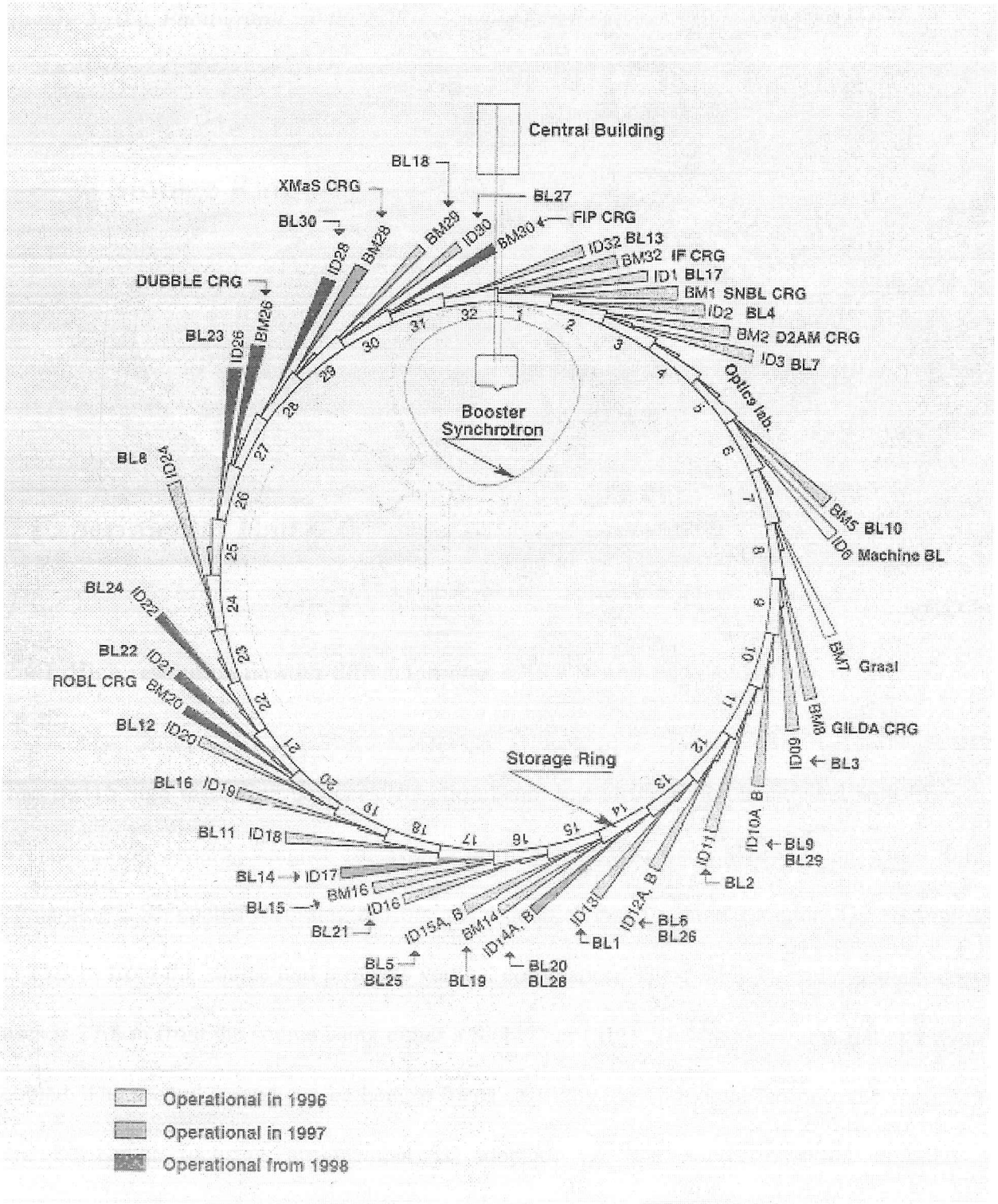

The ESRF was used for resonant X-ray powder diffraction experiments using beamline BM16, see **2.4.1** for more information on these experiments.

*Figure 2.10.2. Photograph of the ESRF showing different components of the synchrotron.*

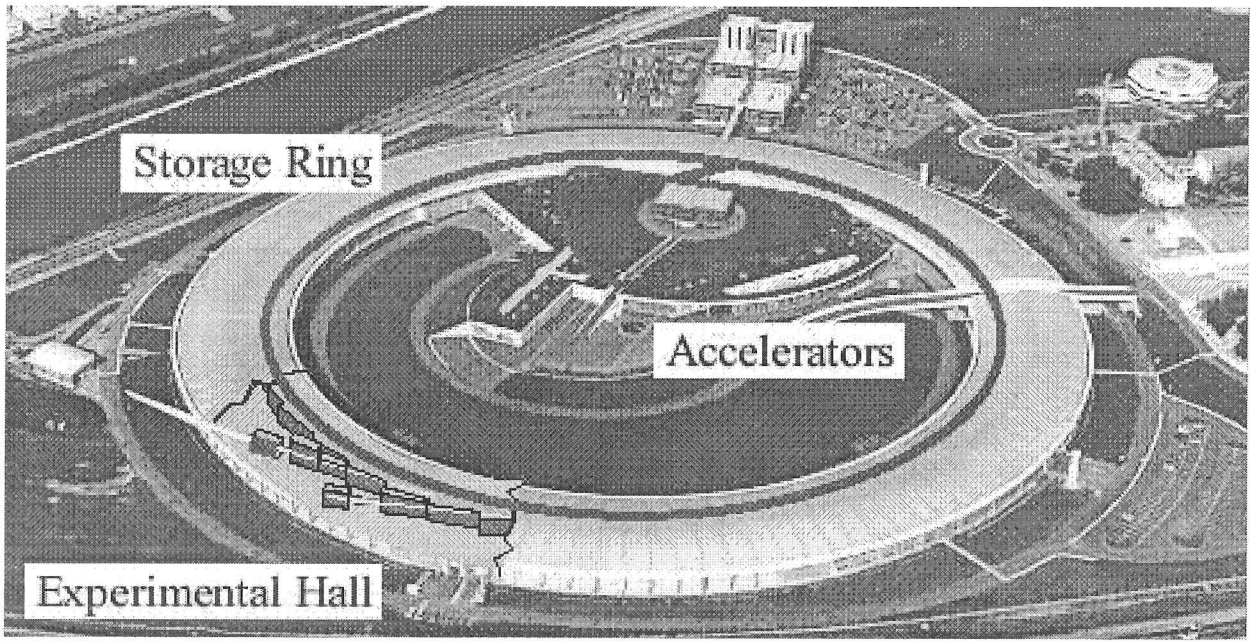


### 2.4.1. High resolution powder diffractometer, ESRF Beamline BM16.

The BM16 high resolution powder diffraction beam line at the ESRF is situated 56m from the SR source on bending magnet 16. The beam line is in two parts. There is an optics hutch containing 2 Rh coated focussing mirrors and a double-crystal monochromator. The first mirror is 25.3 m from the source and provides vertical collimation. The double-crystal monochromator uses is 27.8 m from the source using either a Si(111) or (311). The first crystal is flat and water-cooled. The second crystal can be bent to focus sagittally the horizontal fan onto the sample. A 1:1 horizontal focusing arrangement is adopted, i.e. the source-to-crystal distance is approximately equal to the crystal-to-sample distance, because this does not significantly perturb

the vertical divergence of the beam, and hence maintains the well-collimated beam essential for high angular-resolution. After the monochromator, the optional second mirror is 31.0 m from the source and provides the option to focus the X-rays vertically onto the sample, gaining intensity at the expense of lower angular-resolution. There is also a sample hutch containing a two-circle diffractometer. Figure 2.11.1 shows a schematic diagram of the diffractometer. See Fitch (1995, 1996) for details on the diffractometer.

*Figure 2.11.1. General layout of the BM16 powder-diffraction beamline.*

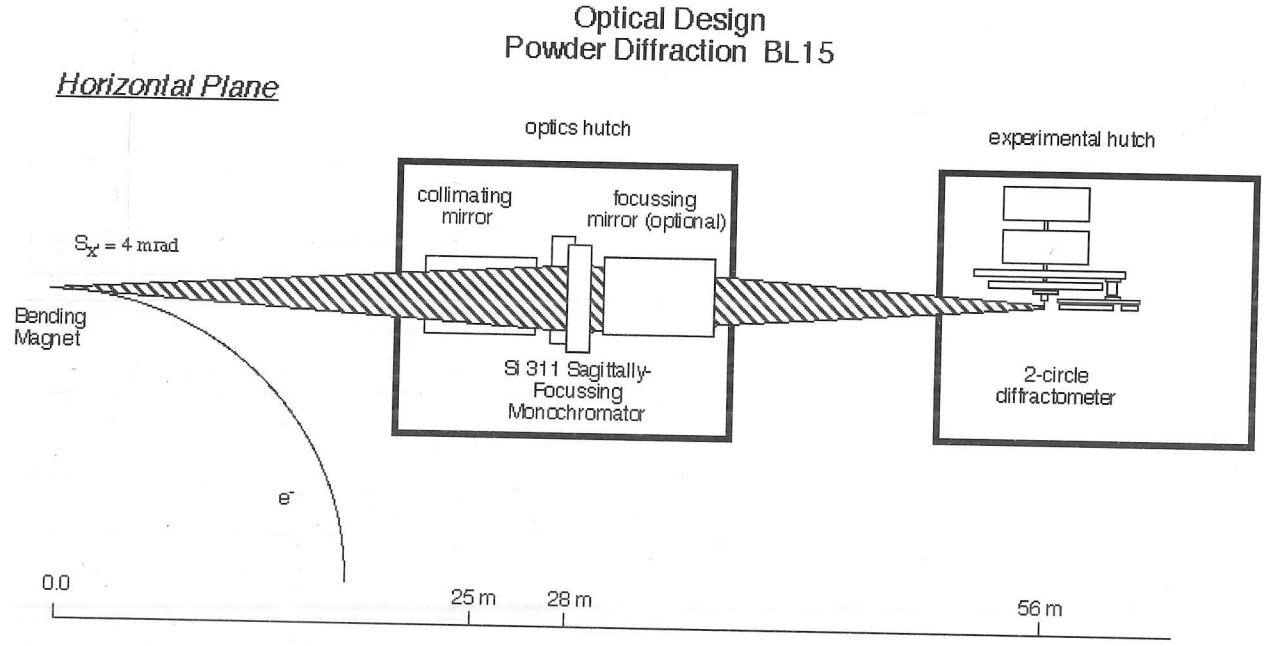


The beam size at the sample is variable, the vertical size is between 0.5-2.0 mm and the horizontal size between 1-20 mm. X-rays in the energy range 5-40 keV ($\lambda$ = 2.5-0.3 Å) can be used, the maximum X-ray flux is at 20.4 keV. The horizontal fan of SR accepted by the beamline is 4 mrad.

The diffractometer was used with a nine-crystal analyser stage (with nine Ge(111) crystals separated by ~2° intervals) as detectors. Data are collected in a continuous scanning mode. This eliminates the dead time of a conventional step scan. Following data collection, the counts from

the nine detectors are rebinned and normalised, to give the equivalent normalised step scan, which is suitable for analysis by standard programs. The diffractometer was used in capillary mode, either at room temperature or at 4 K in a liquid helium cryostat. Figure 2.11.2 shows the diffractometer with the attached cryostat.

Beamline BM16 is designed for powder-diffraction studies with very high angular (optimal instrumental contribution to the peak width of 0.006° 2θ) and energy resolution around 1 eV at 10 keV (i.e. $E/E<10^{-4}$).

*Figure 2.11.2. Photograph of diffractometer on BM16 with cryostat stage attached.*

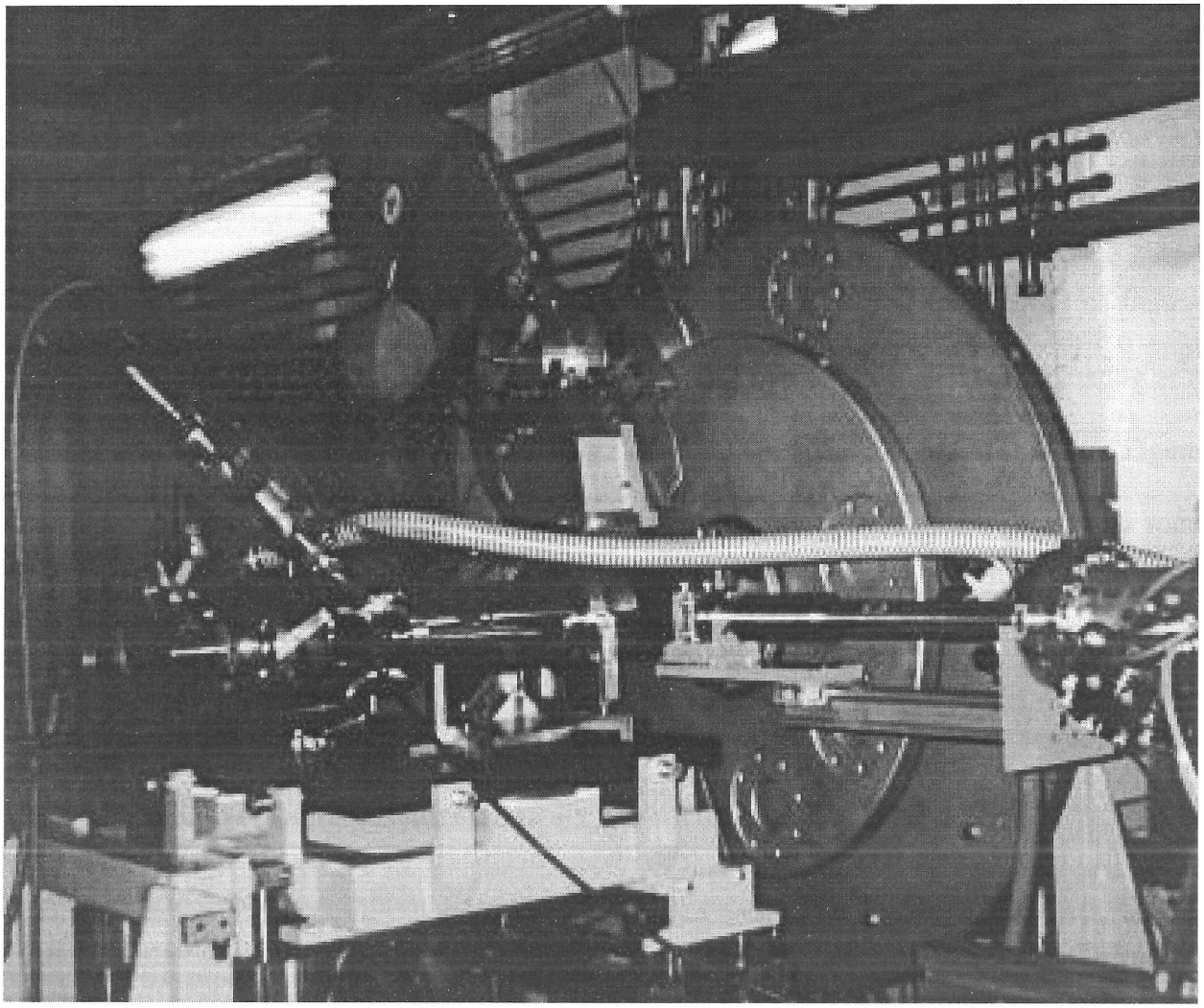

## 2.5. Neutrons.

A complimentary technique to X-ray scattering is **neutron** scattering. A beam of neutrons generated by a nuclear fission reaction can be scattered by the nuclei of atoms.

Neutron diffraction has some advantages over X-ray diffraction in that neutron scattering from low atomic number (Z) elements can be as intense as that from high Z elements unlike for X-rays where scattering increases as $Z^2$. Also magnetic structural information can be readily obtained from neutron scattering experiments unlike in X-ray scattering experiments. However, neutron scattering tends to be weaker than X-ray scattering so larger samples are needed for neutron scattering experiments.

### 2.5.1. Institut Laue-Langevin (ILL).

The ILL high-flux reactor source in Grenoble, France, was used for the neutron scattering experiments. This is the most powerful reactor source of neutrons in the world, operating at a thermal power of 58 MW. Figure 2.12.1 shows a photograph of the ILL reactor hall and Figure 2.12.2 shows the layout of instruments at the ILL. Neutron powder diffraction experiments were done using the D2B and D20 diffractometers, see **2.5.1.1** and **2.5.1.2** for more information on these instruments.

#### 2.5.1.1. D2B high resolution Neutron Powder Diffractometer, ILL.

The diffractometer D2B (Hewat, 1986) is characterised by the very high take-off angle ($135^\circ$) for

the monochromator, which has a relatively large mosaic spread of 20' to compensate for the corresponding intensity ($\Delta\lambda/\lambda$) loss. It is 300 mm high, focusing vertically onto about 50 mm; this large incident vertical divergence is matched by 200 mm high detectors and collimators. A complete diffraction pattern is obtained after about 100 steps of 0.025° 2θ, since the 64 detectors are spaced at 2.5° intervals. Such scans take typically 30 minutes; they are repeated to improve statistics. Figures 2.13.1-2 show a schematic diagram and a photograph of this diffractometer.

*Figure 2.12.1. Photograph of the ILL reactor hall.*

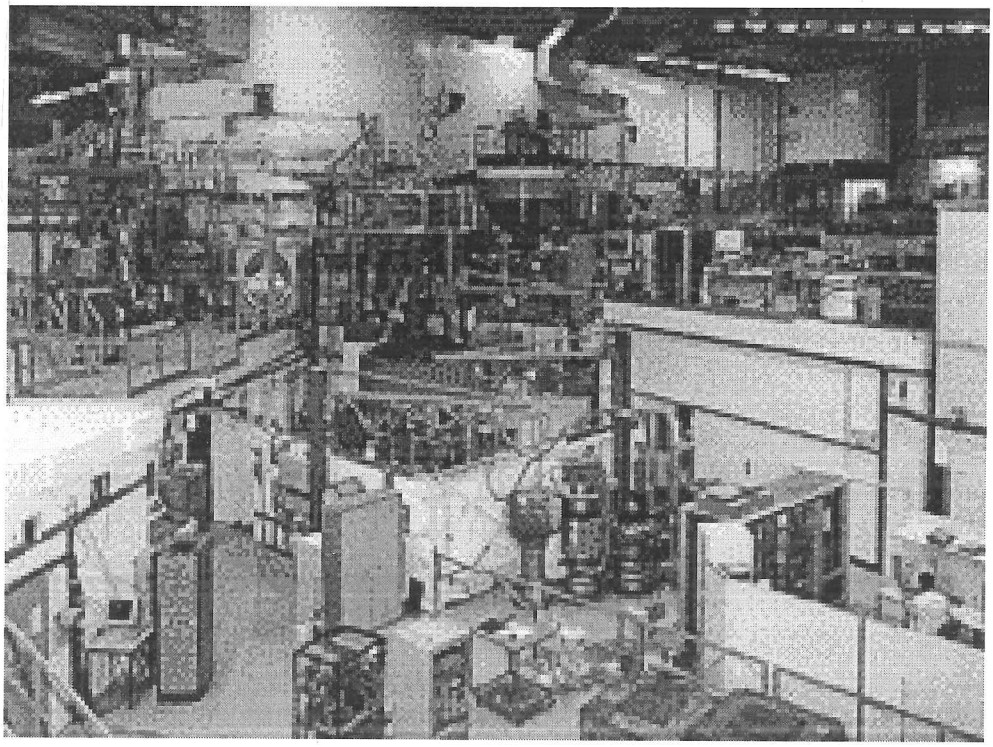

*Figure 2.12.2. ILL experimental instruments.*

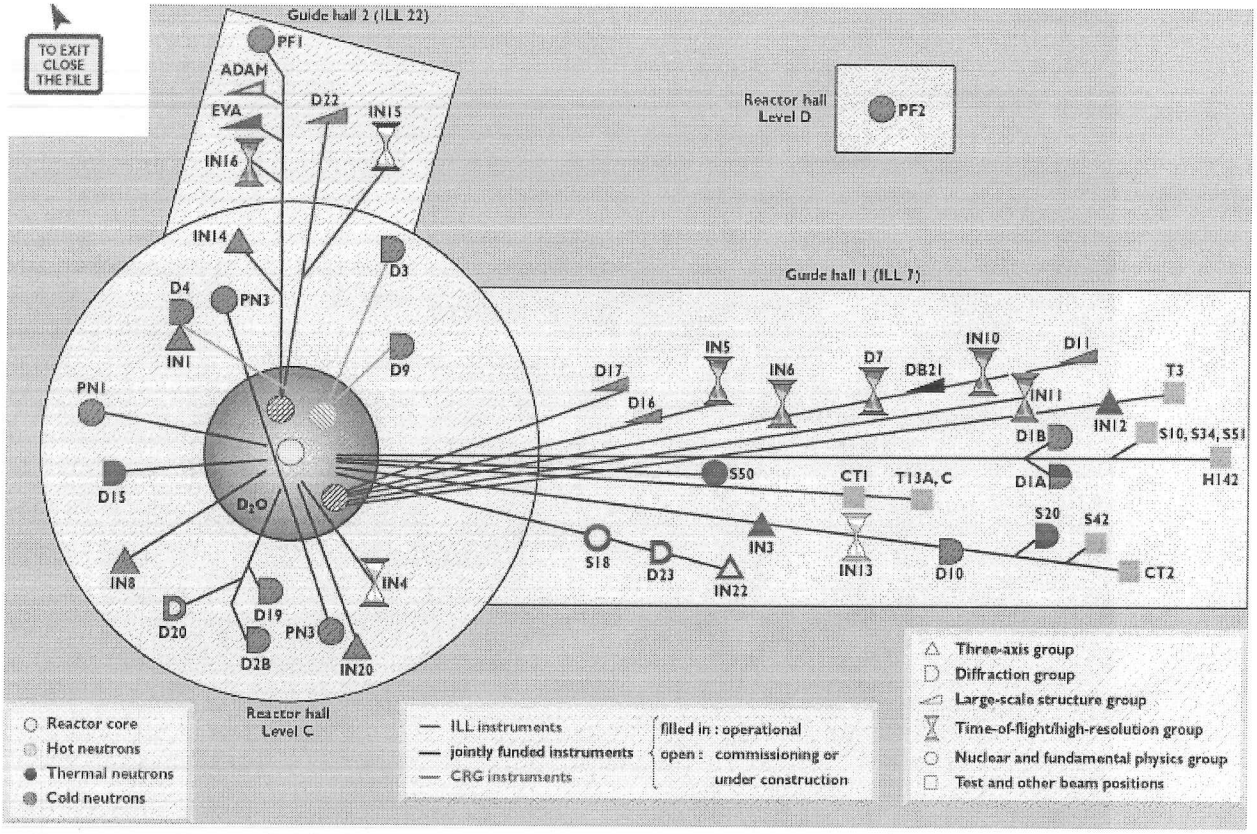


*Figure 2.13.1. Schematic diagram of D2B neutron powder diffractometer.*

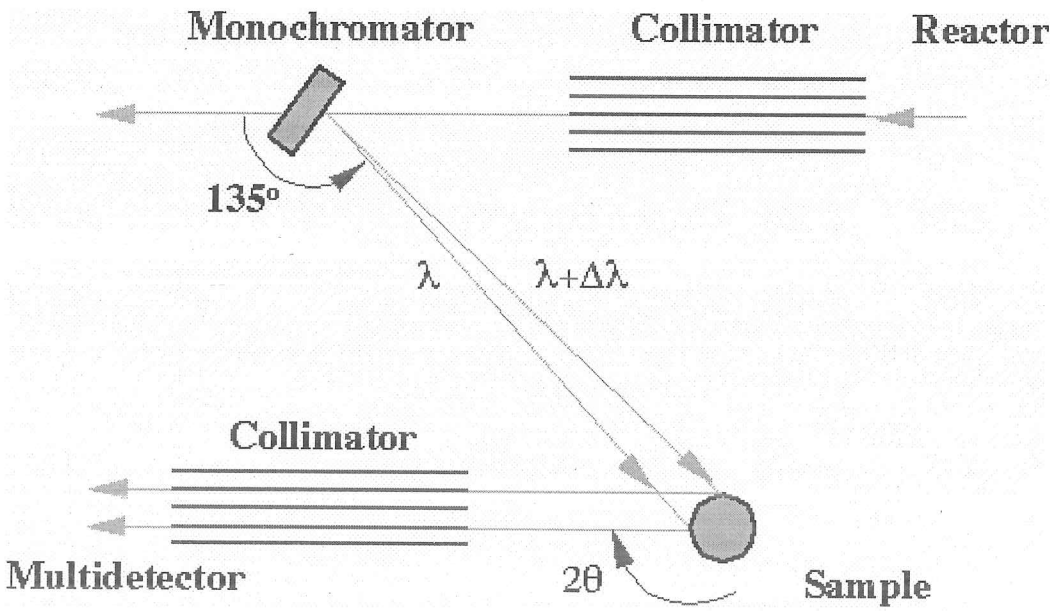

*Figure 2.13.2. Photograph of D2B neutron powder diffractometer.*

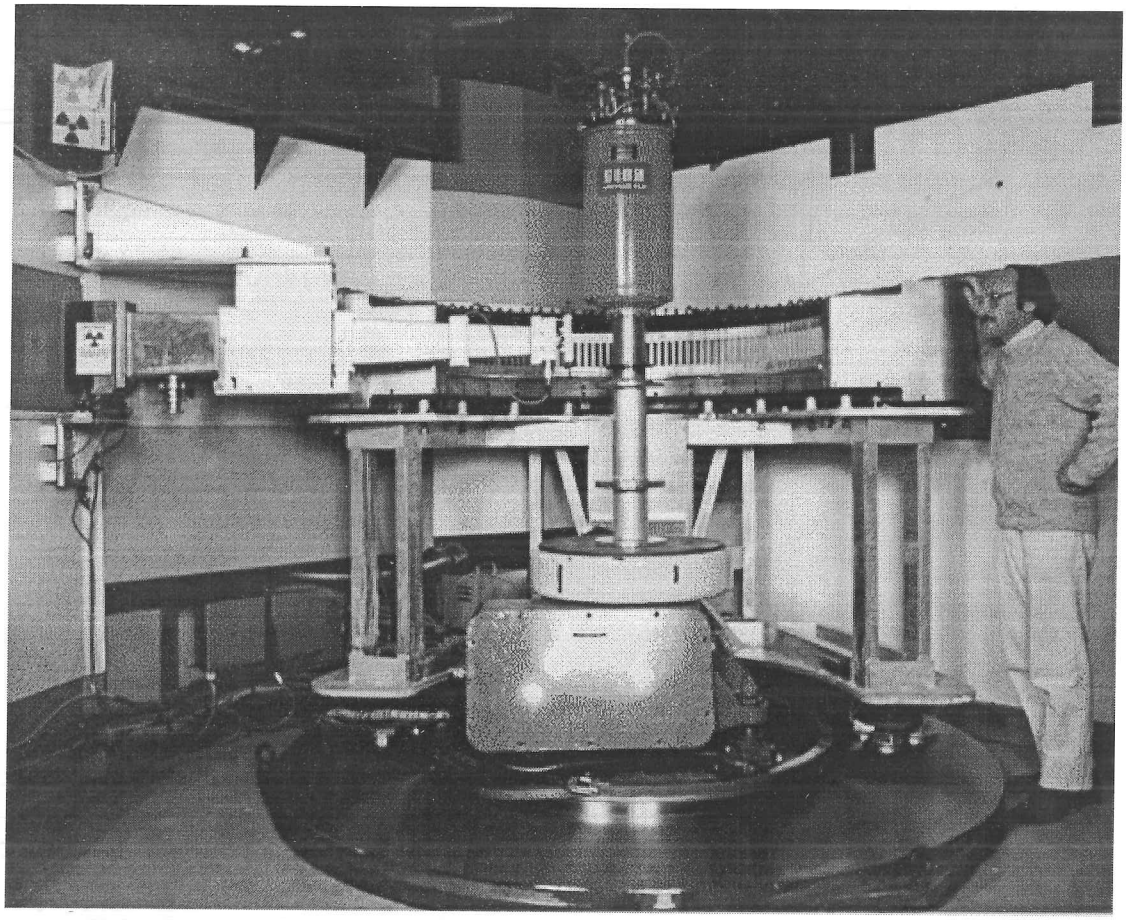

**2.5.1.2. D20 medium resolution Neutron Powder Diffractometer, ILL.**

D20 is a high-flux medium resolution powder-diffractometer equipped with a large-area position-sensitive detector. It operates in a wide range of wavelengths and was used with a cryostat for rapid powder diffraction data collection between 2-280 K with a neutron wavelength of $\lambda = 2.41$ Å. Figure 2.14 shows a schematic diagram of the D20 diffractometer.

*Figure 2.13.2. Photograph of D2B neutron powder diffractometer.*

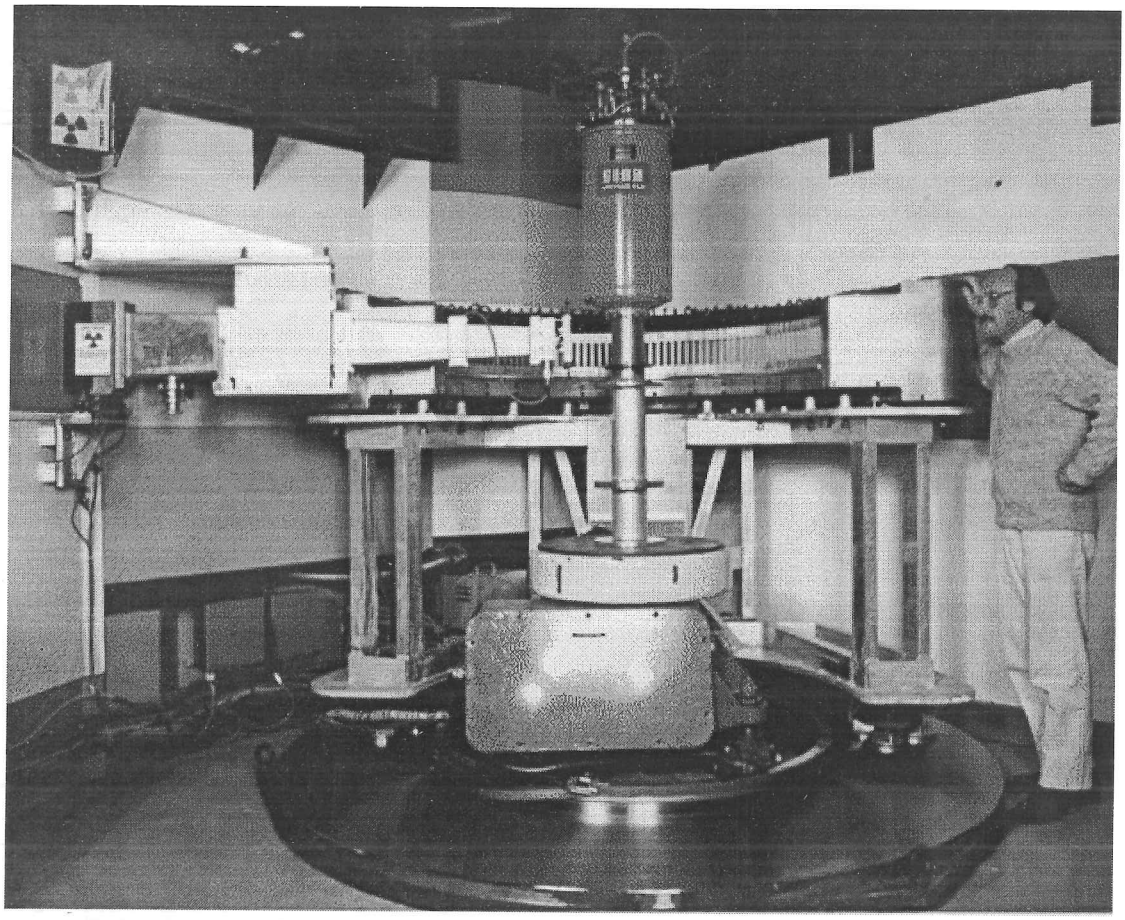

**2.5.1.2. D20 medium resolution Neutron Powder Diffractometer, ILL.**

D20 is a high-flux medium resolution powder-diffractometer equipped with a large-area position-sensitive detector. It operates in a wide range of wavelengths and was used with a cryostat for rapid powder diffraction data collection between 2-280 K with a neutron wavelength of $\lambda = 2.41$ Å. Figure 2.14 shows a schematic diagram of the D20 diffractometer.

*Figure 2.14. D20 neutron powder diffractometer.*

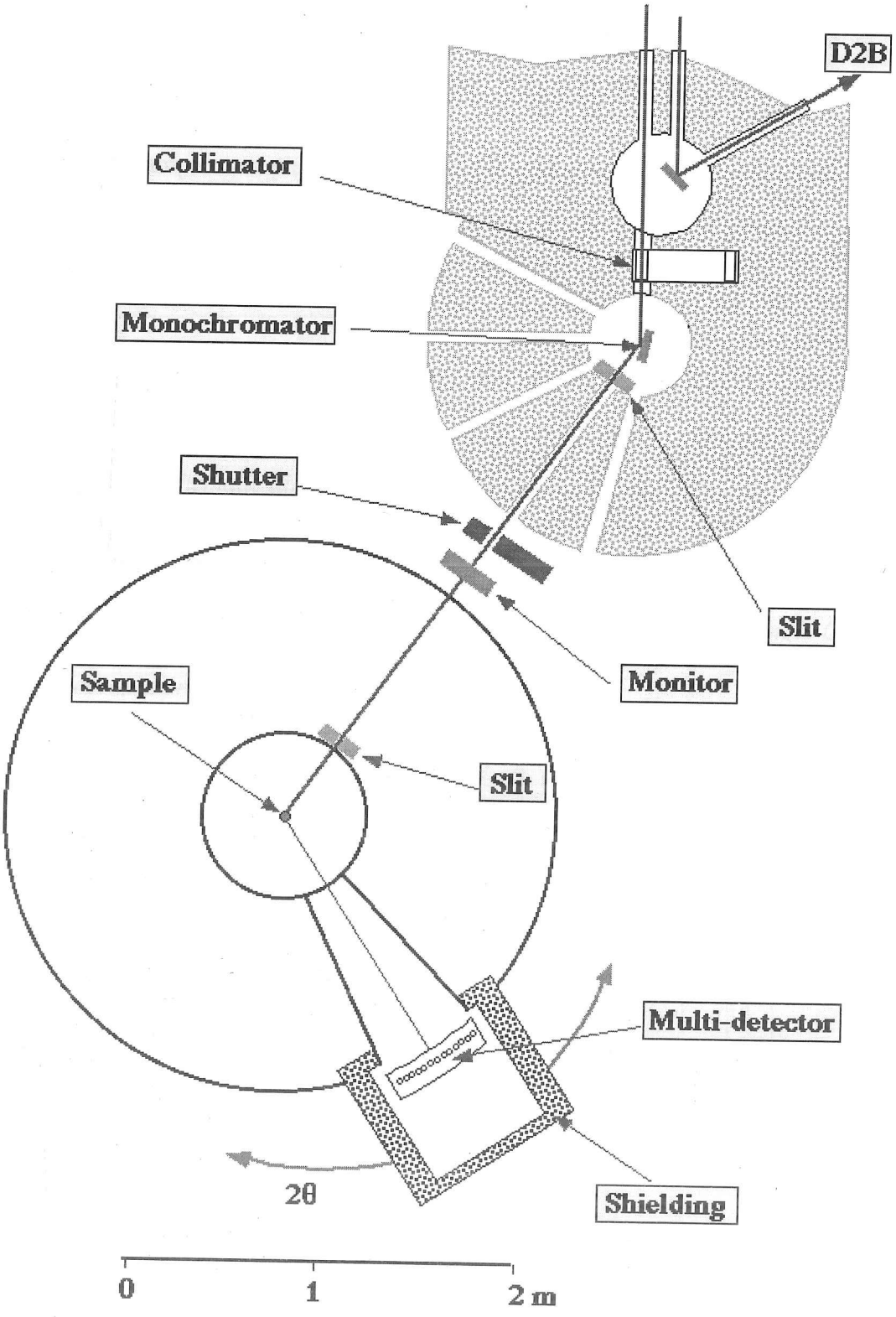

## 2.6. Mössbauer spectrometer.

$^{57}$Fe Mössbauer spectra were collected in transmission geometry using a conventional constant acceleration spectrometer and a $^{57}$Co source diffused into a Rh matrix. A 5mgFe/cm$^2$ layer of powdered sample was placed in a He bath cryostat and an evacuated cryofurnace for low and high temperature experiments respectively. Fe metal was used as a standard. Mössbauer data collection was done in the Laboratoire de Physique de l'Etat Condensé at the Université du Maine, Le Mans, France. Figure 2.15 shows a schematic diagram of the spectrometer used for these experiments.

*Figure 2.15. Schematic diagram of a Mössbauer spectrometer.*

*1. Gamma ray source. 2. Absorber 3. Cryostat 4. Drive Coil 5. Sensor Coil 6. Drive System 7. Data Collector 8. Power for Detector 9. Detector 10. Amplifier 11. Single Channel Analyser 12. Oscilloscopic presentation of spectrum.*

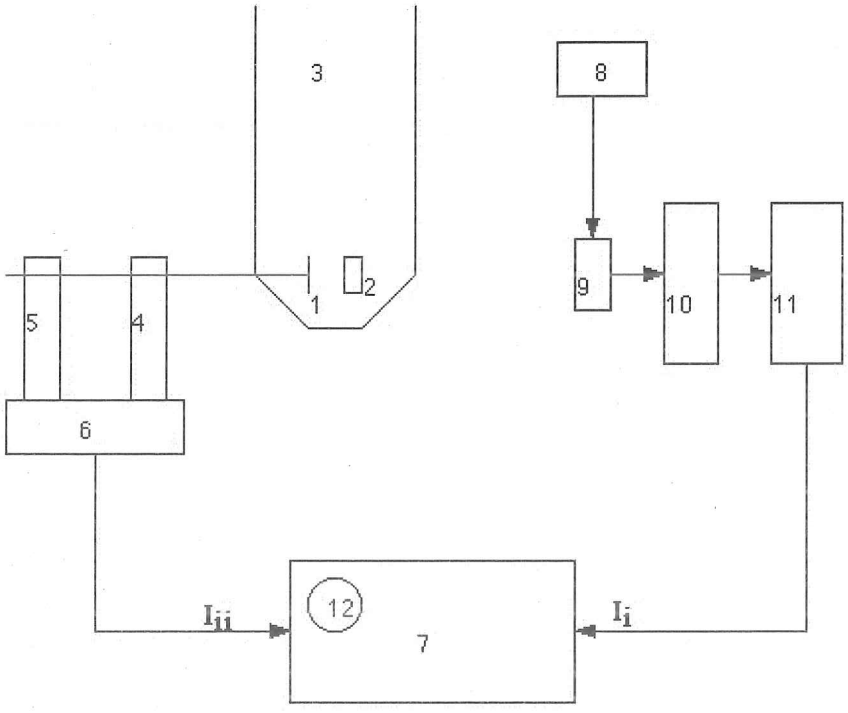

## 2.7. Resistivity measurements.

Resistivity measurements were carried out at the Interdisciplinary Research Centre in Superconductivity in an Oxford Instruments CF1200 liquid helium flow cryostat. The sample probe is contained in a chamber filled with static exchange gas to provide thermal contact between the sample and the walls of the sample space. The temperature is controlled by a balance between helium gas flow from a dewar and a heater. The temperature of the cryostat wall is measured with AuFe/Chromel thermocouple and controlled by an Oxford Instruments ITC4 temperature controller. Sample temperatures were measured using a calibrated silicon diode thermometer which is mounted about 5mm from the sample on a copper block. Using this equipment the sample temperature can be varied in the range 400-4.2 K with an accuracy of 0.1 K.

Resistivity measurements were made on polycrystalline pellets which had been cut into a bar with approximate dimensions 2 mm x 2 mm x 5mm, the sample was mounted onto the sample probe with double sided sellotape. The four probe d.c. technique was used with bare copper wires attached to the sample using colloidal silver paint. Figure 2.16 shows the resistivity apparatus used in this work.

## 2.8. Magnetisation measurements.

Variable temperature magnetisation measurements were also carried out at the Interdisciplinary Research Centre in Superconductivity using a Quantum Design Magnetic Property Measurement System (MPMS). This has two major hardware components, a liquid helium dewar and probe

*Figure 2.16. Resistivity apparatus.*

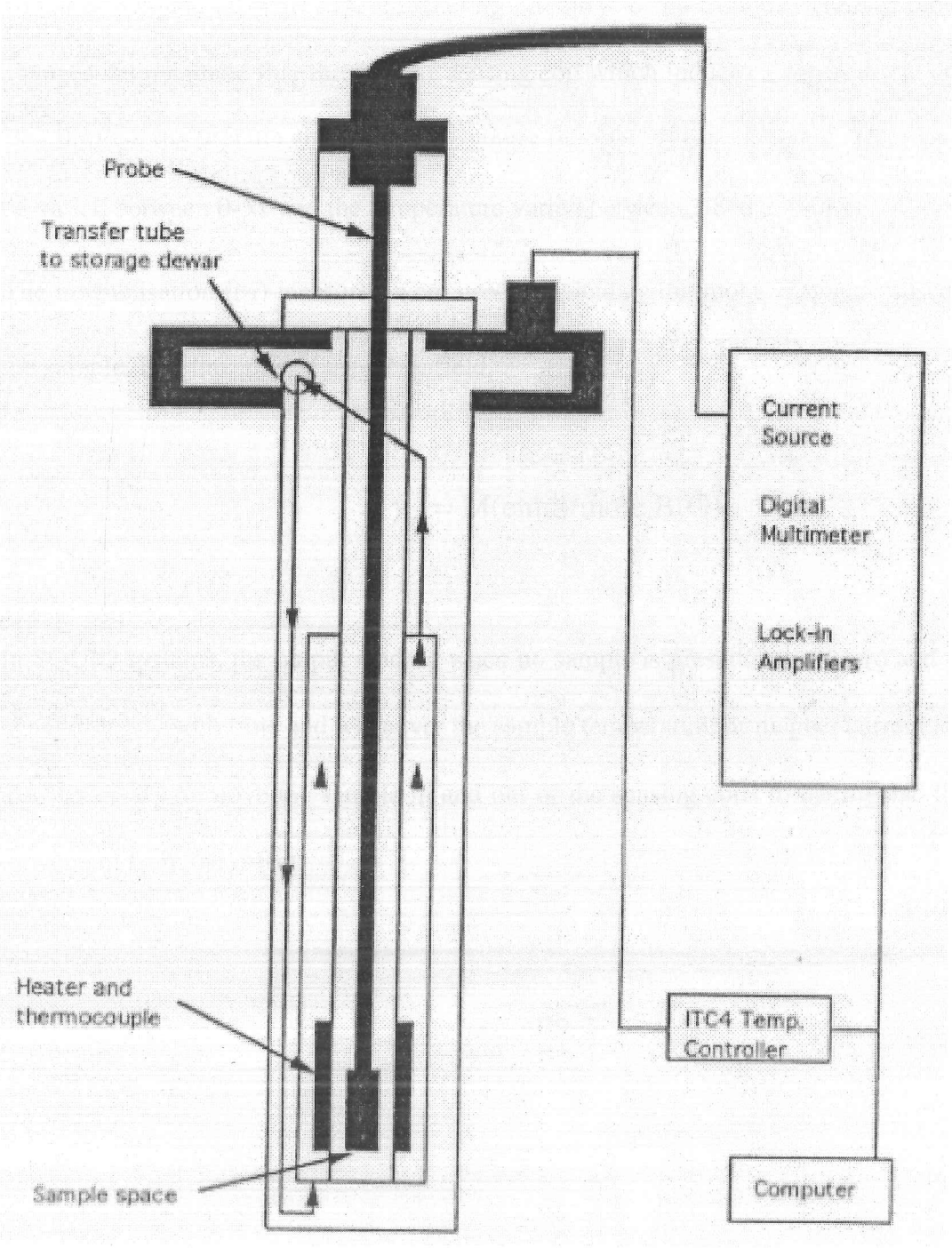


assembly, and the associated control system (see Figure 2.17). The probe integrates a 5.5 T superconducting magnet with a SQUID (Superconducting Quantum Interference Device) detection system. In a SQUID susceptometer, the magnetising field is provided by a

superconducting electromagnet. The sample is surrounded by a superconducting sensing coil, which is coupled through superconducting circuitry to the SQUID. The sample magnetisation changes the magnetic flux through the sensing coil which induces a supercurrent and changes the flux through the SQUID and therefore changes the SQUID output signal. The magnetic field can be varied between 0-5T and the temperature varied between 1.8 and 400K.

The magnetisation (M) measured were used to calculate the molar magnetic susceptibilty $\chi_m$, of the sample. B is the applied magnetic field.

$$\chi_m = M(emu)/mole.B(G)$$

In SQUID systems, the output reading when no sample is present is non-zero and this offset will change slowly with time and whenever the sample temperature or magnet current is changed. It is also necessary to move the sample in and out of the sensing coils to distinguish the true sample movement from the offset.

*Figure 2.17. SQUID apparatus for magnetisation measurements.*

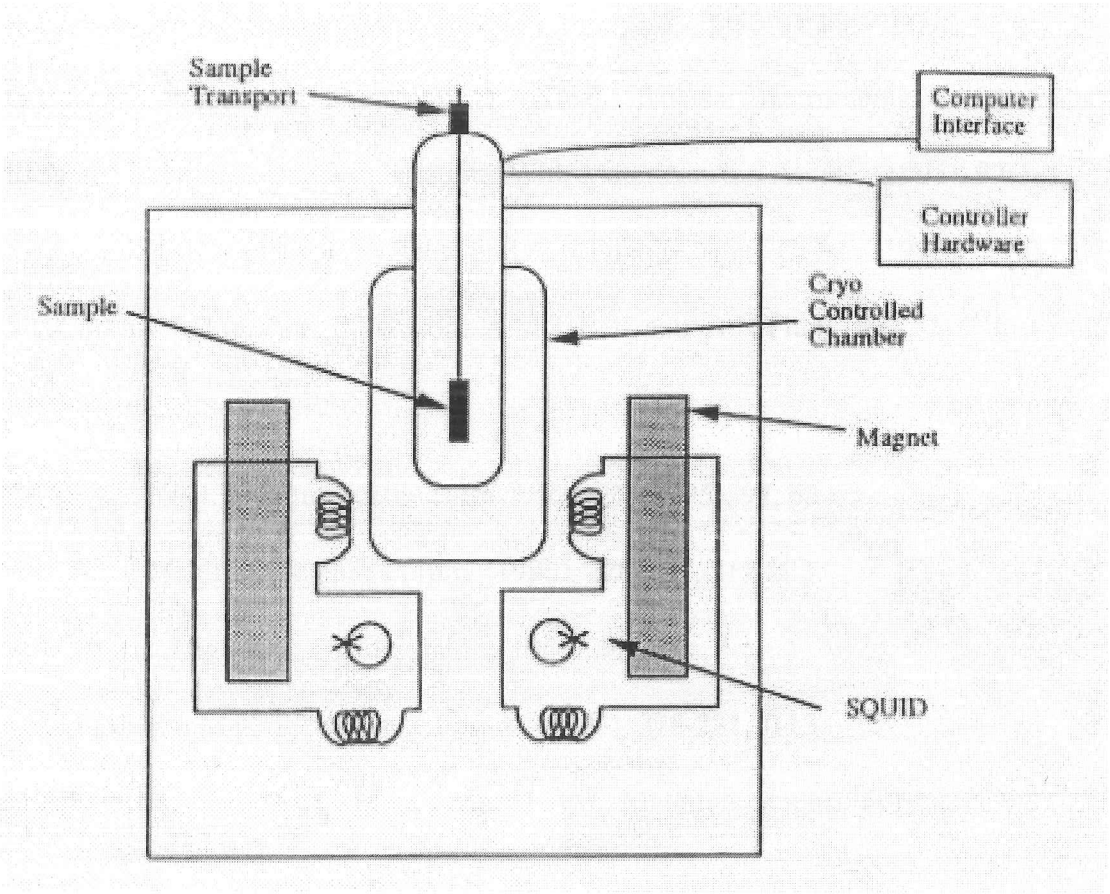

**Chapter 2 - References.**

G.Bushnell-Wye and R.J.Cernik, Rev. Sci. Inst., (1992), **63(1),** 999-1001.

G.Bushnell-Wye, J.L.Finney and J.D.Wicks, Nuclear Instruments & Methods In Physics Research Section B-Beam Interactions With Materials And Atoms, (1995), **97(1-4),** 557-560.

R.J.Cernik, P.K.Murray, P.Pattison, and A.N.Fitch. J. Appl. Cryst., (1990), **23(4)**, 292-296.

S.P.Collins, R.J.Cernik, P.Pattison, A.M.T.Bell and A.N.Fitch, Rev. Sci. Inst., (1992), **63(1),** 1013-1014.

A.N.Fitch, Nucl. Instrum. Methods Phys. Res. B, (1995), **97,** 63-69.

A.N.Fitch, Materials Science Forum, (1996), **228-231**, 219-222.

A.W.Hewat, High Res. Powder. Diff., (1986), **9**, 69.

M.I.McMahon Materials Science Forum, (1998), **278-281**, 1-13.

M.A.Roberts, J.L.Finney and G.Bushnell-Wye, Materials Science Forum, (1998), **278-281**, 318-322.

C.C.Tang, G.Bushnell-Wye and R.J.Cernik, J. Synchrotron Radiation, (1998), **5(3),** 929-931.

# Chapter 3. Structure of Magnetite below the Verwey Transition.

## 3.1. $Fe_3O_4$ and the Verwey Transition.

### 3.1.1. $Fe_3O_4$.

The mixed valent iron oxide $Fe_3O_4$ (magnetite) is a fundamentally important magnetic material. It is a naturally occurring mineral and has been used throughout history as a permanent magnet and compass. Magnetite is the parent material for the ferrites used in modern magnetic recording and data storage devices. The unusual electronic and magnetic properties of magnetite derive from its mixed valent character.

At room temperature $Fe_3O_4$ has the Fd3m cubic inverse spinel crystal structure ($a_o$ = 8.396 Å), see Figure 3.1. There are two types of metal sites in this structure, octahedral sites on which $Fe^{2+}$ and $Fe^{3+}$ cations are disordered and tetrahedral sites which only contain $Fe^{3+}$. Magnetite is a conducting ferrimagnet at room temperature. However at around 120 K this simple crystal structure undergoes a complicated metal to insulator phase transition, the **Verwey Transition**, to a low-symmetry structure. This structure has yet to be completely determined but is thought to have ordered $Fe^{2+}$ and $Fe^{3+}$ cations.

### 3.1.2. Verwey Transition.

The first evidence for a phase transition in $Fe_3O_4$ was a heat capacity anomaly near 120 K reported by Millar (1929). Verwey (1939) showed that the resistivity of magnetite changed anomalously near 120 K and Verwey et al (1947) suggested a possible ordering scheme with $Fe^{2+}$

and $Fe^{3+}$ cations ordered on alternate layers of octahedral sites. However, more recent structural studies of $Fe_3O_4$ have shown that this ordering scheme is more complicated than Verwey's scheme, see Figure 3.2.

*Figure 3.1. Ambient temperature $Fe_3O_4$ spinel structure in **bc** plane. Tetrahedral $FeO_4$ units are given in red and octahedral $FeO_6$ units are given in green. Unit cell is indicated in blue.*

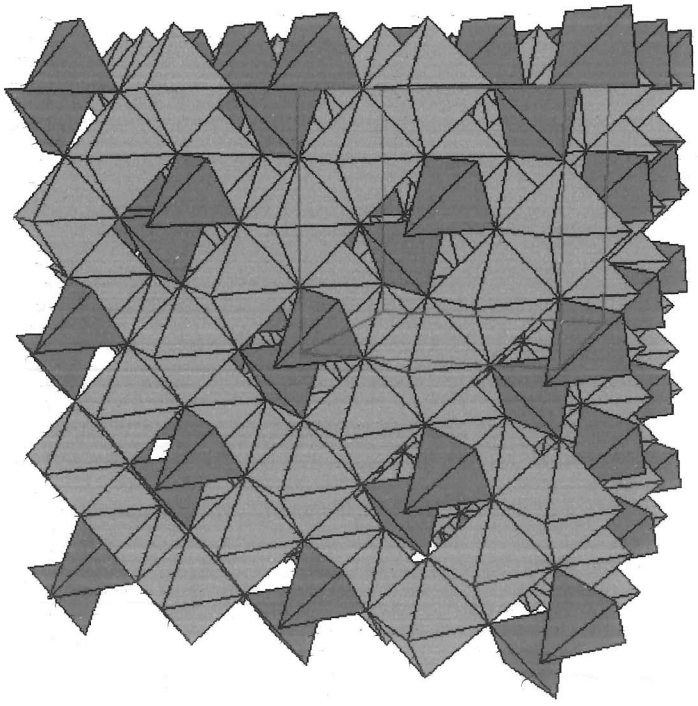

$Fe_3O_4$ is a conductor above the Verwey Transition but this conductivity (approx. 200 $\Omega^{-1}cm^{-1}$), is very low compared to that of a metal (10000 $\Omega^{-1}cm^{-1}$ for Fe metal). However, the behaviour of electrons in this material is not like in a metal, the electron mobility is controlled by polarons (lattice distortions due to localised electrons) and the electrons move by "hopping" between neighbouring disordered Fe cations on octahedral sites in the spinel structure. Below the Verwey Transition the conductivity decreases significantly due to a distortion of the lattice, this traps the mobile electrons by the formation of ordered $Fe^{2+}$ and $Fe^{3+}$ cations, see Cox (1987) for more

information on polarons.

*Figure 3.2. Octahedral site cation ordering scheme for $Fe_3O_4$ below the Verwey Transition temperature as suggested by Verwey et al (1947). Large spheres and small black dots represent $Fe^{3+}$, small spheres and open circles represent $Fe^{2+}$ cations. Projections of the octahedral sites in the xy and yz planes are also given, numbers represent the fraction of the unit cell edge above these planes. Oxygen atoms and tetrahedral $Fe^{3+}$ cations sites are excluded for clarity.*

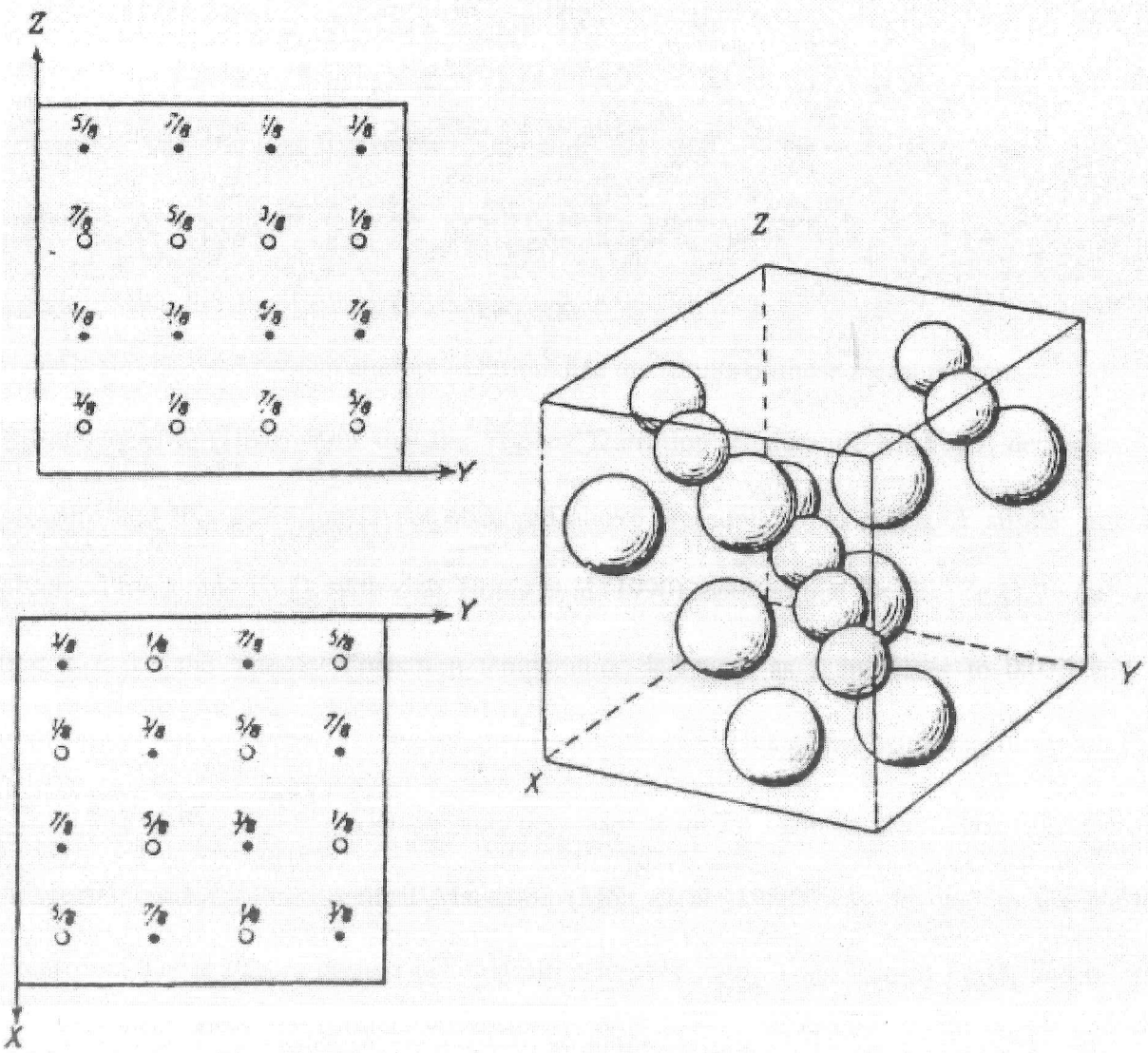


Honig (1995) gave a review of the thermodynamic and electrical transport phenomena in

magnetite around the Verwey transition. This review discusses the variation in Verwey Transition temperature with the Fe/O ratio in magnetite. For single crystal studies of magnetite great care must be taken to prepare a sample free from impurities. These samples need to be annealed to get the correct Fe/O ratios. The variation of the Verwey Transition temperature with stoichiometry has been measured using heat capacity and electrical measurements. The Verwey Transition is only observed over a small Fe/O composition range in magnetite. For $Fe_{3(1-\delta)}O_4$ stoichiometries where $-0.0005 < \delta < 0.0039$ magnetite exhibits a first order phase transition at the Verwey Transition, for stoichiometries where $0.0039 < \delta < 0.0117$ this is a second order phase transition. The Verwey Transition temperature decreases as the Fe/O ratio decreases and as $\delta$ increases. At stoichiometries with $\delta > 0.0117$ the Verwey Transition is not observed as at this stoichiometry the magnetite-haematite phase boundary is reached. Two different theoretical models are discussed which attempt to rationalize the results of these measurements.

Rozenberg et al (1996) show that the Verwey Transition temperature for $Fe_3O_4$ decreases with pressure and this transition is not observed above pressures of 12.5GPa. A similar effect is observed by doping $Fe_3O_4$ with zinc, Honig et al (1990) reported that for $Fe_{3-x}Zn_xO_4$ in the range $0 < x < 0.3$ the Verwey Transition temperature decreases as x increases to 0.036 and the transition is not observed with higher zinc concentrations. This agrees with the studies on $Fe_{3(1-x)}O_4$ as the Verwey Transition temperature decreases as the $Fe^{2+}$ content decreases.

A special issue of Philosophical Magazine (Mott et al, 1980) was devoted to the Verwey Transition. These papers discuss different aspects of Verwey Transition in $Fe_3O_4$ and in other materials which have been found to exhibit a similar transition.

$Ti_4O_7$ has a low temperature ordered phase in which $Ti^{3+}$ and $Ti^{4+}$ cations are ordered, in this phase pairs of $Ti^{3+}$ cations exist as bipolarons, this material reverts to a disordered phase at about

150 K. A similar effect to doping zinc into magnetite is observed when $Ti_4O_7$ is doped with vanadium to form $(Ti_{1-x}V_x)_4O_7$, this decreases the transition temperature between the ordered and disordered phase (Schenkler et al, 1980). Similar transitions are found in $Na_xV_2O_{5-y}$ (ordering of $V^{4+}/V^{5+}$; Dumas et al, 1980) and $Eu_3S_4$ (ordering of $Eu^{2+}/Eu^{3+}$; Holtzberg, 1980).

### 3.1.3. Structural studies below the Verwey Transition.

Tooms et al (1951) did some low temperature X-ray powder diffraction and were the first to find that the $Fe_3O_4$ structure is not cubic below the Verwey Transition, they observed a rhombohedral distortion of the cubic structure. Studies since then have shown the low temperature structure of $Fe_3O_4$ to be more complicated as more sensitive analytical techniques have been applied. These structural studies are summarised below.

Hamilton (1958) did a neutron single-crystal study the results of which confirmed Verwey's orthorhombic ordering scheme below the Verwey Transition. However, a critical neutron scattering experiment just above the Verwey Transition by Fujii et al (1975) disagreed with the Verwey ordering scheme and suggested that this scheme was more complicated. More neutron single-crystal work below the Verwey Transition by Samuelsen et al (1968) showed a lowering of symmetry from cubic to orthorhombic. Yamada et al (1968), performed an electron diffraction study on this "orthorhombic" phase and found that the ordering structure was more complicated than that of Verwey, in this orthorhombic structure $2a_o \times 2a_o \times a_o$ where $a_o$ is the cubic spinel parameter. Shirane et al (1975) also disagree with the Verwey ordering model with $Fe^{2+}$ and $Fe^{3+}$ ordered in the ab plane, not along the c-axis.

An NMR study by Mizoguchi (1978ab) on $Fe_3O_4$ at 4.2 K deduced that $Fe^{2+}$ and $Fe^{3+}$ were

ordered with pairs of $Fe^{2+}$ and $Fe^{3+}$ cations lining up alternately along the a-axis and that groups of $1Fe^{2+}$ and $3Fe^{3+}$ or $3Fe^{2+}$ and $1Fe^{3+}$ cations line up alternately along the b-axis. Iida (1980) deduced from Mössbauer and NMR work that the low temperature structure of $Fe_3O_4$ has the $P2_1/c$ space group.

Vieland (1975) noted that cooling $Fe_3O_4$ through the Verwey Transition in the presence of a magnetic field produced a monoclinic superlattice. A neutron single-crystal study by Iizumi et al (1975), shows superlattice lines below the Verwey Transition.

Rado et al (1975), did some magnetoelectric work at 4.2 K showed no macroscopic directional symmetry and deduced that this structure has space group P1 (triclinic). Siratori et al (1979) have measured the magnetoelectric effect at 77 K and confirm this space group assignment.

Berry et al (1998) did a $^{57}Fe$ Mössbauer study at 4.2 K on a single-crystal of $Fe_3O_4$ cut along 111 and determined that there was 1 tetrahedral $Fe^{3+}$ site and 4 ordered octahedral sites, two $Fe^{3+}$ and two $Fe^{2+}$.

### 3.1.4. Iizumi et al structure determination.

The most recent structure determination of this low temperature phase was by Iizumi et al (1982). The structure of $Fe_3O_4$ was determined at 10 K by single-crystal neutron diffraction, the low temperature structure was determined as monoclinic (space group Cc), with lattice parameters $a = 11.868(2)$ Å, $b = 11.851(2)$ Å, $c = 16.752(4)$ Å and $\beta = 90.20(3)^\circ$. Due to the complexity of this structure, approximate primitive orthorhombic structures were determined. In these structures the lattice parameters are $\sqrt{2}a_o \times \sqrt{2}a_o \times 2a_o$ where $a_o$ is the cubic spinel parameter. These low temperature structures were obtained by atomic displacements from the

cubic spinel structure, these displacements break most of the cubic symmetry elements but as these displacements are small the structure still maintains approximate higher symmetry. Pmca and $Pmc2_1$ orthorhombic space groups with lattice parameters of $a_o/\sqrt{2}$ x $a_o/\sqrt{2}$ x $2a_o$ were used for the approximate structure determinations. These showed no significant variation in Fe-O distances for the octahedral sites as would be expected for $Fe^{2+}$ and $Fe^{3+}$ ordering, these octahedral Fe-O distances are in the range 2.015-2.095Å and correspond to those for disordered $Fe^{2+}$ and $Fe^{3+}$ cations.

In spite of the extensive work done on this problem since Verwey's discovery of this transition the low-temperature structure of $Fe_3O_4$ is still to be completely determined. High resolution synchrotron and neutron powder diffraction techniques have yet to be applied to this challenging problem so these techniques have been used in this structure determination attempt.

### 3.2. Preparative methods.

#### 3.2.1. Synchrotron Sample.

A $Fe_3O_4$ sample was prepared for synchrotron X-ray powder diffraction. $Fe_3O_4$ powder purchased from Johnson Matthey was made into a pellet and heated for 5 days in a sealed evacuated quartz tube at 1173 K, the pellet was wrapped in gold foil to prevent reaction of the pellet with quartz.

#### 3.2.2. Neutron sample.

A second sample was prepared for neutron powder diffraction by mixing stoichiometric amounts

of Fe and $Fe_2O_3$ and heating in a sealed evacuated silica tube for 84 hours at 1273 K.

### 3.3. X-ray Powder Diffraction.

The laboratory X-ray powder diffraction pattern (see section 2.1.1) for the synchrotron $Fe_3O_4$ sample showed that all of the Bragg reflections matched the known spinel $Fe_3O_4$ pattern apart from one weak impurity reflection which matched the strongest line for $Fe_2O_3$ (haematite), see Figure 3.3. No impurity reflections could be seen in the laboratory X-ray powder diffraction pattern for the neutron sample, see Figure 3.4.

*Figure 3.3. Laboratory X-ray powder diffraction pattern for $Fe_3O_4$ synchrotron sample, note presence of $Fe_2O_3$ impurity peak. $Fe_3O_4$ peaks marked with Miller indices.*

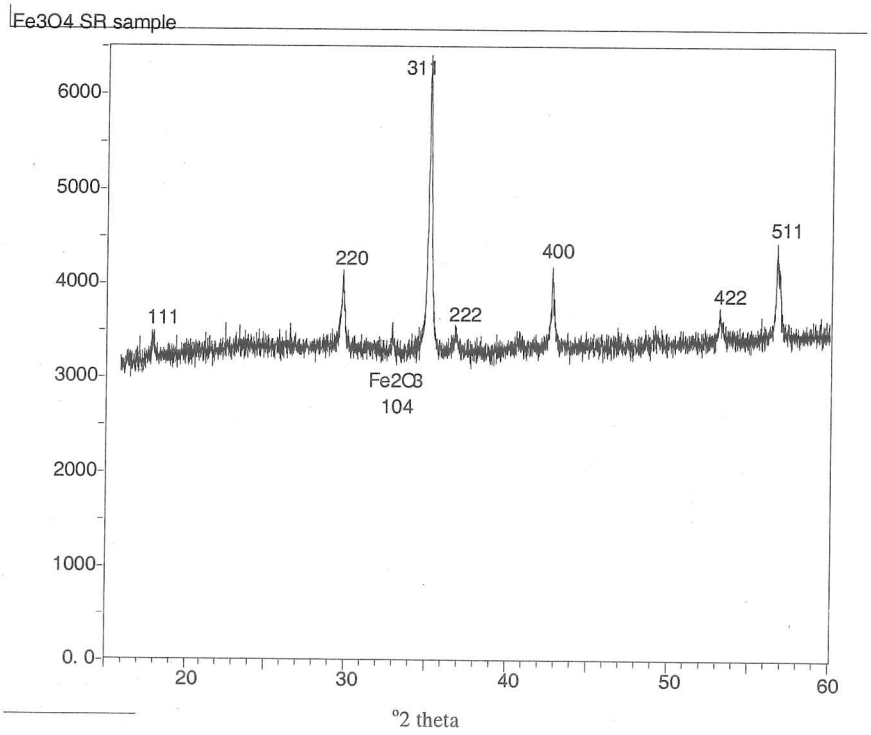

*Figure 3.4. Laboratory X-ray powder diffraction pattern for $Fe_3O_4$ neutron sample, no impurity phases detected. $Fe_3O_4$ peaks marked with Miller indices.*

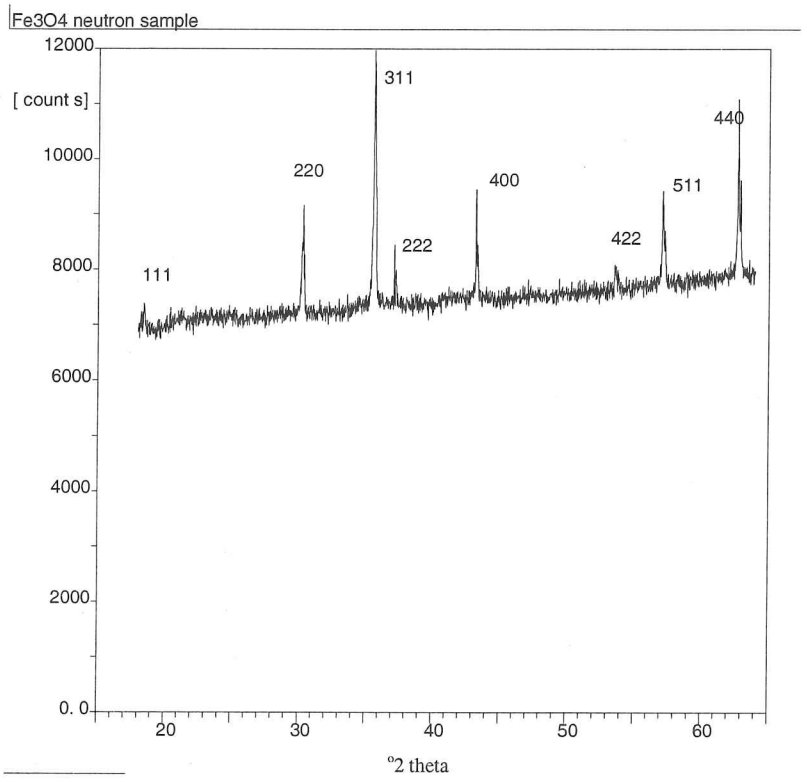


## 3.4. Resistivity.

Resistivity measurements (see section 2.7) were made on the synchrotron $Fe_3O_4$ sample between 305 and 108 K with a cooling rate of 5 K/minute. Figure 3.5 shows the resistivity measurements made between 150 and 108 K, this shows that the resistivity starts to increase around 122 K which is close to the Verwey Transition temperature.

*Figure 3.5. Variation of resistivity plot with temperature for the $Fe_3O_4$ synchrotron sample. The change in resistivity with temperature is clearly visible at the Verwey Transition temperature (122 K) on this logarithmic scale.*

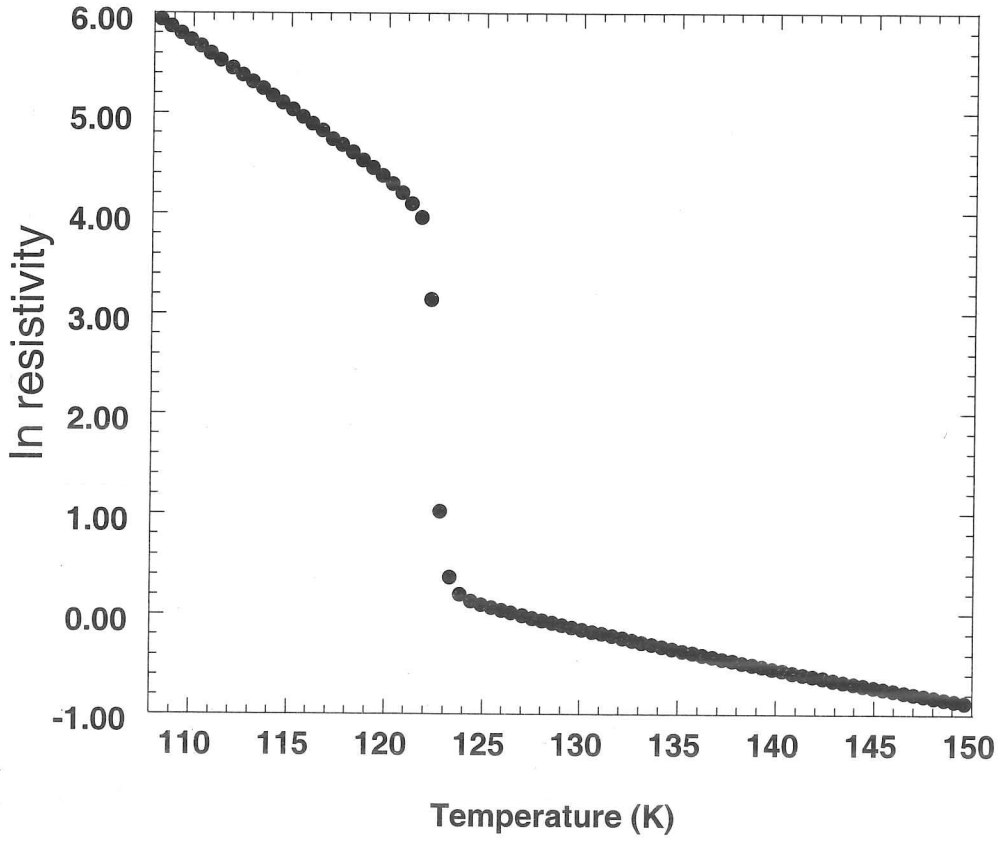


### 3.5. Synchrotron X-ray Powder Diffraction.

A silicon standard sample in a glass capillary was mounted in the cryostat stage on the high resolution powder diffractometer on 9.1 of the Daresbury SRS (see section 2.3.1) to calibrate the monochromator. The monochromator was set at 1Å and a synchrotron X-ray powder diffraction

pattern was measured for the silicon, the refined SR wavelength came out as 1.0015Å.

The synchrotron sample was then loaded into a 0.5mm diameter glass capillary and mounted in the cryostat. A scan at 130 K showed the spinel phase and some haematite impurity lines. The cubic lattice parameter was then refined for the spinel phase as 8.381(2) Å. Repeat scans were then done over the 440 reflection with the temperature being decreased at 5 K intervals down to 100 K. The 440 reflection was split into a doublet by 125 K. Figure 3.6 shows these split reflections.

*Figure 3.6. Splitting of spinel phase 440 reflection with decreasing temperature.*

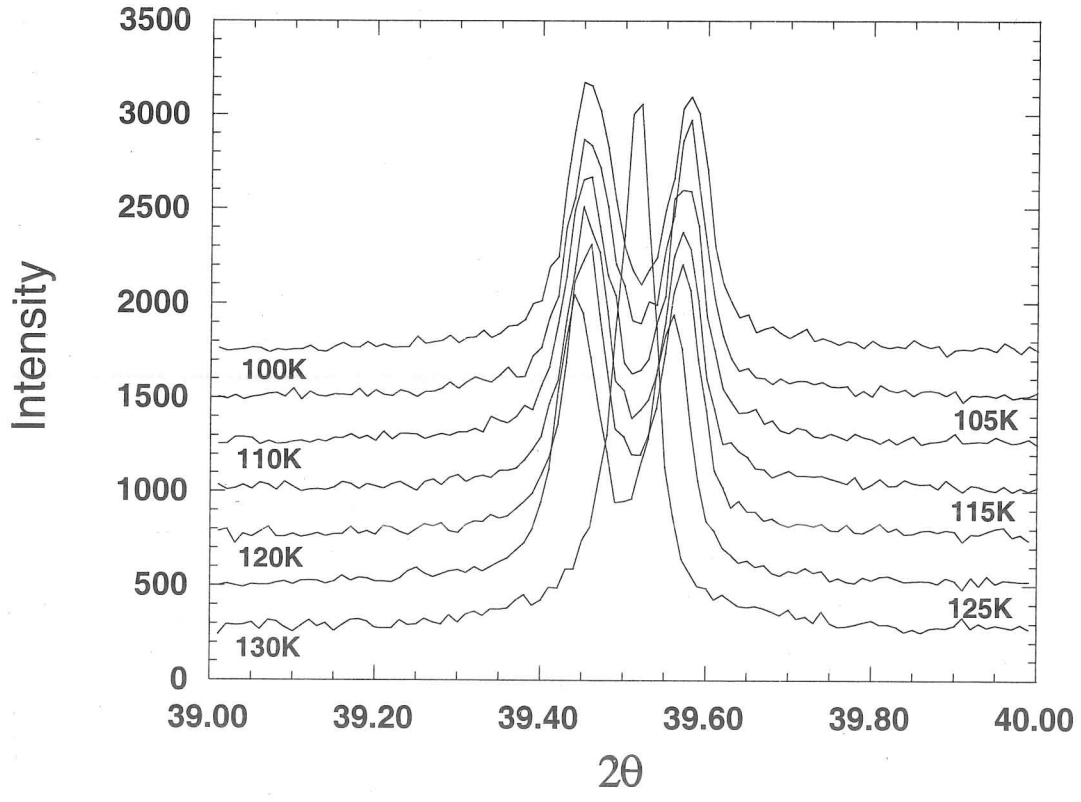


In these doublets the low angle reflection was broader than high angle one, measurements of the

full width at half maximum (FWHM) for these doublets indicate that the breadth of the low angle reflection increases at 110 K, This could be due to this low angle reflection actually being a close overlap of 2 reflections and could suggest that the 440 spinel reflection may split into 3 reflections on passing through the Verwey Transition and the symmetry of the low temperature phase may be orthorhombic or lower, see Table 3.1.

*Table 3.1. Variation of FWHM for split spinel 440 reflection with temperature.*

| Temp. (K) | FWHM low angle (°2θ) | FWHM high angle (°2θ) |
|---|---|---|
| 130 | 0.057 | single peak |
| 125 | 0.064 | 0.060 |
| 120 | 0.059 | 0.058 |
| 115 | 0.060 | 0.056 |
| 110 | 0.070 | 0.058 |
| 105 | 0.068 | 0.055 |
| 100 | 0.069 | 0.061 |
| 60 | 0.070 | 0.054 |

The cryostat was then cooled to 60 K and a long overnight scan was done in the range 1-80 °2θ, several of the single cubic Bragg reflections measured at 130 K were observed to split. Figures 3.7.1-3 compare the diffraction patterns measured at 60 K and 130 K.

In this 60 K pattern there were several split "spinel" reflections indicating a lowering of the crystal structure from cubic. There were no reflections in the 60 K pattern at a lower angle than the spinel 111 reflection therefore no superlattice was observed.

Synchrotron data was also collected on the neutron sample at 60 K using the high resolution powder diffractometer on station 2.3 of the Daresbury SRS (see section 2.3.2). A flat plate sample was used with a synchrotron X-ray wavelength of $\lambda$= 1.30058 Å.

*Figure 3.7.1. Synchrotron X-ray powder diffraction patterns for $Fe_3O_4$ measured at 130 K and 60 K, $\lambda$ = 1.0015Å, 2$\theta$ range 10-30°. Haematite impurity reflections are marked *.*

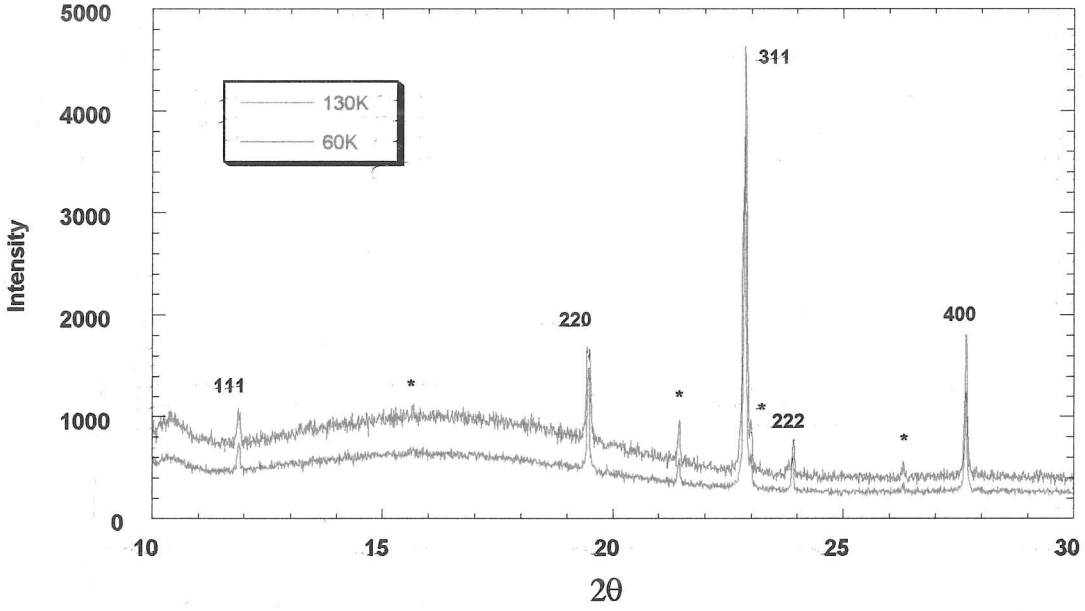


*Figure 3.7.2. Synchrotron X-ray powder diffraction patterns for $Fe_3O_4$ measured at 130 K and 60 K, $\lambda$ = 1.0015Å, 2$\theta$ range 30-40°. Haematite impurity reflections are marked *.*

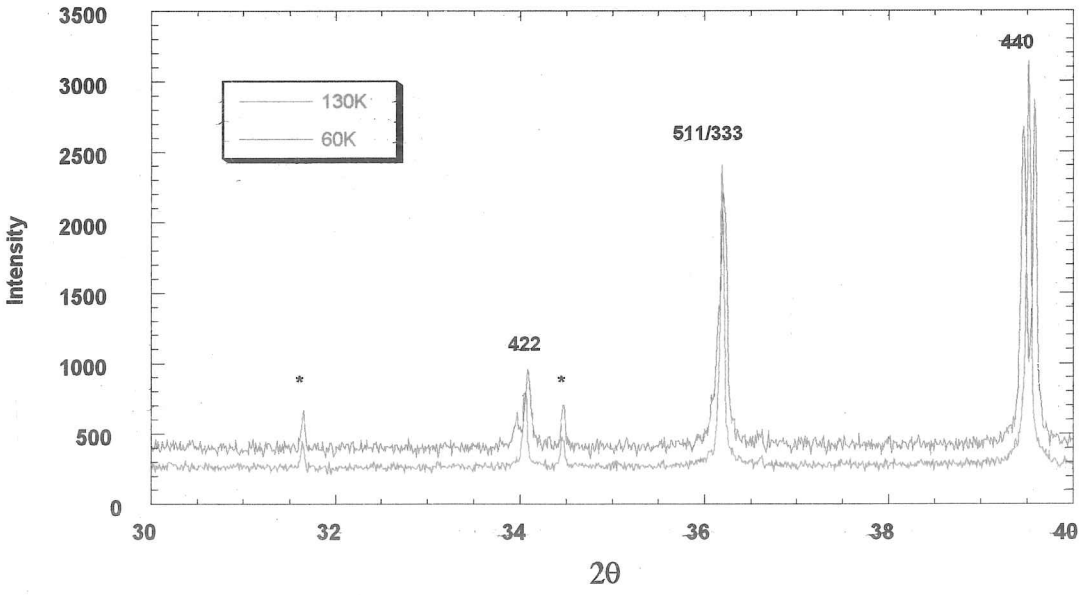

*Figure 3.7.3. Synchrotron X-ray powder diffraction patterns for $Fe_3O_4$ measured at 130 K and 60 K, $\lambda$ = 1.0015Å, 2$\theta$ range 40-50°. Haematite impurity reflections are marked *.*

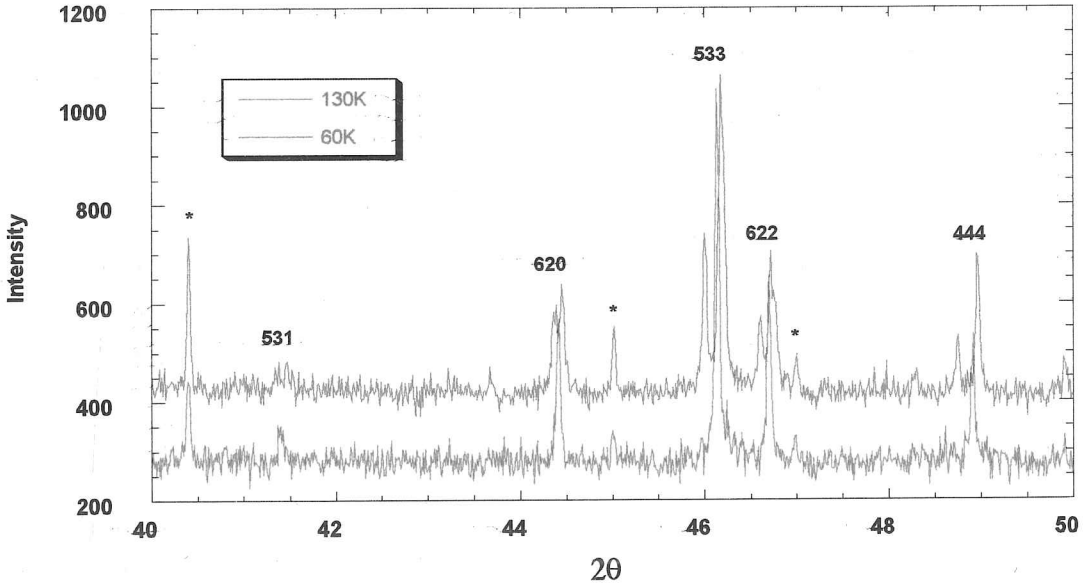


### 3.6. Neutron Powder Diffraction.

#### 3.6.1. D2B.

Neutron powder diffraction data were collected at 60 K using D2B high resolution powder diffractometer at the ILL (see section 2.5.1.1). High resolution powder diffraction data were collected between 4-164° 2θ counting for 36 hours. A shorter neutron powder diffraction scan was also made at 130 K, a small amount of wuestite (FeO) impurity phase was observed in these powder diffraction patterns. Figures 3.8.1-2 show the neutron powder diffraction patterns measured at 130 K and 60 K, note how some of the high angle reflections in the 60 K pattern become broadened and split compared to those measured at 130 K.

*Figure 3.8.1. D2B neutron powder pattern at 130 K.*

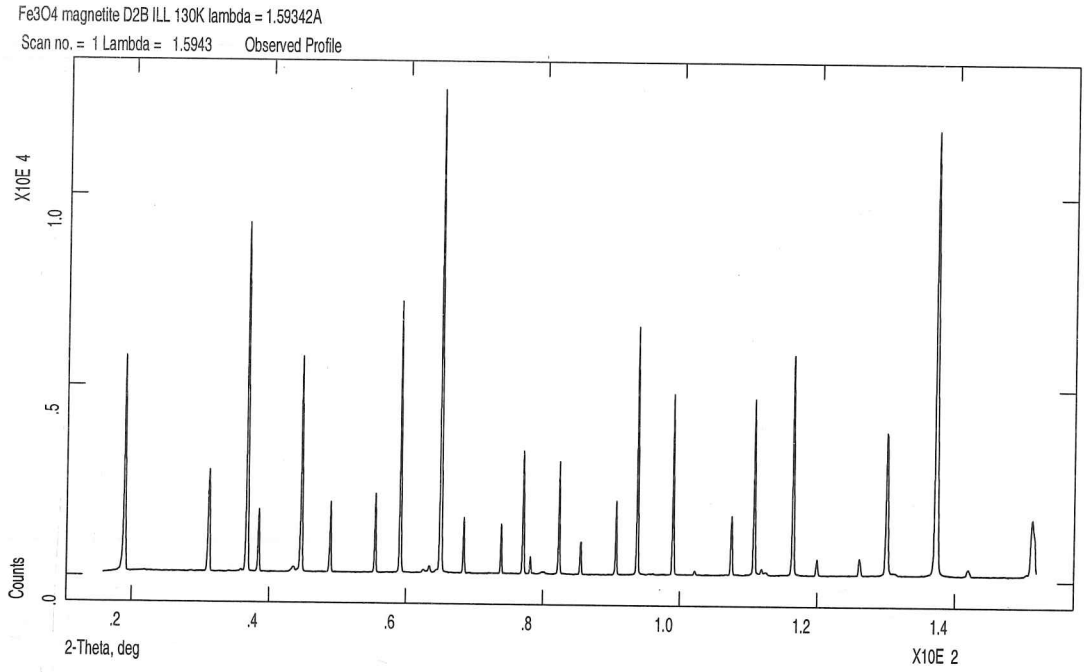


*Figure 3.8.2. D2B neutron powder pattern at 60 K.*

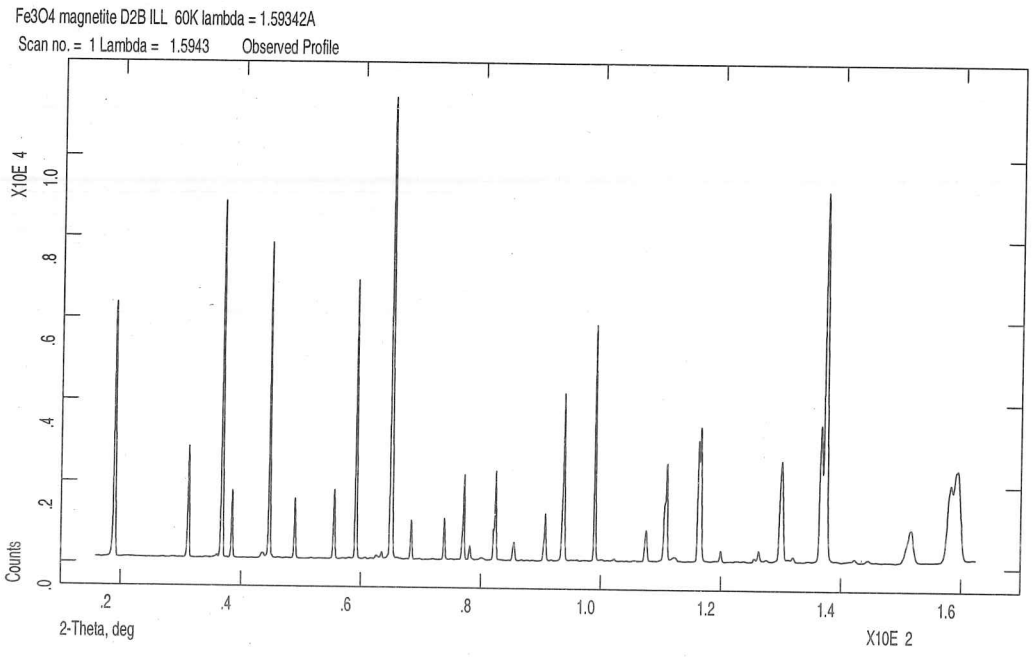

### 3.6.2. D20.

35 neutron powder diffraction patterns were also collected between 2 K and 280 K using the lower resolution powder diffractometer on D20 at ILL (see section 2.5.1.2). Each powder diffraction pattern was collected in 15 minutes. Figure 3.9 shows all of these patterns plotted together, note the change in the patterns around the Verwey Transition temperature.

*Figure 3.9. Plot showing the D20 $Fe_3O_4$ neutron powder patterns collected at different temperatures, note decrease in peak intensities around the Verwey Transition temperature.*

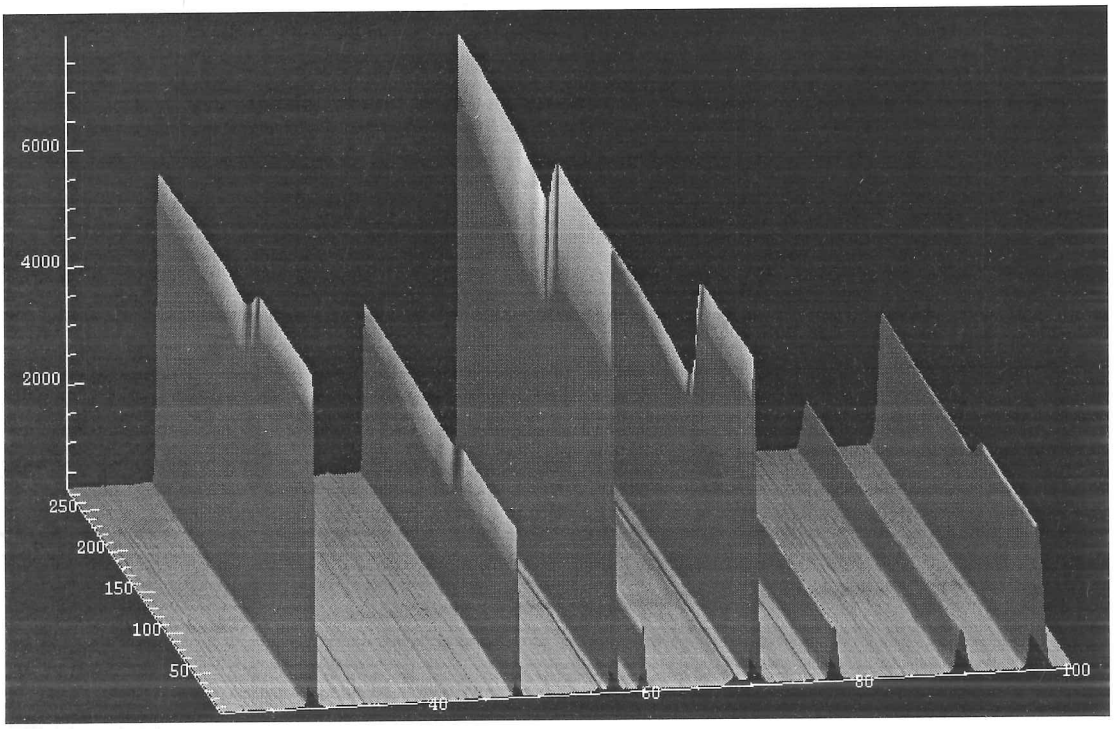


### 3.7. EXAFS.

EXAFS Fe K-edge spectra were measured on the $Fe_3O_4$ neutron sample using the EXAFS spectrometer on station 7.1 at the CCLRC Daresbury Synchrotron Radiation Source (see section

2.3.3). The sample was loaded in a cryostat and the spectra were measured at the between 80-270 K. The aim of this experiment was to see if the octahedral and tetrahedrally co-ordinated Fe-O distances varied with temperature with particular emphasis on any changes around the Verwey Transition temperature.

The spinel structure of $Fe_3O_4$ (Fleet, 1981) was used to model the shells of atoms around the central Fe atom, an inner shell of 1.33 O for the tetrahedrally co-ordinated O atoms was fitted first followed by a second shell of 4 O for the octahedrally co-ordinated O atoms. The occupancies of the shells centred on tetrahedrally co-ordinated Fe are scaled by a third and the occupancies for shells centred on octahedrally co-ordinated Fe are scaled by two thirds as there are twice as many octahedral sites as there are tetrahedral sites. This process continued until 7 shells of atoms had been modelled. Table 3.2 shows the initial interatomic distances and atom shell occupancies for the starting model for EXAFS data analysis.

*Table 3.2. Initial parameters for $Fe_3O_4$ EXAFS refinement, Fe(1) is tetrahedrally co-ordinated and Fe(2) is octahedrally co-ordinated.*

| Central Atom | atom in shell | shell number | distance (Å) | shell occupancy |
|---|---|---|---|---|
| Fe(1) | O | 1 | 1.889 | 1.33 |
| Fe(2) | O | 2 | 2.058 | 4.0 |
| Fe(2) | Fe(2) | 3 | 2.968 | 4.0 |
| Fe(2) | Fe(1) | 3 | 3.480 | 4.0 |
| Fe(1) | Fe(2) | 4 | 3.480 | 4.0 |
| Fe(1) | O | 5 | 3.493 | 4.0 |
| Fe(2) | Fe(2) | 6 | 5.140 | 8.0 |
| Fe(1) | Fe(2) | 7 | 5.452 | 10.67 |

The Daresbury EXBACK, EXCALIB and EXCURV92 programs were used to analyse the EXAFS spectra. Figure 3.10 shows the 270 K EXAFS fits for $Fe_3O_4$. Figure 3.11 and Table 3.3 shows the Fe-O bond lengths for the tetrahedral and octahedral shells of O atoms. There are

*Figure 3.10. 270 K Fe K-edge EXAFS fits for $Fe_3O_4$, upper fit is for EXAFS spectrum and lower fit is for Fourier Transform. Fitted parameters for 7 shells of atoms are also given.*

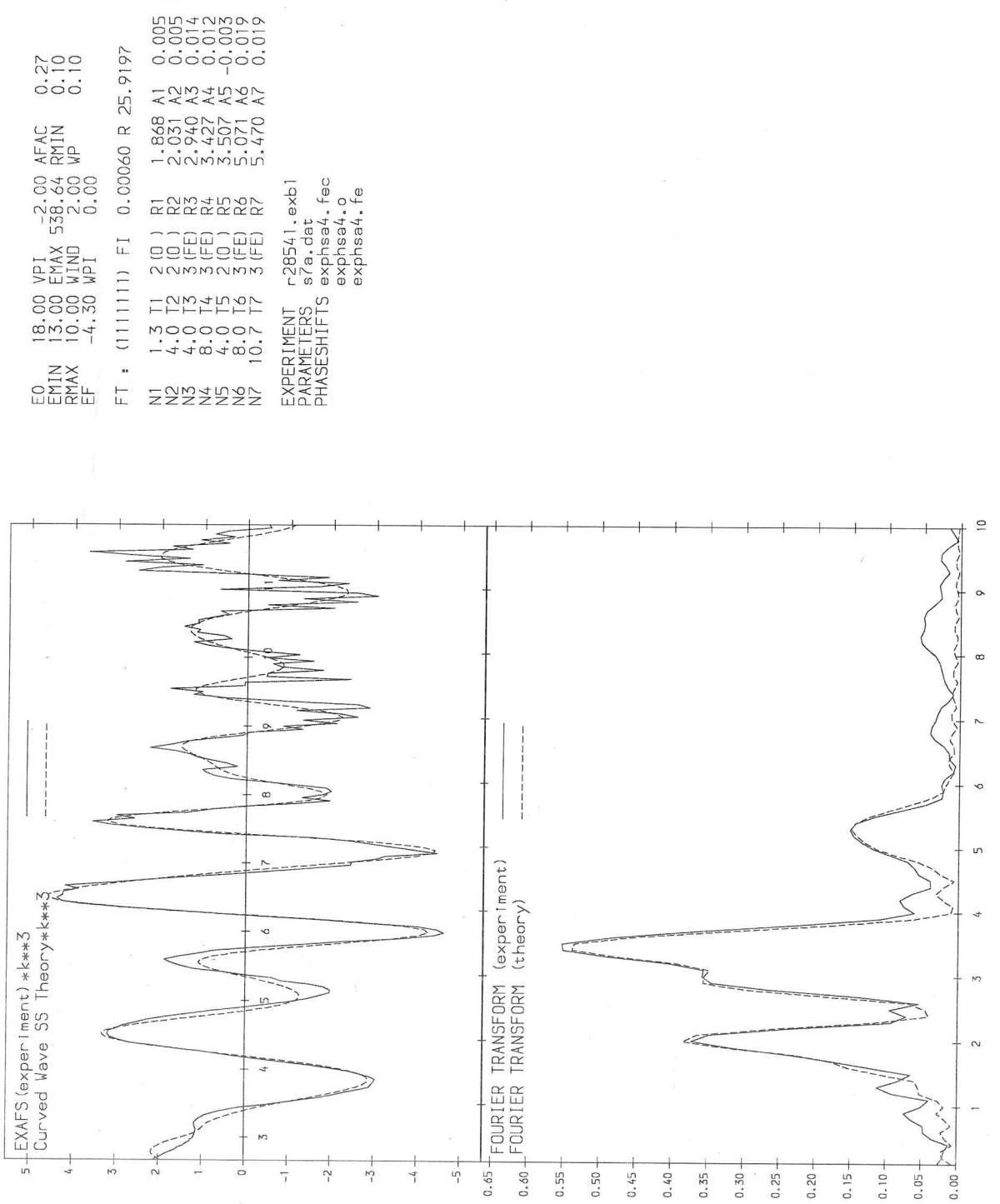

slight changes in Fe-O distance around and just below Verwey Transition temperature of 120 K but there appear to be no significant changes in bond length with temperature.

*Figure 3.11. Variation of Fe-O distances determined by EXAFS with temperature.*

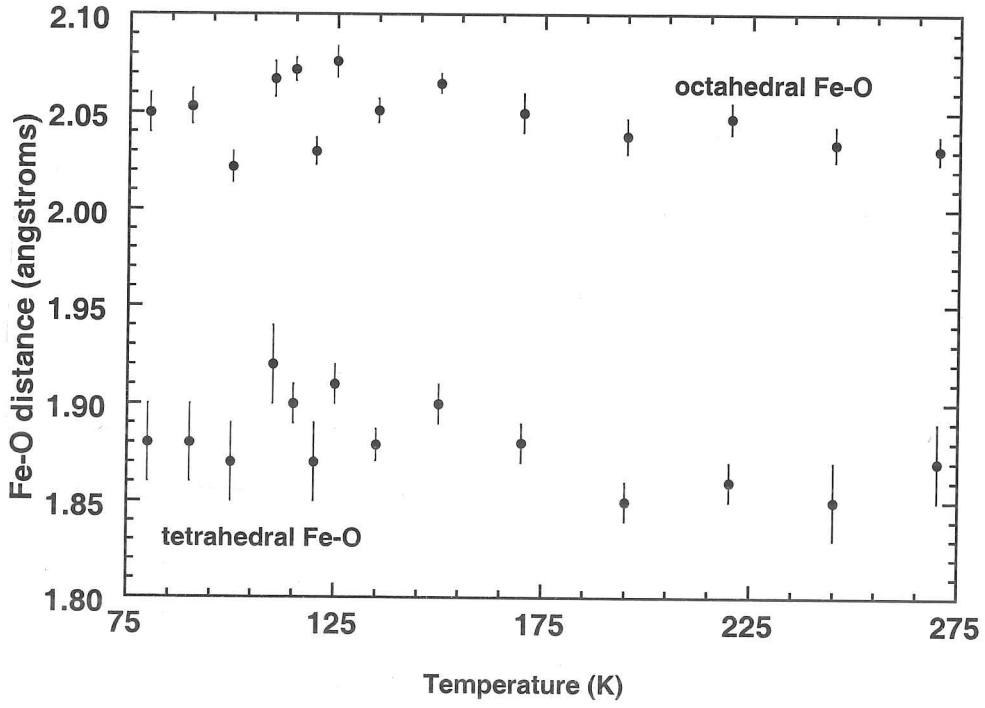


*Table 3.3. Variation of Fe-O distances with temperature determined from EXAFS.*

| Temp. (K) | tetrahedral Fe-O dist. (Å) | octahedral Fe-O dist. (Å) | Temp. (K) | tetrahedral Fe-O dist. (Å) | octahedral Fe-O dist. (Å) |
|---|---|---|---|---|---|
| 80 | 1.88(2) | 2.05(1) | 135 | 1.879(8) | 2.051(6) |
| 90 | 1.88(2) | 2.053(9) | 150 | 1.90(1) | 2.065(5) |
| 100 | 1.87(2) | 2.022(8) | 170 | 1.88(1) | 2.05(1) |
| 110 | 1.92(2) | 2.067(9) | 195 | 1.85(1) | 2.038(9) |
| 115 | 1.90(1) | 2.072(6) | 220 | 1.86(1) | 2.047(8) |
| 120 | 1.87(2) | 2.030(7) | 245 | 1.85(2) | 2.034(9) |
| 125 | 1.91(1) | 2.076(8) | 270 | 1.87(2) | 2.031(7) |

## 3.8. Powder Diffraction Data Analysis.

### 3.8.1. Structure refinement.

Rietveld refinements of the $Fe_3O_4$ structure have taken place using neutron and synchrotron X-ray powder diffraction data collected at 60K. These refinements have been done in the monoclinic P2/c space group. The Iizumi Pmca structure in a $a_o/\sqrt{2}$ x $a_o/\sqrt{2}$ x $2a_o$ unit cell was used as a starting model with the atoms placed on the "ideal" co-ordinates transposed from the cubic spinel structure. In lowering the space group from Pmca to P2/c the number of crystallographically distinct atom sites increases from 12 (6 Fe and 6 O) to 16 (8 Fe and 8 O).

In the Pmca structure there are 2 tetrahedrally co-ordinated Fe sites (Fe1, Fe2), 4 octahedrally co-ordinated Fe sites (Fe3, Fe4, Fe5, Fe6) and 6 O sites (O7, O8, O9, O10, O11, O12). When the space group is lowered in symmetry to P2/c two Fe sites are needed to describe the atomic positions for each of the Pmca Fe3 and Fe4 sites, these have been described as Fe3a, Fe4a, Fe3b and Fe4b in the P2/c refinement. Similarly the Pmca O11 and O12 sites, have been described as O11a, O12a, O11b and O12b in the P2/c refinement. Therefore 16 atom sites were used in the P2/c refinements.

A combined neutron (ILL D2B) and synchrotron X-ray (SRS station 2.3) refinement was attempted but the 2.3 data did not have high enough resolution to refine the monoclinic β angle.

A combined neutron (D2B) and synchrotron X-ray (SRS station 9.1) Rietveld refinement has also been done using GSAS. Due to the presence of impurities in the samples parts of the powder diffraction patterns were excluded due to haematite (synchrotron data) and wuestite (neutron data). However there were problems in fitting the synchrotron pattern in this refinement,

some high angle peaks were not well fitted. As two slightly different $Fe_3O_4$ samples were used to provide the data for this refinement there was a slight mismatch in lattice parameters. As the neutron data had a much higher count rate than the synchrotron data the cell parameters were dominated by that of the neutron fit.

Therefore a neutron only refinement was done. It was not possible to completely refine all of the atomic positions in this refinement. All of the **x** co-ordinates were kept fixed on all Fe sites and on O7-10, as in the Pmca refinement these co-ordinates are on special positions with fixed values of **x**. All **y** co-ordinates were refined apart from those on Fe3a and Fe3b as these were special positions. All **z** co-ordinates were refined apart from those on Fe3a, Fe3b, Fe4a and Fe4b as these were special positions.

At the start of the refinement all Fe sites were constrained to have the same shift on the atomic co-ordinates. All O sites were similarly constrained to have the same shift on the atomic co-ordinates. As the refinement progressed these constraints were gradually lowered until at the end of the refinement the co-ordinates of the Fe1, Fe2, Fe5 and Fe6 sites were refined independently. Fe4a and Fe4b were constrained so that they had the same shift. None of the O co-ordinates were refined independently, instead pairs of O atoms (O7-O8, O9-O10, O11a-O12a and O11b-O12b) were constrained to have the same shift. It was not possible to carry on with the refinement if these constraints were lowered any more.

Separate temperature factors were refined for the tetrahedrally co-ordinated Fe atoms (Fe1 and Fe2 constrained to have the same shift for temperature factors) and refined for the octahedrally co-ordinated Fe atoms and (Fe3a, Fe4a, Fe5, Fe6, Fe4a and Fe4b constrained to have the same shift for temperature factors). All O atoms were constrained to have the same temperature factor. However, all temperature factors were refined with negative values.

The magnetic structure for $Fe_3O_4$ was refined with the magnetic moments parallel to the crystallographic **y** axis as this was the only direction possible in P2/c for Fe atoms on special positions. Separate magnetic moments were refined for the tetrahedrally co-ordinated Fe atoms (Fe1 and Fe2 constrained to have the same magnetic moment) and for the octahedrally co-ordinated Fe atoms (Fe3a, Fe4a, Fe5, Fe6, Fe4a and Fe4b constrained to have the same magnetic moment). The starting value for the tetrahedral ($Fe^{3+}$) moment of $5\mu_B$ was refined to be $3.83(7)\mu_B$ whereas the starting value for the octahedral moment ($Fe^{2.5+}$) of $-4.5\mu_B$ was refined to be $-4.44(5)\mu_B$. The magnitude of the tetrahedral moment should be higher than the octahedral moment as there are more unpaired electrons on $Fe^{3+}$.

The Rietveld refinement (see Figure 3.12) is a reasonably good fit but there are some problems with the refined model. The temperature factors should be positive and the refined magnetic moment for the tetrahedrally co-ordinated Fe atoms should have a greater magnitude than that for the octahedrally co-ordinated Fe atoms. However, not all parameters that could be refined were able to be refined, some weak Bragg reflections in the neutron powder diffraction pattern were not well fitted. The refined structural parameters are given as Table 3.4.

The refined Fe-O distances for the tetrahedrally co-ordinated Fe correspond to those for tetrahedral $Fe^{3+}$ and Fe-O distances for octahedrally co-ordinated correspond to those disordered $Fe^{2.5+}$, there is no evidence in refined bond lengths for cation ordering. The refined Fe-O distances are given in Table 3.5, the corresponding distances from the Iizumi structure are given for comparison. The refined structure is shown in Figures 3.13.1-3 in comparison to the ideal spinel structure in this P2/c cell, note that there is only a slight distortion of the spinel structure in this refined structure.

*Figure 3.12. Rietveld difference plot for 60K neutron refinement in P2/c structure.*

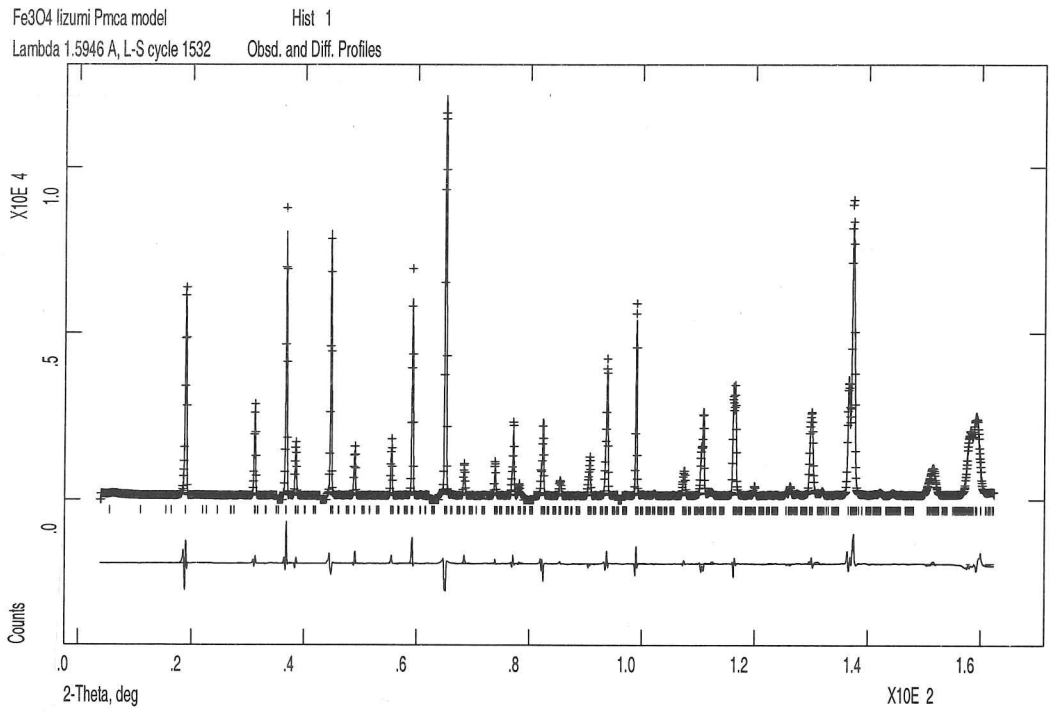


Clearly, the low temperature structure of $Fe_3O_4$ is more complicated than that refined by Iizumi and this refinement. Higher resolution diffraction data would be needed to fully understand this complicated low-temperature structure.

*Table 3.4. Refined structural parameters for $Fe_3O_4$ determined from neutron powder diffraction data collected at 60K.*

| Atom | Wyckoff letter | x | y | z | My ($\mu_B$) | Uiso ($Å^2$) |
|---|---|---|---|---|---|---|
| Fe1 | 4g | 0.25 | 0.005(3) | 0.0641(7) | 3.83(7) | -0.0025(3) |
| Fe2 | 4g | 0.25 | 0.503(1) | 0.1880(7) | 3.83(7) | -0.0025(3) |
| Fe3a | 2c | 0.0 | 0.5 | 0.0 | -4.44(5) | -0.0002(3) |
| Fe4a | 2e | 0.0 | 0.004(3) | 0.25 | -4.44(5) | -0.0002(3) |
| Fe5 | 4g | 0.25 | 0.261(3) | 0.3801(7) | -4.44(5) | -0.0002(3) |
| Fe6 | 4g | 0.25 | 0.759(3) | 0.3774(8) | -4.44(5) | -0.0002(3) |
| O7 | 4g | 0.25 | 0.271(3) | -0.0013(6) | | -0.0019(3) |
| O8 | 4g | 0.25 | 0.739(3) | -0.0013(6) | | -0.0019(3) |
| O9 | 4g | 0.25 | 0.243(3) | 0.2510(7) | | -0.0019(3) |
| O10 | 4g | 0.25 | 0.775(3) | 0.2510(7) | | -0.0019(3) |
| O11a | 4g | -0.004(2) | 0.004(3) | 0.1258(7) | | -0.0019(3) |
| O12a | 4g | -0.004(2) | 0.504(3) | 0.1242(7) | | -0.0019(3) |
| Fe3b | 2b | 0.5 | 0.5 | 0.0 | -4.44(5) | -0.0002(3) |
| Fe4b | 2f | 0.5 | 0.004(3) | 0.25 | -4.44(5) | -0.0002(3) |
| O11b | 4g | 0.512(2) | 0.005(3) | 0.1295(7) | | -0.0019(3) |
| O12b | 4g | 0.512(2) | 0.505(3) | 0.1205(7) | | -0.0019(3) |

R-factors are :- wRp = 9.57% Rp = 7.10% $\chi^2 = 262.1$

Lattice parameters from the neutron refinement at 60 K are :-

a = 5.9412(3) Å b = 5.9290(3) Å c = 16.789(1) Å $\beta = 90.196(4)^\circ$ V = 591.40(2) $Å^3$

Lattice parameters determined from 9.1 synchrotron X-ray data at 60 K are:-

a = 5.9464(1) Å b = 5.9265(2) Å c = 16.7805(5) Å $\beta = 90.238(2)^\circ$ V = 591.36(2) $Å^3$

*Table 3.5. Refined Fe-O bond lengths for $Fe_3O_4$ compared with Iizumi structure.*

| Atoms | bond length (Å) | Iizumi bond length (Å) | Atoms | bond length (Å) | Iizumi bond length (Å) |
|---|---|---|---|---|---|
| Fe1-O7 | 1.92(2) | 1.889(4) | Fe6-O7 | 2.04(2) | 2.058(5) |
| Fe1-O8 | 1.92(2) | 1.867(4) | Fe6-O10 | 2.13(2) | 2.044(5) |
| Fe1-O11a | 1.83(1) | 1.906(4) | Fe6-O11a | 2.06(2) | 2.065(4) |
| Fe1-O11b | 1.900(9) | 1.906(4) | Fe6-O12a | 2.10(2) | 2.065(4) |
| mean Fe1-O | 1.89(2) | 1.892(4) | Fe6-O11b | 2.04(2) | 2.068(4) |
| Fe2-O9 | 1.87(2) | 1.893(4) | Fe6-O12b | 2.07(2) | 2.068(4) |
| Fe2-O10 | 1.93(2) | 1.891(4) | mean Fe6-O | 2.07(2) | 2.062(4) |
| Fe2-O12a | 1.85(1) | 1.866(3) | Fe3b-O7 x2 | 2.01(1) | 2.043(2) |
| Fe2-O12b | 1.93(1) | 1.866(3) | Fe3b-O8 x2 | 2.05(1) | 2.087(3) |
| mean Fe2-O | 1.89(2) | 1.879(4) | Fe3b-O12b x2 | 2.03(1) | 2.085(2) |
| Fe3a-O7 x2 | 2.01(1) | 2.043(2) | mean Fe3b-O | 2.03(1) | 2.072(2) |
| Fe3a-O8 x2 | 2.05(1) | 2.087(3) | Fe4b-O9 | 2.05(2) | 2.041(3) |
| Fe3a-O12a x2 | 2.09(1) | 2.085(2) | Fe4b-O10 | 2.01(2) | 2.057(3) |
| mean Fe3a-O | 2.05(1) | 2.072(2) | Fe4b-O11b | 2.03(1) | 2.020(3) |
| Fe4a-O9 x2 | 2.05(2) | 2.041(3) | mean Fe4b-O | 2.03(1) | 2.039(3) |
| Fe4a-O10 x2 | 2.01(2) | 2.057(3) | mean O7-Fe | 2.00(2) | 2.009(3) |
| Fe4a-O11a x2 | 2.09(1) | 2.020(3) | mean O8-Fe | 2.01(2) | 2.014(3) |
| mean Fe4a-O | 2.05(1) | 2.039(3) | mean O9-Fe | 2.04(2) | 2.017(4) |
| Fe5-O8 | 1.99(2) | 2.015(4) | mean O10-Fe | 2.02(2) | 2.012(4) |
| Fe5-O9 | 2.17(2) | 2.095(4) | mean O11a-Fe | 2.02(2) | 2.017(3) |
| Fe5-O11a | 2.11(2) | 2.077(3) | mean O12a-Fe | 2.02(2) | 2.012(3) |
| Fe5-O12a | 2.06(2) | 2.077(3) | mean O11b-Fe | 2.01(2) | 2.017(3) |
| Fe5-O11b | 2.08(2) | 2.030(3) | mean O12b-Fe | 2.01(2) | 2.012(3) |
| Fe5-O12b | 2.03(2) | 2.030(3) | | | |
| mean Fe5-O | 2.07(2) | 2.054(3) | | | |

*Table 3.5. Refined Fe-O bond lengths for $Fe_3O_4$ compared with Iizumi structure.*

| Atoms | bond length (Å) | Iizumi bond length (Å) | Atoms | bond length (Å) | Iizumi bond length (Å) |
|---|---|---|---|---|---|
| Fe1-O7 | 1.92(2) | 1.889(4) | Fe6-O7 | 2.04(2) | 2.058(5) |
| Fe1-O8 | 1.92(2) | 1.867(4) | Fe6-O10 | 2.13(2) | 2.044(5) |
| Fe1-O11a | 1.83(1) | 1.906(4) | Fe6-O11a | 2.06(2) | 2.065(4) |
| Fe1-O11b | 1.900(9) | 1.906(4) | Fe6-O12a | 2.10(2) | 2.065(4) |
| mean Fe1-O | 1.89(2) | 1.892(4) | Fe6-O11b | 2.04(2) | 2.068(4) |
| Fe2-O9 | 1.87(2) | 1.893(4) | Fe6-O12b | 2.07(2) | 2.068(4) |
| Fe2-O10 | 1.93(2) | 1.891(4) | mean Fe6-O | 2.07(2) | 2.062(4) |
| Fe2-O12a | 1.85(1) | 1.866(3) | Fe3b-O7 x2 | 2.01(1) | 2.043(2) |
| Fe2-O12b | 1.93(1) | 1.866(3) | Fe3b-O8 x2 | 2.05(1) | 2.087(3) |
| mean Fe2-O | 1.89(2) | 1.879(4) | Fe3b-O12b x2 | 2.03(1) | 2.085(2) |
| Fe3a-O7 x2 | 2.01(1) | 2.043(2) | mean Fe3b-O | 2.03(1) | 2.072(2) |
| Fe3a-O8 x2 | 2.05(1) | 2.087(3) | Fe4b-O9 | 2.05(2) | 2.041(3) |
| Fe3a-O12a x2 | 2.09(1) | 2.085(2) | Fe4b-O10 | 2.01(2) | 2.057(3) |
| mean Fe3a-O | 2.05(1) | 2.072(2) | Fe4b-O11b | 2.03(1) | 2.020(3) |
| Fe4a-O9 x2 | 2.05(2) | 2.041(3) | mean Fe4b-O | 2.03(1) | 2.039(3) |
| Fe4a-O10 x2 | 2.01(2) | 2.057(3) | mean O7-Fe | 2.00(2) | 2.009(3) |
| Fe4a-O11a x2 | 2.09(1) | 2.020(3) | mean O8-Fe | 2.01(2) | 2.014(3) |
| mean Fe4a-O | 2.05(1) | 2.039(3) | mean O9-Fe | 2.04(2) | 2.017(4) |
| Fe5-O8 | 1.99(2) | 2.015(4) | mean O10-Fe | 2.02(2) | 2.012(4) |
| Fe5-O9 | 2.17(2) | 2.095(4) | mean O11a-Fe | 2.02(2) | 2.017(3) |
| Fe5-O11a | 2.11(2) | 2.077(3) | mean O12a-Fe | 2.02(2) | 2.012(3) |
| Fe5-O12a | 2.06(2) | 2.077(3) | mean O11b-Fe | 2.01(2) | 2.017(3) |
| Fe5-O11b | 2.08(2) | 2.030(3) | mean O12b-Fe | 2.01(2) | 2.012(3) |
| Fe5-O12b | 2.03(2) | 2.030(3) | | | |
| mean Fe5-O | 2.07(2) | 2.054(3) | | | |

*Figure 3.13.1. Ideal spinel structure (left) for 60K neutron refinement in P2/c structure projected in the* **bc** *plane. Tetrahedral $FeO_4$ units are given in red and octahedral $FeO_6$ units are given in green. Unit cell is indicated in blue. Structure on the right is the same projection of the refined structure in the P2/c cell.*

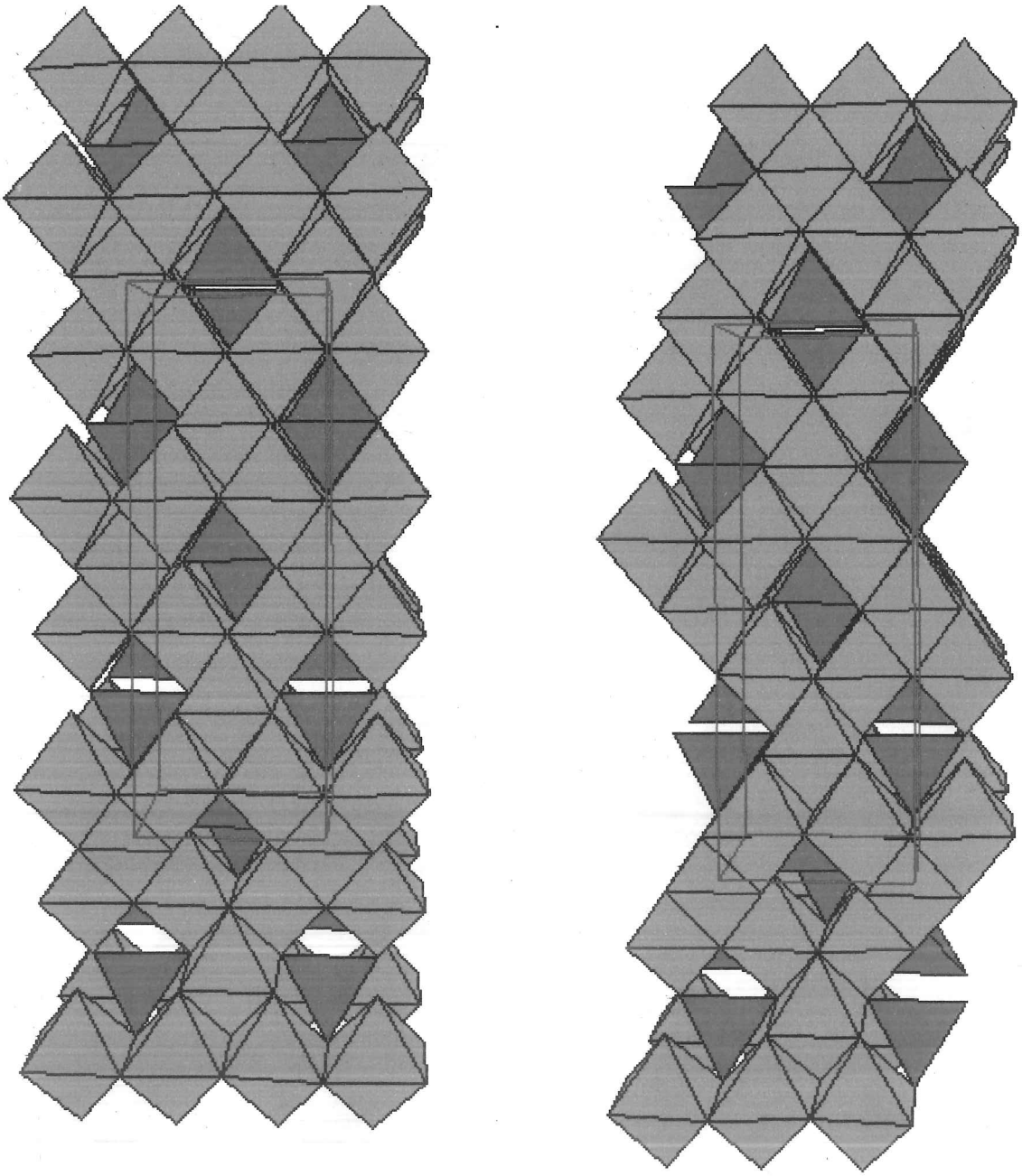

*Figure 3.13.2. Ideal spinel structure (left) for 60K neutron refinement in P2/c structure projected in the ac plane. Tetrahedral $FeO_4$ units are given in red and octahedral $FeO_6$ units are given in green. Unit cell is indicated in blue. Structure on the right is the same projection of the refined structure in the P2/c cell.*

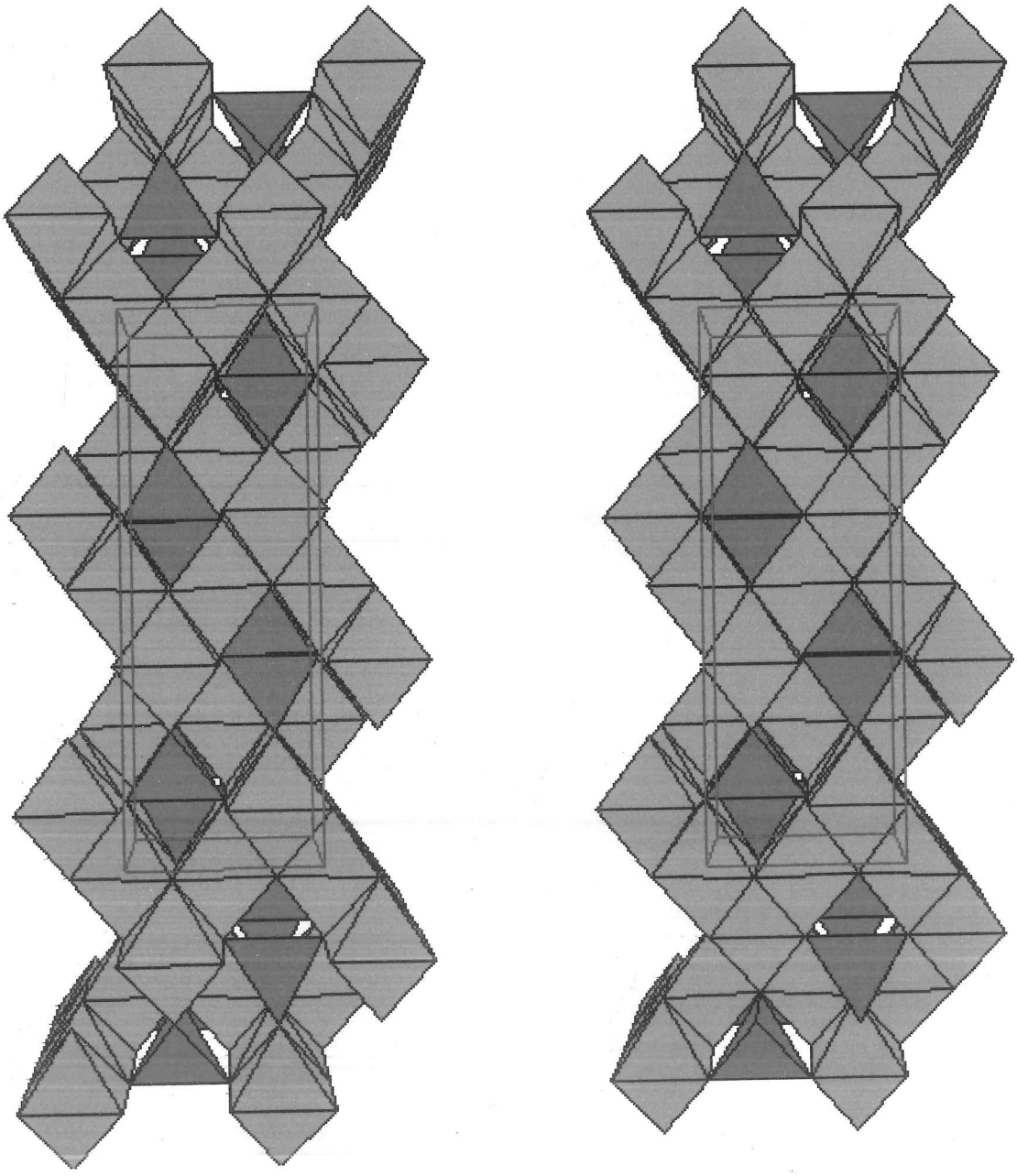

*Figure 3.13.3. Ideal spinel structure (top) for 60K neutron refinement in P2/c structure projected in the **ab** plane. Tetrahedral $FeO_4$ units are given in red and octahedral $FeO_6$ units are given in green. Unit cell is indicated in blue. Lower structure is the same projection of the refined structure in the P2/c cell.*

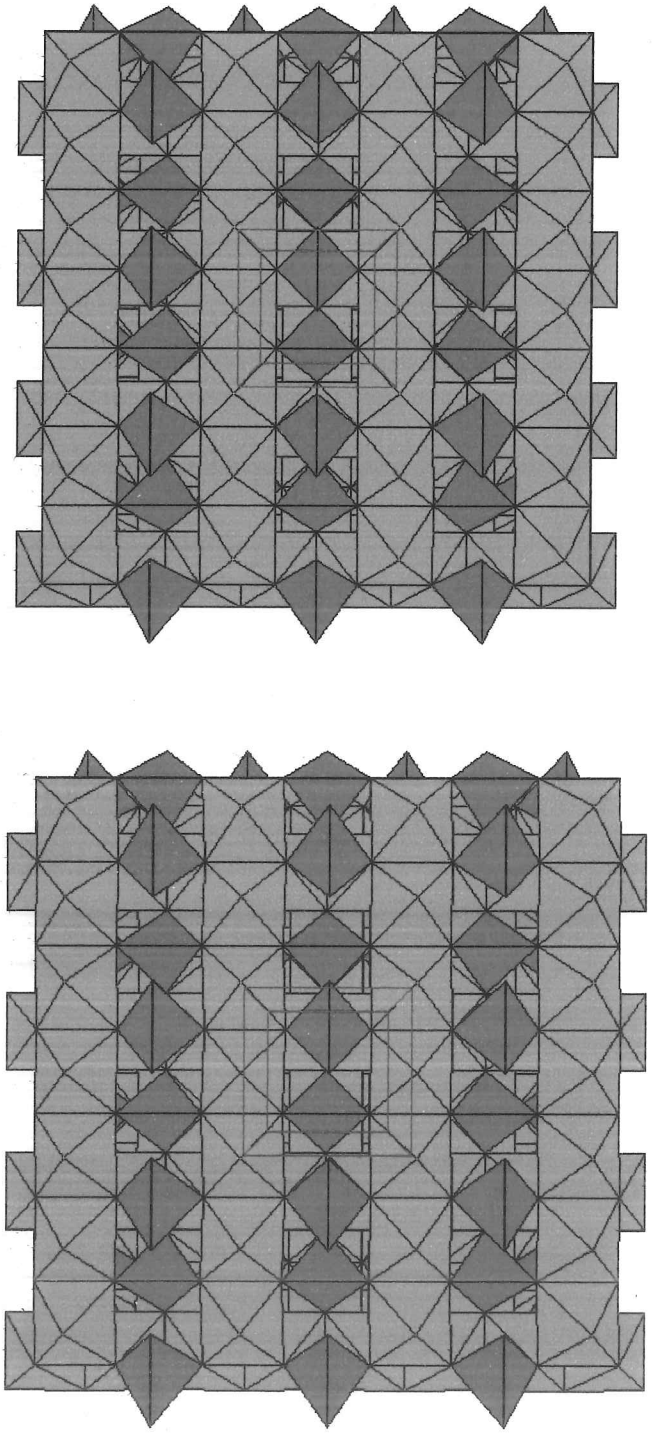

### 3.8.2. D20 Variable temperature study.

The Le Bail method (see section 1.2) option in GSAS was used to fit the D20 data, lattice parameters were obtained from these Le Bail fits. P2/c monoclinic lattice parameters were determined below the Verwey Transition and Fd3m (spinel) cubic lattice parameters were determined above the Verwey Transition, see Table 3.6.

*Table 3.6. D20 refined monoclinic lattice parameters 2-110 K and cubic lattice parameters 115-280 K.*

| T(K) | a (Å) | b (Å) | c (Å) | β(°) | V (Å$^3$) | T(K) | a (Å) | V (Å$^3$) |
|---|---|---|---|---|---|---|---|---|
| 2 | 5.9144(2) | 6.0153(3) | 16.7258(4) | 90.171(5) | 595.05(2) | 125 | 8.3708(3) | 586.55(6) |
| 10 | 5.9215(2) | 6.0119(2) | 16.7255(4) | 90.166(4) | 595.42(2) | 130 | 8.3709(3) | 586.56(6) |
| 20 | 5.9144(2) | 6.0155(3) | 16.7246(4) | 90.170(5) | 595.03(2) | 135 | 8.3710(3) | 586.59(6) |
| 30 | 5.9162(2) | 6.0140(3) | 16.7265(4) | 90.167(5) | 595.13(2) | 140 | 8.3710(3) | 586.60(6) |
| 40 | 5.9151(2) | 6.0180(3) | 16.7237(4) | 90.179(4) | 595.32(2) | 150 | 8.3712(3) | 586.63(7) |
| 50 | 5.9155(2) | 6.0179(3) | 16.7239(4) | 90.176(4) | 595.34(2) | 160 | 8.3711(3) | 586.61(7) |
| 60 | 5.9156(2) | 6.0157(3) | 16.7251(4) | 90.171(5) | 595.19(2) | 170 | 8.3715(3) | 586.68(7) |
| 70 | 5.9163(2) | 6.0143(2) | 16.7270(4) | 90.163(5) | 595.18(2) | 180 | 8.3718(3) | 586.76(7) |
| 80 | 5.9202(2) | 6.0134(2) | 16.7244(4) | 90.165(4) | 595.39(2) | 190 | 8.3723(1) | 586.87(2) |
| 85 | 5.9207(2) | 6.0118(2) | 16.7273(4) | 90.157(4) | 595.38(2) | 200 | 8.3728(3) | 586.97(7) |
| 90 | 5.9155(2) | 6.0145(2) | 16.7267(4) | 90.158(5) | 595.12(2) | 210 | 8.3731(3) | 587.03(7) |
| 95 | 5.9203(2) | 6.0123(2) | 16.7273(4) | 90.152(5) | 595.40(2) | 220 | 8.3736(3) | 587.14(7) |
| 100 | 5.9171(2) | 6.0168(3) | 16.7253(5) | 90.148(5) | 595.45(2) | 230 | 8.3741(3) | 587.24(7) |
| 105 | 5.9185(2) | 6.0146(2) | 16.7292(5) | 90.080(6) | 595.52(2) | 240 | 8.3746(3) | 587.35(7) |
| 110 | 5.9184(2) | 6.0146(2) | 16.7321(5) | 90.053(5) | 595.61(2) | 250 | 8.3753(3) | 587.48(7) |
| 115 | 8.3710(1) | | | | 586.59(2) | 260 | 8.3758(3) | 587.59(7) |
| 120 | 8.3708(3) | | | | 586.55(6) | 270 | 8.3762(3) | 587.69(7) |
| | | | | | | 280 | 8.3768(3) | 587.80(7) |

Figures 3.14.1-3 show how these lattice parameters vary with temperature and Figure 3.15 shows how the full width half maximum peak width and peak intensity for the peak corresponding to the cubic 311 Bragg reflection varies with temperature. These show that the Verwey Transition is clearly visible at 115 K, the step change in volume at this transition clearly shows that this is a first order phase transition.

*Figure 3.14.1. Variation of **a**, **b** and **c** lattice parameters for $Fe_3O_4$ with temperature.*

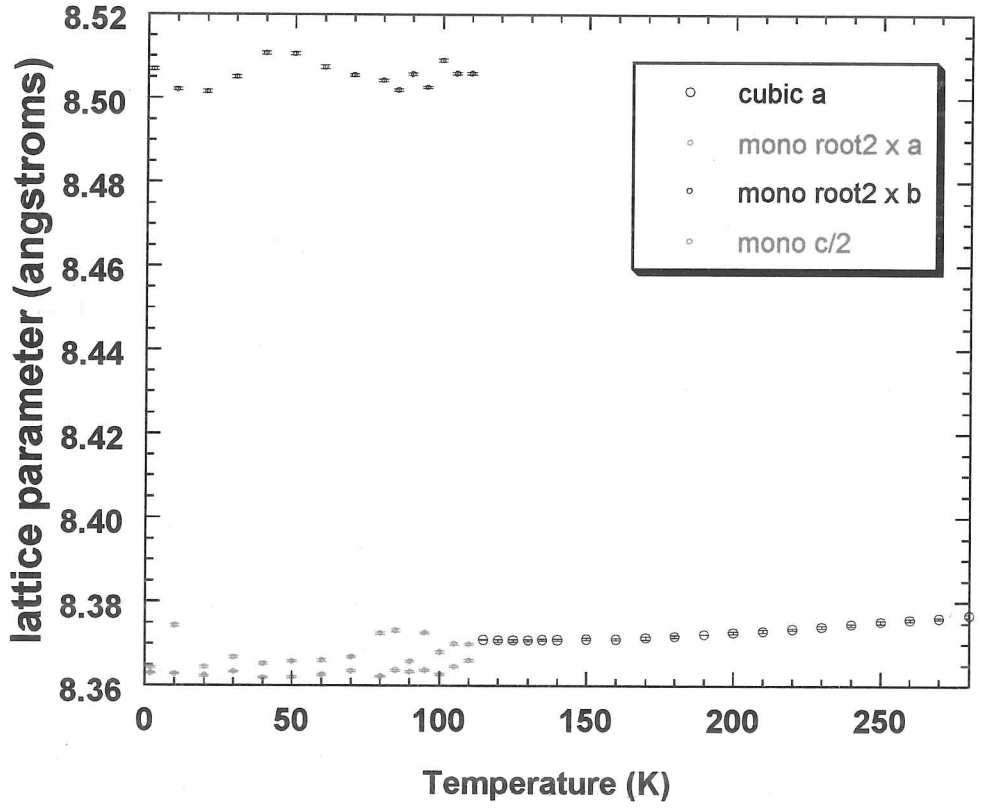

*Figure 3.14.2. Variation of β lattice parameter for $Fe_3O_4$ with temperature.*

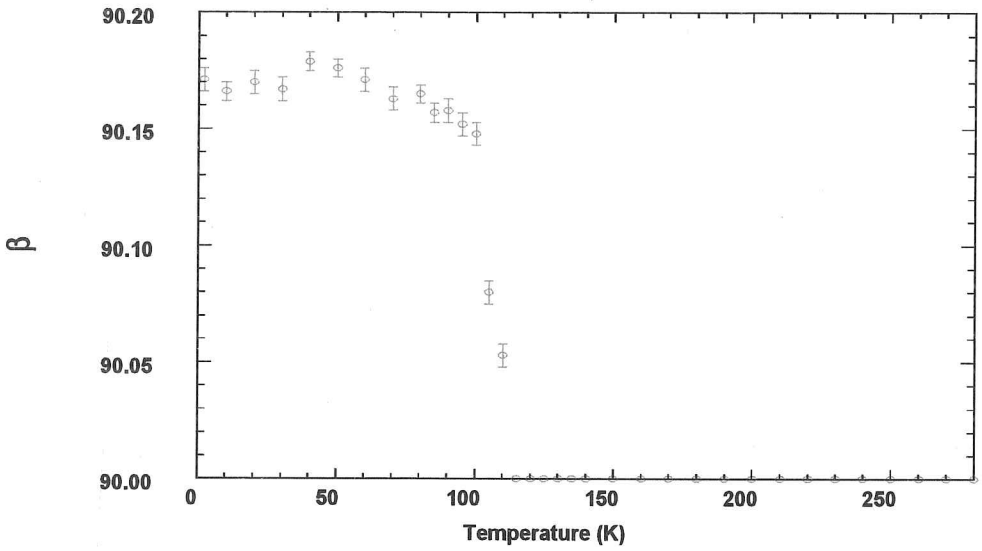


*Figure 3.14.3. Variation of unit cell volume for $Fe_3O_4$ with temperature.*

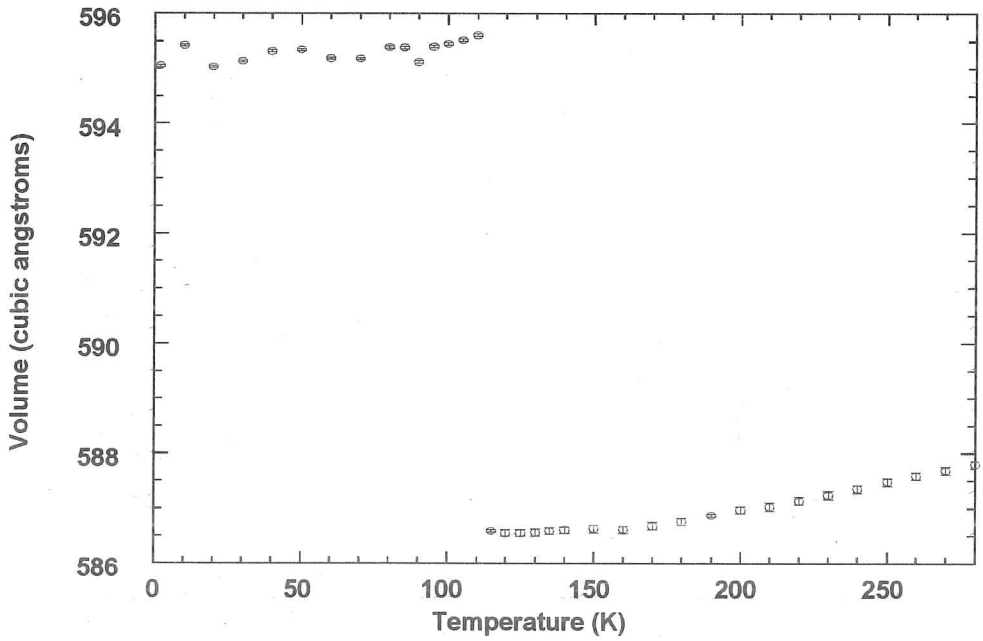

*Figure 3.15. Variation of full width half maximum (blue) and intensity (red) of cubic 311 peak and the equivalent monoclinic peak with temperature.*

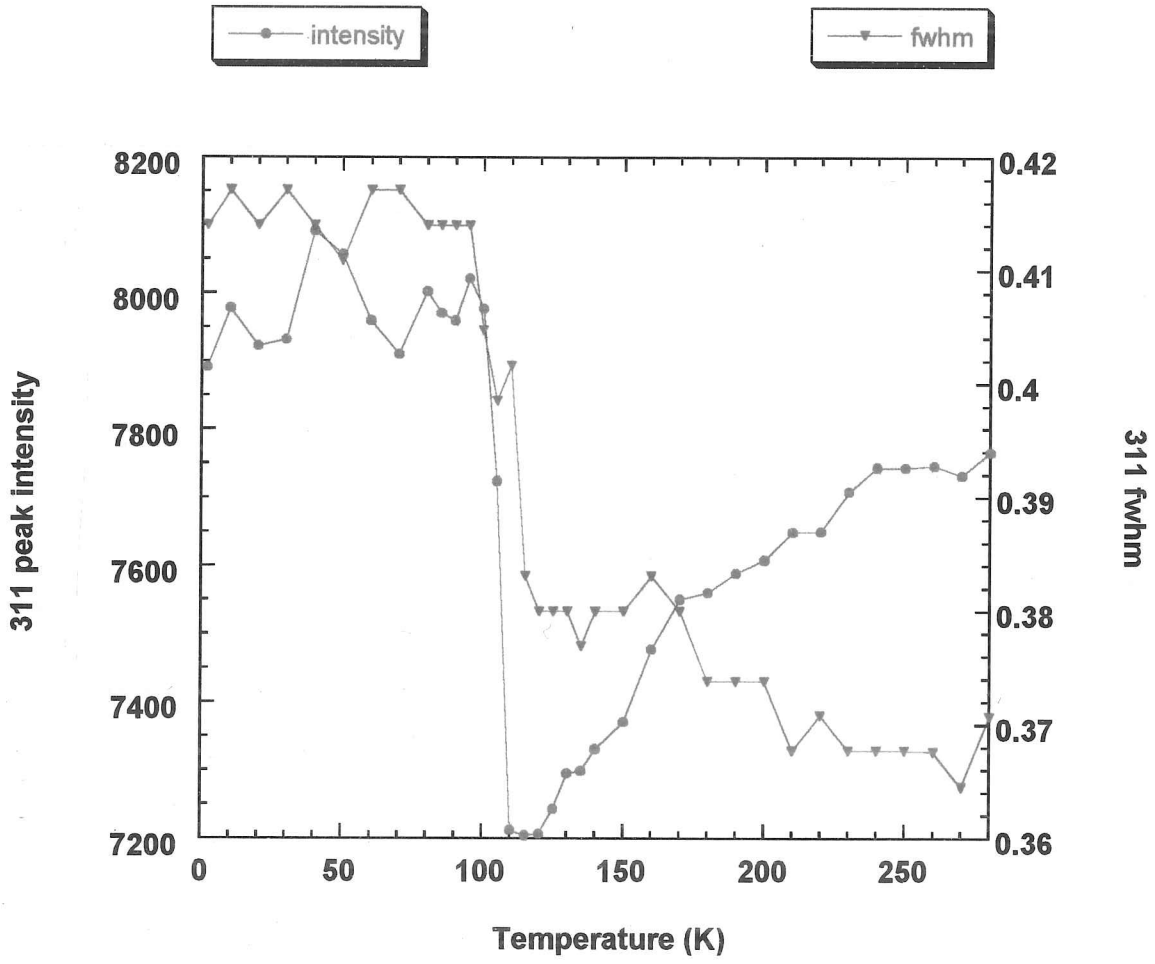


**3.9. Discussion.**

Resistivity measurements and synchrotron X-ray and neutron powder diffraction measurements clearly show the presence of the Verwey Transition in $Fe_3O_4$ at around 120 K. However, different transition temperatures are measured for the synchrotron and neutron $Fe_3O_4$ samples. Resistivity measurements (Figure 3.5) and synchrotron X-ray powder diffraction (Figure 3.6) on the synchrotron sample show a transition between 122-125 K. Neutron powder diffraction measurements on the neutron sample (Figures 3.9, 3.14.1-3 and 3.15) show a transition around

115 K. Table 3.4 shows that the lattice parameters determined for the synchrotron and neutron samples are significantly different. This suggests that these two samples do not have exactly the same stoichiometry. Honig (1995) mentions that the Verwey transition Temperature in $Fe_3O_4$ is dependent on the Fe/O ratio.

The neutron structure refinement is in agreement with the Iizumi structure. The octahedral Fe-O bond lengths are in agreement with those for disordered Fe sites with an average valence of $Fe^{2.5+}$, there is no evidence for cation ordering on the octahedral sites. These structural results do not agree with the resistivity measurements which show a decrease in conductivity below the Verwey Transition temperature due to ordering of $Fe^{2+}$ and $Fe^{3+}$ cations.

The fact that no evidence for charge ordering is detected in the structure determined from powder diffraction would suggest that the charge-ordered domains in the low-temperature structure are small (~10-100 Å) so that any superstructure reflections are too broad and weak to be observed above the background in the diffraction patterns and that charge ordering takes place in very small domains known as **Wigner nanocrystals** (Rozenberg et al, 1996). Chapter 4 compares the structures and magnetic properties of $Fe_3O_4$ and $Fe_2OBO_3$ and also gives more information on Wigner nanocrystals.

The D20 neutron powder diffraction data clearly shows the Verwey Transition (see Figure 3.9), the plots of 311 peak width and lattice parameter against temperature also show the transition at 115K (see Figures 3.14.1-3 and 3.15).

The EXAFS results do not show any significant changes in Fe-O bond distances around the Verwey Transition temperature. The EXAFS technique gives the mean distance from a central atom to a shell of surrounding atoms, any changes due to charge ordering must be too subtle to be detected in the average Fe-O bond distance in the shell of octahedrally co-ordinated O atoms.

### 3.10. Conclusions.

Resistivity measurements on the synchrotron sample of $Fe_3O_4$ show a change in the resistivity at about 122 K, this corresponds with the Verwey Transition. High resolution synchrotron X-ray powder diffraction data has been collected for $Fe_3O_4$ below the Verwey Transition temperature. The cubic 440 reflection for the room temperature spinel structure of $Fe_3O_4$ is observed to split in two at 125 K. Data collected at a temperature of 60 K shows that most of the cubic spinel reflections have become split indicating a lowering of the crystal symmetry on passing through the Verwey Transition. Rietveld refinement using high resolution neutron powder diffraction data collected at 60K shows that the Iizumi crystal structure is basically correct but it was not possible to completely refine this structure. There is no evidence from the crystal structure for any charge ordering on the octahedrally co-ordinated Fe sites, the Fe-O bond lengths correspond to those for an average octahedra Fe site valence of $Fe^{2.5+}$. A lower resolution neutron powder diffraction study has been used to show how the lattice parameters of the $Fe_3O_4$ neutron sample vary between 2-280K. These parameters clearly show the Verwey Transition at 115 K.

EXAFS measurements on the $Fe_3O_4$ neutron sample between 80-270 K do not show any significant changes in mean Fe-O distances around the Verwey Transition temperature.

**Chapter 3 - References.**

F.J.Berry, S.Skinner and M.F.Thomas, J. Phys. Condens. Matter, (1998), **10,** 215-220.

P.A.Cox, The Electronic Structure and Chemistry of Solids, Oxford University Press, (1987) p179-189.

J.Dumas, C.Schenkler and R.Buder, Phil. Mag., (1980), **B42,** 485-486.

M.E.Fleet, Acta Cryst., (1981), **B37,** 917.

Y.Fujii, G.Shirane and Y.Yamada, Phys. Rev., (1975), **B11,** 2036-2041.

W.C.Hamilton, Phys. Rev., (1958), **110**, 1050-1057.

F.Holtzberg, Phil. Mag., (1980), **B42,** 491-495.

J.M.Honig, Journal of Alloys and Compounds, (1995), **229,** 24-39.

J.M.Honig, Z.Kakol, P.Wang and M.Wittenauer, Phys. Rev., (1990), **B42,** 4553-4558.

S.Iida, Phil. Mag., (1980), **B42,** 349-376.

M.Iizumi, T.F.Koetzle, G.Shirane, S.Chikazumi, M.Matsui and S.Todo, Acta Cryst., (1982), **B38,** 2121-2133.

M.Iizumi and G.Shirane, Solid State Commun., (1975), **17,** 433-436.

R.W.Millar, J.Amer. Chem. Soc., (1929), **51,** 215-222.

M.Mizoguchi, J. Phys. Soc. Japan, (1978), **44,** 1501-1512.

M.Mizoguchi, J. Phys. Soc. Japan, (1978), **44,** 1513-1520

N.F.Mott et al, Phil. Mag., (1980), **B42,** 327-498.

G.T.Rado and W.M.Ferrari, Phys. Rev., (1975), **B12,** 5166-5174.

G.K.Rozenberg, G.R.Hearne, J.M.Honig, P.A.Metcalf and M.P.Pasternak, Phys. Rev., (1996), B**53**, 6482-6487.

E.J.Samuelsen, E.J.Bleeker, L.Dobrzynski and T.Riste., J. Appl. Phys., (1968), **39**, 1114-1115.

C.Schenkler and M.Marezio, Phil. Mag., (1980), **B42,** 453-472.

G.Shirane, S.Chikazumi, J.Akimitsu, K.Chiba, M.Matsui and Y.Fujii, J. Phys. Soc. Japan, (1975), **39,** 949-957.

K.Siratori, E.Kita, G.Kaji, A.Tasaki, S.Kimura, I.Shindo and K.Kohn, J. Phys. Soc. Japan, (1979), **47,** 1779-1787.

N.C.Tooms and H.P.Rooksby, Acta Cryst., (1951), **4,** 474-5.

E.J.W.Verwey, Nature, (1939), **144,** 327-8.

E.J.W.Verwey, P.W.Haayman and F.C.Romeijn. J. Chem. Phys., (1947), **15,** 181-187.

L.J.Vieland, Acta Cryst., (1975), **A31,** 753-755.

T.Yamada, K.Suzuki and S.Chikazumi, Appl. Phys. Lett., (1968), **13,** 172-174.

# Chapter 4. Iron Borate.

## 4.1. Introduction and previous study.

$Fe_2BO_4$ ($Fe_2OBO_3$) is a similar material to $Fe_3O_4$, it is derived from magnetite by substitution of boron for trivalent iron. This material contains $Fe^{2+}$ and $Fe^{3+}$ cations which form $FeO_6$ octahedra in a similar way to the octahedral metal site in $Fe_3O_4$. This phase has a warwickite type structure which differs from the spinel arrangement of magnetite, but preserves the edge-sharing octahedral chains containing equal amounts of $Fe^{2+}$ and $Fe^{3+}$ that are responsible for the notable conducting and magnetic properties of the latter.

$Fe_2BO_4$ was originally synthesised by Bertaut (1950). The crystal structure of $Fe_2BO_4$ is based on that of warwickite ($Mg_{1.5}Ti_{0.5}BO_4$, Takeuchi et al, 1950). The present study is a continuation of a previous study (Attfield et al, 1992).

$Fe_2OBO_3$ was synthesised from Fe metal, $Fe_2O_3$ and '$FeBO_3$' (previously made by heating a 1:2 mixture of $Fe_2O_3$ and $H_3BO_3$ in air at 1323 K for 4 days) in stoichiometric proportions. The mixture was pelleted, sealed in an evacuated silica tube and heated at 1373 K for 4 days.

X-ray powder diffraction showed that the dark grey product contained a new phase, identified as $Fe_2OBO_3$ by comparison to other warwickite type materials, and $Fe_3O_4$. The latter phase was removed magnetically to below the limits of detection by X-ray powder diffraction.

Powder neutron diffraction patterns were recorded at 3, 70, 100, 130, 160, and 190 K on the D2B diffractometer (see section 2.5.1.1) at the ILL, Grenoble, France. Data were collected from a 5 g sample in an 8 mm diameter vanadium can over an angular range of 0-160° 2θ at a neutron wavelength of 1.5946 Å. The data were corrected for sample absorption due to boron. Magnetic

Bragg reflections were observed in the patterns collected between 3-130 K but were not observed in the patterns collected at 160 and 190 K.

Rietveld refinement was originally done using these neutron data using the Pnma orthorhombic warwickite type structure as a starting model. However, a room temperature synchrotron X-ray powder diffraction pattern was also measured using the X7A high resolution powder diffractometer on at the National Synchrotron Light Source at the Brookhaven National Laboratory, USA. This showed that some of the Bragg reflections in the powder diffraction pattern that were thought to be due to an orthorhombic model in fact showed a monoclinic splitting. Therefore the crystal structure for the starting model was lowered from orthorhombic Pnma to $P2_1/c$ and the refinements were re-done using both the neutron and synchrotron datasets showing a better fit with the monoclinic starting model.

Two crystallographically distinct metal sites are present in this structure but the average Fe-O bond distances on each site are similar at room temperature (2.08(2)Å for Fe(1) site and 2.10(2)Å for Fe(2) site.) This suggests an average $Fe^{2.5+}$ oxidation state. The β angle decreases in the range 200-300 K, extrapolation suggested that this angle should reach 90 degrees and hence undergo a phase transition from monoclinic to orthorhombic above room temperature. The moments within Fe(1) chains are antiparallel to those in the Fe(2) chains.

Figure 4.1 shows the crystal and magnetic structure for $Fe_2BO_4$. There are frustrated triangular connections within the network of magnetic interactions. The ordered magnetic moment of 3.74(4) μB per Fe site at 3 K is significantly reduced from the ideal value of 4.5 μB due to this frustration.

*Figure 4.1. Projection of the $Fe_2OBO_3$ crystal and magnetic structure in the* **bc** *plane. This shows ribbons of octahedral $FeO_6$ units, the two different crystallographic Fe sites are indicated by light and dark octahedra. The directions of the magnetic moments are indicated by the + and - signs.*

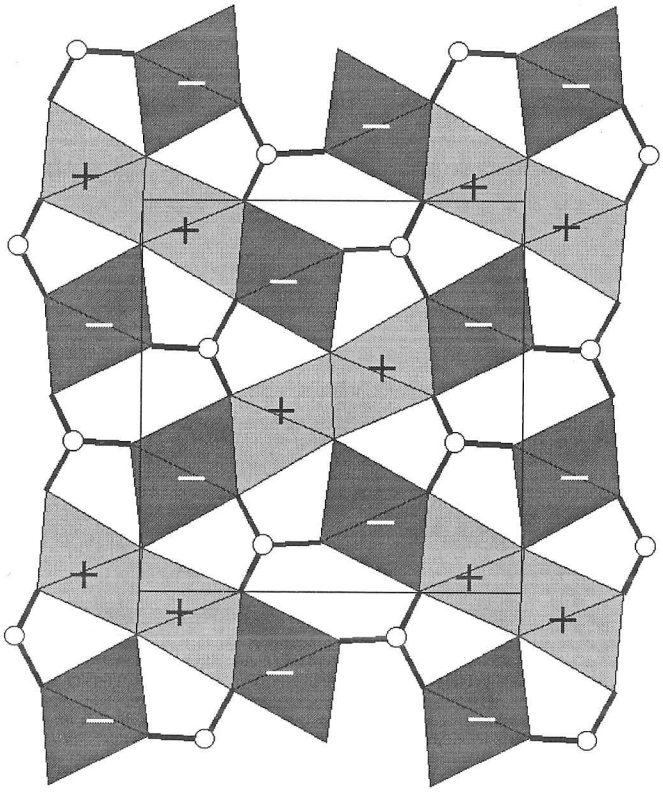

## 4.2. Present study.

### 4.2.1. Daresbury synchrotron radiation powder diffraction work.

High resolution powder diffraction work was done using the diffractometer on station 9.1 of the Daresbury Synchrotron Radiation Source (see section 2.3.1). The sample was loaded in a 0.3 mm diameter borosilicate glass capillary and mounted in a furnace attachment. Powder diffraction scans were made over the 102/10-2 monoclinic doublet in the temperature range 291-373 K. It

was not possible to observe a monoclinic splitting in this doublet but this reflection got sharper as the temperature increased to 315 K, from this we were able to determine that $Fe_2BO_4$ undergoes a phase transition at 315 K, see Figures 4.2 and 4.3.

*Figure 4.2. Plot of peak for monoclinic 102/10-2 doublet showing variation of peak width with temperature. Data was collected using the high resolution synchrotron X-ray powder diffractometer on station 9.1 of the Daresbury SRS, $\lambda = 0.9844$ Å.*

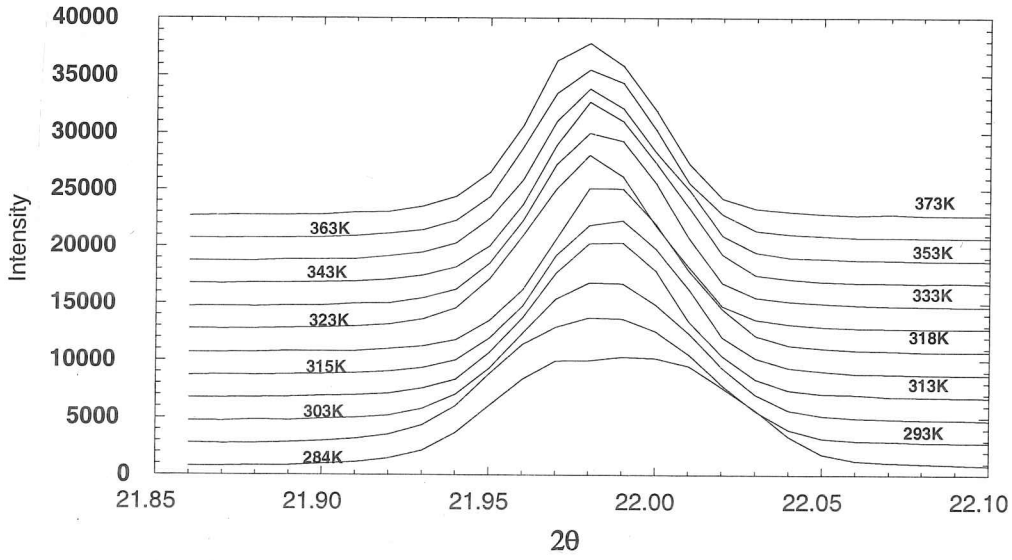


Full high-resolution powder diffraction scans were then done at 291 K, 312 K, 315 K, 318 K and 337 K. However, only the 337 K dataset was suitable for an accurate Rietveld refinement, the orthorhombic structure was then refined by the Rietveld method (Rietveld, 1969) using the MPROF software from the Daresbury Powder Diffraction Program Library (Murray et al, 1990). Bond lengths and angles were determined using BONDLA (Cockcroft 1995). High resolution powder diffraction scans were also done on 9.1 using the new curved image plate detector at 294 K, 301 K, 307 K, 316 K, 325 K, 332 K. All of these datasets were suitable for Rietveld

refinement using GSAS (Larson and von Dreele).

*Figure 4.3. Variation of peak width for monoclinic 102/10-2 doublet showing position of monoclinic-orthorhombic phase transition.*

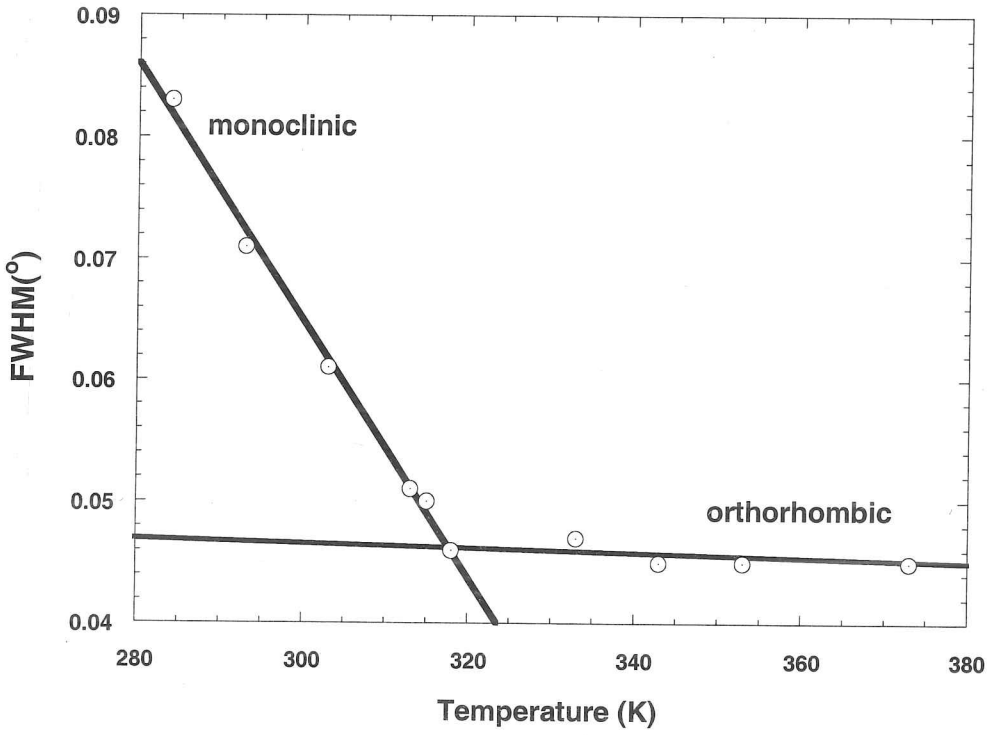


Figure 4.4 shows the image plate scan refinement for the 294 K dataset. Appendix A shows the image plate scan refinements for the 301 K, 307 K, 316 K, 325 K, 332 K datasets and the scintillation counter scan refinement for the 337 K dataset.

*Figure 4.4. Rietveld difference plot for $Fe_2BO_4$ at 294 K, image plate data collected on station 9.1 of the Daresbury SRS, $\lambda$ = 0.6920 Å.*

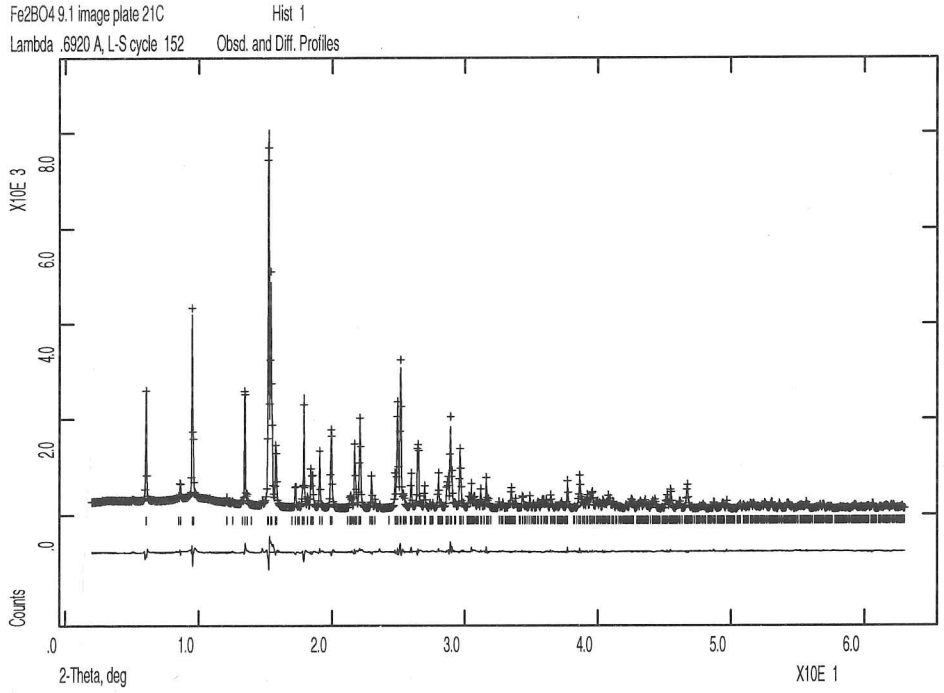


Figure 4.5 shows the monoclinic 102/10-2, 023 and 032 peaks from the image plate data and how they change with temperature. The mismatch of the 294 K peaks is due to a difference in zeropoint as this pattern was not measured in a furnace unlike the other 5 patterns.

The variation with temperature of the refined β lattice parameter from the Daresbury synchrotron studies (all image plate and 337 K scintillation counter data) and the previous D2B neutron study are shown in Figure 4.6. The parameter from the Brookhaven synchrotron study has been excluded as the temperature of this measurement was not recorded accurately.

Tables 4.1 and 4.2 show atomic co-ordinates and bond lengths from the synchrotron X-ray powder diffraction refinements. Table 4.3 shows lattice parameters from both the neutron and synchrotron powder diffraction refinements.

*Figure 4.5. Plot of peak for monoclinic 102/10-2 doublet showing variation of peak width with temperature. Image plate data were collected on station 9.1 of the Daresbury SRS, $\lambda = 0.6920$ Å. Notice how the 102/10-2 doublet becomes sharper with increasing temperature.*

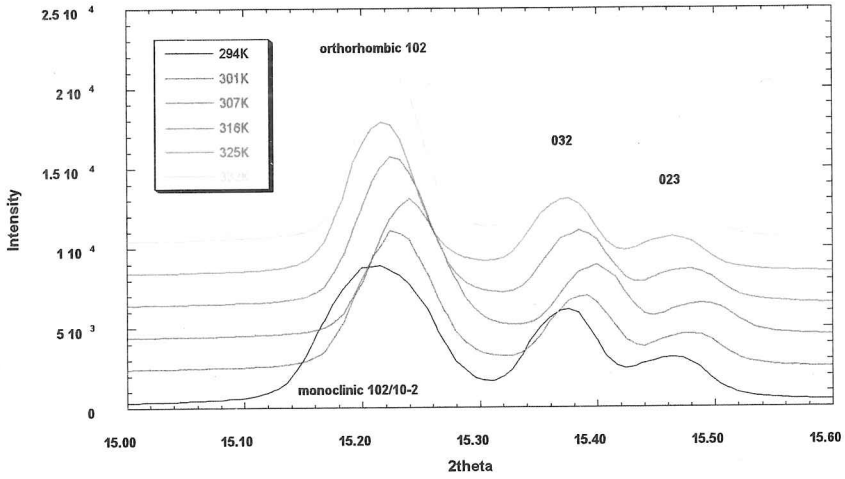


*Figure 4.6. Plot showing variation of β lattice parameter with temperature, data includes results of a previous neutron powder diffraction study (Attfield et al, 1992) with high resolution synchrotron X-ray powder diffraction work.*

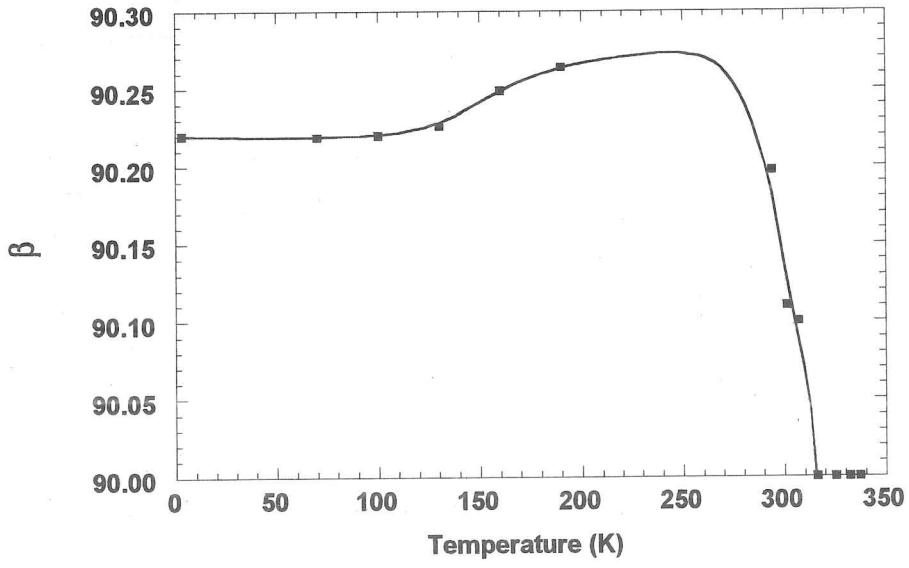

*Table 4.1. Refined atomic co-ordinates, temperature factors and R-factors from synchrotron X-ray powder diffraction (294-337 K).* Note that Fe and B temperature factors were fixed in the 337 K refinement as they could not be refined to positive numbers.

| T (K) | 294 | 301 | 307 | 316 | 325 | 332 | 337 |
|---|---|---|---|---|---|---|---|
| Fe(1): x | 0.7505(5) | 0.7541(9) | 0.7541(10) | 0.75 | 0.75 | 0.75 | 0.75 |
| y | 0.06786(8) | 0.06833(10) | 0.06836(10) | 0.06830(12) | 0.06825(12) | 0.06842(10) | 0.0678(1) |
| z | 0.11857(8) | 0.11843(11) | 0.11837(11) | 0.11834(12) | 0.11851(12) | 0.11811(11) | 0.1178(2) |
| Biso($Å^2$) | 0.25(2) | 0.40(3) | 0.38(3) | 0.45(3) | 0.45(3) | 0.42(3) | 0.25 |
| Fe(2): x | 0.2481(5) | 0.2537(9) | 0.2557(9) | 0.25 | 0.25 | 0.25 | 0.25 |
| y | 0.19467(8) | 0.19462(10) | 0.19464(10) | 0.19467(11) | 0.19468(11) | 0.19472(10) | 0.1943(1) |
| z | 0.39821(8) | 0.39842(11) | 0.39829(11) | 0.39852(12) | 0.39849(12) | 0.39827(11) | 0.3976(2) |
| Biso($Å^2$) | 0.22(2) | 0.35(3) | 0.34(3) | 0.43(3) | 0.38(3) | 0.39(3) | 0.25 |
| B(1): x | 0.7683(33) | 0.787(4) | 0.779(5) | 0.75 | 0.75 | 0.75 | 0.75 |
| y | 0.3785(8) | 0.3776(11) | 0.3777(11) | 0.3770(13) | 0.3784(13) | 0.3784(11) | 0.377(2) |
| z | 0.1634(6) | 0.1661(7) | 0.1659(7) | 0.1663(8) | 0.1657(8) | 0.1666(7) | 0.169(1) |
| Biso($Å^2$) | 0.5(1) | 0.4(2) | 0.6(2) | 1.0(2) | 0.8(2) | 1.0(2) | 0.25 |
| O(1): x | 0.2415(18) | 0.2266(30) | 0.2257(33) | 0.25 | 0.25 | 0.25 | 0.25 |
| y | 0.1188(5) | 0.1178(7) | 0.1184(7) | 0.1185(8) | 0.1183(8) | 0.1186(7) | 0.120(1) |
| z | 0.99161(29) | 0.9911(4) | 0.9903(4) | 0.9906(4) | 0.9908(4) | 0.9905(4) | 0.9860(1) |
| Biso($Å^2$) | 0.39(8) | 0.5(1) | 0.6(1) | 0.6(1) | 0.8(1) | 0.7(1) | 0.20(4) |
| O(2): x | 0.2440(23) | 0.263(4) | 0.270(4) | 0.25 | 0.25 | 0.25 | 0.25 |
| y | 0.00664(34) | 0.0060(4) | 0.0059(4) | 0.0064(5) | 0.0065(5) | 0.0063(4) | 0.0077(7) |
| z | 0.26846(34) | 0.2696(4) | 0.2692(5) | 0.2696(5) | 0.2686(5) | 0.2695(4) | 0.2653(7) |
| Biso($Å^2$) | 0.18(9) | 0.3(1) | 0.3(1) | 0.5(1) | 0.4(1) | 0.5(1) | 0.20(4) |
| O(3): x | 0.7373(23) | 0.725(4) | 0.721(4) | 0.75 | 0.75 | 0.75 | 0.75 |
| y | 0.25451(31) | 0.2542(4) | 0.2545(4) | 0.2536(5) | 0.2542(5) | 0.2536(4) | 0.2533(6) |
| z | 0.2489(4) | 0.2483(5) | 0.2478(5) | 0.2485(5) | 0.2478(5) | 0.2484(4) | 0.2482(7) |
| Biso($Å^2$) | 0.5(1) | 0.4(1) | 0.2(1) | 0.6(1) | 0.9(1) | 0.4(1) | 0.20(4) |
| O(4): x | 0.7687(18) | 0.7825(29) | 0.7811(31) | 0.75 | 0.75 | 0.75 | 0.75 |
| y | 0.3698(5) | 0.3706(7) | 0.3697(7) | 0.3698(8) | 0.3684(8) | 0.3695(7) | 0.371(1) |
| z | 0.01621(30) | 0.0172(4)1 | 0.0172(4) | 0.0174(5) | 0.0167(5) | 0.0177(4) | 0.0156(6) |
| Biso($Å^2$) | 0.88(8) | 1.5(1) | 1.3(1) | 1.5(1) | 1.5(1) | 1.5(1) | 0.20(4) |
| $R_p$ % | 4.4 | 3.8 | 3.8 | 4.2 | 4.6 | 3.8 | 14.7 |
| $R_{wp}$ % | 5.9 | 5.8 | 5.9 | 6.6 | 6.8 | 6.0 | 20.8 |
| $\chi^2$ | 0.78 | 0.75 | 0.74 | 1.01 | 1.04 | 1.78 | 1.57 |

*Table 4.2. Refined Fe-O and B-O distances (Å) for $Fe_2OBO_3$ from synchrotron X-ray powder diffraction (294-337 K).*

| T (K) | 294 | 301 | 307 | 316 | 325 | 332 | 337 |
|---|---|---|---|---|---|---|---|
| Fe1-O1 (Å) | 2.051(5) | 2.101(9) | 2.104(9) | 2.0335(27) | 2.0335(28) | 2.0338(24) | 2.062(3) |
| Fe1-O1 (Å) | 2.012(5) | 1.969(9) | 1.966(9) | 2.0335(27) | 2.0335(28) | 2.0338(24) | 2.062(3) |
| Fe1-O1 (Å) | 2.026(4) | 2.014(6) | 2.020(6) | 2.021(6) | 2.021(7) | 2.023(6) | 2.014(3) |
| Fe1-O2 (Å) | 2.203(6) | 2.174(10) | 2.158(10) | 2.1931(33) | 2.1867(33) | 2.1956(29) | 2.170(4) |
| Fe1-O2 (Å) | 2.166(6) | 2.211(10) | 2.226(10) | 2.1931(33) | 2.1867(33) | 2.1956(29) | 2.170(4) |
| Fe1-O3 (Å) | 2.1261(30) | 2.118(4) | 2.119(4) | 2.114(4) | 2.115(4) | 2.115(4) | 2.119(4) |
| mean Fe1-O (Å) | 2.097(5) | 2.098(8) | 2.099(8) | 2.098(4) | 2.096(4) | 2.099(4) | 2.100(4) |
| Fe2-O1 (Å) | 1.952(4) | 1.955(6) | 1.951(6) | 1.949(7) | 1.952(7) | 1.949(6) | 1.924(2) |
| Fe2-O2 (Å) | 2.1334(31) | 2.132(4) | 2.135(4) | 2.131(5) | 2.136(5) | 2.133(4) | 2.139(4) |
| Fe2-O3 (Å) | 2.199(6) | 2.246(9) | 2.264(10) | 2.1790(34) | 2.1848(35) | 2.1788(29) | 2.178(4) |
| Fe2-O3 (Å) | 2.156(6) | 2.117(9) | 2.105(9) | 2.1790(34) | 2.1848(35) | 2.1788(29) | 2.178(4) |
| Fe2-O4 (Å) | 1.971(5) | 1.955(9) | 1.961(9) | 2.0232(33) | 2.0160(32) | 2.0259(29) | 2.024(3) |
| Fe2-O4 (Å) | 2.068(5) | 2.094(8) | 2.085(9) | 2.0232(33) | 2.0160(32) | 2.0259(29) | 2.024(3) |
| mean Fe2-O (Å) | 2.080(5) | 2.083(8) | 2.084(8) | 2.081(4) | 2.082(4) | 2.082(4) | 2.078(3) |
| B-O2 (Å) | 1.358(7) | 1.353(9) | 1.352(10) | 1.351(11) | 1.347(11) | 1.338(9) | 1.371(5) |
| B-O3 (Å) | 1.410(7) | 1.398(9) | 1.395(9) | 1.385(10) | 1.390(10) | 1.395(9) | 1.375(6) |
| B-O4 (Å) | 1.363(5) | 1.377(7) | 1.375(7) | 1.377(8) | 1.381(8) | 1.379(7) | 1.419(11) |
| mean B-O (Å) | 1.377(6) | 1.376(8) | 1.374(9) | 1.37(1) | 1.37(1) | 1.371(8) | 1.388(8) |

*Table 4.3. Refined lattice parameters for $Fe_2OBO_3$ from neutron (3-190 K) and synchrotron X-ray powder diffraction (294-337 K).*

| T (K) | a (Å) | b (Å) | c (Å) | β (°) | V (Å$^3$) |
|---|---|---|---|---|---|
| 3 | 3.16879(8) | 9.3835(3) | 9.2503(3) | 90.220(1) | 275.05(3) |
| 70 | 3.16929(9) | 9.3838(2) | 9.2497(3) | 90.219(2) | 275.08(3) |
| 100 | 3.1700(1) | 9.3847(2) | 9.2498(3) | 90.220(2) | 275.17(3) |
| 130 | 3.1715(2) | 9.3846(4) | 9.2483(5) | 90.226(2) | 275.26(5) |
| 160 | 3.1735(2) | 9.3852(6) | 9.2468(7) | 90.249(2) | 275.40(7) |
| 190 | 3.1750(1) | 9.3878(3) | 9.2469(4) | 90.264(1) | 275.62(3) |
| 294 | 3.17626(3) | 9.3846(1) | 9.2398(1) | 90.197(1) | 275.417(8) |
| 301 | 3.17418(4) | 9.3805(1) | 9.2353(1) | 90.110(1) | 274.985(9) |
| 307 | 3.17426(4) | 9.3813(1) | 9.2360(1) | 90.100(1) | 275.035(8) |
| 316 | 3.17507(5) | 9.3846(1) | 9.2390(1) | 90 | 275.29(1) |
| 325 | 3.17543(4) | 9.3872(1) | 9.2416(1) | 90 | 275.477(9) |
| 332 | 3.17589(4) | 9.3907(1) | 9.2457(1) | 90 | 275.743(7) |
| 337 | 3.1777(4) | 9.398(1) | 9.253(1) | 90 | 276.33(9) |

### 4.2.2. Magnetisation and resistivity measurements.

Four probe resistivity (see section 2.7) measurements were performed on a sintered bar from 412 K to 240 K below which the resistance was too large to be measured accurately. The change in slope of resistivity against 1/T is at 315 K, this temperature is in agreement with the crystallographic phase transition, see Figure 4.7. The magnetisation (see section 2.8) of a powdered sample of $Fe_2OBO_3$ was measured between 4 and 300 K in fields of 0.05, 0.5 and 5.0 T on a SQUID magnetometer, see Figure 4.8. The sample was cooled in zero field prior to measurement. A small field dependence of the high temperature paramagnetic susceptibilities was found due to traces of ferrimagnetic $Fe_3O_4$. This contribution was estimated by extrapolating the 300 K susceptibility to 1/B = 0 and was then subtracted from the three sets of measurements,

giving the susceptibilities shown in Figure 4.9.

*Figure 4.7. Variation of ln ρ (resistivity) with 1/T. The decrease in resistivity passing through the phase transition is by a factor of ~3.*

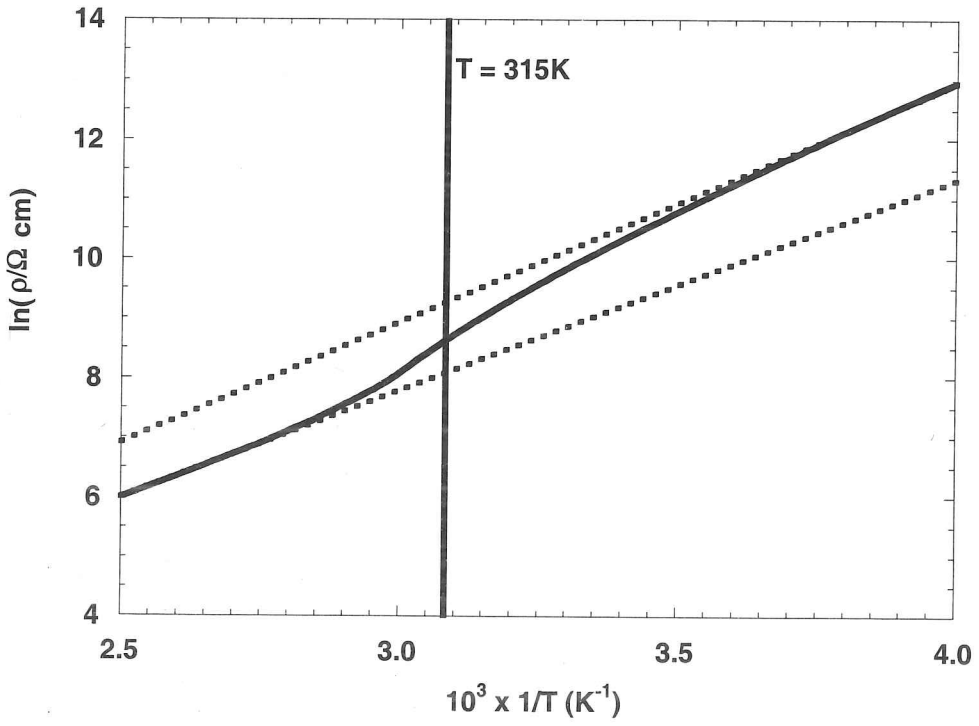


These magnetisation and susceptibility measurements show that $Fe_2OBO_3$ is ferromagnetic below $T_C$ = 155 K. Below the magnetic phase transition, the moments within each chain are ferromagnetically ordered and lie close to the **a** axis direction. The net saturated magnetic moment of ~0.03 $\mu_B$ per Fe atom in a 0.05 T field is only 0.8% of the sublattice moment found by neutron diffraction, this is characteristic of 'L type' ferrimagnetism (Néel, 1948), which arises from the inexact cancellation of the spontaneous magnetisations from the Fe(1) and Fe(2) sites

due to their structural inequivalence. This has previously been observed in the pure $Fe^{3+}$ compound $Fe_2(SO_4)_3$ (Long et al, 1979) which has two crystallographically inequivalent Fe sites, and in also the pure $Fe^{3+}$ compound $Fe_2(MoO_4)_3$ (Battle et al, 1982) has four crystallographically inequivalent Fe sites.

*Figure 4.8. Variation of magnetisation with temperature, data measured at three different magnetic field strengths.*

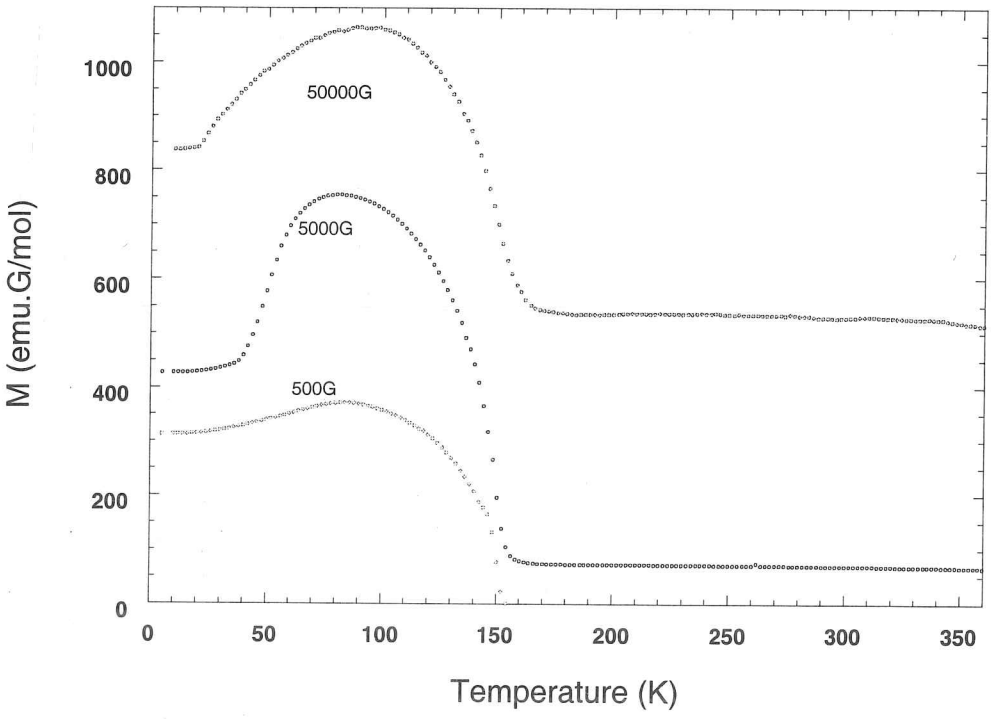

*Figure 4.9. Variation of susceptibility with temperature. Susceptibility was determined from magnetisation data given in Figure 4.8.*

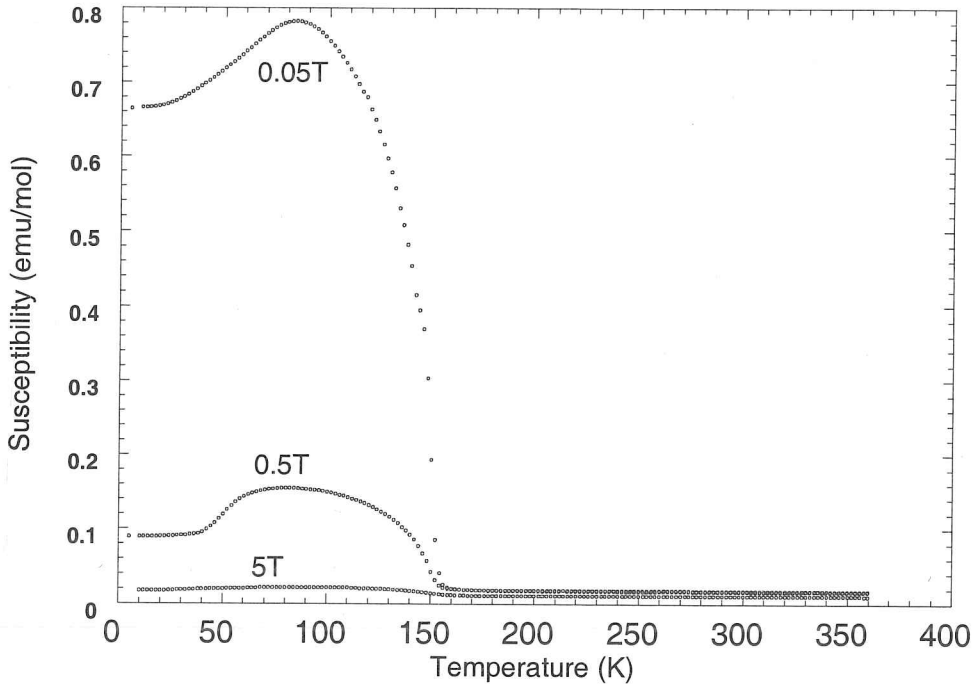


### 4.2.3. Mössbauer Spectrometry.

$^{57}$Fe Mössbauer spectra were measured at several temperatures comprised within the range 4.2 - 550 K. The Mössbauer hyperfine parameters were refined using MOSFIT software which compares a theoretical spectrum with the experimental ones, the difference being minimised by means of a least square method (Teillet et al). The spectra collection and analysis were performed in collaboration with Prof. Jean-Marc Greneche at the Université du Maine. The values of isomer shift are quoted relative to that of metallic iron at 300 K. We assumed that the f factor values

were independent on the nature of the iron probe, i.e. the proportions of each iron sites were directly proportional to the absorption area of the corresponding contribution.

#### 4.2.3.1. 300 K.

Figure 4.10 shows the spectrum recorded at 300 K, it exhibits a quadrupolar structure with the presence *a priori* of four different lines. The refinement was first done with three doublets but a better agreement (essentially around 1.2 mm/s) is obtained with 4 quadrupolar doublets. The hyperfine parameters which are listed in Table 4.4 are clearly consistent with the presence of three $Fe^{2+}$ components and 1 $Fe^{3+}$ component in nearby equiprobable proportions.

*Figure 4.10. Fitted Mössbauer spectrum at 300 K with 4 doublet components. 3 components are for $Fe^{2+}$ and 1 for $Fe^{3+}$, each component is plotted with a different colour.*

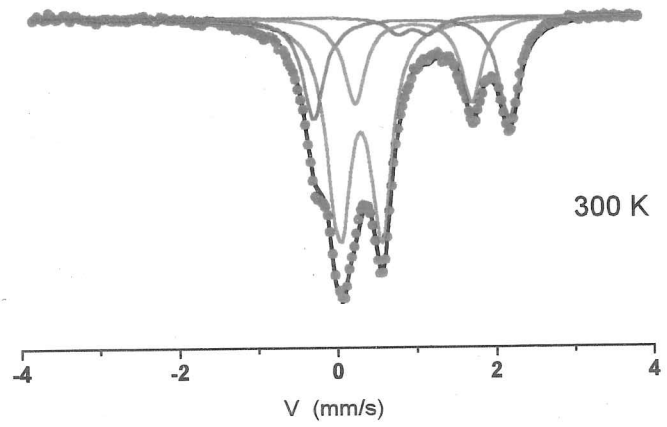

*Table 4.4. Mössbauer parameters at 300 K IS = isomer shift, Δ= quadrupole splitting (±0.02mm/s).*

| T (300 K) | IS (±0.02mm/s) | Δ (±0.02mm/s) | % (± 2) |
|---|---|---|---|
| $Fe^{3+}$ | 0.41 | 0.52 | 51 |
| $Fe^{2+}$ | 1.08 | 0.38 | 4 |
| $Fe^{2+}$ | 1.08 | 1.48 | 21 |
| $Fe^{2+}$ | 1.08 | 2.44 | 24 |

**4.2.3.2. 77 K and 4.2 K.**

The second stage consisted in recording spectra at 77 K and at 4.2 K. Figures 4.11 and 4.12.1-3 show that the hyperfine structure strongly differs from that observed at 300 K, clearly evidenced by the presence of magnetically ordered Fe-based components, i.e. the spectra were measured below the magnetic ordering temperature. Different fitting procedures were proposed involving two main components of $Fe^{2+}$ and $Fe^{3+}$, each of them resulting from the superposition of several subcomponents to take into account various cationic neighbouring of iron sites. Finally, it is necessary to introduce at least 6 components, 2 corresponding to $Fe^{3+}$ and 4 corresponding to $Fe^{2+}$. Some of these components exhibit broad lines (much higher than the natural line width) consequently these could be decomposed into even more components. The values of hyperfine parameters (isomer shift, quadrupolar shift and hyperfine field) confirm the presence of $Fe^{3+}$ and $Fe^{2+}$ in a stoichiometric 50:50 ratio. The spectrum at 77 K shows two components ($Fe^{2+}$ and $Fe^{3+}$) both resulting from superposition of subcomponents, see Figure 4.11. At 4.2 K 3 different fits to the spectrum are given with 2, 4 and 5 different components, see Figures 4.12.1-3.

*Figure 4.11. Fitted Mössbauer spectrum at 77 K with 2 sextuplet components. 1 component is for $Fe^{2+}$ and 1 for $Fe^{3+}$, each component results from superposition of subcomponents and is plotted with a different colour.*

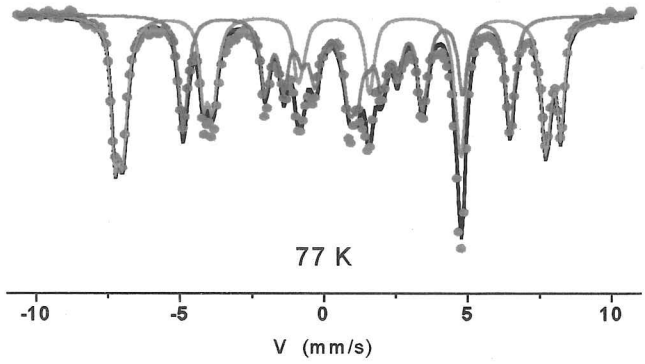


*Figure 4.12.1. Fitted Mössbauer spectrum at 4.2 K with 2 sextuplet components. 1 component is for $Fe^{2+}$ and 1 for $Fe^{3+}$, each component results from superposition of subcomponents and is plotted with a different colour.*

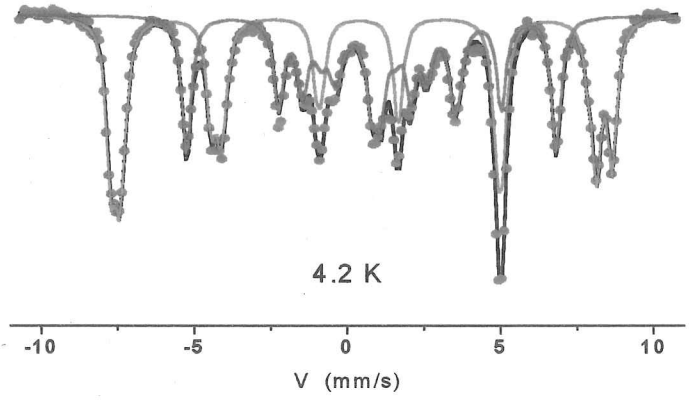


After these experiments were carried out at the temperatures usually used for Mössbauer experiments, it was decided to investigate in greater detail the temperature dependence of the hyperfine structure of this material. Four temperature ranges have been considered: below the magnetic ordering temperature $T_N$ which was found around 190 K, and above $T_N$ from 190-270

*Figure 4.12.2. Fitted Mössbauer spectrum at 4.2 K with 4 sextuplet components, each component is plotted with a different colour.*

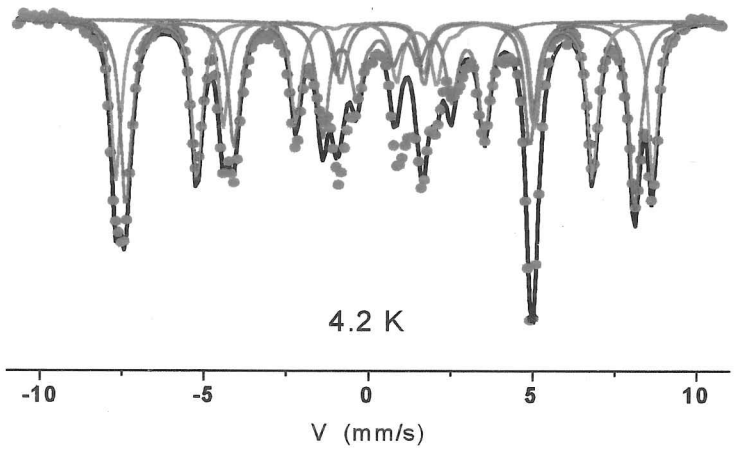


*Figure 4.12.3. Fitted Mössbauer spectrum at 4.2 K with 5 sextuplet components, each component is plotted with a different colour.*

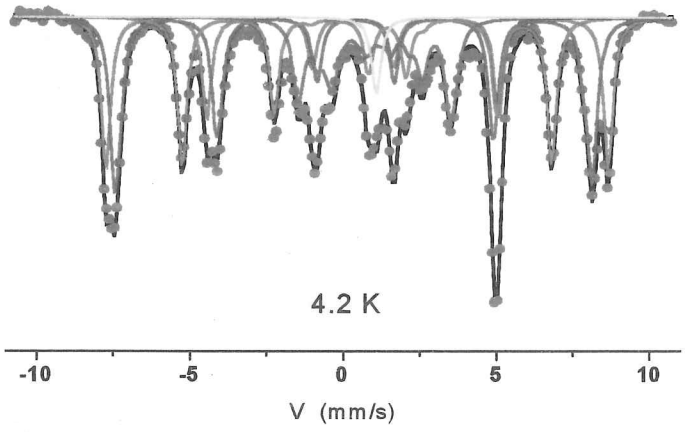


K (below the phase transition), from 300-400 K and above 400 K. Figure 4.13 shows raw Mössbauer spectra measured at 190, 270, 320, 340, 450 and 500 K, note the change in the spectra between 270-340 K corresponding to the crystallographic phase transition.

*Figure 4.13. Mössbauer spectra measured at 190, 270, 320, 340, 450 and 500 K.*

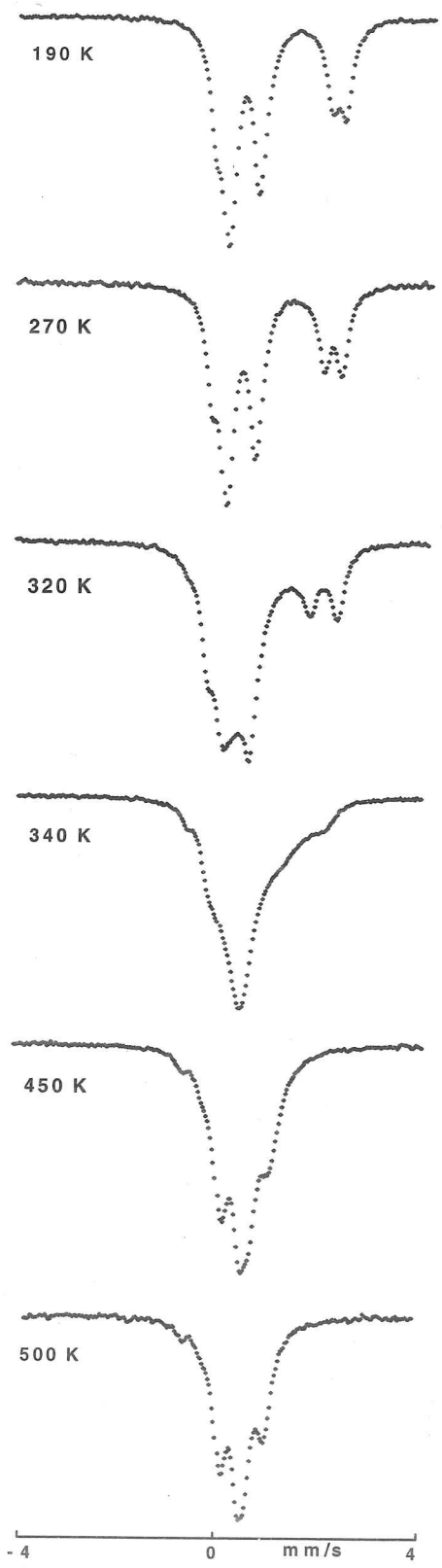

#### 4.2.3.3. $T < T_N$.

Some spectra were recorded at 20, 40 and 60 K: they exhibit hyperfine structures similar to those obtained at 4.2 K and 77 K and the same fitting procedure as previously mentioned, was introduced to describe these spectra. Table 4.5 shows results of Mössbauer refinements in the magnetic region between 4.2-120 K, these refinements are for a model with 3 $Fe^{2+}$ and 2 $Fe^{3+}$ components. No refined data are given for the temperature range 160-180 K due to the very complex structure around the magnetic phase transition, as described below.

*Table 4.5. Mössbauer parameters refined in magnetic region at 4.2 K, 20 K, 40 K, 77 K and 120 K. IS = isomer shift (±0.02mm/s), 2ε = quadrupole shift (±0.02mm/s), and HF = hyperfine field (±0.5 T).*

| Temperature (K) | 4.2 | 20 | 40 | 77 | 120 |
|---|---|---|---|---|---|
| $Fe^{3+}$ IS (mm/s) | 0.54 | 0.54 | 0.53 | 0.53 | 0.51 |
| $Fe^{3+}$ 2ε (mm/s) | 0.16 | 0.18 | 0.17 | 0.17 | 0.15 |
| $Fe^{3+}$ HF (T) | 50.6 | 50.6 | 50.2 | 47.9 | 44.2 |
| $Fe^{3+}$ IS (mm/s) | 0.52 | 0.53 | 0.52 | 0.52 | 0.50 |
| $Fe^{3+}$ 2ε (mm/s) | -0.05 | -0.05 | -0.03 | -0.04 | -0.05 |
| $Fe^{3+}$ HF (T) | 48.9 | 47.9 | 47.7 | 45.4 | 41.9 |
| $Fe^{2+}$ IS (mm/s) | 1.24 | 1.22 | 1.23 | 1.26 | 1.29 |
| $Fe^{2+}$ 2ε (mm/s) | 0.59 | 0.59 | 0.66 | 0.56 | 0.50 |
| $Fe^{2+}$ HF (T) | 13.8 | 13.8 | 13.3 | 13.0 | 12.8 |
| $Fe^{2+}$ IS (mm/s) | 1.24 | 1.25 | 1.23 | 1.22 | 1.19 |
| $Fe^{2+}$ 2ε (mm/s) | 2.5 | 2.5 | 2.5 | 2.5 | 2.5 |
| $Fe^{2+}$ HF (T) | 35.4 | 35.3 | 35.1 | 33.1 | 30.0 |
| $Fe^{2+}$ IS (mm/s) | 1.23 | 1.23 | 1.19 | 1.20 | 1.20 |
| $Fe^{2+}$ 2ε (mm/s) | -0.15 | -0.18 | -0.12 | -0.14 | -0.15 |
| $Fe^{2+}$ HF (T) | 15.1 | 15.3 | 15.3 | 14.6 | 13.7 |

The spectrum recorded at 160 K, close to the magnetic ordering temperature, exhibits a very complex hyperfine structure, especially in the centre; this suggests the presence of some

paramagnetic iron giving rise to a quadrupolar component "hidden with the envelope of magnetic components"; such a behaviour might be consistent with presence of idle spin induced by topological frustration (triangular units). More experiments would be needed in the temperature range 120-180 K to further investigate this region. In the 120 K, 160 K and 180 K fitted spectra, 2 components are fitted for $Fe^{2+}$ and $Fe^{3+}$ resulting from superposition of subcomponents, see Figures 4.14-16.

*Figure 4.14. Fitted Mössbauer spectrum at 120 K with 2 sextuplet components. 1 component is for $Fe^{2+}$ and 1 for $Fe^{3+}$, each component results from superposition of subcomponents and is plotted with a different colour.*

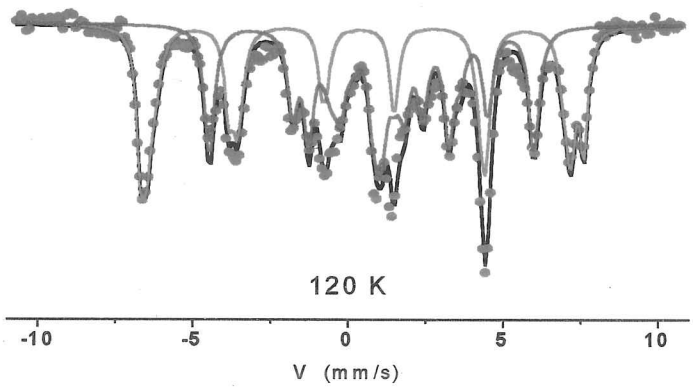


The 185 K and 190 K spectra are fitted with 4 components. At 185 K (see Figure 4.17) one observes a quasi quadrupolar structure but the lines remain broadened while at 190 K (see Figure 4.18) lines are narrow. From the Mössbauer data it seems that the $T_c$ for the magnetic phase transition is between 185 and 190 K. However, this temperature is 35-40 K higher than that estimated from magnetic measurements and neutron diffraction. Further Mössbauer experiments will have to be performed to clarify the magnetic phase transition temperature and to understand the temperature dependence of hyperfine fields of both $Fe^{2+}$ and $Fe^{3+}$ components.

*Figure 4.15. Fitted Mössbauer spectrum at 160 K with 2 sextuplet components. 1 component is for $Fe^{2+}$ and 1 for $Fe^{3+}$, each component results from superposition of subcomponents and is plotted with a different colour.*

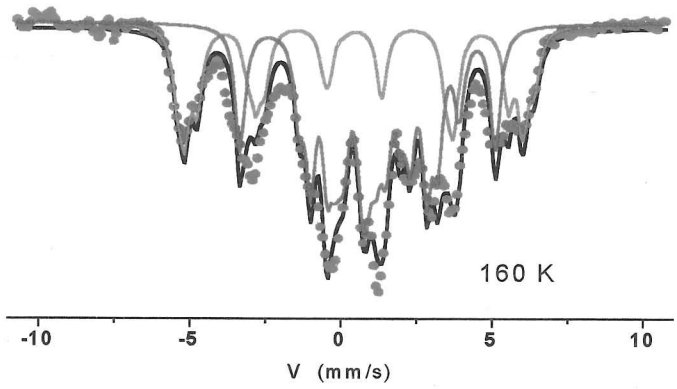


*Figure 4.16. Fitted Mössbauer spectrum at 180 K with 2 doublet components. Sextuplets have now collapsed to doublets as the sample passes through the magnetic phase transition. 1 component is for $Fe^{2+}$ and 1 for $Fe^{3+}$, each component results from superposition of subcomponents and is plotted with a different colour.*

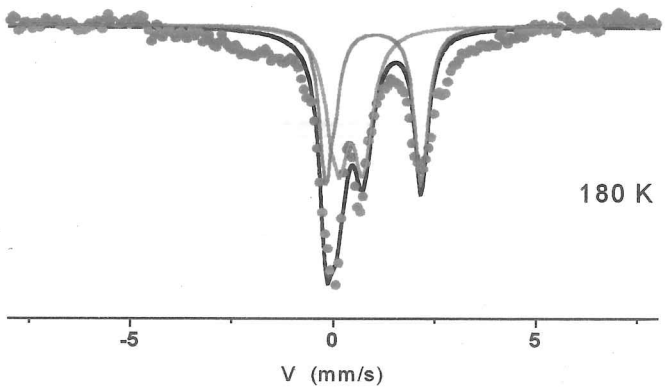

*Figure 4.17. Fitted Mössbauer spectrum at 185 K with 4 doublet components. 2 components are for $Fe^{2+}$ and 2 for $Fe^{3+}$, each component is plotted with a different colour.*

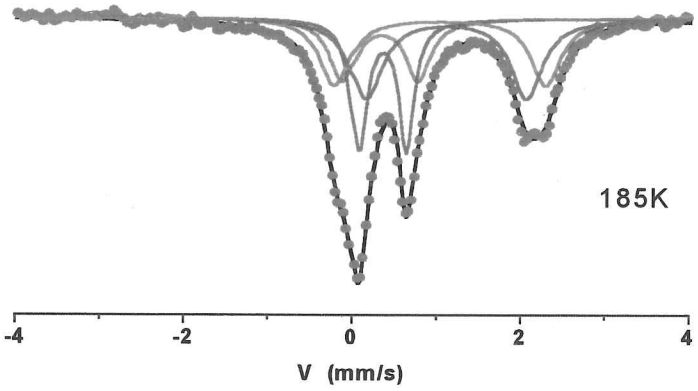


*Figure 4.18. Fitted Mössbauer spectrum at 190 K with 4 doublet components. 2 components are for $Fe^{2+}$ and 2 for $Fe^{3+}$, each component is plotted with a different colour.*

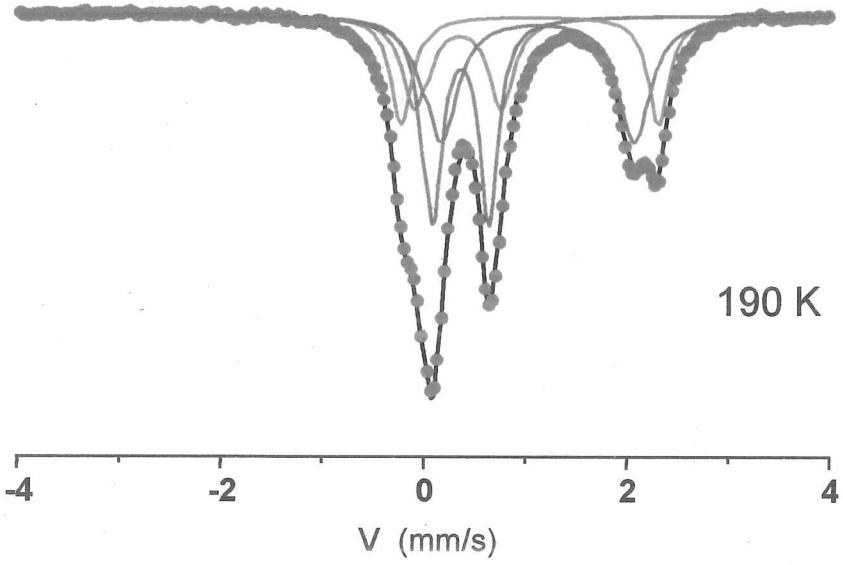

#### 4.2.3.4. 190-300 K.

In this region the hyperfine structure remains temperature independent, except for a decrease of external splitting with increasing temperature which is usual for $Fe^{2+}$: $3d^6$ (composed of both lattice and valence contributions), whereas the quadrupolar splitting of $Fe^{3+}$ ($3d^5$) is temperature independent, because it results only from the lattice contribution. The Mössbauer spectra between 185 K and 270 K can be fitted by 4 equiprobable doublet components of equal intensity, two with isomer shifts of 1.1-1.2 mm/s and two with an isomer shift of ~0.35 mm/s, corresponding to equal amounts of $Fe^{2+}$ and $Fe^{3+}$ each localised at the Fe(1) and Fe(2) sites.

Figures 4.19.1-2 show two fitted spectra measured at 240 K, the first spectrum is for a fit where the occupancies of each component fixed at 25% and the second is for a fit where these occupancies have been allowed to refine.

*Figure 4.19.1. Fitted Mössbauer spectrum at 240 K with 4 doublet components. 2 components are for $Fe^{2+}$ and 2 for $Fe^{3+}$, each component is plotted with a different colour. Intensities of each component were constrained so that each contributed 25% to the fitted spectrum.*

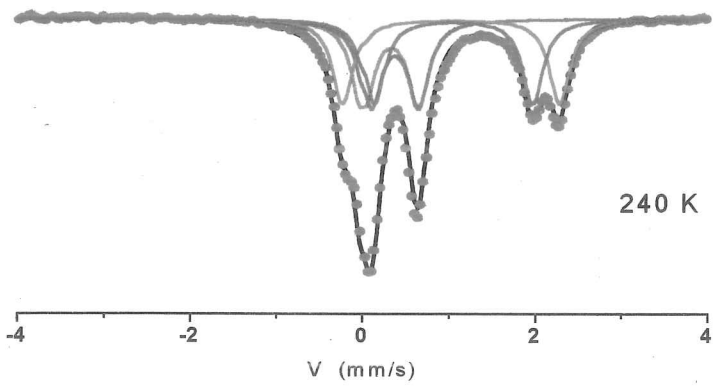

*Figure 4.19.2. Fitted Mössbauer spectrum at 240 K with 4 doublet components. 2 components are for $Fe^{2+}$ and 2 for $Fe^{3+}$, each component is plotted with a different colour. Intensities of each component were allowed to refine freely.*

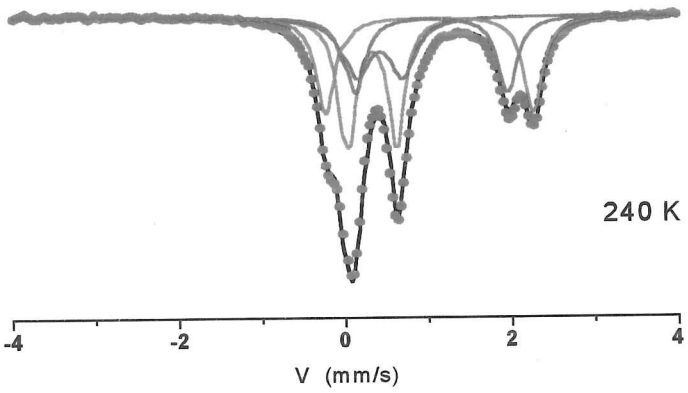


Table 4.6 shows results of Mössbauer refinements in the paramagnetic region between 185-220 K, these refinements are for a model with 2 $Fe^{2+}$ and 2 $Fe^{3+}$ components.

*Table 4.6. Mössbauer parameters refined in paramagnetic region, 185-240 K, IS = isomer shift (± 0.02 mm/s) and Δ = quadrupole splitting (± 0.02 mm/s).*

| Temperature (K) | 185 | 190 | 220 | 240 |
|---|---|---|---|---|
| $Fe^{3+}$ IS (mm/s) | 0.45 | 0.45 | 0.45 | 0.44 |
| $Fe^{3+}$ Δ (mm/s) | 0.96 | 0.87 | 0.87 | 0.88 |
| $Fe^{3+}$ IS (mm/s) | 0.47 | 0.46 | 0.46 | 0.46 |
| $Fe^{3+}$ Δ (mm/s) | 0.57 | 0.56 | 0.56 | 0.55 |
| $Fe^{2+}$ IS (mm/s) | 1.15 | 1.16 | 1.14 | 1.13 |
| $Fe^{2+}$ Δ (mm/s) | 2.45 | 2.50 | 2.50 | 2.50 |
| $Fe^{2+}$ IS (mm/s) | 1.22 | 1.22 | 1.19 | 1.18 |
| $Fe^{2+}$ Δ (mm/s) | 1.88 | 1.90 | 1.85 | 1.82 |

#### 4.2.3.5. 300-400 K.

This temperature range contains the phase transition temperature and the doublets broaden and coalesce due to the exchange of $Fe^{2+}$ and $Fe^{3+}$ environments through hopping of the extra electron. The hyperfine structure is strongly temperature dependent but it is very difficult *a priori* to reproduce such spectra with one physical fitting model. Consequently, no refined results are given for the temperature range 300-400 K due to the problems of fitting the spectra which become broad passing through this phase transition. However, the mean isomer shift can be estimated, Figure 4.20 shows how this decreases linearly with increasing temperature in this range. This suggests that the isomer shifts have values intermediate between those for $Fe^{2+}$ and $Fe^{3+}$ in this range and therefore there is some electron transfer between $Fe^{2+}$ and $Fe^{3+}$. Such a behaviour is consistent with conductivity measurements and is presumably due to some fast electron transfer through oxygen atoms.

*Figure 4.20. Variation with temperature of mean $^{57}Fe$ isomer shift determined from Mössbauer refinements.*

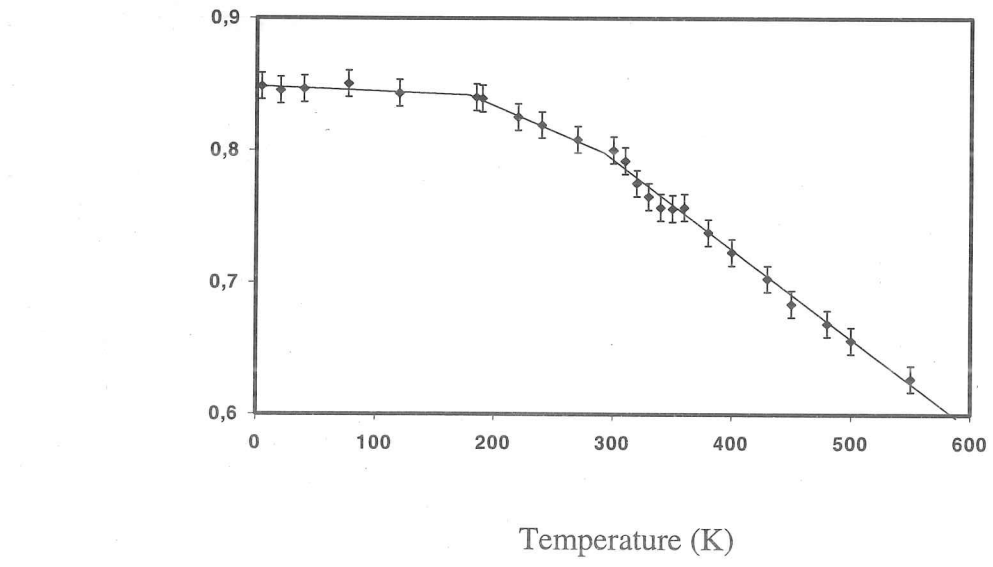

#### 4.2.3.6. 400 K and above.

The spectra exhibit a more simple hyperfine structure with one pronounced central single line and two satellite lines. In spite of this simple structure three different fitting procedures are possible, these are :-

(i) a central single broad line and a doublet (with same isomer shift value) corresponding to two $Fe^{2.5+}$ components but with very different quadrupolar splitting, this is not realistic, see Figure 4.21.1.

(ii) two partially overlapped doublets with very different isomer shifts but similar quadrupolar splittings, corresponding to $Fe^{2+}$ and $Fe^{3+}$ components, again this is not realistic, see Figure 4.21.2.

(iii) two strongly overlapped doublets with slightly different isomer shifts and quadrupolar splitting, corresponding to intermediate valence $Fe^{2+x}$ and $Fe^{3-x}$ states, this model is in agreement with that determined from the crystal structure above the phase transition temperature and this model has been used for all refinements in this temperature region, see Figure 4.21.3. Models (i) and (ii) are not realistic as in this temperature region the $Fe^{2+}$ and $Fe^{3+}$ cations are becoming disordered with an intermediate average valence. If the cations are becoming disordered it would seem plausible that the isomer shift and quadrupolar splittings for each Fe site would have similar values. The first two models have very different parameters for the two Fe sites.

#### 4.2.3.6. 400 K and above.

The spectra exhibit a more simple hyperfine structure with one pronounced central single line and two satellite lines. In spite of this simple structure three different fitting procedures are possible, these are :-

(i) a central single broad line and a doublet (with same isomer shift value) corresponding to two $Fe^{2.5+}$ components but with very different quadrupolar splitting, this is not realistic, see Figure 4.21.1.

(ii) two partially overlapped doublets with very different isomer shifts but similar quadrupolar splittings, corresponding to $Fe^{2+}$ and $Fe^{3+}$ components, again this is not realistic, see Figure 4.21.2.

(iii) two strongly overlapped doublets with slightly different isomer shifts and quadrupolar splitting, corresponding to intermediate valence $Fe^{2+x}$ and $Fe^{3-x}$ states, this model is in agreement with that determined from the crystal structure above the phase transition temperature and this model has been used for all refinements in this temperature region, see Figure 4.21.3. Models (i) and (ii) are not realistic as in this temperature region the $Fe^{2+}$ and $Fe^{3+}$ cations are becoming disordered with an intermediate average valence. If the cations are becoming disordered it would seem plausible that the isomer shift and quadrupolar splittings for each Fe site would have similar values. The first two models have very different parameters for the two Fe sites.

*Figure 4.21.1. Fitted Mössbauer spectrum at 550 K with a central single broad line and a doublet (with same isomer shift value) corresponding to two $Fe^{2.5+}$ components but with very different quadrupolar splitting, this is not realistic, each component is plotted with a different colour.*

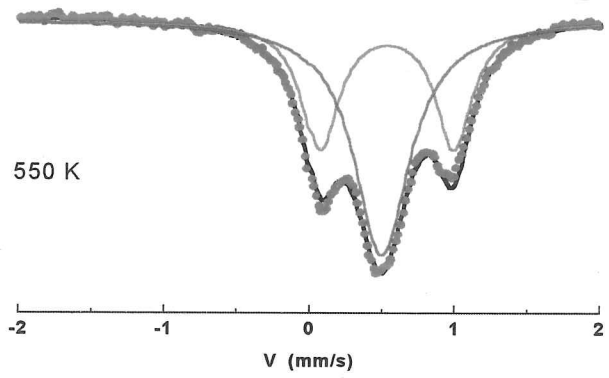


*Figure 4.21.2. Fitted Mössbauer spectrum at 550 K with two partially overlapped doublets with very different isomer shifts but similar quadrupolar splittings, corresponding to $Fe^{2+}$ and $Fe^{3+}$ components, again this is not realistic, each component is plotted with a different colour.*

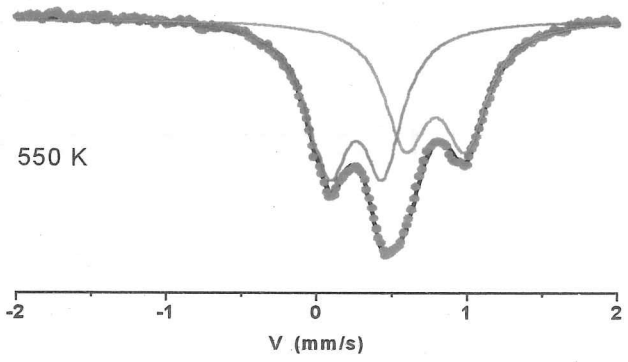

*Figure 4.21.3. Fitted Mössbauer spectrum at 550 K. This fit has two strongly overlapped doublets with slightly different isomer shifts and quadrupolar splittings, this corresponds to intermediate valence $Fe^{2+x}$ and $Fe^{3-x}$ states.*

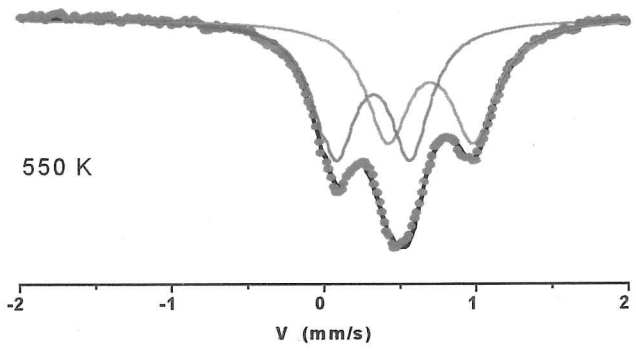


Table 4.7 shows results of Mössbauer refinements in the paramagnetic region between 380-550 K, these refinements are for the third model mentioned above with 2 Fe components with intermediate valence $Fe^{2+x}$ and $Fe^{3-x}$ states.

*Table 4.7. Mössbauer parameters refined in paramagnetic region, 380-550 K, IS = isomer shift (± 0.02 mm/s) and Δ = quadrupole splitting (± 0.02 mm/s).*

| Temperature (K) | 430 | 450 | 480 | 500 | 550 |
|---|---|---|---|---|---|
| $Fe^{3-x}$ IS (mm/s) | 0.40 | 0.41 | 0.40 | 0.39 | 0.37 |
| $Fe^{3-x}$ Δ (mm/s) | 0.38 | 0.38 | 0.38 | 0.37 | 0.36 |
| $Fe^{2+x}$ IS (mm/s) | 0.93 | 0.93 | 0.91 | 0.90 | 0.88 |
| $Fe^{2+x}$ Δ (mm/s) | 0.38 | 0.37 | 0.38 | 0.38 | 0.42 |

The refined isomer shift using the third model for the $Fe^{3-x}$ state is 0.46 mm/s and the shift for the $Fe^{2+x}$ state is 0.84 mm/s. The fitted isomer shifts from the incorrect second model which assumes completely ordered cations are 0.37 mm/s for $Fe^{3+}$ and 0.85 mm/s for $Fe^{2+}$. By interpolating

between the isomer shifts for the ordered and disordered it is possible to estimate the value of x for the disordered cation valences at 550 K to be approximately 0.15, i.e. the approximate disordered cation valences are $Fe^{2.15+}$ and $Fe^{2.85+}$.

### 4.2.4. High Resolution Electron Microscopy (HREM).

Electron diffraction and HREM studies were carried out using a 200 kV JEOL 2010 electron microscope by Dr. Richard Retoux of the Laboratoire des Fluorures, Université du Maine, Le Mans, France. Lattice images were simulated using the multislice method for different crystal thicknesses with the EMS programs (Stadelman, 1987). Reciprocal lattices were reconstructed from electron diffraction patterns and this confirmed the pseudo-orthorhombic unit cell of $Fe_2OBO_3$, there is no evidence for any superlattice. Figure 4.22 shows a [100] HREM image, there are regular contrasts over large zones showing that this phase is well ordered with no intergrowths of other phases. Image simulations for defocus values of ~150 Å show the boron atoms as white regions between the black $FeO_6$ octahedra (cf Figure 4.1) and agrees with the observed image.

## 4.3. Discussion.

$Fe_2OBO_3$ is a material related to magnetite, $Fe_3O_4$. Magnetite has an inverse spinel structure at room temperature, it has a charge description of $(Fe^{2+}Fe^{3+})Fe^{3+}O_4$. The bracketed $(Fe^{2+}Fe^{3+})$ cations are found within chains of edge sharing $FeO_6$ octahedra interconnected by the additional, tetrahedrally co-ordinated, $Fe^{3+}$. The spins on the two octahedral cations order ferromagnetically

below the Curie temperature $T_c$ = 858 K. This facilitates the spin-conserving transfer of the

*Figure 4.22. A [100] HREM image of $Fe_2OBO_3$.*

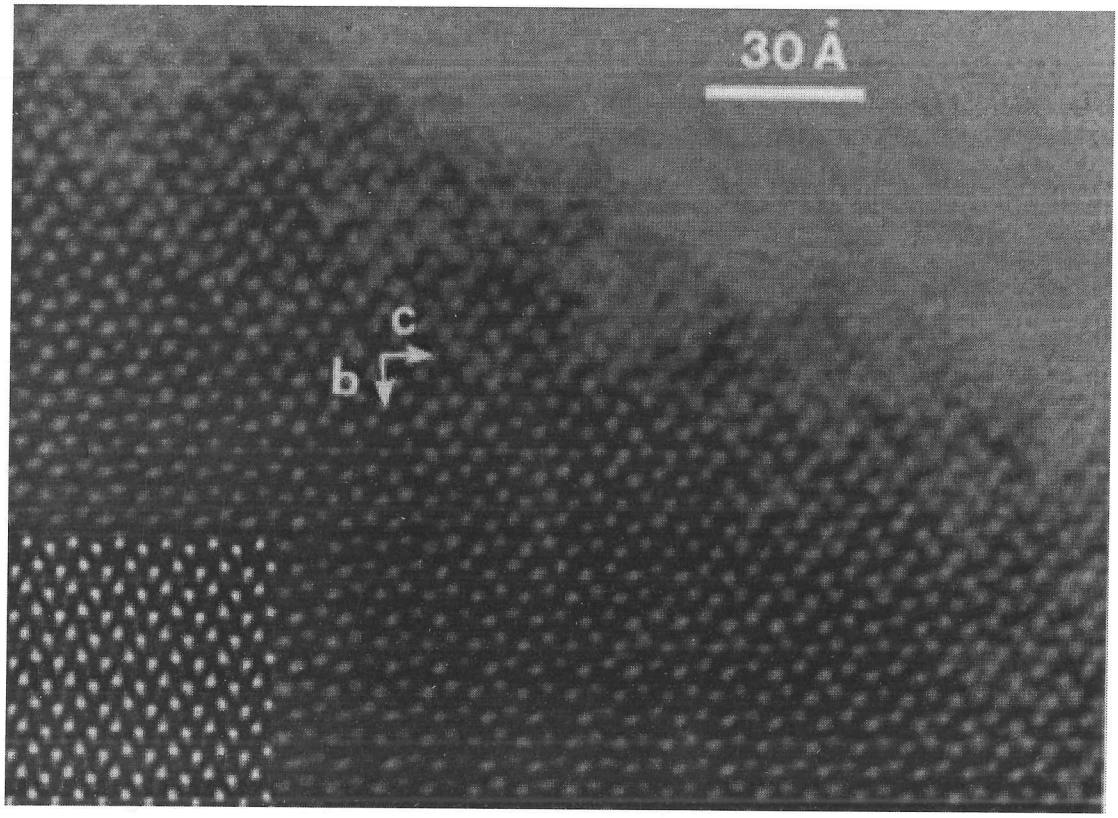


"extra" electron from $Fe^{2+}$ to $Fe^{3+}$ resulting in an appreciable conductivity of ~$10^2 \Omega^{-1}cm^{-1}$. In the Verwey Transition (Verwey, 1939) in $Fe_3O_4$ at ~120 K there is a sharp decrease in conductivity accompanied by a complex lattice distortion due to $Fe^{2+}/Fe^{3+}$ charge-ordering. If the tetrahedral $Fe^{3+}$ is replaced by boron this converts the inverse spinel $Fe_3O_4$ into warwickite $Fe_2OBO_3$, see Figure 4.1.

This warwickite type structure is common for $MM'OBO_3$ oxoborates. Several oxoborate warwickite materials are known with the Pnma orthorhombic structure, e.g. $Mg_{1.5}Ti_{0.5}OBO_3$ (Takeuchi et al, 1950), $NiScOBO_3$ (Bluhm et al, 1990), $ZnFeOBO_3$ (Bluhm et al, 1995a), $FeCoOBO_3$ (Buerger et al, 1972), $FeMnOBO_3$ (Bluhm et al, 1995b), $Co_{1.5}Ti_{0.5}OBO_3$ (Bluhm et al, 1995c), $Co_{1.5}Zr_{0.5}OBO_3$ (Bluhm et al, 1995c), $MgAlOBO_3$ (Fang et al, 1965) and $MgScOBO_3$

(Norrestam, 1989). Monoclinically distorted structures have also been reported for $MnAl_{0.5}Y_{0.5}OBO_3$ (Bluhm et al, 1995a), $Mg_{0.76}Mn_{1.24}OBO_3$ (Norrestam, 1989) and $Mn_2OBO_3$ (Norrestam et al, 1995).

In the warwickite structure infinite chains of edge-sharing octahedra lie parallel to the a axis and form four octahedron wide 'ribbons' by sharing edges with neighbouring chains. These are linked into a three dimensional network by sharing corners with other ribbons and the triangular $BO_3$ groups. An important feature of the $Fe_2OBO_3$ structure is that two crystallographically distinct chains of octahedral iron sites, Fe(1) and Fe(2), are present.

### 4.3.1. Magnetic phase transition.

The first of two phase transitions observed for $Fe_2OBO_3$ is a magnetic ordering phase transition. This magnetic structure is almost antiferromagnetic, but there is a small ferromagnetic component due to the inequivalence of the two crystallographically distinct Fe sublattices. Therefore below the transition magnetic structure shows L-type ferrimagnetism (magnetic moments saturate at different rates, see Figure 4.23). Magnetisation (Figure 4.8) and susceptibility (Figure 4.9) measurements show the onset of this transition at $\mathbf{T_c = 155\ K}$. Neutron powder diffraction work (Attfield et al, 1992) is in agreement with this transition temperature as magnetic Bragg reflections are observed at 130 K but are not observed at 160 K. However, Mössbauer spectroscopy work shows evidence for a quadrupolar shift due to the presence of a magnetic field up to **185 K** (Figures 4.11-17).

This discrepancy in the measurement of the transition temperature may be due to the presence of defects and frustration in the crystal structure creating more chemical environments for the Fe cations which will be observed as the Mössbauer technique can observe short range order.

However, it is clear that a more detailed Mössbauer study needs to be done in this temperature region.

*Figure 4.23. Schematic diagram illustrating the different saturation rates of magnetic moments in L-type ferrimagnetism. The difference in magnetisation is due to the difference between magnetic moments.*

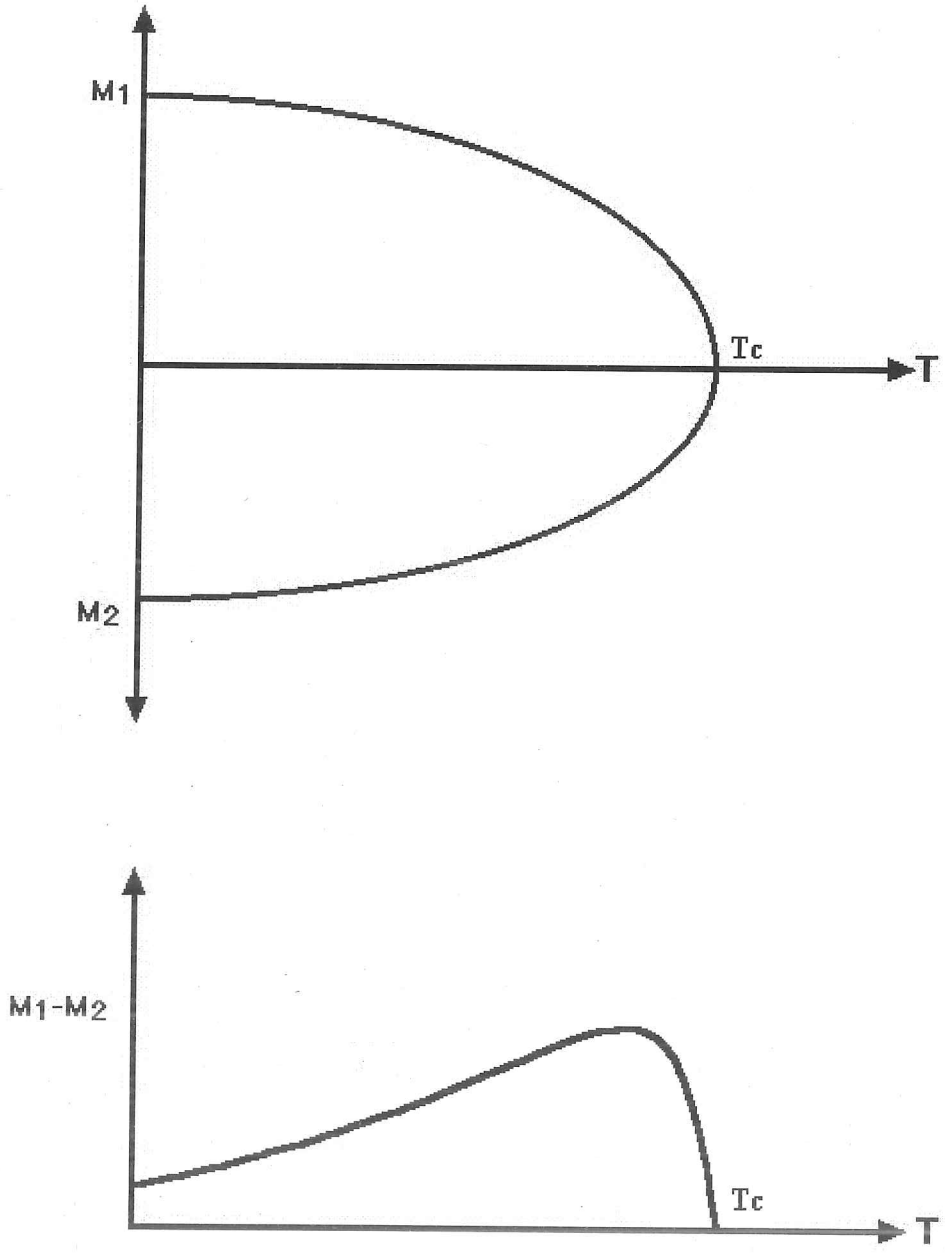


Above the magnetic phase transition but below room temperature the Mössbauer spectra can be

fitted with 4 components corresponding to 2 $Fe^{2+}$ and 2 $Fe^{3+}$ environments with the $Fe^{2+}/Fe^{3+}$ in a stoichiometric 50:50 ratio. However, the monoclinic crystal structure of $Fe_2OBO_3$ in this temperature region shows the presence of two equivalent $Fe^{2.5+}$ sites. This indicates that the localised $Fe^{2+}/Fe^{3+}$ order is not reflected in the crystallographic long range order.

### 4.3.2. Crystallographic phase transition.

The second of two phase transitions observed for $Fe_2OBO_3$ is a crystallographic phase transition. High resolution synchrotron X-ray powder diffraction shows a change in the crystal structure from $P2_1/c$ to Pnma at 315 K (Figures 4.2-3). Figure 4.6 shows how the monoclinic β angle, determined from the previous neutron powder diffraction study (Attfield et al, 1992) and the current synchrotron work, varies between 3 K and 337 K and shows how β decreases approaching the phase transition temperature. Resistivity measurements (Figure 4.7) confirm the presence of this phase transition at this temperature.

Both the $P2_1/c$ and Pnma crystal structures have two structurally distinct Fe sites. Both types of $FeO_6$ octahedra are very distorted, with Fe-O bond lengths varying between 1.92 and 2.23 Å at 3 K (Attfield et al, 1992), the mean Fe(1)-O and Fe(2)-O distances of 2.085(2) and 2.082(2) Å are equal within their errors indicating that both sites have an average charge of $Fe^{2.5+}$. Comparing the difference between these values to that between the usual 300 K $Fe^{2+}$-O and $Fe^{3+}$-O distances of 2.16 and 2.02Å, enables the deviation of the charge at each site from the average $Fe^{2.5+}$ value to be estimated as 0.01. Table 4.2 shows that there is little or no difference between the mean Fe-O distances for both Fe sites between 294 K and 337 K indicating that the average charge of $Fe^{2.5+}$ on each site is maintained over the temperature range including the crystallographic phase

fitted with 4 components corresponding to 2 $Fe^{2+}$ and 2 $Fe^{3+}$ environments with the $Fe^{2+}/Fe^{3+}$ in a stoichiometric 50:50 ratio. However, the monoclinic crystal structure of $Fe_2OBO_3$ in this temperature region shows the presence of two equivalent $Fe^{2.5+}$ sites. This indicates that the localised $Fe^{2+}/Fe^{3+}$ order is not reflected in the crystallographic long range order.

### 4.3.2. Crystallographic phase transition.

The second of two phase transitions observed for $Fe_2OBO_3$ is a crystallographic phase transition. High resolution synchrotron X-ray powder diffraction shows a change in the crystal structure from $P2_1/c$ to Pnma at 315 K (Figures 4.2-3). Figure 4.6 shows how the monoclinic $\beta$ angle, determined from the previous neutron powder diffraction study (Attfield et al, 1992) and the current synchrotron work, varies between 3 K and 337 K and shows how $\beta$ decreases approaching the phase transition temperature. Resistivity measurements (Figure 4.7) confirm the presence of this phase transition at this temperature.

Both the $P2_1/c$ and Pnma crystal structures have two structurally distinct Fe sites. Both types of $FeO_6$ octahedra are very distorted, with Fe-O bond lengths varying between 1.92 and 2.23 Å at 3 K (Attfield et al, 1992), the mean Fe(1)-O and Fe(2)-O distances of 2.085(2) and 2.082(2) Å are equal within their errors indicating that both sites have an average charge of $Fe^{2.5+}$. Comparing the difference between these values to that between the usual 300 K $Fe^{2+}$-O and $Fe^{3+}$-O distances of 2.16 and 2.02Å, enables the deviation of the charge at each site from the average $Fe^{2.5+}$ value to be estimated as 0.01. Table 4.2 shows that there is little or no difference between the mean Fe-O distances for both Fe sites between 294 K and 337 K indicating that the average charge of $Fe^{2.5+}$ on each site is maintained over the temperature range including the crystallographic phase

transition.

In the Mössbauer spectra measured between 270-380 K (Figures 4.10, 4.13 and 4.19.1-2), the temperature range containing the phase transition, the doublets corresponding to 2 $Fe^{2+}$ and 2 $Fe^{3+}$ components broaden and coalesce. This is due to the exchange of $Fe^{2+}$ and $Fe^{3+}$ environments through hopping of the extra electron as the material is close to the transition.

The Mössbauer spectra measured between 380-550 K (Figures 4.13 and 4.21.1-3), show two well defined doublets consistent with rapid electron hopping between structurally distinct $Fe^{2+x}$ and $Fe^{3-x}$ sites. This short range Mössbauer structure is in agreement with that obtained from the Pnma crystal structure above the phase transition.

Figure 4.20 shows how the mean refined Mössbauer isomer shift parameters vary with temperature. The decrease in mean isomer shift is due to electron transfer between $Fe^{2+}$ and $Fe^{3+}$ to form environments with an intermediate valence. This behaviour is consistent with resistivity measurements and is presumed to be due to some fast electron transfer through oxygen atoms.

### 4.3.3. Charge ordering.

It is therefore apparent that below the crystallographic phase transition at 315 K the charges on the Fe cations become ordered, the charge distribution below the transition is $(Fe(1)_{0.5}{}^{2+}Fe(1)_{0.5}{}^{3+})(Fe(2)_{0.5}{}^{2+}Fe(2)_{0.5}{}^{3+})OBO_3$.

In the high temperature Pnma structure the Fe cations are on mirror planes as shown schematically in part (a) of Figure 4.24. Below the phase transition the cation charges become ordered as shown in the simple alternating scheme in part (b) of Figure 4.24, this will destroy the mirror symmetry and repulsions cause the ribbons of octahedra to tilt and hence the monoclinic β

angle increases slightly below the phase transition. The a-axis periodicity should increase by a

*Figure 4.24.*

*Part a, The arrangement of sites within a ribbon of 4 $Fe^{2.5+}$ sites (grey circles) in orthorhombic $Fe_2OBO_3$ above the charge-ordering transition.*

*Part b, A possible ordering scheme of $Fe^{2+}$ (white circles) and $Fe^{3+}$ (black circles) below the charge-ordering transition showing an anti-phase boundary (dotted line) that preserves the sense of the monoclinic distortion.*

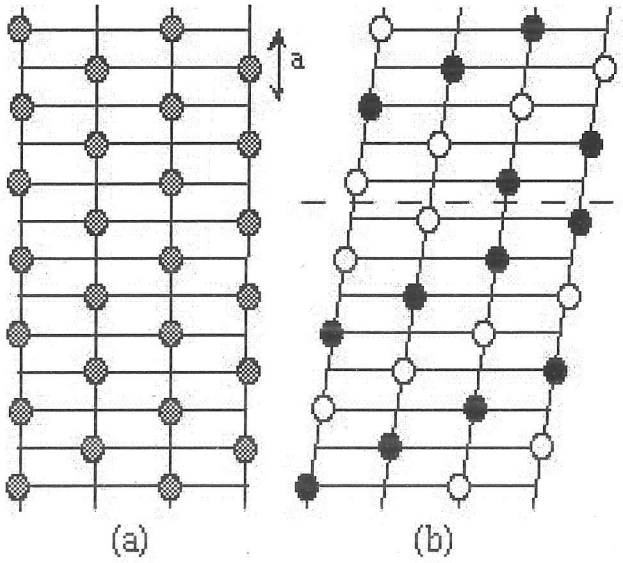


factor of 2 (or some larger integer) but this is not observed in the X-ray and neutron powder diffraction results. This suggests that the charge-ordered domains in the monoclinic structure are small (~10-100 Å) so that any superstructure reflections are too broad and weak to be observed above the background in the diffraction patterns. This may reflect a large defect concentration such as the anti-phase boundary shown in part (b) of Figure 4.24 which preserves the direction of the monoclinic distortion, but do not propagate the coherent multiplying of the lattice periodicity. Therefore, the observed long-range monoclinic lattice distortion can arise from charge ordering within much smaller domains known as **Wigner nanocrystals** (Rozenberg et al, 1996). The large

defect concentration could also explain the extra Fe components observed in the in the Mössbauer spectra determined in the ferromagnetic region.

Wigner nanocrystals may also be present in $Fe_3O_4$ below the Verwey Transition, the low temperature crystal structure of $Fe_3O_4$ (Iizumi et al, 1982; also see Chapter 3) also shows an average $Fe^{2.5+}$ charge on the octahedral sites so the long-race structural distortion below the Verwey Transition may also be due to nanoscale charge ordering.

$Fe_3O_4$ and $Fe_2OBO_3$ both undergo a magnetic transition at which ferromagnetic ordering occurs within the octahedral ($Fe^{2+}Fe^{3+}$) chains, and a structural transition associated with a fall in electronic conductivity. The differences between the transitions in the two materials stem from their different structures and the replacement of paramagnetic $Fe^{3+}$ by diamagnetic $B^{3+}$. In $Fe_3O_4$, strong, non-frustrated magnetic superexchange interactions between the octahedral ($Fe^{2+}_{0.5}Fe^{3+}_{0.5}$) and tetrahedral $Fe^{3+}$ spins result in a high magnetic ordering temperature ($T_c$ = 858 K) and ferromagnetic alignment of the octahedral $Fe^{2+}$ and $Fe^{3+}$ moments.

This leads to a facile transfer from $Fe^{2+}$ to $Fe^{3+}$ of the minority spin electron with its associated lattice distortion (a polaron) via a double exchange mechanism, which is also responsible for the conducting ferromagnetic state of mixed valent manganese oxide perovskites. The latter ferromagnetic conductors display giant magnetoresistances, and the same effect has recently been observed in polycrystalline $Fe_3O_4$ due to intergranular transport of the spin-polarised electrons. Long range magnetic order in $Fe_3O_4$ enables the conducting state to persist to a relatively low temperature until the Verwey transition occurs at 120 K. Weaker superexchange pathways through the borate group and magnetic frustration in $Fe_2OBO_3$ lead to a much lower ordering temperature ($T_c$ = 155 K) so that polaron hopping in the high temperature paramagnetic region has an appreciable activation energy (0.35 eV) as neighbouring $Fe^{2+}$ and $Fe^{3+}$ moments are not

defect concentration could also explain the extra Fe components observed in the in the Mössbauer spectra determined in the ferromagnetic region.

Wigner nanocrystals may also be present in $Fe_3O_4$ below the Verwey Transition, the low temperature crystal structure of $Fe_3O_4$ (Iizumi et al, 1982; also see Chapter 3) also shows an average $Fe^{2.5+}$ charge on the octahedral sites so the long-race structural distortion below the Verwey Transition may also be due to nanoscale charge ordering.

$Fe_3O_4$ and $Fe_2OBO_3$ both undergo a magnetic transition at which ferromagnetic ordering occurs within the octahedral ($Fe^{2+}Fe^{3+}$) chains, and a structural transition associated with a fall in electronic conductivity. The differences between the transitions in the two materials stem from their different structures and the replacement of paramagnetic $Fe^{3+}$ by diamagnetic $B^{3+}$. In $Fe_3O_4$, strong, non-frustrated magnetic superexchange interactions between the octahedral ($Fe^{2+}_{0.5}Fe^{3+}_{0.5}$) and tetrahedral $Fe^{3+}$ spins result in a high magnetic ordering temperature ($T_c$ = 858 K) and ferromagnetic alignment of the octahedral $Fe^{2+}$ and $Fe^{3+}$ moments.

This leads to a facile transfer from $Fe^{2+}$ to $Fe^{3+}$ of the minority spin electron with its associated lattice distortion (a polaron) via a double exchange mechanism, which is also responsible for the conducting ferromagnetic state of mixed valent manganese oxide perovskites. The latter ferromagnetic conductors display giant magnetoresistances, and the same effect has recently been observed in polycrystalline $Fe_3O_4$ due to intergranular transport of the spin-polarised electrons. Long range magnetic order in $Fe_3O_4$ enables the conducting state to persist to a relatively low temperature until the Verwey transition occurs at 120 K. Weaker superexchange pathways through the borate group and magnetic frustration in $Fe_2OBO_3$ lead to a much lower ordering temperature ($T_c$ = 155 K) so that polaron hopping in the high temperature paramagnetic region has an appreciable activation energy (0.35 eV) as neighbouring $Fe^{2+}$ and $Fe^{3+}$ moments are not

aligned. This results in polaron localisation at a much higher temperature (315 K) and with a much broader transition than in $Fe_3O_4$, which is above the Curie transition so that a conducting ferromagnetic state is not found in $Fe_2OBO_3$.

However, an exact equipartition of divalent and trivalent ions over the two cation sites is not found in other warwickite type materials. Partial cation segregation is observed in many mixed metal warwickites such as $FeMnOBO_3$ and $MgScOBO_3$. Nor is charge equipartition found in other mixed valent iron oxoborates, as the structurally related phase $Fe^{2+}{}_2Fe^{3+}O_2BO_3$ (Swinnea et al, 1983) shows an unequal charge distribution over four octahedral Fe sites.

In the isostructural Mn analogue, $Mn_2OBO_3$, $Mn^{2+}$ and $Mn^{3+}$ ions each occupy only one site and therefore the charge distribution is $Mn(1)^{3+}Mn(2)^{2+}OBO_3$, there is a Jahn-Teller distortion at the Mn(1) site and the mean Mn(1)-O and Mn(2)-O distances are 2.064 and 2.178 Å. Clearly the charge ordering is not like that in $Fe_2OBO_3$.

## 4.4. Conclusions.

Two phase transitions have been found for $Fe_2OBO_3$. Magnetisation and susceptibility measurements indicate that a magnetic phase transition takes place at $T_c$ = 155 K and this is confirms a previous neutron powder diffraction study. At this transition $Fe_2OBO_3$ changes from L-type ferrimagnetic to paramagnetic as the temperature increases.

However, Mössbauer spectroscopy indicates that this transition takes place with a $T_c$ between 185-190 K. This discrepancy may be due to the presence of defects and frustration in the crystal structure which can only be observed as the Mössbauer technique can observe short range order. However, it is clear that a more detailed Mössbauer study needs to be done in this temperature

region to fully explain this difference in transition temperature.

A crystallographic phase transition in which a low temperature $P2_1/c$ warwickite structure changes to a Pnma structure at 315 K. This structure has been determined from high resolution synchrotron X-ray powder diffraction and has been confirmed by Mössbauer spectroscopy and resistivity measurements. Mössbauer spectroscopy indicates the presence of four ordered Fe cation sites below the transition temperature and two disordered sites above this temperature. It is thought that this charge ordering is not observed in the refined crystal structure due to the presence of Wigner nanocrystals with such a small size that superlattice reflections due to this ordering are not observable in the diffraction work.

The charge-ordering of the Fe cations in this transition is thought to be analogous to the Verwey Transition in $Fe_3O_4$.

## Chapter 4 - References.


J.P.Attfield, J.F.Clarke and D.A.Perkins, Physica B., (1992), **180,** 581-584.

P.D.Battle, A.K.Cheetham, G.J.Long, and G.Longworth, Inorg. Chem., (1982), **21**, 4223-4228.

E.F.Bertaut, Acta Cryst., (1950), **3,** 473.

K.Bluhm, H.K.Muller-Buschbaum, Z.Anorg. Allg. Chem., (1990), **585**, 87.

K.Bluhm and S.Busche, Z.Naturforsch., Teil B, (1995), **50**, 1146.

K.Bluhm and A.Utzolino, Z.Naturforsch., Teil B, (1995), **50**, 1450.

K.Bluhm and A.Utzolino, Z.Naturforsch., Teil B, (1995), **50**, 1653.

M.J.Buerger and V.Venkatakrishnan, Mater. Res. Bull., (1972), **7,** 1201.

J.K.Cockcroft, (1995) BONDLA v3.03. Birkbeck College London.

J.H.Fang, R.E.Newnham, Min. Mag. & J. Min. Soc., (1965), **35**, 196.

A.C.Larson and R.B. von Dreele, LANSCE, MS-H805, Los Alamos National Laboratory.

G.J.Long, G.Longworth, P.D.Battle, A.K.Cheetham, R.J.Thundathil and D.Beveridge, Inorg. Chem., (1979), **18**, 624.

M.Iizumi, T.F.Koetzle, G.Shirane, S.Chikazumi, M.Matsui and S.Todo, Acta Cryst., (1982), **B38,** 2121-2133.

A.D.Murray, J.K.Cockcroft and A.N.Fitch, (1990) PDPL. Powder Diffraction Program Library, University College London.

L.Néel, Ann. Phys. (Paris), (1948), **12(3),** 137.

R.Norrestam, Z.Krist., (1989), **189,** 1.

R.Norrestam, M.Kritikos and A.Sjoerdin, J.Solid State Chem., (1995), **114**, 311.

H.M.Rietveld, J. Appl. Cryst., (1969), **2** 65-71.

G.K.Rozenberg, G.R.Hearne, M.P.Pasternak, P.A.Metcalf and J.M.Honig. Phys. Rev., (1996), **B53,** 6482-7.

P.A.Stedelman, Ultramicroscopy, (1987), **21**, 131.

J.S.Swinnea and H.Steinfink, American Mineralogist, (1983), **68**, 827-832.

Y.Takeuchi, T.Watanabe and T.Ito, Acta Cryst., (1950), **3**, 98-107.

J. Teillet and F. Varret, unpublished program.

E.J.W.Verwey, Nature, (1939), **144,** 327-8.

# Chapter 5. Resonant Scattering Test Experiment on CsI at the ESRF.

## 5.1 Introduction.

Resonant scattering diffraction experiments require synchrotron X-ray wavelengths close to the X-ray absorption edges of interest. The atomic scattering factor for X-rays is $\mathbf{f = f^n + f' + if''}$, where $\mathbf{f^n}$ is due to non-resonant (Thomson) scattering, the $\mathbf{f'}$ and $\mathbf{f''}$ terms are due to resonant scattering (see section 1.5), the intensity of X-ray scattering is proportional to the square of **f**. The closer the X-ray wavelength is to the absorption edge the greater the magnitude of these resonant terms and consequently the greater the contribution of resonant scattering to the experiment. Clearly if a high energy resolution X-ray source was to be used for such an experiment this would be advantageous to maximise the resonant contribution.

The high resolution powder diffractometer on beamline BM16 at the ESRF (see section 2.4.1) would seem to be an ideal X-ray source for a resonant scattering experiment due to the high X-ray flux and energy resolution available on this beamline. Therefore a test experiment has been done with this instrument to see if large resonant scattering effects can be observed using the high X-ray energies available at the ESRF.

## 5.2. Caesium Iodide.

Caesium Iodide (CsI) has one of the simplest of all known crystal structures. This is a body centred cubic CsCl-type structure, space group Pm3m, a = 4.5667 Å (Rymer et al, 1951), consisting of two large polarisable and **isoelectronic** ions $Cs^+$ and $I^-$. The powder diffraction

pattern for CsI consists of alternating Bragg reflections with Miller indices (**hkl**) for which the sum of (**h + k + l**) are odd or even. The intensities of Bragg reflections with an odd sum of (**h + k + l**) (hereafter referred to as **odd** reflections) consist of the square of the difference in scattering between $Cs^+$ and $I^-$, whereas intensities of Bragg reflections with an even sum of (**h + k + l**) (hereafter referred to as **even** reflections) consist of the square of the sum of scattering between $Cs^+$ and $I^-$. Therefore alternate Bragg reflections in an ordinary non-resonant laboratory diffraction pattern for CsI would appear to be absent as scattering from isoelectronic ions $Cs^+$ and $I^-$ would cancel out, only the even reflections would be visible.

However, in the case of a resonant scattering X-ray powder diffraction pattern for CsI the contribution of the resonant component to the X-ray scattering means that the odd reflections should be visible. Figure 5.1 shows how the non-resonant $\mathbf{f^n}$ and resonant $\mathbf{f'}$ scattering terms for Cs and I vary with sin ($\theta/\lambda$). The $\mathbf{f'}$ values are calculated using the FPRIME (Cromer, 1983) program in GSAS (Larson and von Dreele), these values were calculated with $\lambda$ = 0.3453 Å for Cs and with $\lambda$ = 0.3741 Å for I as these values of $\lambda$ are close to the Cs and I K absorption edges. The $\mathbf{f'}$ term is always negative close to the absorption edges, the sign of this term has been reversed so that the non-resonant and resonant terms can be viewed on the same axis scale. At small values of sin ($\theta/\lambda$) Figure 5.1 shows that the resonant contribution to the X-ray scattering is much weaker than the non-resonant contribution and therefore these odd reflections are much weaker than the neighbouring even ones. However, as sin ($\theta/\lambda$) increases the relative contribution due to resonant scattering increases so the relative intensity of the odd reflections increases compared to the neighbouring even reflections. If it is possible to collect powder diffraction data with sin ($\theta/\lambda$) ~ 3 it should then be possible to observe neighbouring odd and even reflections with similar intensities.

*Figure 5.1. Variation of non-resonant scattering f and resonant scattering -f′ for Cs and I with sin (θ/λ) when λ is close to the Cs and I K absorption edges.*

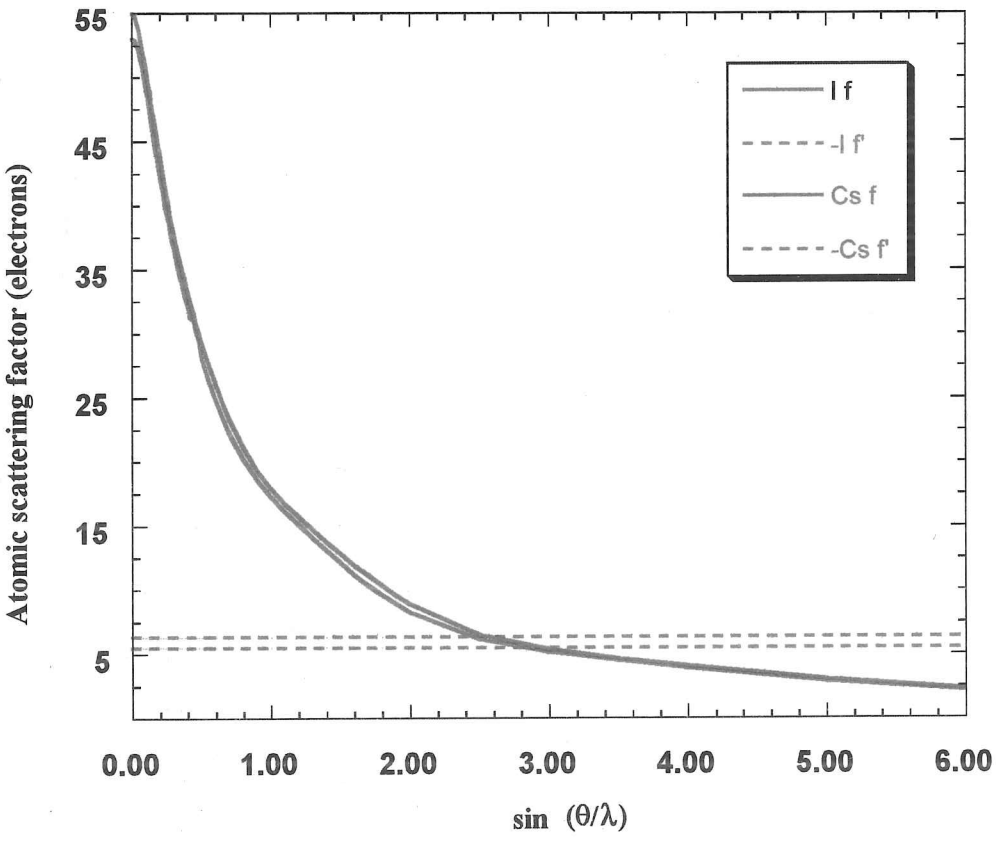


The presence of these odd reflections in the CsI powder diffraction pattern makes CsI an ideal sample for a resonant scattering test experiment as it should be possible to observe the effects of resonant scattering without any overlap from non-resonant scattering.

**5.3. Sample preparation.**

CsI purchased from the Aldrich chemical company was used for this experiment. The material

was heated in a furnace overnight under flowing Ar at 773 K to make the sample more crystalline. Laboratory X-ray powder diffraction using the Philips diffractometer (see section 2.1.1) showed the sample to be well crystalline and single-phase. The cubic lattice parameter was refined as 4.5702(7) Å. Figure 5.2 shows this laboratory powder diffraction pattern.

*Figure 5.2. Laboratory X-ray powder diffraction pattern for CsI, note that only Bragg reflections for which the sum of (h + k + l) is even are observed.*

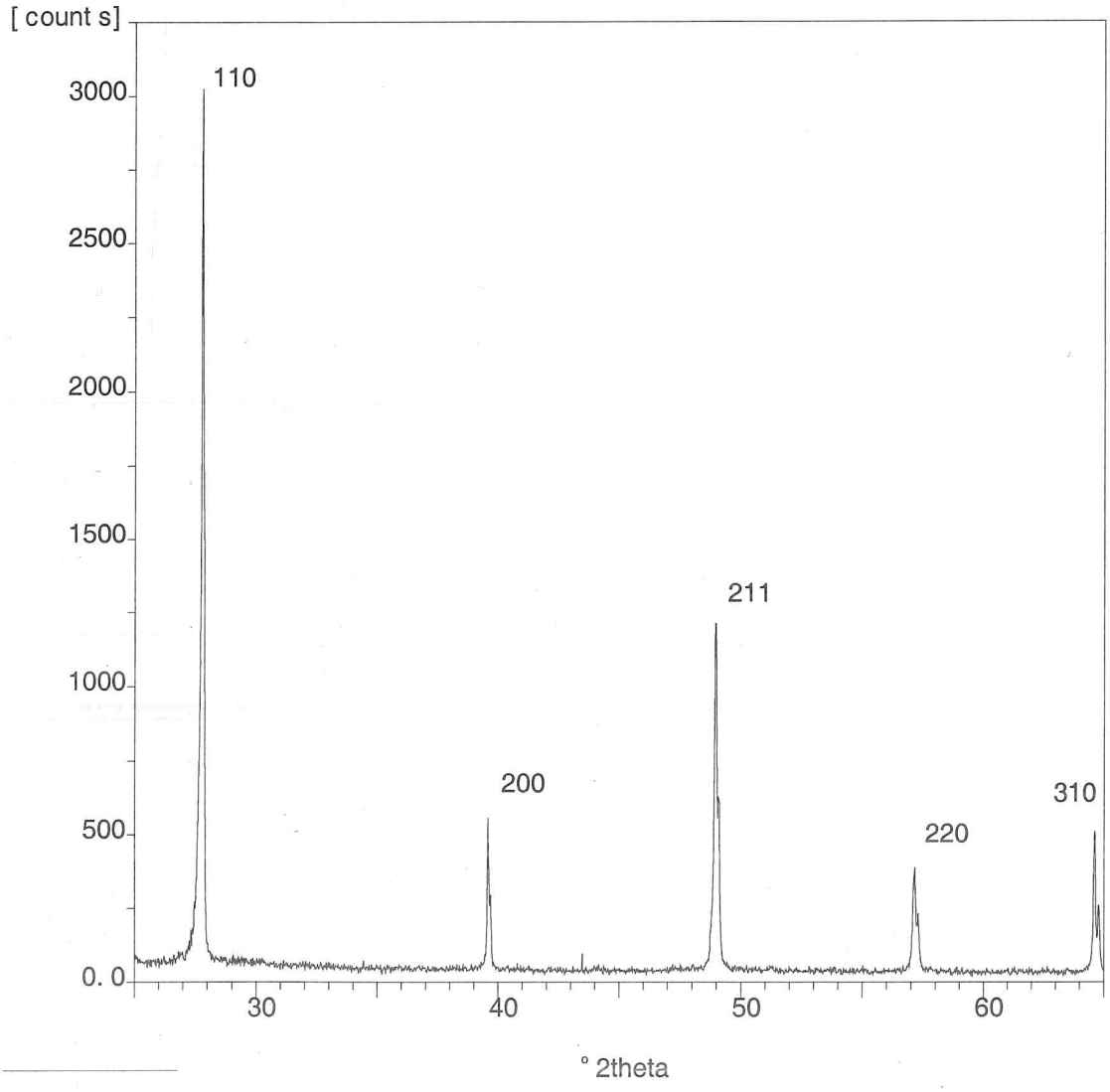

## 5.4. Synchrotron X-ray powder diffraction.

Cs and I both have high energy, short wavelength X-ray K absorption edges, the Cs edge is at $\lambda$ = 0.3453 Å and the I edge is at $\lambda$ = 0.3741 Å. These X-ray wavelengths are accessible using the high resolution powder diffractometer on beamline BM16 at the European Synchrotron Radiation Facility.

### 5.4.1. ESRF experiment at room temperature.

The CsI sample was loaded into a 0.5mm diameter borosilicate glass capillary and was mounted on the high resolution powder diffractometer on ESRF beamline BM16. Full powder diffraction scans were measured at room temperature between 4 and 140° 2θ, these scans were measured with SR wavelengths set at the Cs K-edge (0.3453 Å), I K-edge (0.3741 Å) and off the absorption edges at 0.3900 Å.

However, it was not possible to see any diffraction peaks in these patterns above 40° 2θ. It was thought that the presence of two large ions in this structure meant that no Bragg reflections with a large sin (θ/λ) were observable due to large temperature factors.

A multiwavelength Rietveld (Rietveld, 1969) refinement was done using GSAS with powder diffraction scans measured at the Cs and I K-edges and away from the edges, no data was used with 2θ > 44° as no Bragg reflections could be observed and no data was used with 2θ < 10° due to the problems of fitting the asymmetric low-angle reflections in GSAS. Ionic X-ray scattering factors were used in the refinement.

Table 5.1 shows some parameters for this refinement, the $f'$ parameter for Cs was refined for the

Cs K edge pattern and the $f'$ parameter for I was also refined for the I K-edge pattern, all other $f'$ and $f''$ parameters were fixed. Figures 5.3.1-6 show the Rietveld difference plots for the Cs K-edge, I K-edge and off-edge refinements.

*Table 5.1. Refined parameters from CsI room temperature experiment, $f'$ and $f''$ are given in units of electrons/atom.*

| Element | x | y | z | $U_{iso}$ (Å$^2$) | $f'/f''$ (Cs K-edge) | $f'/f''$ (I K-edge) | $f'/f''$ (off-edge) |
|---|---|---|---|---|---|---|---|
| $Cs^+$ | 0.0 | 0.0 | 0.0 | 0.0283(3) | -6.2(2)/0.6 | -2.4/0.7 | -2.1/0.7 |
| $I^-$ | 0.5 | 0.5 | 0.5 | 0.0237(2) | -1.9/3.1 | -9.0(1)/0.6 | -2.9/0.6 |

| Histogram | wavelength (Å) | $R_{wp}$ | $R_p$ |
|---|---|---|---|
| 1 (Cs K-edge) | 0.345300 | .0898 | .0642 |
| 2 (I K-edge) | 0.374105(3) | .1439 | .1079 |
| 3 (off-edge) | 0.390037(2) | .0900 | .0683 |
| powder total | | .0965 | .0699 |

Lattice parameters. a = 4.56965(2) Å V = 95.422(1) Å$^3$. $\chi^2$ = 3.492 for 27 refined parameters.

*Figure 5.3.1. CsI room temperature Rietveld difference plot for Cs K-edge pattern, 10-25° 2θ.*

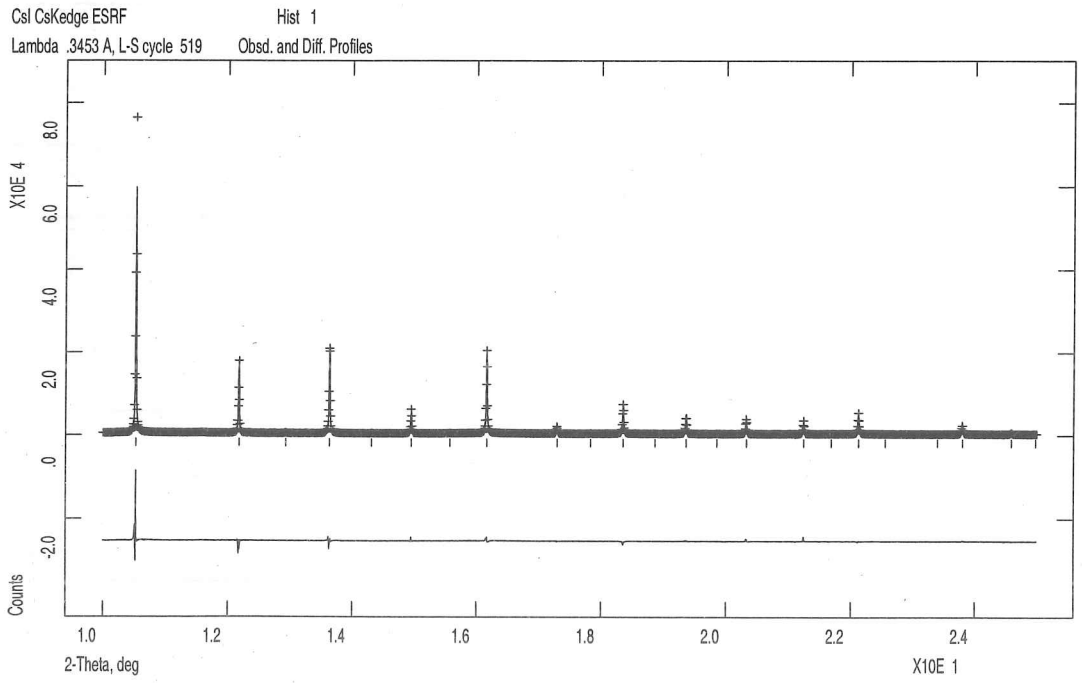

*Figure 5.3.2. CsI room temperature Rietveld difference plot for Cs K-edge pattern, 25-44° 2θ.*

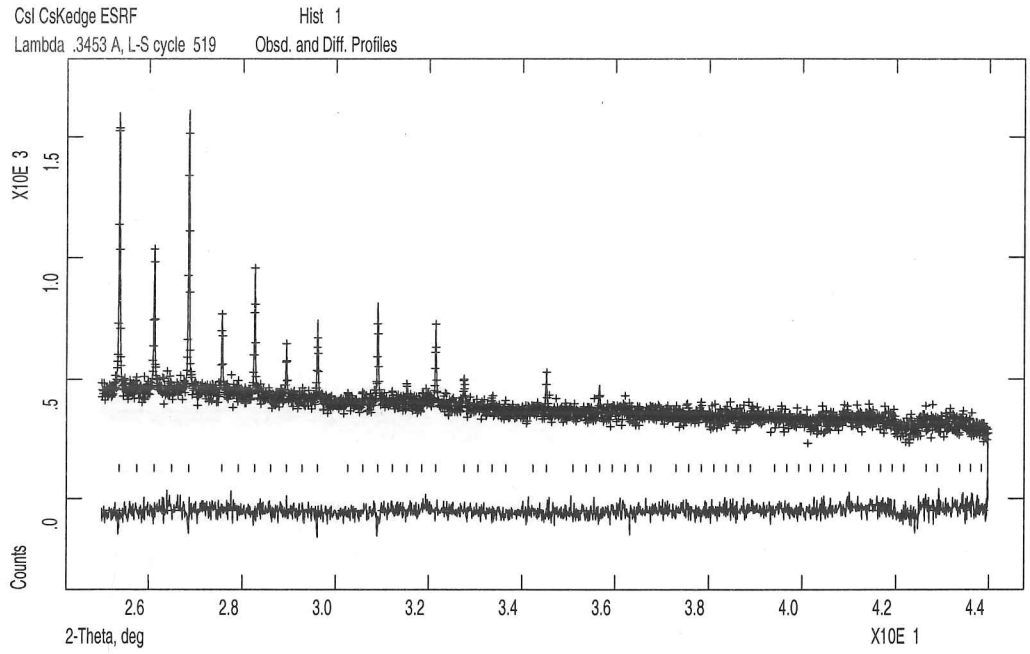


*Figure 5.3.3. CsI room temperature Rietveld difference plot for I K-edge pattern, 10-25° 2θ.*

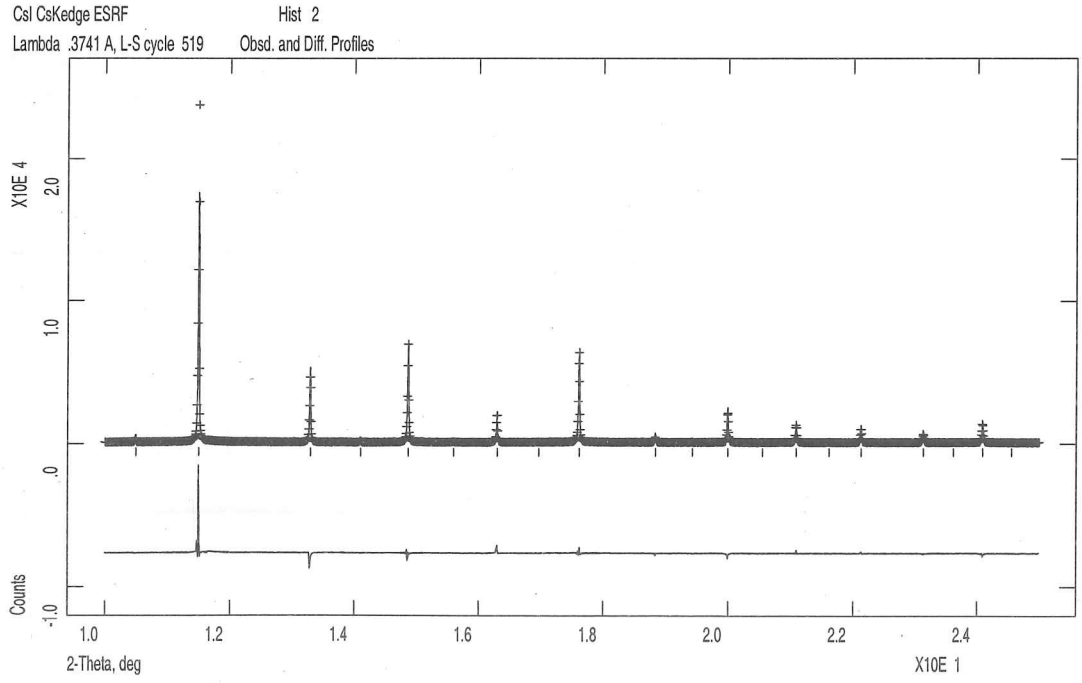

*Figure 5.3.4. CsI room temperature Rietveld difference plot for I K-edge pattern, 25-44° 2θ.*

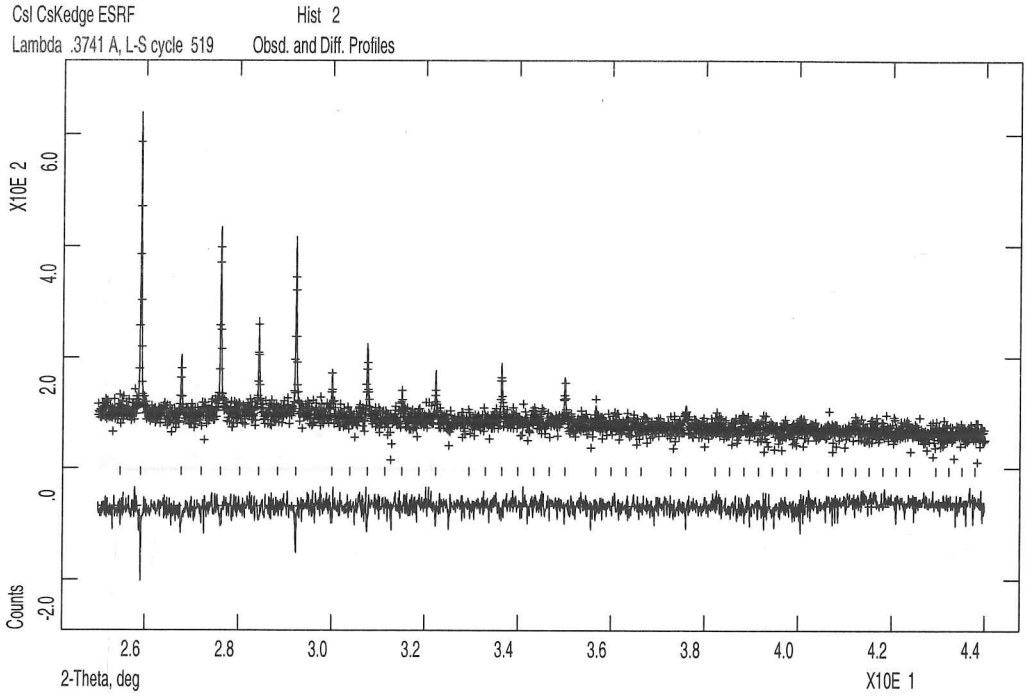


*Figure 5.3.5. CsI room temperature Rietveld difference plot for off-edge pattern, 10-25° 2θ.*

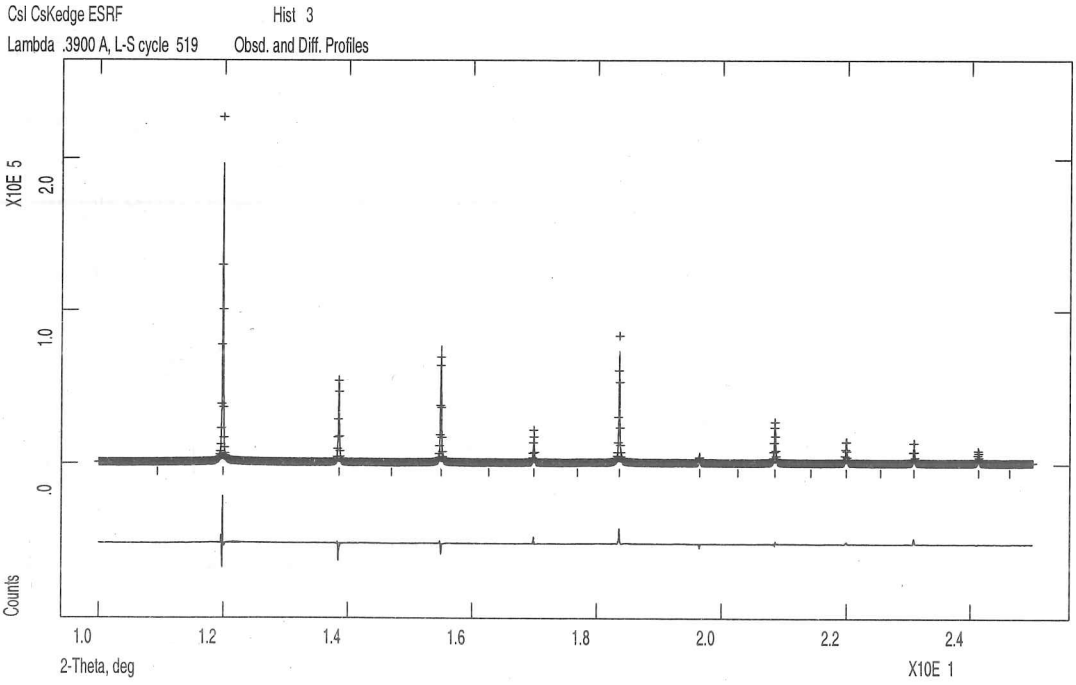

*Figure 5.3.6. CsI room temperature Rietveld difference plot for off-edge pattern, 25-44° 2θ.*

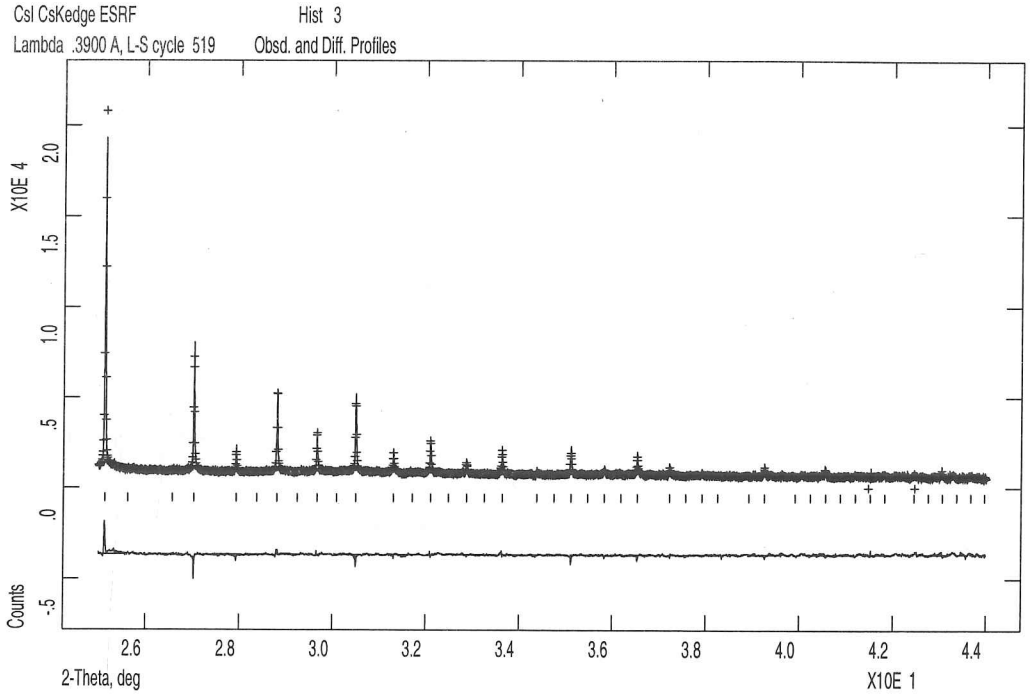


### 5.4.2. ESRF experiment at 4 K.

The experiment was repeated again using BM16, this time the powder diffraction data was collected in a liquid helium cooled cryostat to reduce the temperature factor and consequently increase the sin (θ/λ) range of observable peaks.

A short scan was done at room temperature with the SR wavelength set to the I K-edge. As the room temperature lattice parameter for this sample was known this SR wavelength was refined as 0.373963(1) Å from this data.

The sample was then cooled to 4 K and powder data was collected at the I K-edge and off-edge (0.3900 Å). Due to the reduction in temperature factors it was possible to collect powder diffraction data out to 86° 2θ at the I K-edge and to 90° 2θ off-edge. Due to the large number of

data points collected the both the I K-edge and off-edge patterns had to be split into 3 separate histograms for GSAS data analysis.

As before multiwavelength Rietveld refinement was done using GSAS with powder diffraction scans measured at the I K-edge and away from this edge, no data was used with $2\theta < 10^{\circ}$ due to the problems of fitting the asymmetric low-angle reflections in GSAS. Due to problems with X-ray scatter from the wall of the cryostat vessel above $43^{\circ}$ $2\theta$ in the off-edge powder diffraction pattern all data in this region was excluded as the background was not even. Ionic X-ray scattering factors were used in the refinement. Table 5.2 shows some parameters for this refinement, the $\mathbf{f}'$ parameter for I was refined for the I K-edge pattern, all other $\mathbf{f}'$ and $\mathbf{f}''$ parameters were fixed. It was not possible to refine the Cs and I temperature factors to positive values. It was thought that these parameters were negative as the GSAS instrument parameter file was not set up properly for both a pre and post-sample monochromator and as the temperature factors should be very small due to the low temperature this caused these factors to go negative. Figures 5.4.1-7 show the Rietveld difference plots for the I K-edge and off-edge refinements.

*Table 5.2. Refined parameters from CsI 4K experiment, $f'$ and $f''$ are given in units of electrons/atom.*

| Element | x | y | z | $U_{iso}$ (Å$^2$) | f'/f'' (IK-edge) | f'/f'' (off-edge) |
|---|---|---|---|---|---|---|
| $Cs^+$ | 0.0 | 0.0 | 0.0 | -0.0006(1) | -2.4/0.7 | -2.1/0.7 |
| $I^-$ | 0.5 | 0.5 | 0.5 | -0.0013(2) | -6.2(2)/3.5 | -2.9/0.6 |

| Histogram | wavelength (Å) | $R_{wp}$ | $R_p$ |
|---|---|---|---|
| 1 (I K-edge) | 0.37367 | .1603 | .1378 |
| 2 (I K-edge) | 0.37367 | .1867 | .1538 |
| 3 (I K-edge) | 0.37367 | .1853 | .1455 |
| 4 (off-edge) | 0.390029(2) | .1933 | .1507 |
| powder total | | .1757 | .1499 |

Lattice parameters. a = 4.50819(1) Å V = 91.624(1) Å$^3$. $\chi^2$ = 4.234 for 23 refined parameters.

*Figure 5.4.1. CsI 4K Rietveld difference plot for I K-edge pattern, 10-25° 2θ.*

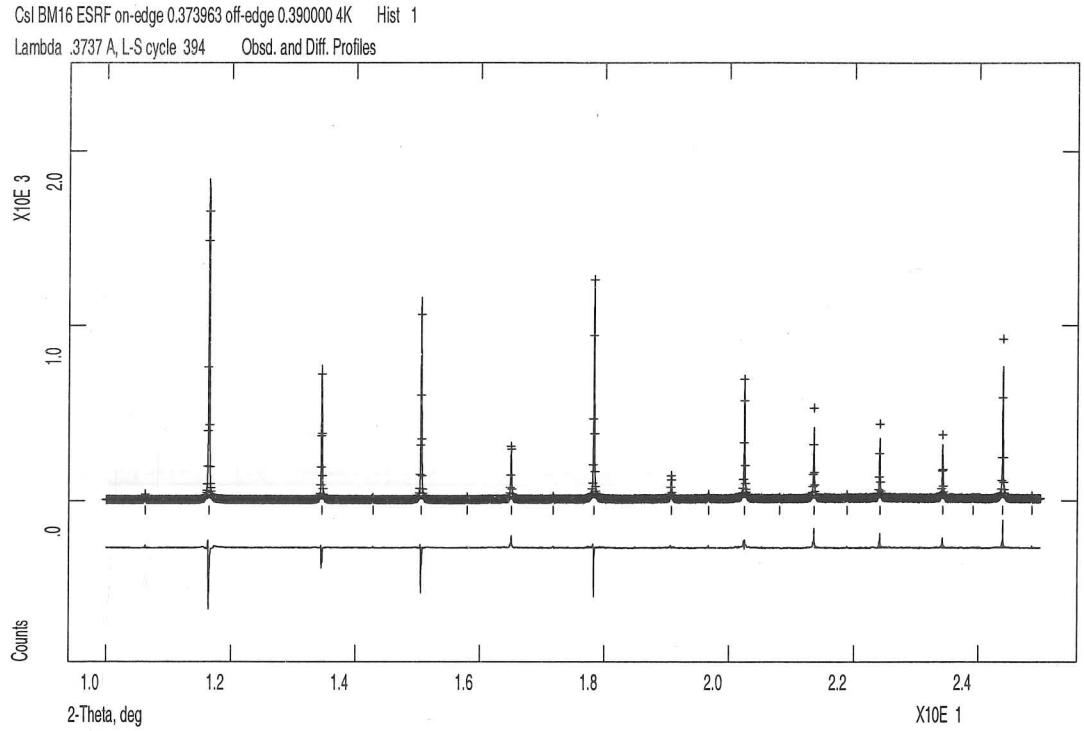


*Figure 5.4.2. CsI 4K Rietveld difference plot for I K-edge pattern, 25-43° 2θ.*

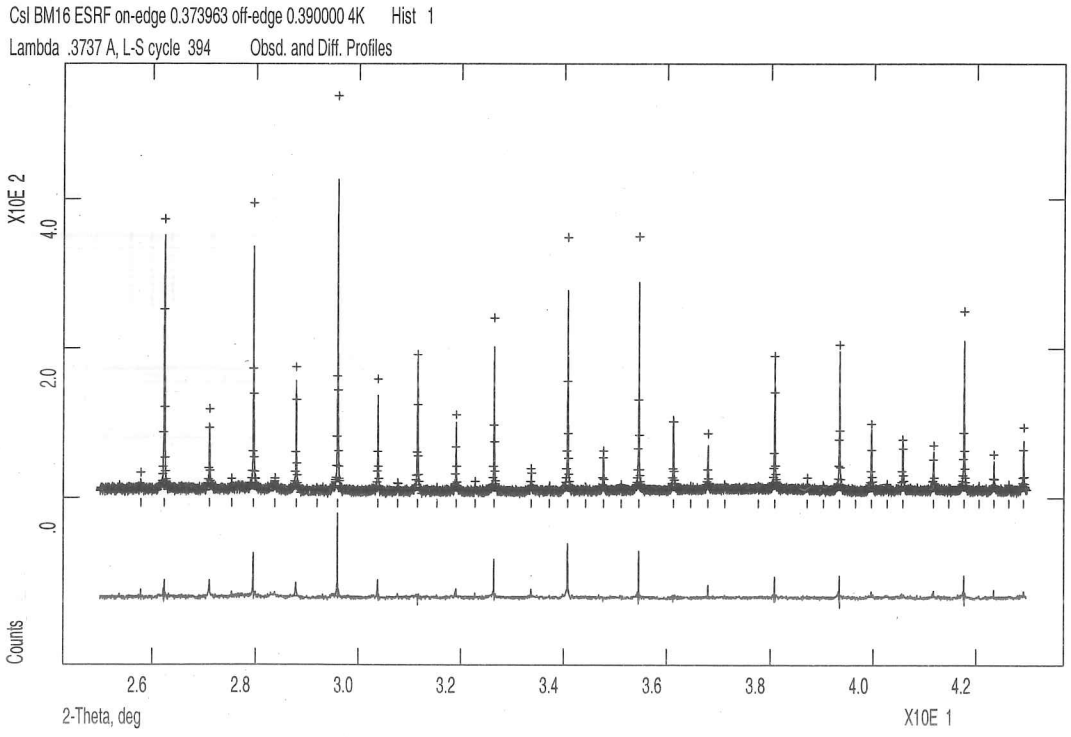

*Figure 5.4.3. CsI 4K Rietveld difference plot for I K-edge pattern, 43-63° 2θ.*

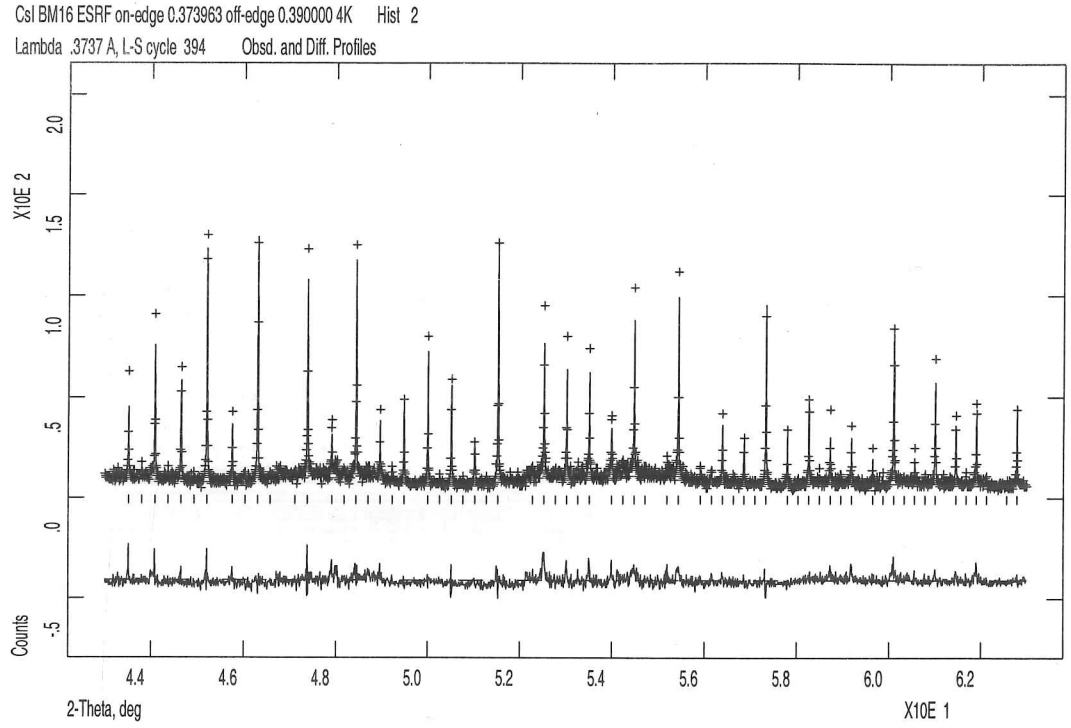


*Figure 5.4.4. CsI 4K Rietveld difference plot for I K-edge pattern, 63-82° 2θ.*

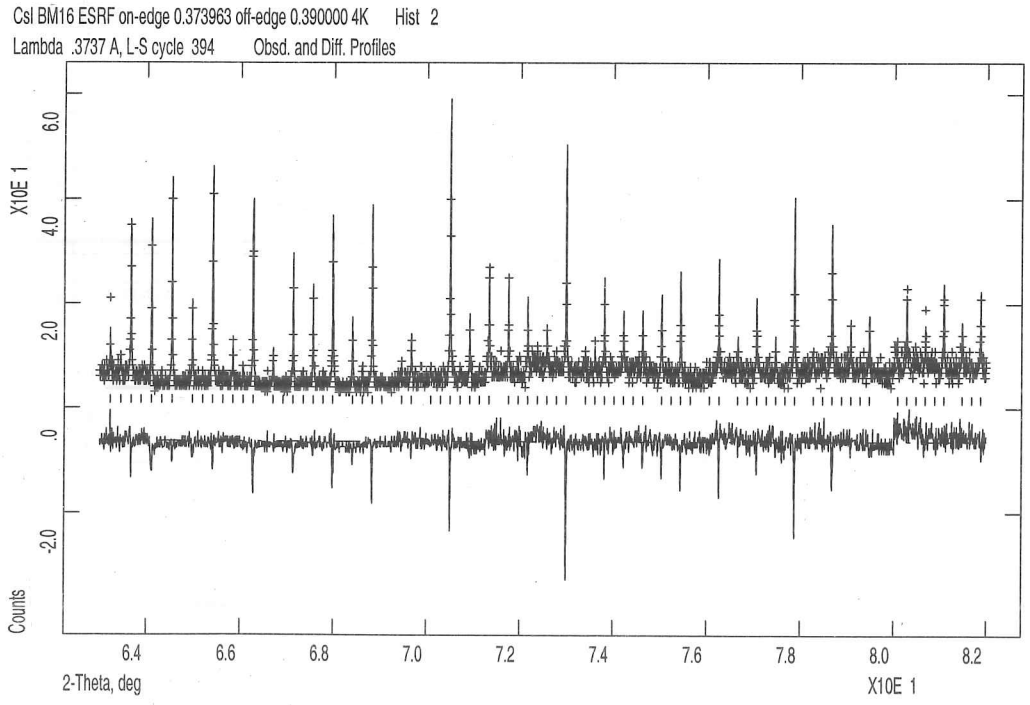

*Figure 5.4.5. CsI 4K Rietveld difference plot for I K-edge pattern, 82-86° 2θ.*

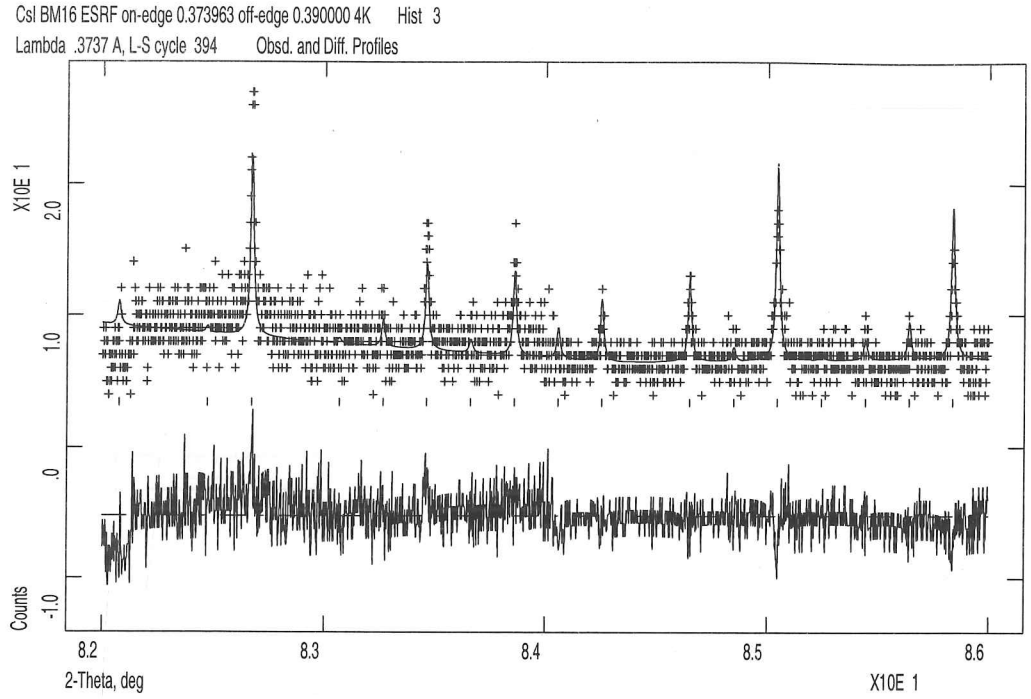


*Figure 5.4.6. CsI 4K Rietveld difference plot for off-edge pattern, 10-25° 2θ.*

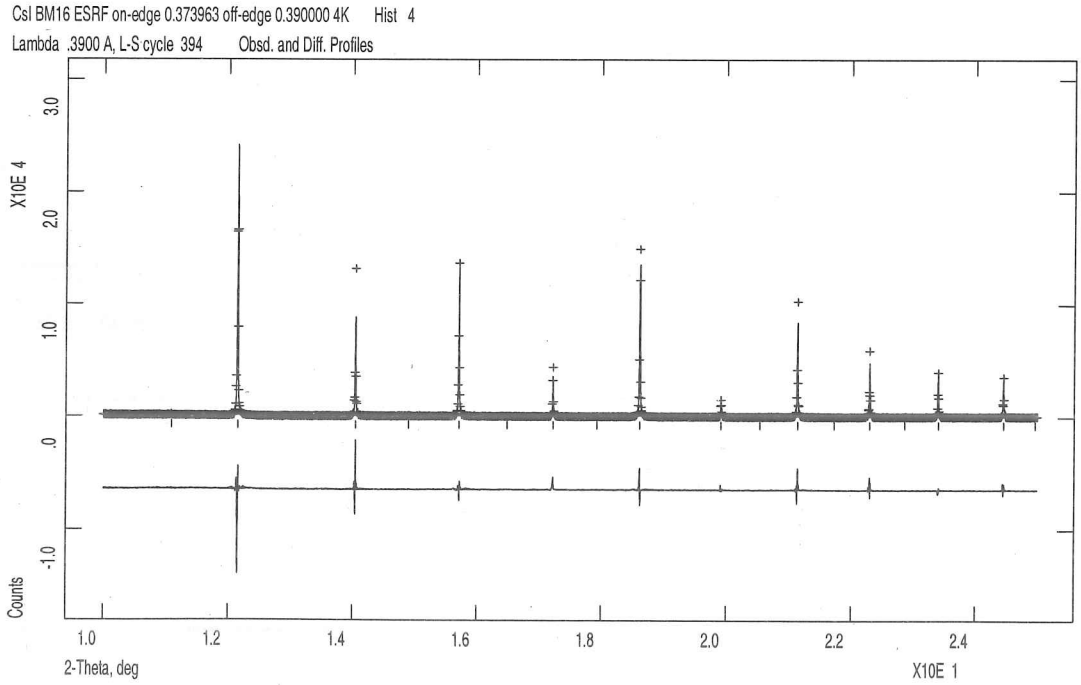

*Figure 5.4.7. CsI 4K Rietveld difference plot for off-edge pattern, 25-43° 2θ.*

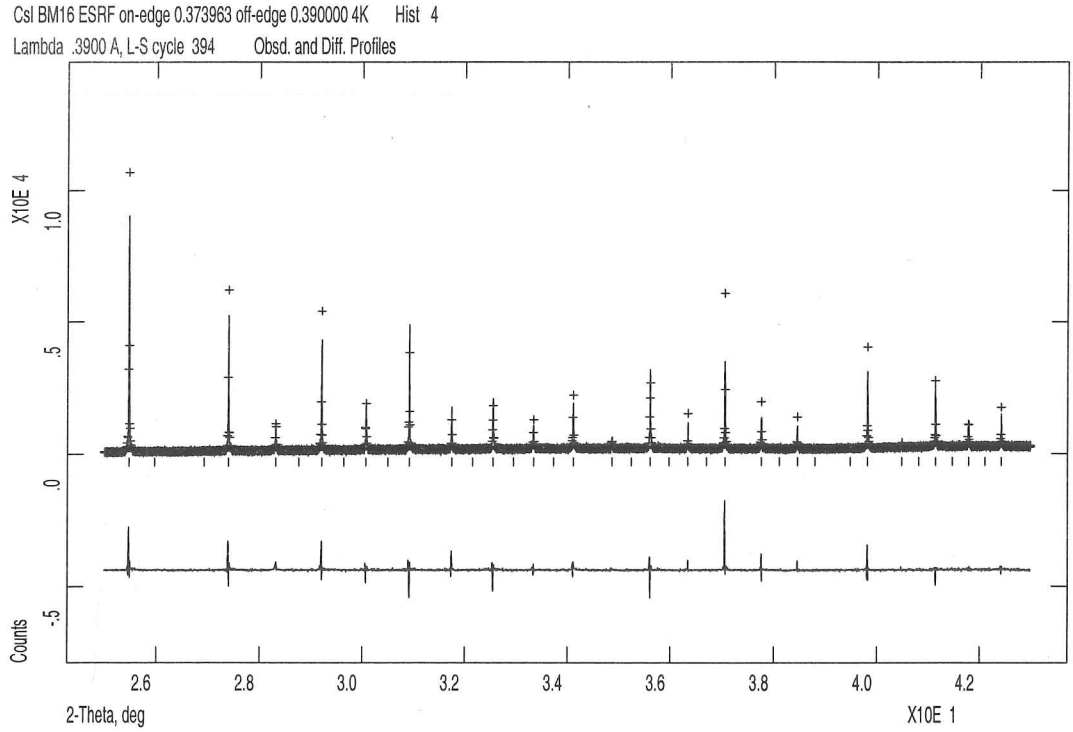


## 5.4. Discussion.

This test experiment was a success in that $\mathbf{f}'$ parameters have been successfully refined from the powder diffraction data collected on BM16. The Cs and I $\mathbf{f}'$ parameters from the room temperature scans have been refined as -6.2(2) electrons/atom (Cs) and -9.0(1) electrons/atom (I). The refined I $\mathbf{f}'$ parameter from the 4K scans is -6.2(2) electrons/atom. All of these parameters are large enough so that significant resonant scattering should be observed in this data and this is what is seen.

Figure 5.5 shows the 100 Bragg reflection from the room temperature powder diffraction collected at the Cs K-edge. This first odd reflection is very weak (peak intensity of 800 counts) compared to the 110, the first even reflection (peak intensity of 146000 counts!) but is clearly

visible due to the high flux and resolution of the BM16 powder diffractometer.

*Figure 5.5. Room temperature 100 (odd) Bragg reflection for CsI collected at the Cs K-edge.*

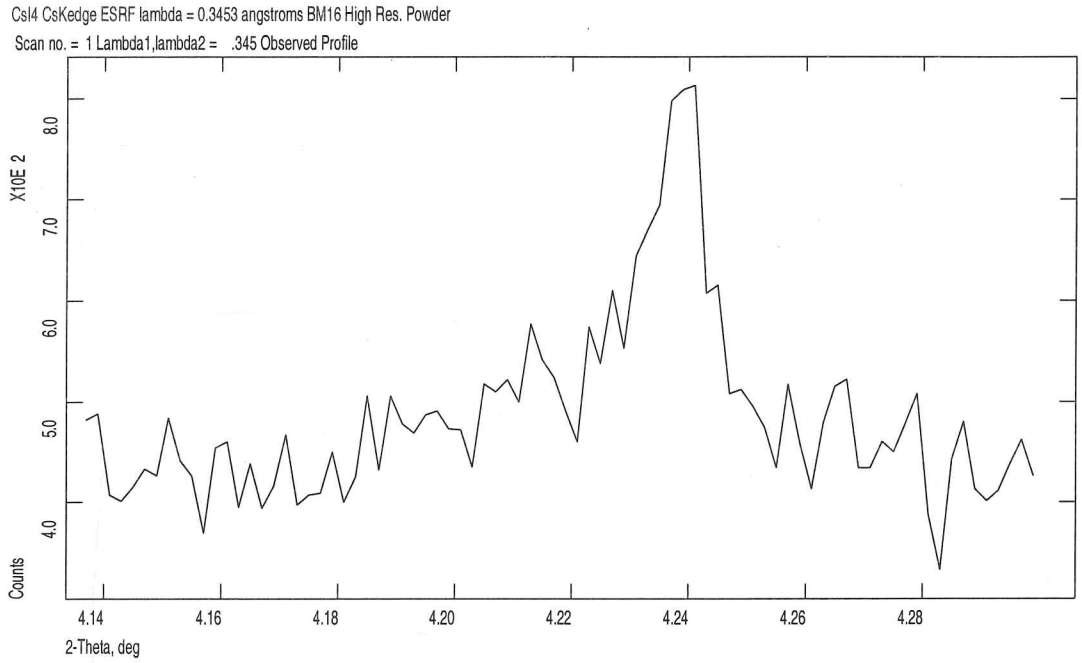


However, with the room temperature data it was not possible to collect any powder diffraction data at a high enough value of sin ($\theta/\lambda$) so that the intensities of any neighbouring odd and even reflections were of the same order of magnitude. Powder diffraction peaks were only visible out to sin ($\theta/\lambda$) ~ 1. Figure 5.1 shows that at this value the resonant contribution to diffraction is still much weaker than the non-resonant contribution.

The data collected at 4K did show powder diffraction peaks, in spite of the problems due to the cryostat, out to sin ($\theta/\lambda$) ~ 1.9. Figure 5.1 shows that at this value that although resonant contribution to diffraction is weaker than the non-resonant contribution there is now a **significant** resonant contribution to the scattering.

Figure 5.6 shows three neighbouring peaks in the 4K I K-edge powder diffraction pattern for CsI. The peak at 73.4° 2θ is due to the **1280** (even) Bragg reflection and the peak at 73.8° 2θ is due to

the convolution of the **1185** and **1354** (even) Bragg reflections. However, the 73.6°2θ peak between these two even Bragg reflection peaks is due to the convolution of the **1281**, **1274**, **10.103**, **1362**, **1432** and **988** Bragg reflections all of which are **odd**. This shows neighbouring odd and even Bragg reflections with intensities of the same order of magnitude.

*Figure 5.6. Neighbouring odd and even peaks in the 4K I K-edge powder diffraction pattern for CsI. 73.4°2θ peak due to even **1280**, 73.6°2θ peak due to odd **1281**, **1274**, **10.103**, **1362**, **1432** and **988**, 73.8°2θ peak due to even **1185** and **1354**.*

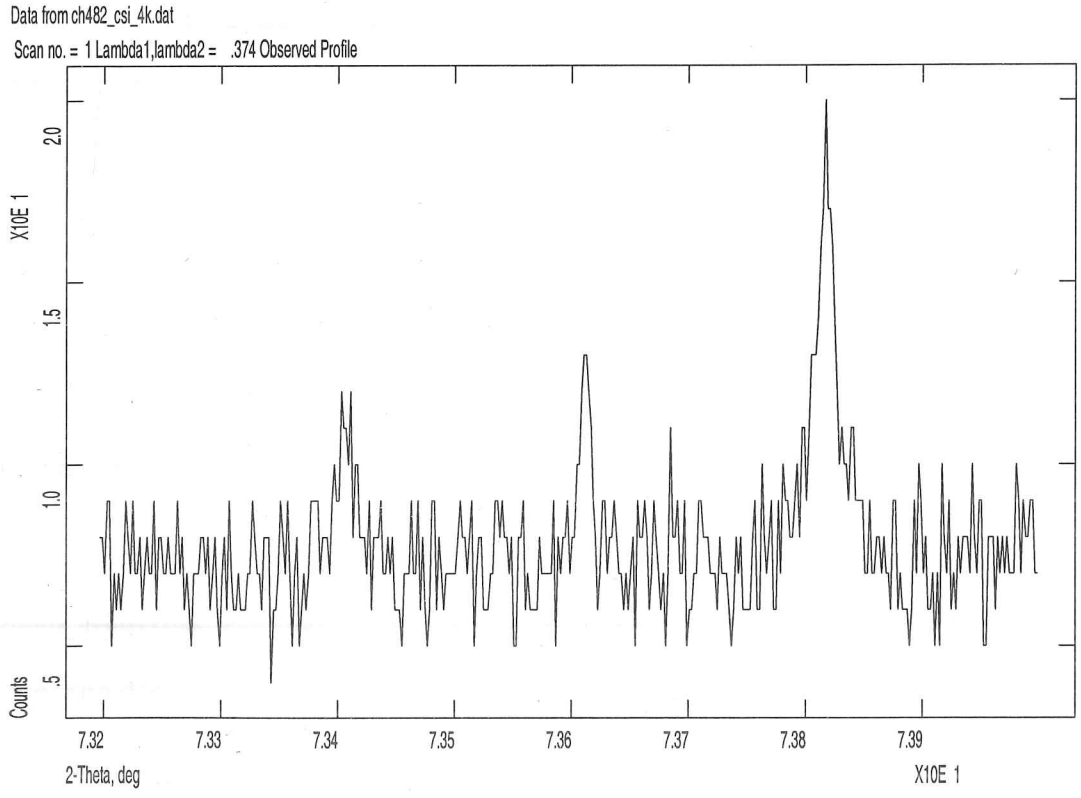


Table 5.3 compares these refined **f'** values with other values from similar refinements in the literature. These refined **f'** resonant scattering parameters are comparable with **f'** values refined from other K-edge synchrotron X-ray structure determinations although the magnitude of the **f'**

values is less than those determined at $L_{III}$-edges as there is a greater cross-section for X-ray absorption at the $L_{III}$-edge compared to the K-edge.

*Table 5.3. Comparison of refined f' parameters from this work with some literature values. P and SC in the final column refer to powder and single crystal structure determinations.*

| Stoichiometry | λ (Å) | edge | f' e/atom | Reference | |
|---|---|---|---|---|---|
| CsI | 0.3453 | Cs K | -6.2(2) | this work | P |
| CsI | 0.374105 | I K | -9.0(1) | this work | P |
| CsI (4K) | 0.37367 | I K | -6.2(2) | this work | P |
| $\alpha$-$Fe_2O_3$ | 1.7452 | Fe K | -6.94(3) | Attfield (1991) | P |
| $Eu_3O_4$ | 1.7771 | Eu $L_{III}$ | -23(3) | Attfield (1990) | P |
| $Yb_2O_3$ | 1.3875 | Yb $L_{III}$ | -21.2(2) | Will et al (1987) | P |
| $\alpha$-$Fe_2PO_5$ | 1.74018 | Fe K | -10.0(2) | Warner et al (1992) | P |
| $GaCl_2$ | 1.19568 | Ga K | -12.9(1) | Wilkinson et al (1991) | P |
| $CsC_4H_5O_6$ | 2.473 | Cs $L_{III}$ | -27.1(9) | Phillips et al (1978) | SC |
| $NaUO_2(NO_3)_3$ | 0.72177 | U $L_{III}$ | -19.4(3) | Templeton and Templeton (1982) | SC |
| NaSm[edta].$8H_2O$ | 1.8455 | Sm $L_{III}$ | -31.5(1) | Templeton et al (1982) | SC |
| NaGd[edta].$8H_2O$ | 1.7019 | Gd $L_{III}$ | -31.9(4) | Templeton et al (1982) | SC |
| $K_2PtCl_4$ | 1.07249 | Pt $L_{III}$ | -23.1(5) | Templeton and Templeton (1985) | SC |

## 5.5. Conclusions.

A resonant scattering test experiment on CsI has been successfully carried out using the high resolution powder diffractometer on beamline BM16 at the ESRF. Cs K-edge and I K-edge resonant scattering parameters have been successfully refined from powder diffraction data collected at room temperature and in a cryostat at 4K. These are the first resonant scattering parameters refined for such a high energy K-edge.

**Chapter 5 - References.**

J.P.Attfield, J. Chem. Soc. Chem. Commun., (1991), 229-231.

J.P.Attfield, Nature, (1990), **343,** 46-49.

D.T.Cromer, J. Appl. Cryst., (1983), **16**, 437.

A.C.Larson and R.B. von Dreele, LANSCE, MS-H805, Los Alamos National Laboratory.

J.C.Phillips, D.H..Templeton, L.K.Templeton and K.J.Hodgson, Science, (1978), **201,** 257-9.

H.M.Rietveld, J. Appl. Cryst., (1969), **2**, 65-71.

T.B.Rymer and P.G. Hambling, Acta Cryst., (1951), **4,** 565.

D.H.Templeton and L.K.Templeton, Acta Cryst., (1982), **A38,** 62-67.

D.H.Templeton and L.K.Templeton, Acta Cryst., (1985), **A41,** 365-371.

L.K.Templeton, D.H.Templeton, R.P.Phizackerley and K.J.Hodgson, Acta Cryst., (1982), **A38,** 74-78.

J.K.Warner, A.K.Cheetham, D.E.Cox and R.B. von Dreele, J. Am. Chem. Soc., (1992), **114,** 6074-6080.

G.Will, N.Masciocchi, M.Hart and W.Parrish, Acta Cryst., (1987), **A43,** 677-683.

A.P.Wilkinson, A.K.Cheetham and D.E.Cox, Acta Cryst., (1991), **B47,** 155-167.

# Chapter 6. Structure determination of 4-(2'3'4'-trifluorophenyl)-1235-dithiadiazolyl.

## 6.1. Introduction.

The group headed by Dr. Jeremy Rawson in the University Chemical Laboratory have been investigating the structure-property relationships of a series of dithiadiazolyl radicals **1** (Rawson et al, 1995; Banister et al, 1997a, Smith et al, 1998ab). In these systems the unpaired spin-density is localised on the $N_2S_2$ ring fragment and to a first approximation the electronic properties of this ring are unaffected by the substituent **R**. The steric and electrostatic properties of the substituent can be used to modify molecular structure. In a majority of cases, these radicals dimerise in the solid state through a 4-centre 2-electron, spin paired interaction at the sulphur atoms (Rawson et al, 1995). The substituent R has been modified to overcome this dimerisation process and use these radicals as building blocks for molecular magnets (Smith et al, 1998a).

It has recently been found that the β-phase of the fluorinated derivative, **1a**, undergoes a phase transition to a weakly ferromagnetic state at 36K (Banister et al, 1996; Palacio et al, 1997bc; Smith et al, 1998ab). In order to achieve a greater understanding of the role which both cyano and fluoro substituents play in structure determination a systematic survey of a series of fluorinated derivatives (Banister et al, 1997a; Smith et al, 1998b). A number of structures have been determined and frequently exhibit ribbon or sheet-like structural motifs (Smith et al, 1998b; Cordes et al, 1992). The low-dimensionality of the structures and weak intermolecular forces make these compounds difficult to prepare as suitable single-crystals for structure determination by X-ray diffraction (Smith, 1998; Antorrena et al, in preparation; Rawson et al, in preparation). An example of such a derivative is 4-(2'3'4'-trifluorophenyl)-1235-dithiadiazolyl, **1b**.

**Samples of 1b were prepared (Smith, 1998) by Nick Smith of the Rawson group.** 2,3,4-trifluorobenzonitrile (0.98g, 6.24mmol) was reacted with $Li[N(SiMe_3)_2]$ (1.10g, 6.58mmol) in $Et_2O$ to yield a black solution. Slow addition of $SCl_2$ at 273 K yielded an immediate orange precipitate, which was stirred for a further 3 hours at room temperature, prior to filtration and drying *in vacuo*. THF (15ml) and Zn/Cu couple (0.380 g, 5.84 mmol) were added and the suspension stirred for 18 hours. The crude product was dried *in vacuo* and purified by vacuum sublimation (363 K, $10^{-2}$ Torr), yielding green-black **1b** (0.306 g, 21%) as polycrystalline bundles which provided satisfactory elemental analyses and mass spectrum. High-purity, polycrystalline samples were prepared by triple sublimation under vacuum. Figure 6.1 shows chemical formulae for dithiadiazolyl radicals discussed in this chapter.

*Figure 6.1. Chemical formulae for dithiadiazolyl radicals.*

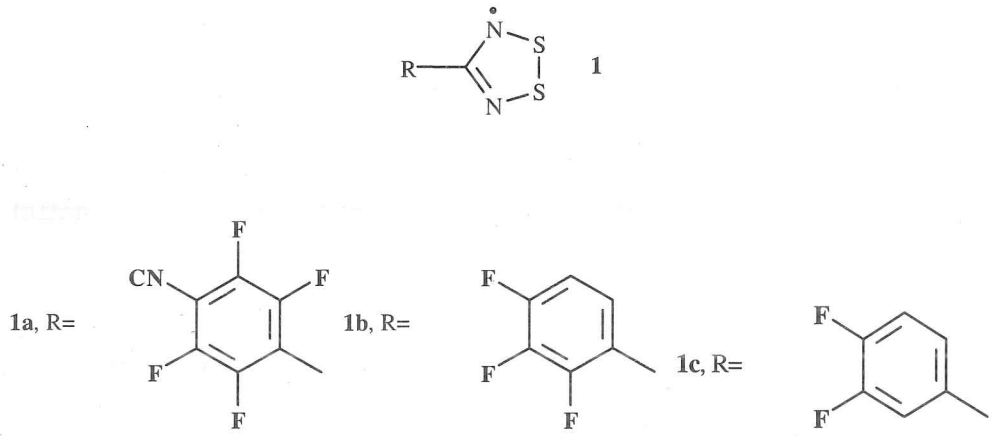

## 6.2. High resolution synchrotron X-ray powder diffraction data collection.

A sample of **1b** was sealed in a 0.5mm diameter borosilicate glass capillary and high resolution synchrotron X-ray powder diffraction data was collected using station 2.3 (see section 2.3.2) at the CCLRC Daresbury Synchrotron Radiation Source. Multiple powder diffraction scans were collected with a synchrotron X-ray wavelength of 1.2000 Å over an angular range of 3-43 $^{\circ}2\theta$, no diffraction peaks could be observed at higher angles. These data were summed and normalised to make the powder diffraction pattern used for this structure determination.

The data were indexed using TREOR (Werner et al, 1985), $P2_1/n$ monoclinic lattice parameters were refined to be a = 11.543(4) Å b = 20.666(8) Å c = 7.045(2) Å and $\beta = 100.35(4)^{\circ}$. These lattice parameters and space group are indicative of two molecules in the asymmetric unit by analogy with the structure of **1c** (Smith et al, 1998a).

## 6.3. Structure determination.

### 6.3.1. Patterson methods.

Structure factors were determined from this powder diffraction data using the Le Bail method (see section 1.2) in GSAS (Larson and von Dreele). These structure factors were used to produce a Patterson map but it was not possible to determine a suitable starting model for Rietveld refinement from this map.

### 6.3.2. 4-(3'4'-difluorophenyl)-1235-dithiadiazolyl analogue starting model.

The difluorinated analogue of **1b**, 4-(3'4'-difluorophenyl)-1235-dithiadiazolyl, **1c** (Smith et al, 1998a) has a monoclinic $P2_1/n$ structure with lattice parameters which are not too dissimilar to those of **1b**, a = 7.543 Å b = 11.193 Å c = 18.688 Å and $\beta = 93.87^{\circ}$. It was thought that this structure could be used as a suitable starting model for Rietveld (Rietveld, 1969) structure refinement.

The lattice parameters of **1c** were first converted to the $P2_1/n11$ space group setting

**1b,** a = 11.543 Å b = 20.666 Å c = 7.045 Å $\beta = 100.35^{\circ}$ - $P12_1/n1$

**1c,** a = 11.193 Å b = 18.688 Å c = 7.543 Å $\alpha = 93.87^{\circ}$ - $P2_1/n11$

so there was an approximate correspondence between the unit cell edges and then the **1c** co-ordinates were transposed into the **1b** unit cell. The **1c** hydrogen in the 2' position was then replaced with a fluorine atom to produce the **1b** starting model for Rietveld refinement. Inter and intramolecular constraints were then applied to this starting model so that interatomic distances in the **1b** starting model were constrained to be the same as those in **1c**.

However, Rietveld refinement using this starting model did not produce a good fit between observed and calculated diffraction patterns and this refinement process had to be abandoned.

### 6.3.3. Global optimisation method.

The global optimisation method (see section 1.6.1) was used by Dr. Kenneth Shankland and

Prof. Bill David of the ISIS division, Rutherford Appleton Laboratory, to produce a suitable starting model.

Correlated integrated intensities were extracted from the powder diffraction pattern using a Pawley refinement (Pawley, 1981) as implemented in program SR15LS (David et al, 1992). A good fit to the data ($\chi^2$=1.7, $R_{wp}$=5.98%) was obtained. An internal co-ordinate description of a single molecule was constructed using standard bond lengths, angles and torsions, see Table 6.1.

*Table 6.1. An internal co-ordinate description of a single molecule. The final three columns contain the atom numbers corresponding to the distance, angle and torsion from the current atom respectively. For example, atom 7 lies at a distance of 1.4 Å from atom 2, makes an angle of 120° with atoms 2 and 1, and makes a torsion angle of 180° with atoms 2, 1 and 6.*

| Atom | Distance | Angle | Torsion | $\#_D$ | $\#_A$ | $\#_T$ |
|---|---|---|---|---|---|---|
| C | 0.000 | 0 | 0 | 0 | 0 | 0 |
| C | 1.400 | 120.0 | 0 | 1 | 0 | 0 |
| C | 1.400 | 120.0 | 0 | 2 | 1 | 0 |
| C | 1.400 | 120.0 | 0 | 3 | 2 | 1 |
| C | 1.400 | 120.0 | 0 | 4 | 3 | 2 |
| C | 1.400 | 120.0 | 0 | 5 | 4 | 3 |
| F | 1.370 | 120.0 | 180.0 | 2 | 1 | 6 |
| F | 1.370 | 120.0 | 180.0 | 3 | 2 | 1 |
| F | 1.370 | 120.0 | 180.0 | 4 | 3 | 2 |
| H | 1.000 | 120.0 | 180.0 | 5 | 4 | 3 |
| H | 1.000 | 120.0 | 180.0 | 6 | 5 | 4 |
| C | 1.473 | 120.0 | 180.0 | 1 | 6 | 5 |
| N | 1.345 | 119.0 | variable* | 12 | 1 | 6 |
| N | 1.345 | 119.0 | 180.0 | 12 | 1 | 13 |
| S | 1.630 | 114.0 | 0 | 13 | 12 | 14 |
| S | 1.630 | 114.0 | 0 | 14 | 12 | 13 |

* This torsion angle was varied throughout the structure solution

The position, orientation and conformation of two such molecules within the refined unit cell were postulated and the level of agreement between the trial structure and the experimental

diffraction data quantified by a global optimisation model building method (David et al, 1998). Table 6.2 shows the results of the global optimisation.

*Table 6.2. Details of the simulated annealing global optimisation structure solution.*

| | |
|---|---|
| Data range used | 5°-35° |
| Number of intensities extracted | 221 |
| Internal degrees of freedom (per molecule) | 1 |
| External degrees of freedom (per molecule) | 7 |
| Total number of trial structures generated | 1,444,800 |
| Total time to solution (minutes) | 24.42 |
| Time per structure (milliseconds) | 1.01 |
| Initial temperature ($\chi^2$ units) | 200.0 |
| Final temperature ($\chi^2$ units) | 30.4 |
| Initial $\chi^2$ for intensities | 660.6 |
| Final $\chi^2$ for intensities | 19.1 |
| Average deviation from refined structure | 0.061 Å |
| Maximum deviation from refined structure | 0.110 Å |

## 6.4. Rietveld refinement.

The structure was refined using the global optimisation starting model by the Rietveld method using GSAS. It was possible to refine all atomic co-ordinates independently in this refinement but this produced a structure which did not have flat trifluorophenyl or dithiadiazolyl rings, this was not thought to be a chemically sensible structure. The asymmetric unit of **1b** comprises two crystallographically independent molecules, with each molecule containing a dithiadiazolyl ring and a trifluorophenyl ring. Each atom in each ring was given the same shift in the refinement to keep each ring flat. 28 different parameters were refined, isotropic temperature factors were refined for all atoms with the same value for sites with the same element. Refined structural parameters are given as Table 6.3. Table 6.4 shows selected bond lengths and angles for this structure. Figure 6.2 shows that the Rietveld difference plot for this refinement has a close match between the observed and calculated powder diffraction patterns.

*Table 6.3. Refined structural parameters for 4-(2'3'4'-trifluorophenyl)-1235-dithiadiazolyl.*

a = 11.5452(3) Å b = 20.6567(5) Å c = 7.0510(1) Å  = 100.368(1)° V = 1654.1(1) Å$^3$

Space group $P2_1/n$. X-ray density: 1.873 g cm$^{-3}$

$R_{wp}$ = 0.0782 $R_p$ = 0.0632 $\chi^2$ = 1.417.

| ATOM | x | y | z | Uiso (Å$^2$) |
|---|---|---|---|---|
| S1 | .3982(6) | .0561(5) | .8091(7) | 0.068(4) |
| S2 | .2264(6) | .0886(5) | .7814(7) | 0.068(4) |
| S3 | .2065(7) | .0974(5) | .3100(8) | 0.068(4) |
| S4 | .3821(7) | .0712(5) | .3464(8) | 0.068(4) |
| F1 | .397(1) | -.1416(6) | .8004(9) | 0.081(4) |
| F2 | .316(1) | -.2672(6) | .7323(9) | 0.081(4) |
| F3 | .079(1) | -.2900(6) | .5973(9) | 0.081(4) |
| F4 | .3854(9) | -.1265(6) | .376(1) | 0.081(4) |
| F5 | .3204(9) | -.2536(6) | .287(1) | 0.081(4) |
| F6 | .1009(9) | -.2807(6) | .070(1) | 0.081(4) |
| N1 | .3626(6) | -.0198(5) | .7711(7) | 0.065(8) |
| N2 | .1672(6) | .0172(5) | .7396(7) | 0.065(8) |
| N3 | .1563(7) | .0247(5) | .2554(8) | 0.065(8) |
| N4 | .3560(7) | -.0051(5) | .2968(8) | 0.065(8) |
| C1 | .201(1) | -.1009(6) | .6997(9) | 0.090(6) |
| C2 | .280(1) | -.1533(6) | .7336(9) | 0.090(6) |
| C3 | .239(1) | -.2164(6) | .6992(9) | 0.090(6) |
| C4 | .119(1) | -.2279(6) | .6309(9) | 0.090(6) |
| C5 | .040(1) | -.1759(6) | .5971(9) | 0.090(6) |
| C6 | .081(1) | -.1124(6) | .6315(9) | 0.090(6) |
| C7 | .2459(6) | -.0309(5) | .7394(7) | 0.090(6) |
| C8 | .1989(9) | -.0894(6) | .204(1) | 0.090(6) |
| C9 | .2769(9) | -.1399(6) | .269(1) | 0.090(6) |
| C10 | .2440(9) | -.2042(6) | .224(1) | 0.090(6) |
| C11 | .1331(9) | -.2179(6) | .114(1) | 0.090(6) |
| C12 | .0551(9) | -.1674(6) | .0494(1) | 0.090(6) |
| C13 | .0880(9) | -.1031(6) | .0943(1) | 0.090(6) |
| C14 | .2408(7) | -.0201(5) | .2552(8) | 0.090(6) |
| H1 | -.046(1) | -.1842(6) | .5483(9) | 0.24(9) |
| H2 | .024(1) | -.0753(6) | .6073(9) | 0.24(9) |
| H3 | -.0241(9) | -.1771(6) | -.029(1) | 0.24(9) |
| H4 | .0322(9) | -.0670(6) | .048(1) | 0.24(9) |

*Table 6.4. Bond lengths and angles for 4-(2'3'4'-trifluorophenyl)-1235-dithiadiazolyl.*

Intramolecular distances (Å).

| ATOMS | DIST | ATOMS | DIST | ATOMS | DIST | ATOMS | DIST |
|---|---|---|---|---|---|---|---|
| S1-S2 | 2.07(1) | C1-C6 | 1.40(2) | S3-S4 | 2.07(1) | C8-C13 | 1.40(1) |
| S1-N1 | 1.63(2) | C1-C2 | 1.41(2) | S3-N3 | 1.63(1) | C8-C9 | 1.40(2) |
| S2-N2 | 1.63(2) | C2-C3 | 1.39(2) | S4-N4 | 1.63(1) | C9-C10 | 1.40(2) |
| F1-C2 | 1.37(2) | C3-C4 | 1.40(2) | F4-C9 | 1.37(1) | C10-C11 | 1.40(1) |
| F2-C3 | 1.37(2) | C4-C5 | 1.40(2) | F5-C10 | 1.37(2) | C11-C12 | 1.40(2) |
| F3-C4 | 1.37(2) | C5-C6 | 1.40(2) | F6-C11 | 1.37(2) | C12-C13 | 1.40(2) |
| N1-C7 | 1.35(1) | H1-C5 | 1.00(2) | N3-C14 | 1.35(1) | H3-C12 | 1.00(2) |
| N2-C7 | 1.35(2) | H2-C6 | 1.00(2) | N4-C14 | 1.35(1) | H4-C13 | 1.00(2) |
| C1-C7 | 1.54(2) | | | C8-C14 | 1.53(2) | | |

Intramolecular angles (degrees).

| ATOMS | ANGLE | ATOMS | ANGLE |
|---|---|---|---|
| S2-S1-N1 | 95.0(6) | S4-S3-N3 | 95.1(6) |
| S1-S2-N2 | 95.0(7) | S3-S4-N4 | 95.0(6) |
| S1-N1-C7 | 114.0(9) | S3-N3-C14 | 114.0(7) |
| S2-N2-C7 | 114.0(7) | S4-N4-C14 | 114.0(8) |

Intermolecular S-S distances (Å).
S1-S4 3.252(8), S2-S3 3.298(8).
Torsion angle N1-C7-C1-C2 12.25°.
Torsion angle C9-C8-C14-N4 23.03°.

*Figure 6.2. Rietveld difference plot for structure refinement of 4-(2'3'4'-trifluorophenyl)-1235-dithiadiazolyl.*

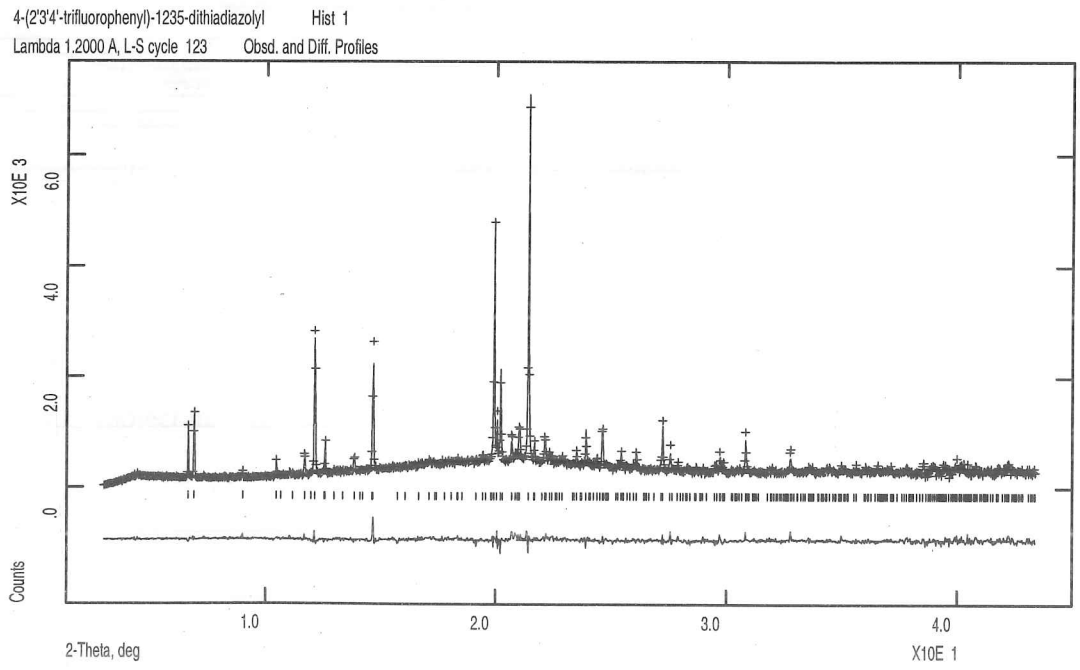

*Table 6.4. Bond lengths and angles for 4-(2'3'4'-trifluorophenyl)-1235-dithiadiazolyl.*

Intramolecular distances (Å).

| ATOMS | DIST | ATOMS | DIST | ATOMS | DIST | ATOMS | DIST |
|---|---|---|---|---|---|---|---|
| S1-S2 | 2.07(1) | C1-C6 | 1.40(2) | S3-S4 | 2.07(1) | C8-C13 | 1.40(1) |
| S1-N1 | 1.63(2) | C1-C2 | 1.41(2) | S3-N3 | 1.63(1) | C8-C9 | 1.40(2) |
| S2-N2 | 1.63(2) | C2-C3 | 1.39(2) | S4-N4 | 1.63(1) | C9-C10 | 1.40(2) |
| F1-C2 | 1.37(2) | C3-C4 | 1.40(2) | F4-C9 | 1.37(1) | C10-C11 | 1.40(1) |
| F2-C3 | 1.37(2) | C4-C5 | 1.40(2) | F5-C10 | 1.37(2) | C11-C12 | 1.40(2) |
| F3-C4 | 1.37(2) | C5-C6 | 1.40(2) | F6-C11 | 1.37(2) | C12-C13 | 1.40(2) |
| N1-C7 | 1.35(1) | H1-C5 | 1.00(2) | N3-C14 | 1.35(1) | H3-C12 | 1.00(2) |
| N2-C7 | 1.35(2) | H2-C6 | 1.00(2) | N4-C14 | 1.35(1) | H4-C13 | 1.00(2) |
| C1-C7 | 1.54(2) | | | C8-C14 | 1.53(2) | | |

Intramolecular angles (degrees).

| ATOMS | ANGLE | ATOMS | ANGLE |
|---|---|---|---|
| S2-S1-N1 | 95.0(6) | S4-S3-N3 | 95.1(6) |
| S1-S2-N2 | 95.0(7) | S3-S4-N4 | 95.0(6) |
| S1-N1-C7 | 114.0(9) | S3-N3-C14 | 114.0(7) |
| S2-N2-C7 | 114.0(7) | S4-N4-C14 | 114.0(8) |

Intermolecular S-S distances (Å).
S1-S4 3.252(8), S2-S3 3.298(8).
Torsion angle N1-C7-C1-C2 12.25°.
Torsion angle C9-C8-C14-N4 23.03°.

*Figure 6.2. Rietveld difference plot for structure refinement of 4-(2'3'4'-trifluorophenyl)-1235-dithiadiazolyl.*

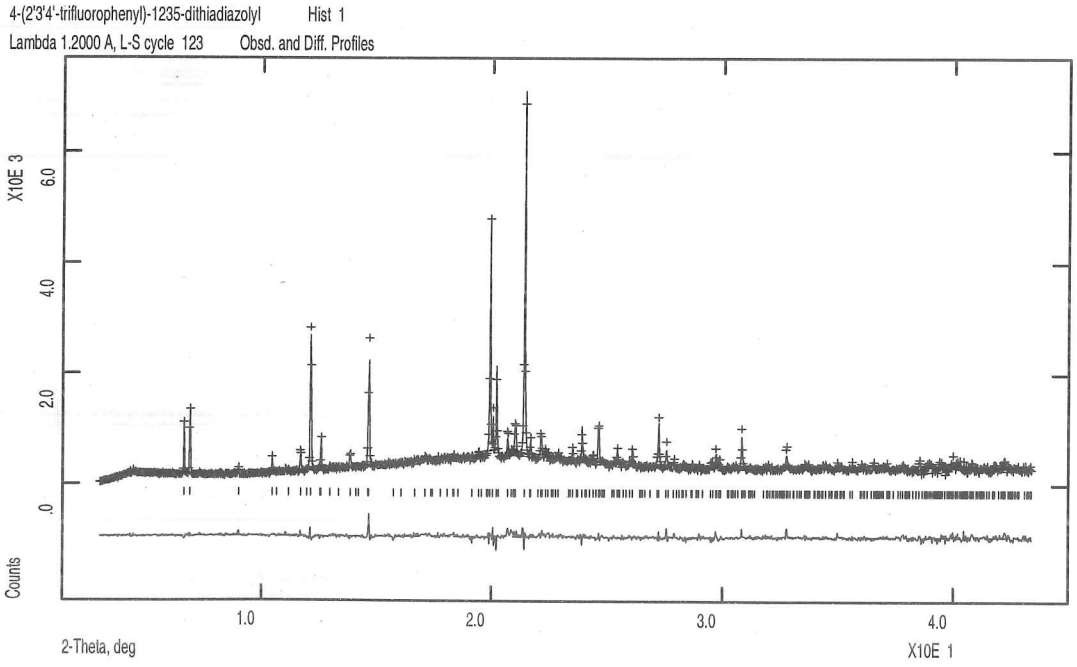

## 6.5. Discussion.

The two crystallographically independent molecules of are **1b** lined via a $\pi^*$-$\pi^*$ interaction between singly-occupied molecular orbitals in a cis-antarafacial geometry with S...S distances at 3.252(6) and 3.298(7) Å respectively. Figure 6.3 shows how these two molecules are arranged in the asymmetric unit. This interaction is the most common structural motif in the solid state structures of aromatic derivatives of **1**. These pairs of dimers stack down the crystallographic **c** axis with longer inter-dimer S...S contacts at 3.835(8) and 3.776(7) Å.

*Figure 6.3. Asymmetric unit of **1b** showing atom labelling scheme.*

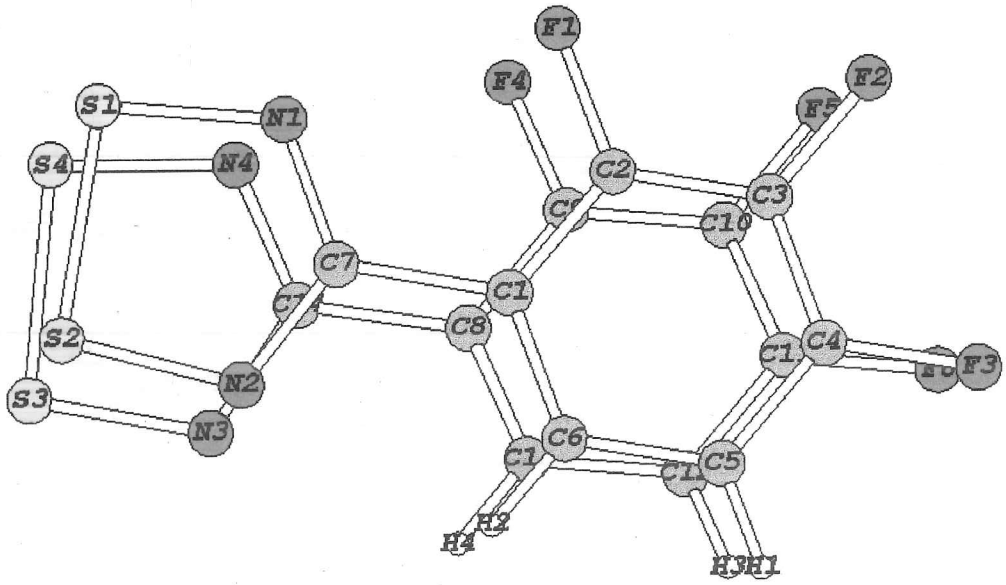


Within the molecular **ab** plane, molecules are linked together in a ribbon-like structure, maximising the $S^+...F^-$ molecular dipole interactions (Rawson et al, 1998b) in a manner reminiscent of other 3,4-difluorophenyl derivatives of **1**, (Smith, 1998; Rawson et al, in preparation), see Figure 6.4. Between these chains there are electrostatic $S^+...N^-$ and $H^+...F^-$

interactions between heterocyclic rings which induce neighbouring chains to align anti-parallel.

*Figure 6.4. View of* ***1b*** *in the* ***ab*** *plane, illustrating the dipolar* $S^{+}...F^{-}$ *interactions along the (horizontal) crystallographic* ***b*** *axis and the* $S^{+}...N^{-}$ *and* $H^{+}...F^{-}$ *interactions along the (vertical) crystallographic* ***a*** *axis. The unit cell edges are marked as blue lines.*

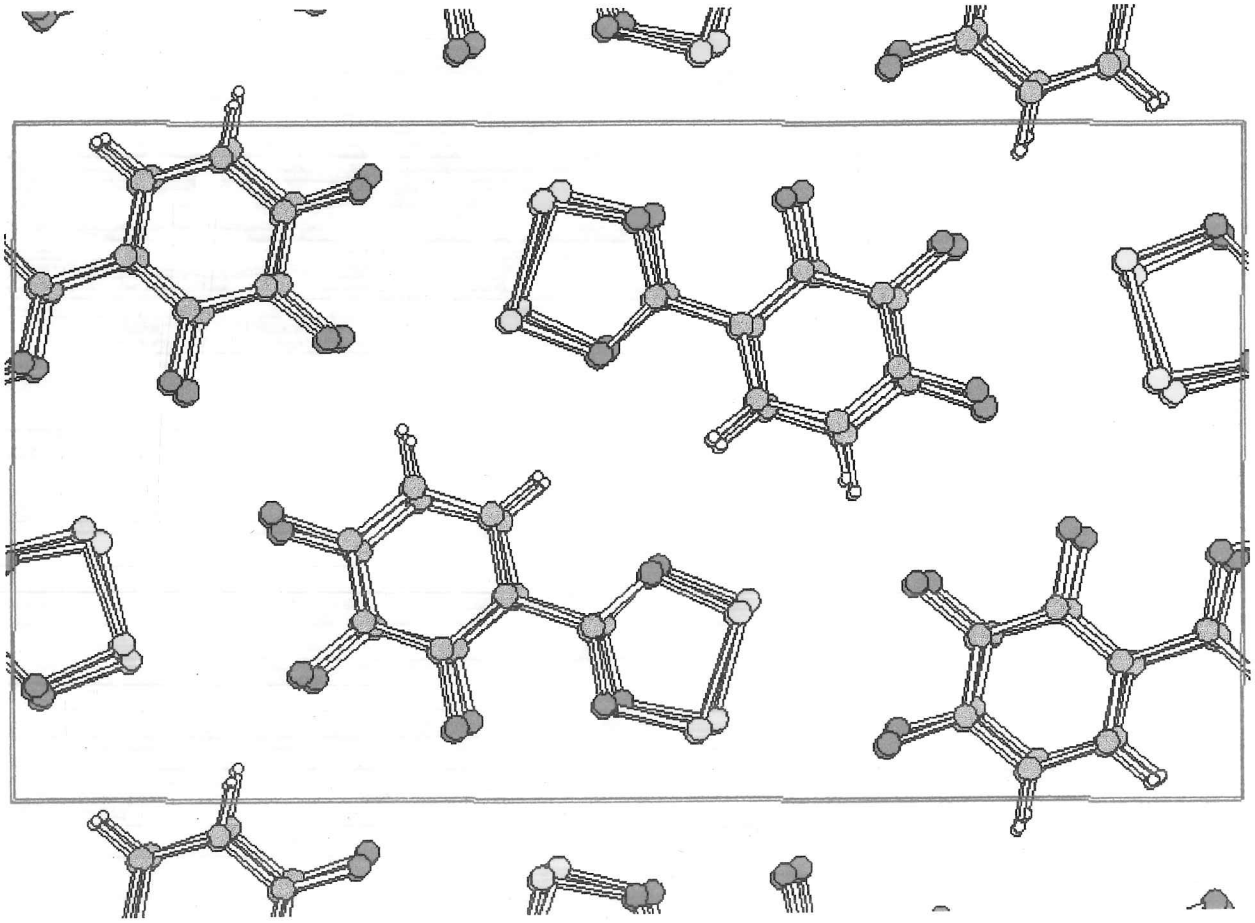

Figure 6.5 shows a plot of the structure in the **bc** plane, notice the torsional twist between the trifluorophenyl and dithiadiazolyl rings. Figure 6.6 shows the structure of **1c** for comparison, notice how the molecules are offset in this structure with no $\pi^{*}$-$\pi^{*}$ interaction between neighbouring molecules and no dimerisation. This explains why it was not possible to get a suitable Rietveld starting model for **1b** using the structure of **1c**. Torsion angles between the trifluorophenyl and dithiadiazolyl rings in each **1b** molecule are 12.25 and 24.32 degrees.

*Figure 6.5. View of* ***1b*** *in the* ***bc*** *plane, notice the torsional twist between the two heterocyclic trifluorophenyl and dithiadiazolyl rings. The crystallographic* ***b*** *axis is in the horizontal plane and the* ***c*** *axis is vertical, The unit cell edges are marked as blue lines.*

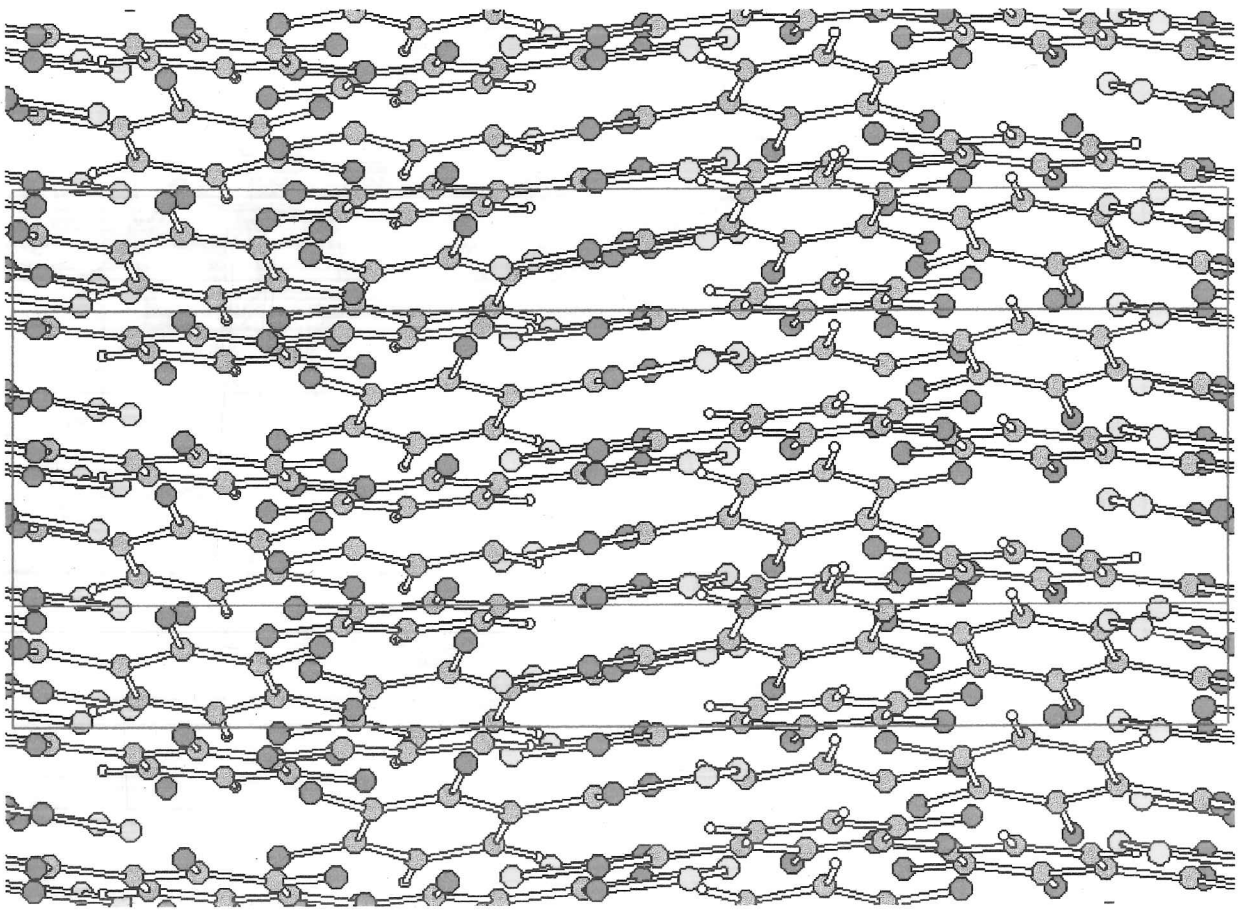

## 6.6. Conclusions.

The crystal structure of 4-(2'3'4'-trifluorophenyl)-1235-dithiadiazolyl has been determined from high resolution synchrotron X-ray powder diffraction data using the global optimisation model building method and Rietveld refinement. This material exists as a dimer with $\pi^{*}$-$\pi^{*}$ interactions between neighbouring heterocyclic dithiadiazolyl rings and between neighbouring

*Figure 6.6. View of* ***1c*** *in the* ***bc*** *plane, notice how the molecules are offset unlike in 4-(2'3'4'-trifluorophenyl)-1235-dithiadiazolyl. The crystallographic* ***c*** *axis is in the horizontal plane and the* ***b*** *axis is vertical, The unit cell edges are marked as blue lines.*

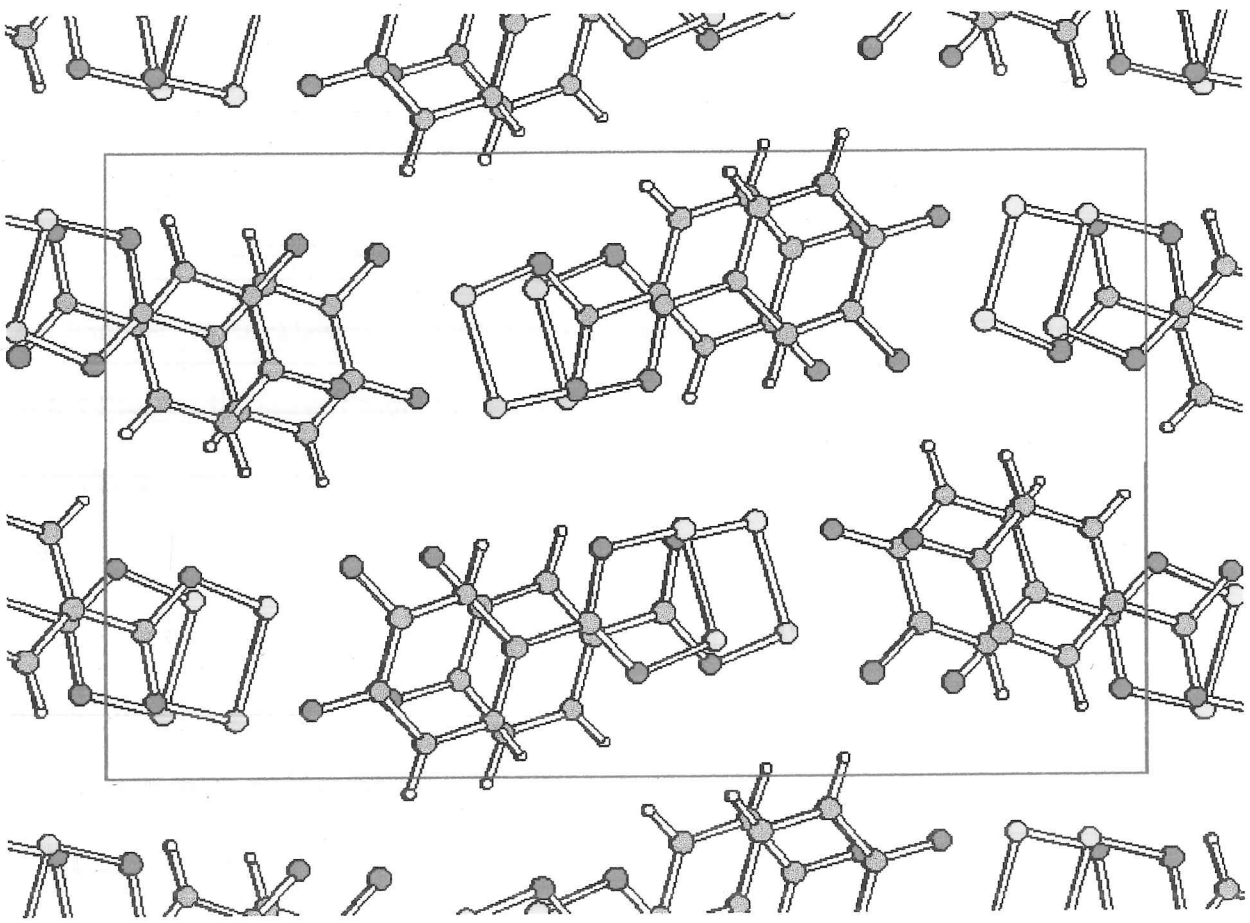

trifluorophenyl rings, this is not the same interaction that exists in the analogous 4-(3'4'-difluorophenyl)-1235-dithiadiazolyl material.

This is one of the first structures determined using the global optimisation model building method which has two separate molecules in the asymmetric unit.

## Chapter 6 - References.

G.Antorrena, A.J.Banister, N.Bricklebank, W.Clegg, R.B.Copley, M.R.J.Elsegood, A.E.Goata, J.A.K.Howard, I.Lavender, F.Palacio, J.M.Rawson, and J.N.B.Smith, J.Mat.Chem., in preparation.

A.J.Banister, A.S.Batsanov, O.G.Dawe, P.L.Herbertson, J.A.K.Howard, S.Lynn, I.May, J.N.B.Smith, J.M.Rawson, T.E.Rogers, B.K.Tanner, G.Antorrena and F.Palacio, J.Chem. Soc., Dalton Trans., (1997), 2539-41.

A.J.Banister, N.Bricklebank, I.Lavender, J.M.Rawson, C.I.Gregory. B.K.Tanner, W.Clegg and M.R.J.Elsegood, Angew. Chem. Int. Ed. Engl., (1996), **35**, 2533-5.

A.W.Cordes, R.C.Haddon, R.G.Hicks, R.T.Oakley and T.T.M.Palstra, Inorg. Chem., (1992), **31**, 1802-8.

W. I. F. David, R. M. Ibberson and J. C. Matthewman, (1992), Rutherford Appleton Laboratory Report, RAL-92-032.

W. I. F. David, K. Shankland and N. Shankland, Chem. Commun., (1998), 931.

A.C.Larson and R.B. von Dreele, LANSCE, MS-H805, Los Alamos National Laboratory.

F.Palacio, G.Antorrena, M.Castro, R.Burriel, J.M.Rawson, J.N.B.Smith, N.Bricklebank, J.Novoa and C.Ritter, Phys. Rev. Lett,. (1997), **79**, 2336-9.

F.Palacio, M.Castro, G.Antorrena, R.Burriel, C.Ritter, N.Bricklebank, J.M.Rawson, and J.N.B.Smith, Mol. Cryst. Liq. Cryst. (1997), **306**, 293-300.

G. S. Pawley, J. Appl. Cryst., (1981), **14**, 357.

J.M.Rawson, A.J.Banister and I Lavender, Adv. Heterocycl. Chem, (1995), **62**, 137-247.

J.M.Rawson, J.N.B.Smith, A.J.Banister, A.S.Batsunov and J.A.K.Howard, J.Chem.Soc., Dalton Trans, in preparation.

H.M.Rietveld, J. Appl. Cryst., (1969), **2**, 65-71.

J.N.B.Smith, PhD thesis, University of Cambridge, (1998).

J.N.B.Smith, J.M.Rawson, G.Antorrena and F.Palacio, J.Mat. Chem., submitted for publication (1998).

J.N.B.Smith, J.M.Rawson, G.Antorrena and F.Palacio, Mol. Cryst. Liq. Cryst. (Proc. VI Int. Conf. Mol. Magn.), accepted for publication (1998).

P.E.Werner, L.Eriksson and M.Westdahl. J. Appl. Cryst., (1985), **18(5)**, 367-370.

## Appendix A - Rietveld difference plots for $Fe_2BO_4$ 301-337 K.

*Figure A.1, Rietveld difference plot for $Fe_2BO_4$ at 301 K, image plate data collected on station 9.1 of the Daresbury SRS, $\lambda$ = 0.6920 Å.*

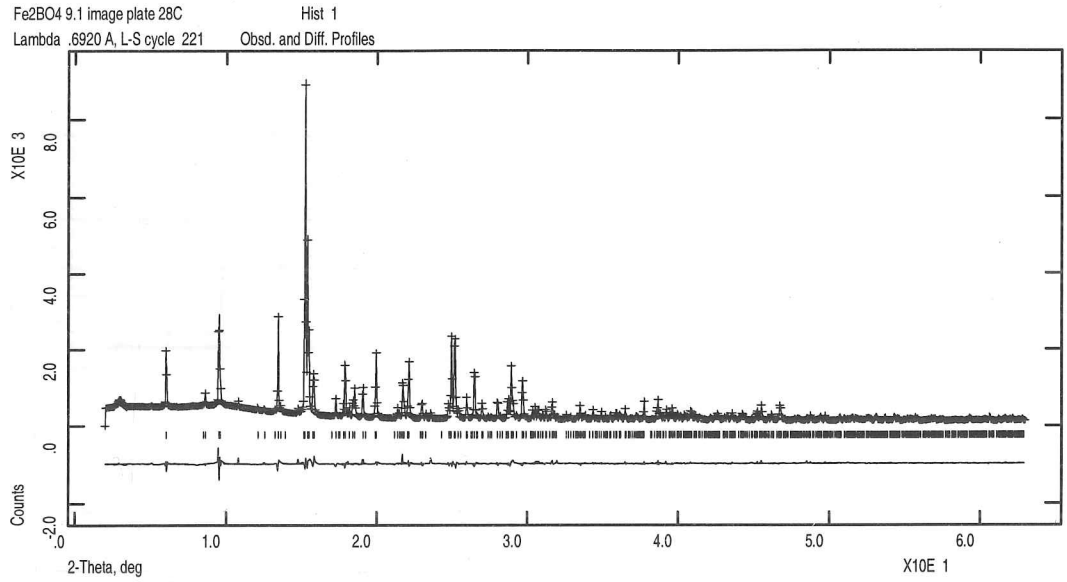


*Figure A.2, Rietveld difference plot for $Fe_2BO_4$ at 307 K, image plate data collected on station 9.1 of the Daresbury SRS, $\lambda$ = 0.6920 Å.*

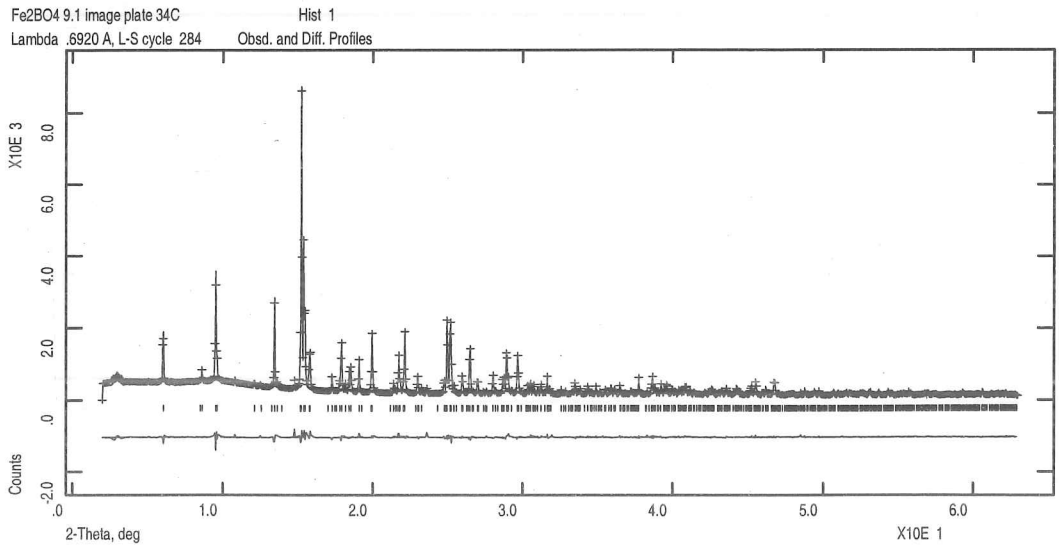

*Figure A.3, Rietveld difference plot for $Fe_2BO_4$ at 316 K, image plate data collected on station 9.1 of the Daresbury SRS, $\lambda$ = 0.6920 Å.*

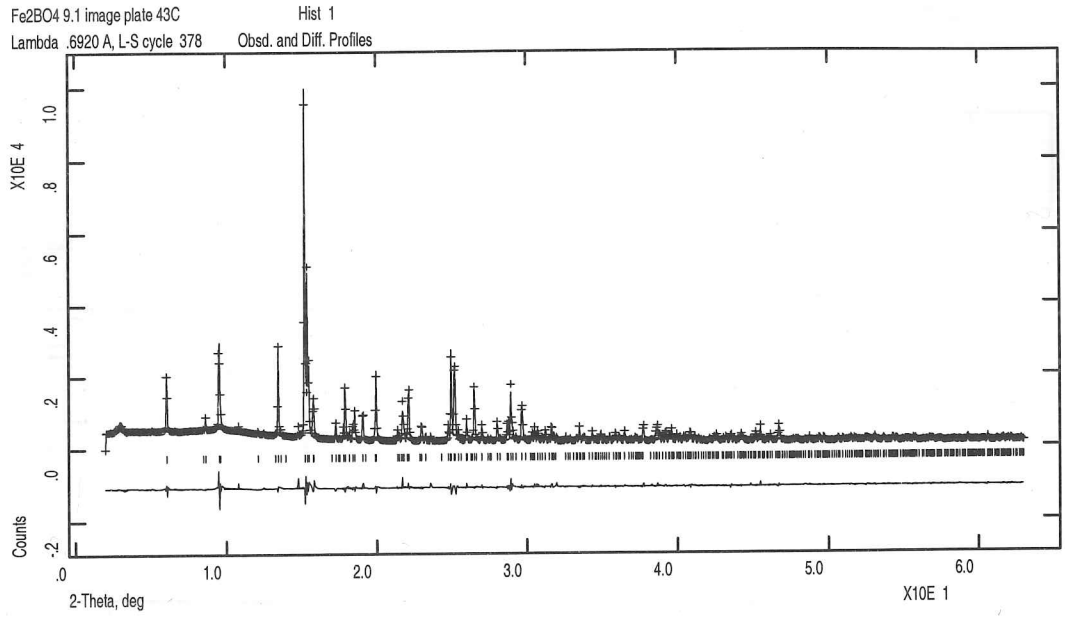


*Figure A.4, Rietveld difference plot for $Fe_2BO_4$ at 325 K, image plate data collected on station 9.1 of the Daresbury SRS, $\lambda$ = 0.6920 Å.*

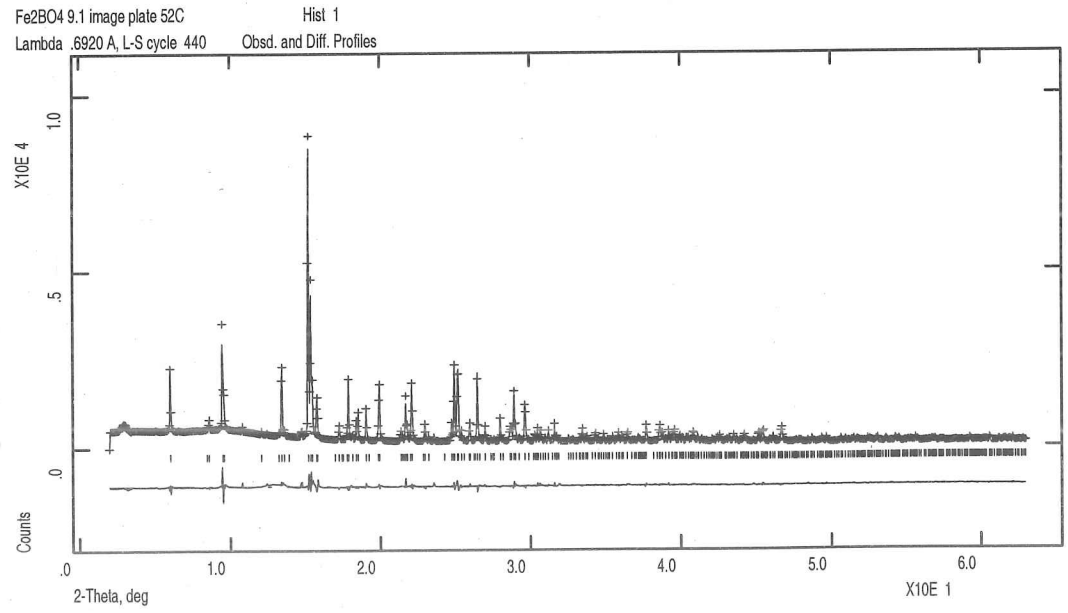

*Figure A.5, Rietveld difference plot for $Fe_2BO_4$ at 332 K, image plate data collected on station 9.1 of the Daresbury SRS, $\lambda = 0.6920$ Å.*

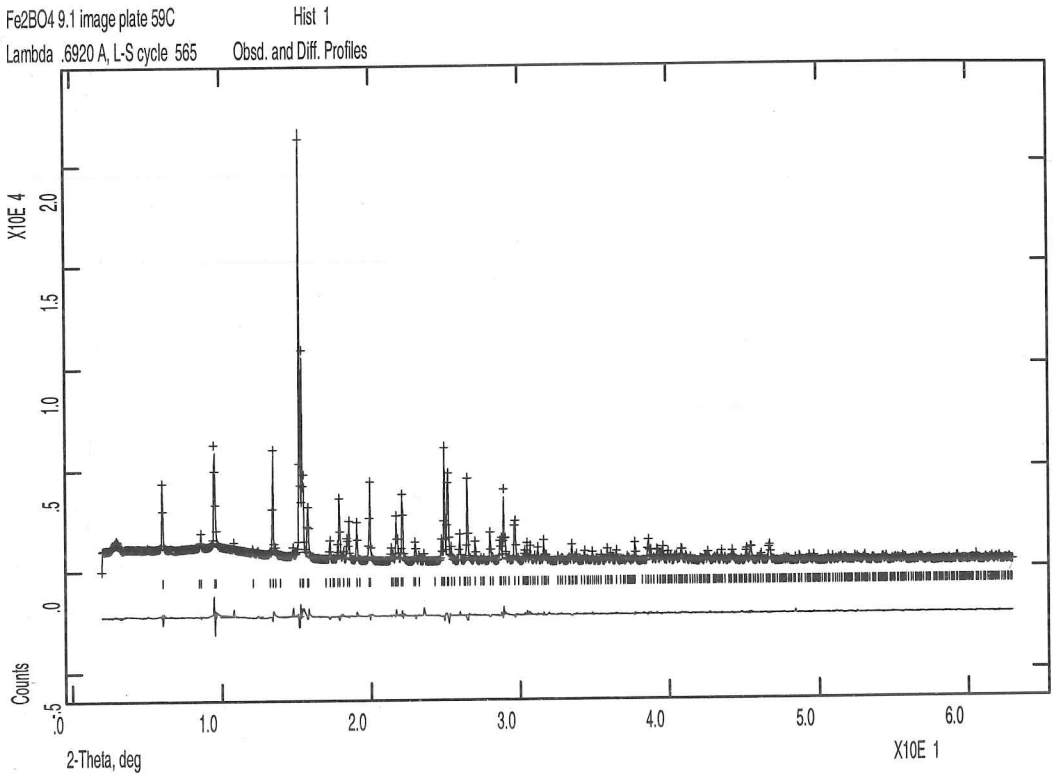

*Figure A.6, Rietveld difference plot for $Fe_2BO_4$ at 337 K, data collected using a scintillation counter detector on station 9.1 of the Daresbury SRS, $\lambda$ = 0.9844 Å.*

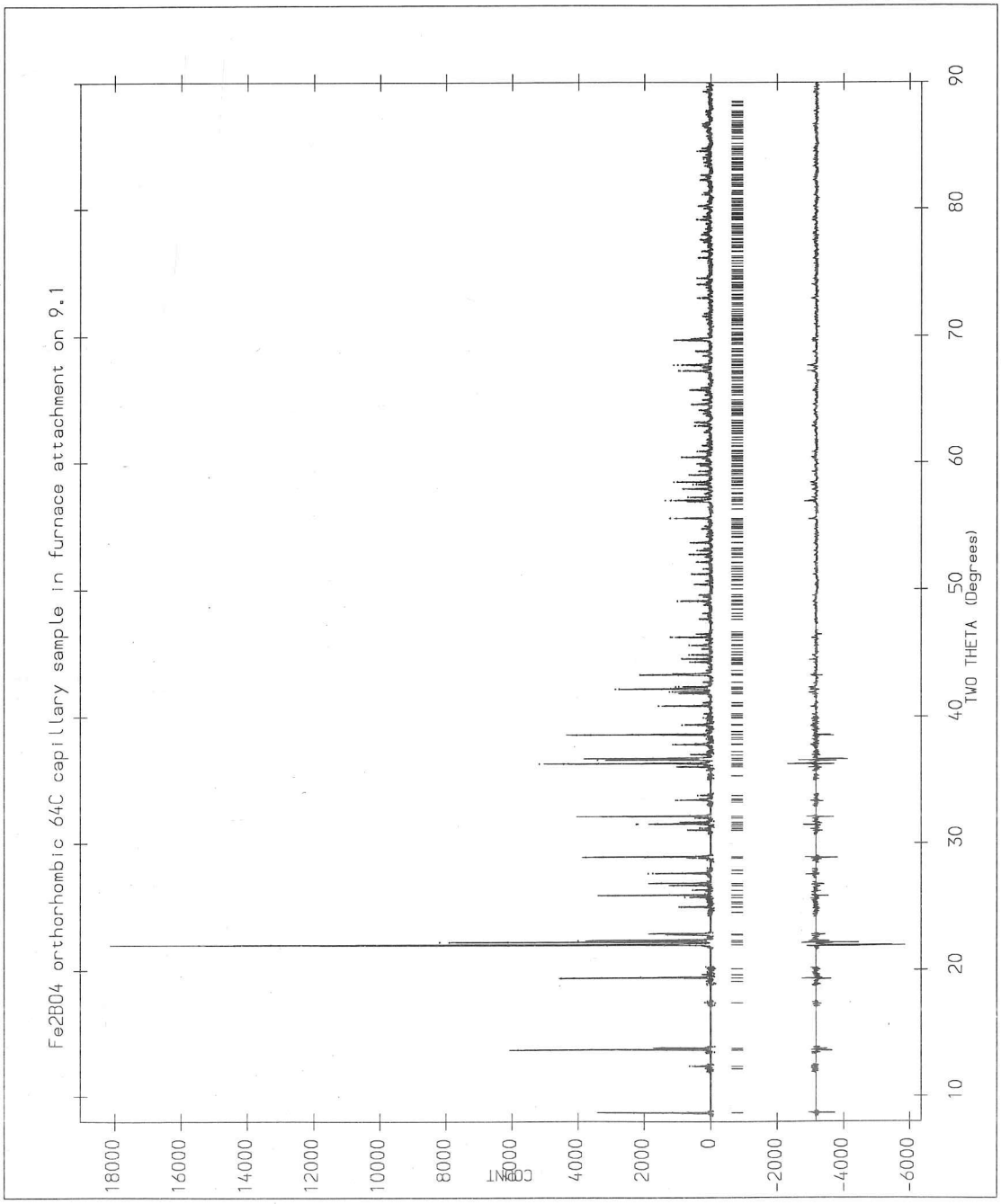

## Appendix B - Publications and conference presentations of work in this thesis.

Crystal Structure and Magnetic Properties of $Fe_2OBO_3$.

**A.M.T.Bell,** L.M.Rodriguez-Martinez, J.P.Attfield, R.J.Cernik, J.F.Clarke and D.A.Perkins. Materials Science Forum, (1998), **278-281,** 708-713.

Synthesis, Structure and Properties of a semivalent Iron Oxoborate, $Fe_2OBO_3$.

J.P.Attfield, **A.M.T.Bell,** L.M.Rodriguez-Martinez, J.M.Greneche, R.Retoux, M.Leblanc, R.J.Cernik, J.F.Clarke and D.A.Perkins. Journal of Materials Chemistry, (1999), 9, 205-209.

Wigner Nanocrystals in $Fe_2OBO_3$. J.P.Attfield, **A.M.T.Bell,** L.M.Rodriguez-Martinez, J.M.Greneche, R.J.Cernik, J.F.Clarke and D.A.Perkins. Nature, (1998), **396,** 655-658.

Synchrotron X-ray powder diffraction study of 4-(2',3',4'-trifluorophenyl)-1,2,3,5-dithiadiazolyl; Crystal structure determination using a global optimisation method.

**A.M.T.Bell,** J.N.B.Smith, J.P.Attfield, J.M.Rawson, K.Shankland and W.I.F.David. Submitted to New J. Chem.

SRS users meeting, CCLRC Daresbury Laboratory, September 1996. (Poster)

Royal Society of Chemistry Polar Solids meeting, University of Sussex, December 1996. (Poster)

British Crystallographic Association Spring meeting, University of Leeds, April 1997. (Poster)

5th European Powder Diffraction Conference, Parma, Italy, May 1997. (Poster)